JOURNAL OF RESEARCH

OF THE U.S. GEOLOGICAL SURVEY

SEPTEMBER–OCTOBER 1977
VOLUME 5, NUMBER 5

Scientific notes and summaries of investigations in geology, hydrology, and related fields

U.S. DEPARTMENT OF THE INTERIOR

UNITED STATES DEPARTMENT OF THE INTERIOR
CECIL D. ANDRUS, Secretary
GEOLOGICAL SURVEY
V. E. McKelvey, Director

For sale by Superintendent of Documents, U.S. Government Printing Office, Washington, DC 20402. Annual subscription rate, $18.90 (plus $4.75 for foreign mailing). Make check or money order payable to Superintendent of Documents. Send all subscription inquiries and address changes to Superintendent of Documents at above address.

Purchase single copy ($3.15) from Branch of Distribution, U.S. Geological Survey, 1200 South Eads Street, Arlington, VA 22202. Make check or money order payable to U.S. Geological Survey.

Library of Congress Catalog-card No. 72-600241.

The Journal of Research is published every 2 months by the U.S. Geological Survey. It contains papers by members of the Geological Survey and their professional colleagues on geologic, hydrologic, topographic, and other scientific and technical subjects.

Correspondence and inquiries concerning the Journal (other than subscription inquiries and address changes) should be directed to Anna M. Orellana, Managing Editor, Journal of Research, Publications Division, U.S. Geological Survey, 321 National Center, Reston, VA 22092.

Papers for the Journal should be submitted through regular Division publication channels.

The Secretary of the Interior has determined that the publication of this periodical is necessary in the transaction of the public business required by law of this Department. Use of funds for printing this periodical has been approved by the Director of the Office of Management and Budget through June 30, 1980.

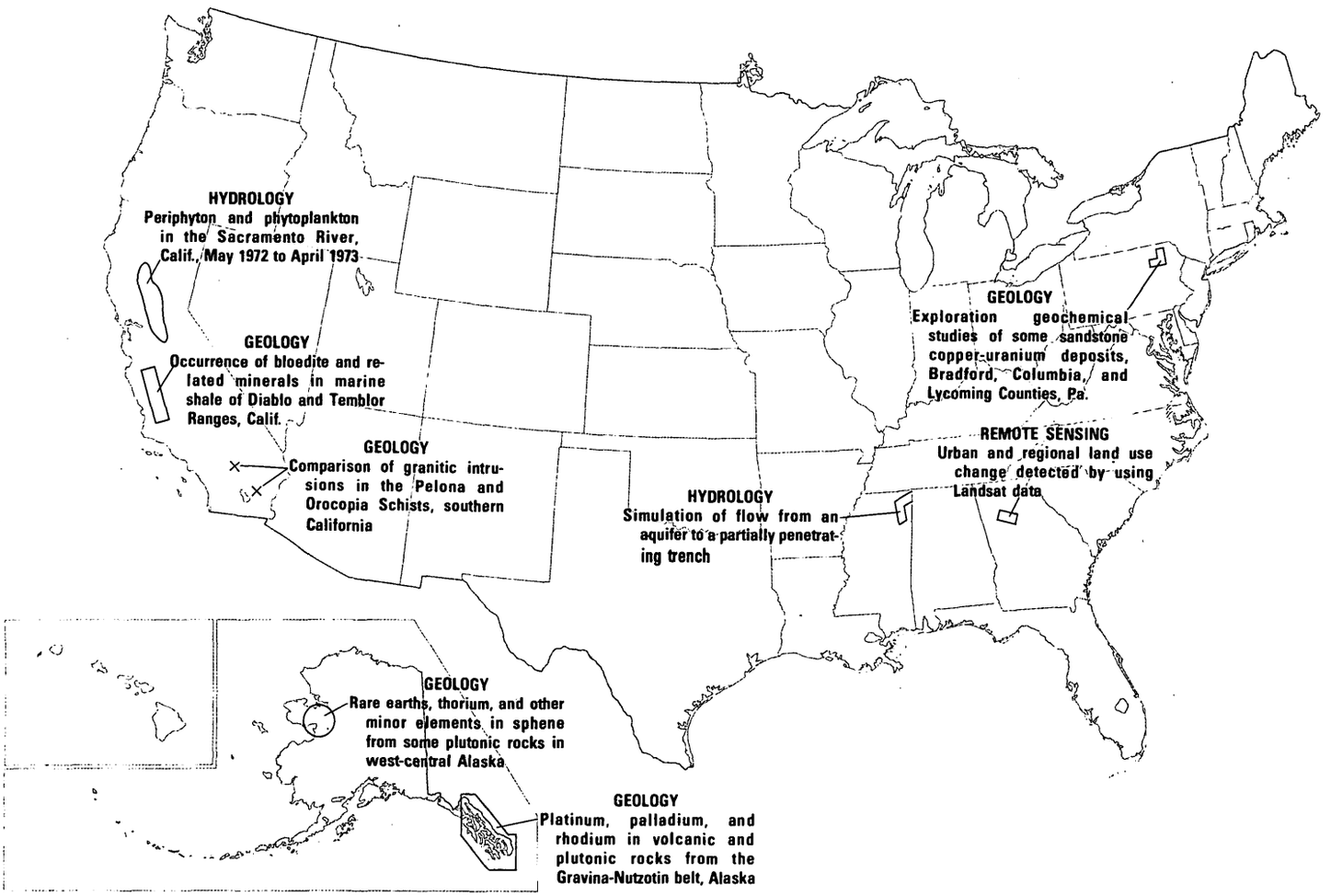

GEOGRAPHIC INDEX TO ARTICLES

See "Contents" for articles concerning areas outside the United States and articles without geographic orientation.

JOURNAL OF RESEARCH

of the

U.S. Geological Survey

Vol. 5 No. 5 Sept.–Oct. 1977

CONTENTS

SI UNITS AND U.S. CUSTOMARY EQUIVALENTS

[SI, International System of Units, a modernized metric system of measurement. All values have been rounded to four significant digits except 0.01 bar, which is the exact equivalent of 1 kPa. Use of hectare (ha) as as alternative name for square hectometer (hm^2) is restricted to measurement of land or water areas. Use of liter (L) as a special name for cubic decimeter (dm^3) is restricted to the measurement of liquids and gases; no prefix other than milli should be used with liter. Metric ton (t) as a name for megagram (Mg) should be restricted to commercial usage, and no prefixes should be used with it. Note that the style of meter^2 rather than square meter has been used for convenience in finding units in this table. Where the units are spelled out in text, Survey style is to use square meter]

SI unit		U.S. customary equivalent	
Length			
millimeter (mm)	=	0.039 37	inch (in)
meter (m)	=	3.281	feet (ft)
	=	1.094	yards (yd)
kilometer (km)	=	0.621 4	mile (mi)
	=	0.540 0	mile, nautical (nmi)
Area			
centimeter^2 (cm^2)	=	0.155 0	inch^2 (in^2)
meter^2 (m^2)	=	10.76	feet^2 (ft^2)
	=	1.196	yards^2 (yd^2)
	=	0.000 247 1	acre
hectometer^2 (hm^2)	=	2.471	acres
	=	0.003 861	section (640 acres or 1 mi^2)
kilometer^2 (km^2)	=	0.386 1	mile^2 (mi^2)
Volume			
centimeter^3 (cm^3)	=	0.061 02	inch^3 (in^3)
decimeter^3 (dm^3)	=	61.02	inches^3 (in^3)
	=	2.113	pints (pt)
	=	1.057	quarts (qt)
	=	0.264 2	gallon (gal)
	=	0.035 31	foot^3 (ft^3)
meter^3 (m^3)	=	35.31	feet^3 (ft^3)
	=	1.308	yards^3 (yd^3)
	=	264.2	gallons (gal)
	=	6.290	barrels (bbl) (petroleum, 1 bbl=42 gal)
	=	0.000 810 7	acre-foot (acre-ft)
hectometer^3 (hm^3)	=	810.7	acre-feet (acre-ft)
kilometer^3 (km^3)	=	0.239 9	mile^3 (mi^3)
Volume per unit time (includes flow)			
decimeter^3 per second (dm^3/s)	=	0.035 31	foot^3 per second (ft^3/s)
	=	2.119	feet^3 per minute (ft^3/min)
Volume per unit time (includes flow)—Continued			
decimeter^3 per second (dm^3/s)	=	15.85	gallons per minute (gal/min)
	=	543.4	barrels per day (bbl/d) (petroleum, 1 bbl=42 gal)
meter^3 per second (m^3/s)	=	35.31	feet^3 per second (ft^3/s)
	=	15 850	gallons per minute (gal/min)
Mass			
gram (g)	=	0.035 27	ounce avoirdupois (oz avdp)
kilogram (kg)	=	2.205	pounds avoirdupois (lb avdp)
megagram (Mg)	=	1.102	tons, short (2 000 lb)
	=	0.984 2	ton, long (2 240 lb)
Mass per unit volume (includes density)			
kilogram per meter^3 (kg/m^3)	=	0.062 43	pound per foot^3 (lb/ft^3)
Pressure			
kilopascal (kPa)	=	0.145 0	pound-force per inch^2 (lbf/in^2)
	=	0.009 869	atmosphere, standard (atm)
	=	0.01	bar
	=	0.296 1	inch of mercury at 60°F (in Hg)
Temperature			
temp kelvin (K)	=	[temp deg Fahrenheit (°F) + 459.67]/1.8	
temp deg Celsius (°C)	=	[temp deg Fahrenheit (°F) − 32]/1.8	

The policy of the "Journal of Research of the U.S. Geological Survey" is to use SI metric units of measurement except for the following circumstance:

When a paper describes either field equipment or laboratory apparatus dimensioned or calibrated in U.S. customary units and provides information on the physical features of the components and operational characteristics of the equipment or apparatus, then dual units may be used. For example, if a pressure gage is calibrated and available only in U.S. customary units of measure, then the gage may be described using SI units in the dominant position with the equivalent U.S. customary unit immediately following in parentheses. This also applies to the description of tubing, piping, vessels, and other items of field and laboratory equipment that normally are described in catalogs in U.S. customary dimensions.

S. M. LANG, *Metrics Coordinator,*
U.S. Geological Survey

Jour. Research U.S. Geol. Survey
Vol. 5, No. 5, Sept.–Oct. 1977, p. 529–534

URBAN AND REGIONAL LAND USE CHANGE DETECTED BY USING LANDSAT DATA

By WILLIAM J. TODD,[1] Sioux Falls, S. Dak.

Abstract.—The Atlanta Regional Commission and the Earth Resources Observation Systems Data Center participated in a demonstration of the use of Landsat digital data to detect land use change in the Atlanta, Ga., area. Temporal overlays combining Landsat band-5 data from October 1972 and 1974 were made by using the General Electric Image 100 system. The 1972 data were divided by the 1974 data, and low ratios indicate areas where land use and land cover had changed. These low ratios were classified into a land-use-change theme. A classification based on the use of the four bands of the multispectral scanner data, taken in 1974, yielded six land use categories: (1) Commercial-industrial-multifamily, (2) single-family residential, (3) cleared land, (4) open space, (5) forested land, and (6) water. These six 1974 categories and the change theme were combined to determine changes between 1972 and 1974.

Metropolitan areas often occupy large expanses of terrain. They include areas of diverse land use and land cover and are under the jurisdiction of many municipal and county governmental agencies. Only in the past few decades have regional planning agencies been created which are responsible for multicounty areas. Because a metropolitan area may be very large, often exceeding 5,000 km^2, it is difficult for a regional agency to monitor land use change.

In the fall of 1975, the ARC (Atlanta Regional Commission)—a regional planning agency responsible for a seven-county area including the city of Atlanta—and the EROS (Earth Resources Observation Systems) Data Center participated in a project to demonstrate the use of satellite data to detect land-use and land-cover change. The technique involved comparing data obtained from NASA's (National Aeronautics and Space Administration's) orbiting Landsat-1 satellite in October 1972 and in October 1974. Areas of change in land use and land cover were mapped by using digital interpretation equipment and specialized computer processing of the Landsat data available at the EROS Data Center.

Collaborating on this project were D. R. Hood, EROS Data Center; C. Blackman and J. R. Wilson, Jr., ARC; and G. W. Spann, Metrics, Inc. The author gratefully acknowledges their assistance.

[1] Technicolor Graphic Services, Inc., Sioux Falls, S. Dak.

INFORMATIONAL REQUIREMENT

The ARC anticipates completion of a map that depicts major land use in the greater Atlanta region in 1974. The problem that confronts ARC is how to update that map. The ARC comprehensive regional planning process requires that the land-use and land-cover map be updated annually, if possible.

A traditional means of land use inventory and updating employs black-and-white vertical aerial photography at scales of about 1:20,000 (Richter, 1969; Dill and Otte, 1970). Recently, high-altitude photographs at scales of 1:120,000 or smaller have been used successfully in experiments on detection of land-use and land-cover change (Lins and Milazzo, 1972; Place and Wray, 1972). Photointerpretation is a well-documented technique for data collection, and reasonably accurate results are expected. For the ARC region, the principal disadvantage of using aerial photography is that it is not available on a regular basis. Aerial photographic coverage is obtained at irregular intervals by the U.S. Geological Survey, NASA, the Agricultural Stabilization and Conservation Service, other Federal agencies, and certain State agencies, but not periodically over the entire ARC region. Regular photographic coverage of ARC's seven-county area would be expensive to obtain.

Satellite data may be an alternative to aerial photography for updating land-use and land-cover maps (Alexander, 1973; Anuta and Bauer, 1973). NASA has launched two orbiting satellites—Landsat-1 in 1972 and Landsat-2 in 1975—for collecting Earth resources data. Data from the Landsats are theoretically available for much of the Earth's surface every 9 days, if cloud cover is minimal. To date, an acceptable Landsat scene has been available over the ARC region about once every 3 months. Each Landsat image includes 185 by 185 km, and only one or two consecutive scenes are

needed to cover the entire ARC region. The resolution, that is, the smallest unit area for which the satellite data is collected and then sampled, is approximately 0.45 hectares. Individual trees and houses are not large enough to be detected, but larger urban and regional land cover types such as residential, commercial and industrial, water, and forested areas may be mapped. The same capability exists for monitoring changes such as subdivision construction, commercial strip development, industrial plant expansion, and clear cutting in forested areas.

ACTUAL AND POTENTIAL USERS

A number of administrative or political organizations consider the urban region in their planning and policy decisions. Federal, State, and local agencies all are concerned with development patterns and land use change within the urban region.

At the Federal level, numerous agencies within a number of large departments—Interior, Agriculture, Transportation, Commerce, and Housing and Urban Development—have direct or indirect interest in land use within the urban region. Within the U.S. Department of the Interior, several organizations—the Geological Survey, National Park Service, Fish and Wildlife Service, Bureau of Land Management, and Bureau of Reclamation among others—have direct responsibility for land and resource management of areas within the urban region. Within the U.S. Department of Agriculture, the Agricultural Stabilization and Conservation Service, Forest Service, and Soil Conservation Service are three organizations whose interests are related principally to areas that are not built up within the urban region. Other organizations—Urban Mass Transportation Administration (Department of Transportation), National Oceanic and Atmospheric Administration (Department of Commerce), Community Planning and Development (Department of Housing and Urban Development), Public Health Service (Department of Health, Education, and Welfare), the Environmental Protection Agency, and NASA—also have active programs which are related to the urban region. The type and extent of involvement in the element of land use and environmental concerns is varied, indeed. Federal programs range from direct management of designated areas (for example, National Park Service) to consultation and advice services for land use management (for example, Agricultural Stabilization and Conservation Service) to funding of State and local agencies for plan implementation (for example, Urban Mass Transportation Administration).

At the State level, the element of monitoring change in urban and regional patterns becomes more important in certain respects, depending upon the State's degree of urbanization. Many States have departments of transportation, planning, and natural resources. Similar to the level of Federal involvement in the urban region, State agencies are varied in their relationship to the problems of the urban region. Certain State agencies, such as transportation and public health, may be directly concerned with urban growth and planning. Others, such as State planning and community development, may be more administrative in their relationship (for example, approving local master plans or reviewing local applications for types of Federal assistance).

At the local level, regional planning agencies (multicounty), county governments, and city governments must deal directly with the problems of the urban region. Within these local governments, planning divisions, zoning offices, transportation sections, engineering offices, parks and recreation divisions, and waste-disposal offices, directly or indirectly use land-use-change data frequently, both in current operations and in planning and projection of future trends.

APPROACH TO THE ANALYSIS OF LANDSAT DATA

NASA has launched two satellites—Landsat-1 in 1972 and Landsat-2 in 1975—which orbit the Earth at an altitude of 915 km. Data are collected by multispectral scanners aboard the Landsats in four portions of the electromagnetic spectrum—band 4, 0.5 to 0.6 μm (visible green); band 5, 0.6 to 0.7 μm (visible red); band 6, 0.7 to 0.8 μm (reflective infrared); and band 7, 0.8 to 1.1 μm (reflective infrared). Thus, four elements of data are available for a particular area every time a satellite makes a pass.

Each Landsat satellite passes over the same nominal area every 18 days, but the orbits are staggered, resulting in coverage every 9 days over a given area.

Two general data formats are available from Landsat—photographic (image) products and CCT's (computer compatible tapes). The photographic products—film or paper and available at different scales—contain the entire Landsat scene. The largest standard scale available from the EROS Data Center is 1:250,000. Entire Landsat scenes are also stored on CCT's, but in digital format. A single Landsat scene contains 3240 elements (samples) of data for each of 2340 lines—over 7.5 million individual picture elements, commonly called pixels. A pixel is the smallest area on the Earth's surface for which the Landsats can record reflected electromagnetic radiation. The pixel is 79 by 57 m, or about 0.45 ha, from the nominal orbital altitude.

For detection of land-use and land-cover change, it is important to choose Landsat dates when phenological and seasonal differences are minimal. Data from two passes of Landsat-1 were used—October 15, 1972 (ID 1084–15433 and ID 1084–15440), and October 5, 1974 (ID 1804–15325)—for the ARC project. Digital data from the CCT's on the two dates were temporally overlaid for further processing. Not all of the ARC seven-county area was analyzed for the test. The six 29.3 by 29.3 km subscenes, totaling 5151 km², that were analyzed include most of the Atlanta region.

Digital image analysis

To illustrate the technique used in the test, a small part of the region (fig. 1) is used throughout this report. The 22.5 km² area is located approximately 22 km northeast of downtown Atlanta, immediately east of the Perimeter Highway (Interstate 285) which encircles Atlanta, and includes the Interstate 85 and Norcross Southern industrial districts. This part of the Atlanta region experienced many land-use and land-cover changes between 1972 and 1974, not atypical of a dynamic urban-rural fringe zone of a large metropolitan area.

In figure 1, two aerial photographs of the site are shown. The upper photograph is from a high-altitude color infrared aerial photograph taken by NASA in October 1972. The lower photograph was taken by the U.S. Geological Survey in February 1975. Landsat band-5 images of the same area are shown in figure 2; as the upper image was taken in October 1972 and the lower in October 1974, a very close temporal correlation exists between the two images and the two aerial photographs. Interstate 85 gently winds from the southwest to the northeast portion of the area and

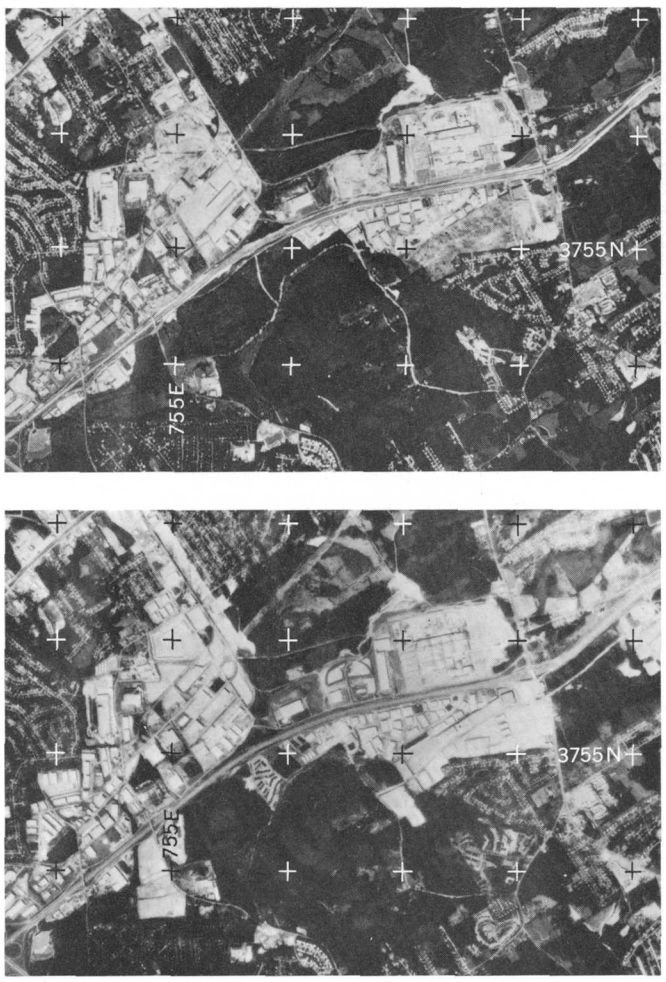

FIGURE 1.—Aerial photographs of northeastern Atlanta region. Upper, October 1972 (NASA). Lower, February 1975 (USGS). Approximate location of UTM 1.0-km tick marks (zone 16) indicates scale and direction.

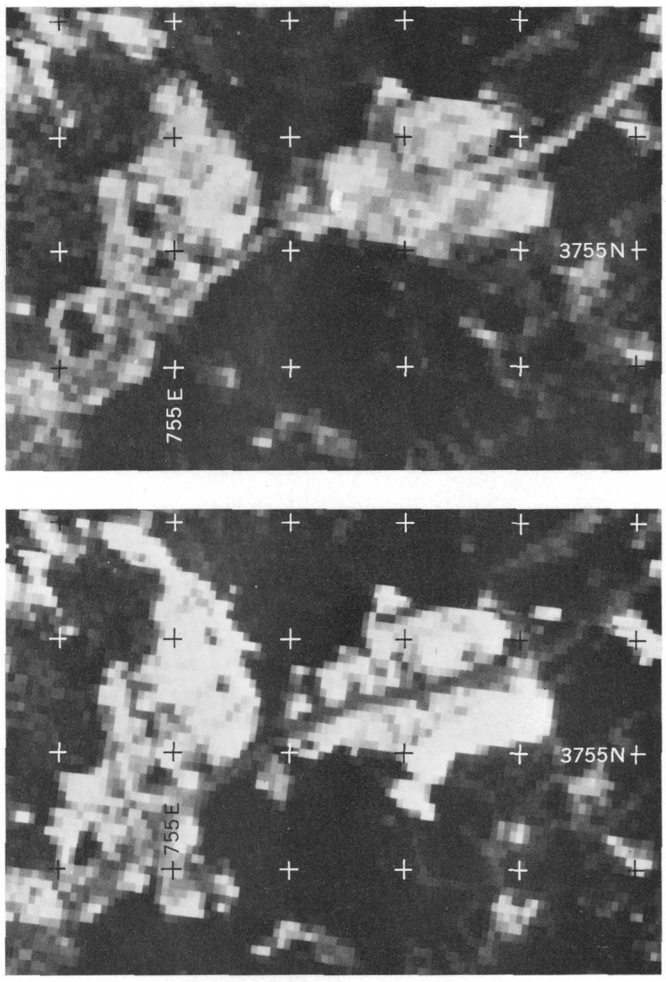

FIGURE 2.—Landsat band-5 images of northeastern Atlanta region. Upper, October 1972 (1084–15433–5). Lower, October 1974 (1804–15325–5). Approximate location of UTM 1.0-km tick marks (zone 16) indicates scale and direction.

is evident on both the aerial photographs and Landsat images. Large industrial and commercial complexes adjacent to the interstate are areas largely void of vegetation; such areas have brightly reflecting surfaces—rooftops, streets, parking lots—and have lighter tones on the imagery. Forested areas such as the large tract located in the south-central portion of the figure have a dark reflectance in the visible wavelengths and consequently appear dark on the Landsat images and aerial photographs. Residential areas are distinguished on the aerial photographs by their development pattern—rows of houses along closely spaced streets—and on the Landsat images by the coarse texture.

Visual interpretation—manual detection and delineation—of land-use and land-cover changes may be made by direct comparison of the two Landsat images, but the General Electric Image 100 system allows the land-use-change areas to be extracted digitally, by man interacting with the system. Change detection using digital Landsat data is essentially a process of comparing data from two different dates on a pixel to pixel basis, after the data have been digitally overlaid. A technique termed "ratioing" was used in the Image 100 system to detect change. Ratioing involves dividing the intensity of reflected EMR (electromagnetic radiation) in one band from one Landsat date by the intensity of EMR of the same band of another Landsat date on a pixel to pixel basis (fig. 3, upper image). In all areas where the reflected EMR is approximately the same for each scene (that is, the same type of land cover in each scene), the result of the division is nearly 1.0 and such areas appear gray on the upper image of figure 3. In other areas where land use and land cover had changed from one date to the next, the quotient is significantly different from 1.0. Areas with low reflectance values (dark tones) in 1972 and high reflectance values (light tones) in 1974, (for example, a forested area which was cleared for construction of an industrial plant) have low ratios and appear dark on the image of ratioed data. Conversely, areas with high reflectance values in 1972 and low reflectance values in 1974 (for example, a construction site that was landscaped during the time period) have high ratios and appear light on the ratio image.

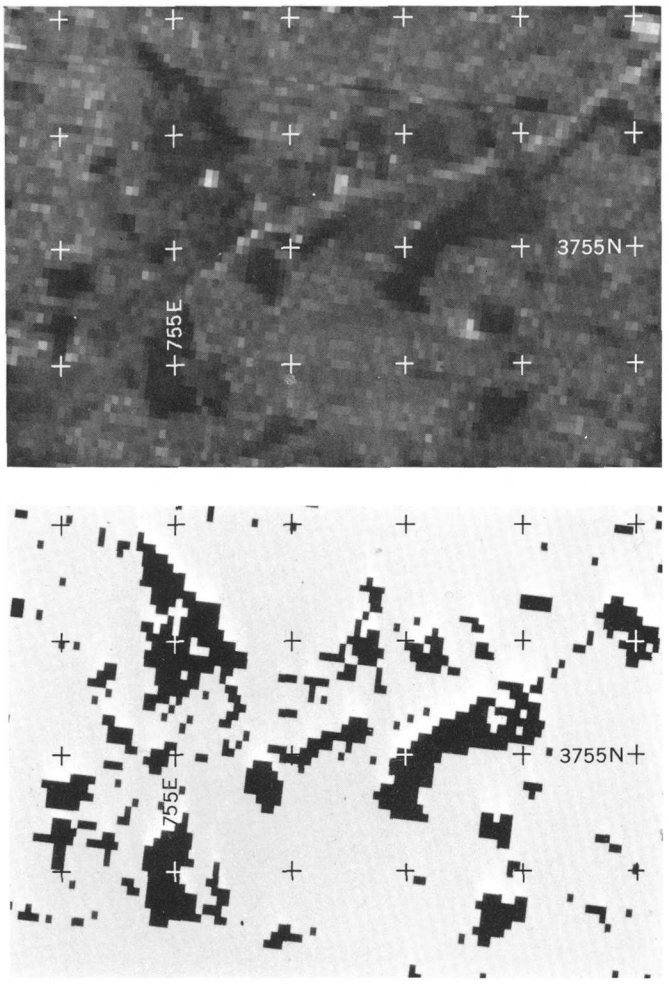

FIGURE 3.—Digital analysis of temporal overlay of Landsat band-5 data. Upper, ratioed data (band 5, 1972, divided by band 5, 1974). Lower, land-use-change theme extracted from ratioed data. Approximate location of UTM 1.0-km tick marks (zone 16) indicates scale and direction.

Large areas of land-use and land-cover changes are evident on the ratio image, particularly areas with low ratios that indicate a large amount of construction activity—extension of the existing urban and built-up area—from 1972 to 1974. Another step in the change-detection procedure was taken, namely digital extraction (that is, separation, classification) of the areas with dark tones (low ratios) from the remainder of the area. The lower image of figure 3 illustrates the result of the extraction—a land-use-change category (dark areas).

Comparison of the change map with the two aerial photographs (fig. 1) indeed indicates that the location and extent of significant large areas have been detected successfully. (The identity of the types of changes themselves is considered separately below.) There are some scattered small areas of change which are probably resulting from "noise" in the raw digital data. (This might be reduced by use of an automatic noise-reduction algorithm.)

The map of land-use and land-cover change is shown overlaid onto the aerial photographs (fig. 4). For purposes of this analysis, change areas with 3 or fewer pixels (1.4 ha) were eliminated from consideration.

Extensive warehousing and wholesaling establishments were constructed in the Interstate 85 industrial

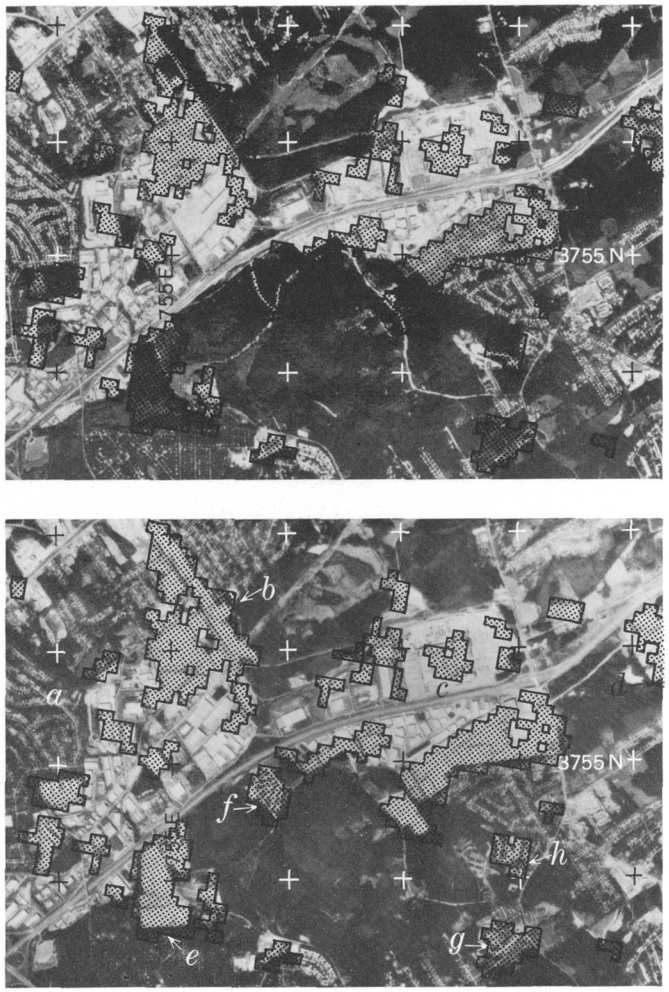

FIGURE 4.—Map of land-use and land-cover change overlaid onto aerial photographs of northeastern Atlanta region. Upper, October 1972 (NASA). Lower, February 1975 (USGS): *a*, I–85 industrial park development; *b*, new warehouse and wholesale development; *c*, industrial park development; *d*, land cleared for industrial expansion; *e*, land cleared for industrial and commercial development; *f*, Knollwood Apartments; *g*, Westwood Apartments; and *h*, Kelton Woods and Colony North Apartments. Approximate location of UTM 1.0-km tick marks (zone 16) indicates scale and direction.

district in the northwestern part of the area from 1972 to 1974. As shown in the 1972 aerial photograph, portions of that land were forested in 1974, while the remainder was nonforested open space. Two large areas—one in the southwest and another in the northeast—were cleared for industrial or commercial expansion in the 2-year period. Forested sites were cleared for the construction of four multifamily residential developments in the south-central sector of the area: Knollwood Apartments, Westwood Apartments, Kelton Woods, and Colony North. Multifamily residential land use can be distinguished from single family on the aerial photographs (fig. 1) by the larger structures of the former and on the Landsat imagery (fig. 2) by their brighter tones.

Exemplary accuracy level

Quantitative assessment of the accuracy level of the ratioing technique involved evaluation of a 136-km² area, which included the area represented in the illustrations. The total change category in this test area consisted of 2549 Landsat pixels (1147 ha) in 438 separate areas. Elimination of the 3-pixel (1.4-ha) areas and smaller left 106 areas consisting of a total pixel count of 2108 (949 ha).

The change map was compared with the aerial photographs (fig. 1), and each of the 106 areas was checked to determine (1) whether or not land use change had occurred and (2) how much larger or smaller the change area should have been. The overall evaluation showed that 91.4 percent of the category of land-use and land-cover change—which included 78 percent of the total number of change areas—were correctly identified as change. The difference in areas of land-use and land-cover change, determined by visual inspection of aerial photographs and the Landsat-derived information, averages 2.6 pixels (1.2 ha) and is based on comparison of 82 areas (mean size was 23.5 pixels or 10.6 ha) correctly identified in the Landsat information as areas of land-use or land-cover change. Areas incorrectly identified as change averaged much smaller (7.6 pixels or 3.4 ha) than those correctly identified. It is significant to note, finally, that all areas larger than 1.4 hectares in which land use and land cover had changed in the 2-year period were categorized as change areas using the ratioing technique.

Categorization of type of land-use and land-cover change

During the ARC tests of land-use-change detection, an additional mode of digital processing was applied to the Landsat data—that of categorizing the type of land-use and land-cover change, not merely its location. The procedure involved two steps: (1) Categorizing the 1974 Landsat data into land-use and land-cover types, and (2) combining the 1974 categorization with the change map to determine type of change in the 2-year period.

Initially, all four bands (4, 5, 6, and 7) of the 1974 Landsat multispectral scanner data were used to subdivide the ARC area into six broad land-use and land-cover types: Single-family residential, commercial-industrial-multifamily, cleared land, forested, open space, and water. (The reader is reminded that only

band 5 was used to extract the land-use-change category.) The resulting 1974 land-use and land-cover map was combined with the 1972–4 change map to categorize areas of change. Areas classified as both single-family residential in 1974 and change from 1972–4 could then be designated "new single-family residential constructed between 1972 and 1974."

An accuracy check of the change categorization procedures was made for the same area used for the change map evaluation. For the single-family residential category, 10 of 19 areas of change were correct, while 53 of 63 areas of the combined class commercial-industrial-multifamily and cleared land were correct. No areas of change for the other three land-use and land-cover categories—forested, open space, water—were found in this area.

In an operational mode, a regional planning agency will, indeed, be required to ground check the results of the Landsat digital processing. Ratioing a pair of Landsat scenes will quickly produce a map showing areas of land-use and land-cover change in a particular region; categorization of type of change will give the agency an important headstart towards allocation of manpower resources for field verification. Analysis of the 5000-km^2 area in the Atlanta region was accomplished in less than 1 workweek; the amount of field checking will depend upon resources available.

POSSIBLE END PRODUCTS

Digital analysis of overlaid Landsat data of different times can provide (1) a map showing change, (2) tabular aggregations of area change by desired geographic areas, such as counties, census tracts, and ecological zones, and (3) computer compatible storage (for example, magnetic tape) of land-use-change data.

Data on land-use and land-cover change can be stored on computer tapes and be readily processed to produce different types of maps and overlays for different user's needs. Maps at a scale of 1:50,000 or larger can be produced, as well as small-scale maps for publication purposes (for example, 1:500,000 or smaller). Map projection can also be changed to make overlays for different user's base maps. The change polygons on the map of land-use and land-cover change can be indicated in color or black-and-white, drawn perhaps by a computer-driven plotter, and reproduced as paper products or transparent overlays.

Tabular aggregation of the change data by type of change and geographic areas is readily accomplished by overlaying boundaries onto the Landsat data, very similar to overlaying the multitemporal Landsat data. After the geographic areas and change data are overlaid, simple tallying of change pixels may be made by unit. Another possibility is to tally the change data by contiguous aggregations of change pixels, that is, the number and size of change areas. For example, the tallying may indicate the number of change areas which were found in Fulton County and then list the areas and their acreage. Change areas may also be tallied for other breakdowns, including traffic zones, enumeration districts, soil type, and ownership.

USE OF THE END PRODUCTS

The kinds of use of the data on land-use and land-cover change depend on the user. Many Federal and State agencies will only be concerned with coarse tabular aggregations of change data for entire urban regions. A large State agency, for example, may be interested in yearly indications of urban growth acreage as input to the formation of a statewide land use policy. Local agencies, however, may use maps and tabular data for more detailed analysis. Multicounty, county, or municipal maps of land-use and land-cover change might be prepared with tabular aggregations at smaller units, as input to planning models and decisionmaking.

REFERENCES CITED

Alexander, R. H., 1973, Land use classification and change analysis using ERTS–1 imagery in CARETS, *in* Symposium on significant results obtained from the Earth Resources Technology Satellite-1: NASA, Goddard Space Flight Center, v. 1, sec. B, p. 923–930.

Anuta, Paul, and Bauer, M., 1973, An analysis of temporal data for crop species classification and urban change detection: West Lafayette, Ind., Purdue Univ., Lab. for Applications of Remote Sensing, LARS Inf. Note 110873, 85 p.

Dill, H. W., Jr., and Otte, R. C., 1970, Urbanization of lands in the western states: U.S. Dept. Agriculture, Econ. Research Service, ERS–428, 30 p.

Lins, H. F., Jr., and Milazzo, V. A., 1972, The use of small-scale multi-band photography for detecting land use change, *in* Proceedings of the 8th international symposium on remote sensing of environment: Ann Arbor, Environmental Research Inst. Michigan, v. 1, p. 325–343.

Place, J. L., and Wray, J. R., 1972, Automated plotting and update of land use maps and related information in south-central Arizona, *in* Proceedings of the 3rd annual conference on remote sensing in arid lands: Tucson, Arizona Univ., Office of Arid Lands Studies, p. 328–343.

Richter, D. M., 1969, Sequential urban change: Photogramm. Eng., v. 35, p. 764–770.

Jour. Research U.S. Geol. Survey
Vol. 5, No. 5, Sept.–Oct. 1977, p. 535–540

SIMULATION OF FLOW FROM AN AQUIFER TO A PARTIALLY PENETRATING TRENCH

By STANLEY A. LEAKE, Jackson, Miss.

Prepared in cooperation with the U.S. Army Corps of Engineers, Nashville District

Abstract.—Construction of the Tennessee-Tombigbee Waterway in northeast Mississippi will involve dewatering as much as 46 m of an unconfined aquifer near the Tennessee Valley divide. Dewatering by trenching is one of the proposed methods. Methods of calculating effects of dewatering by trenching have been heretofore limited to situations where ideal conditions such as isotropic aquifers and fully penetrating trenches occur. In order to study the effects of trenching on the water table in the more complicated hydrologic system in northeast Mississippi, a two-dimensional cross-sectional digital model was developed from an existing two-dimensional digital model. To make the solutions obtained from the model applicable to any aquifer thickness or other hydrologic condition, a technique for nondimensional simulation was developed. With these techniques, nondimensional water-surface profiles were generated for given stages of trench penetration of the aquifer and for different ratios of anisotropy.

The Tennessee-Tombigbee Waterway is a project undertaken by the U.S. Army Corps of Engineers to shorten shipping distances from the Gulf of Mexico to the Tennessee River valley. Construction in the northernmost part of the project, known as the divide section (fig. 1), will necessitate prior dewatering of as much as 46 m of an unconfined or semiconfined aquifer over a 43-km stretch through the Tennessee Valley divide. Because of the immensity of the required dewatering, several methods are being studied to determine which one is suitable for this project. Among the proposed methods is dewatering by trenching.

The evaluation of transient flow from an unconfined aquifer to a trench or river is not a simple hydraulic problem because the descriptive flow equation is nonlinear. For situations where the trench fully penetrates the aquifer and flow is essentially horizontal, solutions have been published. Among the most versatile of these solutions is one developed by Yeh (1970), who solved the one-dimensional flow equation by using numerical techniques and published a nondimensional solution in a tabular form with values of remaining head given in percent as a function of time, drawdown in the trench, distance from the trench, and initial head, specific yield, and hydraulic conductivity of the aquifer. Perhaps the most widely used solution for this problem is one put forth by Glover (1973), who approached the problem by linearization of the flow equation. The analytical solution to the resultant equation includes the probability integral or error function. This solution is applicable when the change in thickness of the aquifer is not large compared with the total thickness of the aquifer. Several other solutions using linearization and transformation techniques have been published, but none of these one-dimensional solutions is applicable to problems involving partially penetrating trenches and anisotropic conditions.

The aquifer to be dewatered in the project area generally consists of thick deposits of sand that contain discontinuous clay beds. Pumping tests in the area indicate varying rates of vertical flow in the upper 61 m.

One of the proposed ways of trenching this material is by making a trench that partially penetrates the aquifer and by deepening it at selected points in time until the water level in the adjacent aquifer is at the desired altitude. This procedure along with the apparent anisotropy of the aquifer complicates the problem of determining the water level in the aquifer for a given time. Because of these complications, a digital model was chosen to solve the problem.

DEVELOPMENT OF A CROSS-SECTIONAL MODEL

If a trench is assumed to be straight and infinitely long and if the aquifer properties do not change in the direction of the trench, all flow is parallel to the plane perpendicular to the axis of the trench. This being the case, the solution is one that results from solving the two-dimensional ground-water flow equation as applied to a cross section of the aquifer (fig. 2). A finite-difference model developed by Trescott, Pinder, and

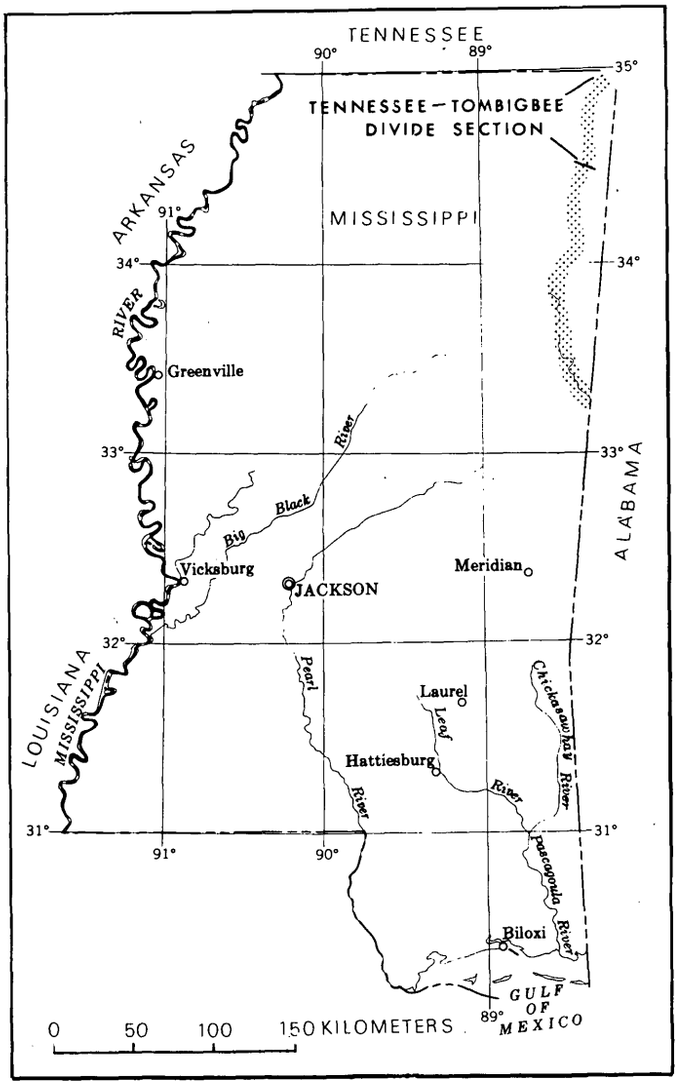

FIGURE 1.—Location of the Tennessee-Tombigbee Divide section.

Larson (1976) solves the equation. It was modified to match the boundary conditions of this problem.

If a strip of the aquifer of uniform thickness is to be simulated, then the governing two-dimensional flow equation is

$$K_{xx}b\,\frac{\partial^2 h}{\partial x^2} + K_{yy}b\,\frac{\partial^2 h}{\partial y^2} = S_s b\,\frac{\partial h}{\partial t}\,, \quad (1)$$

where x = distance in horizontal direction,
y = distance in vertical direction,
b = thickness of strip,
h = head in aquifer,
K_{xx}, K_{yy} = principal components of the hydraulic conductivity tensor,
S_s = specific storage, and
t = time.

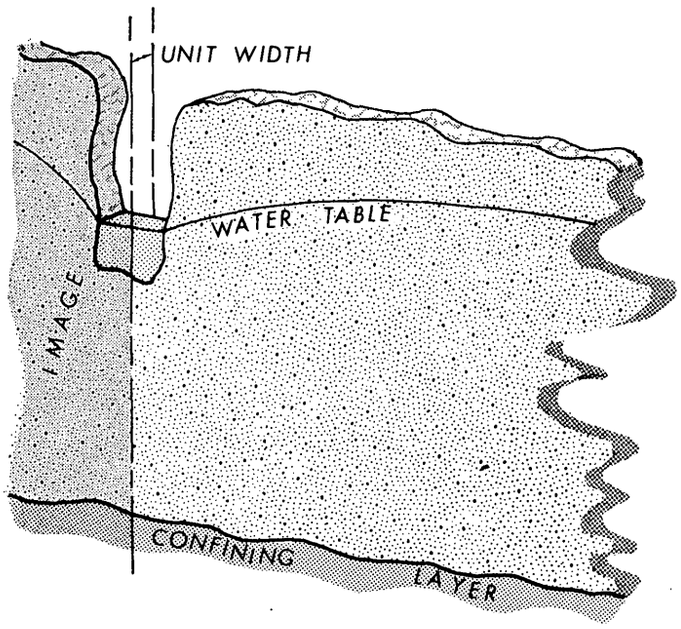

FIGURE 2.—Hydrologic system as modeled.

Assumptions made in using this equation are that K_{xx} is not a function of x, K_{yy} is not a function of y, and K_{xx} and K_{yy} are alined with the coordinate directions x and y, respectively. Boundaries are defined as the confining bed of the aquifer and the water table.

In the cross-sectional finite-difference grid (fig. 3), the cells in the top row are assumed to simulate water-table conditions. Head change at a water-table cell (fig. 4) is a function of, among other things, the specific yield (S_y) of the aquifer and dimensions of the cell. In the finite-difference model, the storage coefficient (S) or the specific yield (S_y) is the volume of water that the aquifer releases from storage per unit decrease in head per unit surface area. A different representation of the specific yield must be used when translating to cross section from plan view. The volume of water released from a water-table cell in cross-sectional configuration with a head decline of h_0-h as shown in figure 4 is $\Delta x b(h_0-h)S_y$. In plan view the same volume is given by $\Delta x \Delta y(h_0-h)S_y$. A correction for this can be made by assigning a storage coefficient value of $S_y b/\Delta y$ for water-table cells.

The thickness of the strip (b) can conveniently be chosen as a unit length. With this choice, the flow into the trench, designated as a constant-head boundary, has the units of discharge per unit length per side.

In designing the finite-difference grid network, the bottom coincides with the base of the aquifer which is assumed to be a horizontal plane and zero datum. Likewise, the top of the grid network is taken as the water table. With this design, the initial head values are equal

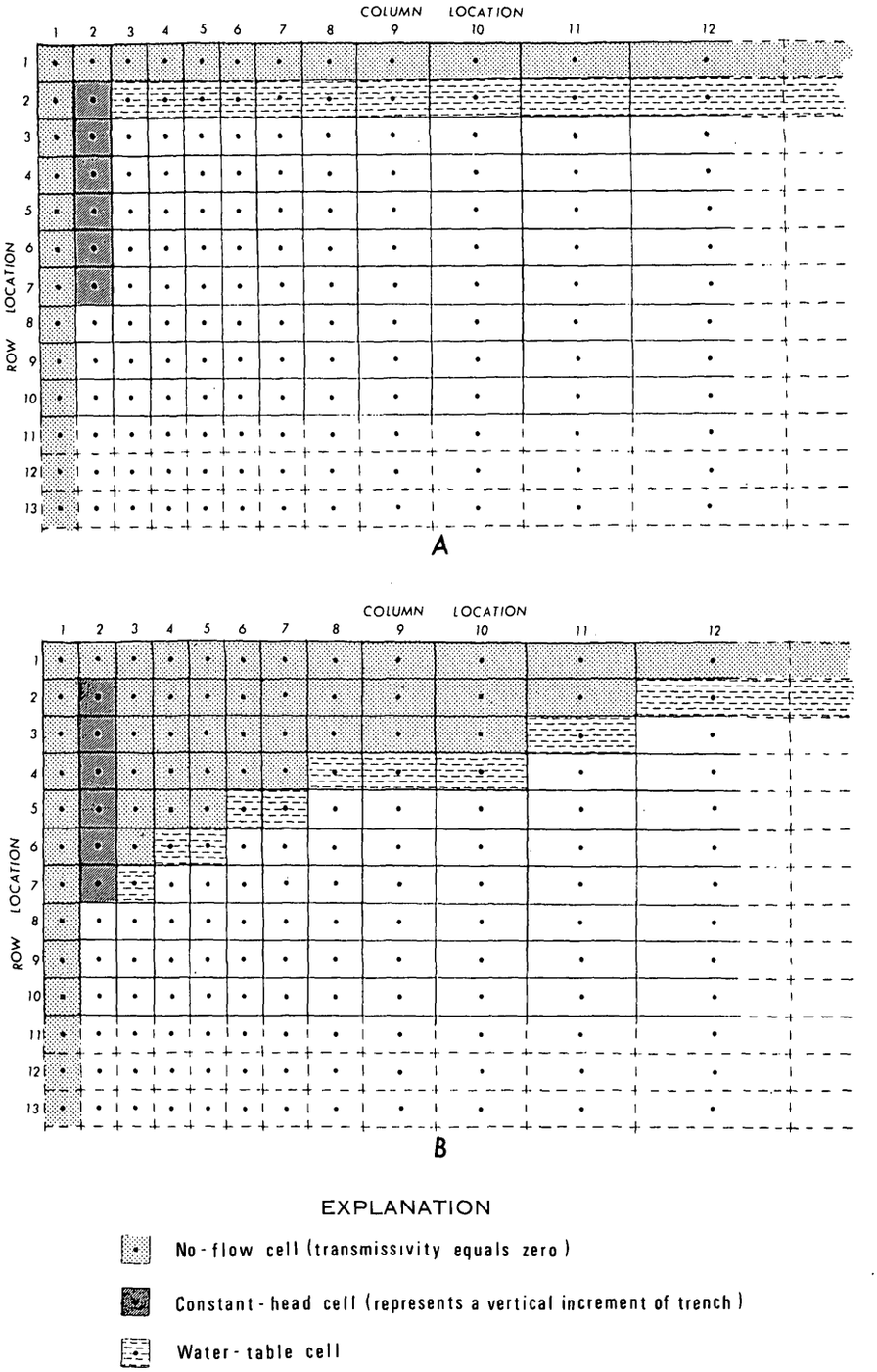

FIGURE 3.—Finite-difference grid used in movable-boundary cross-sectional model simulating the effects of a partially penetrating trench. *A*, Finite-difference grid at start of simulation. *B*, Finite-difference grid at some point in simulation time.

to the summation of the Δy's, which is the saturated thickness.

To simulate the downward movement of the water table during the dewatering process, the following procedure is used. After each time interval, the head at the water-table cell in each column (fig. 3) is checked to see if it has declined to a value less than the distance from the bottom of the aquifer to the center of the

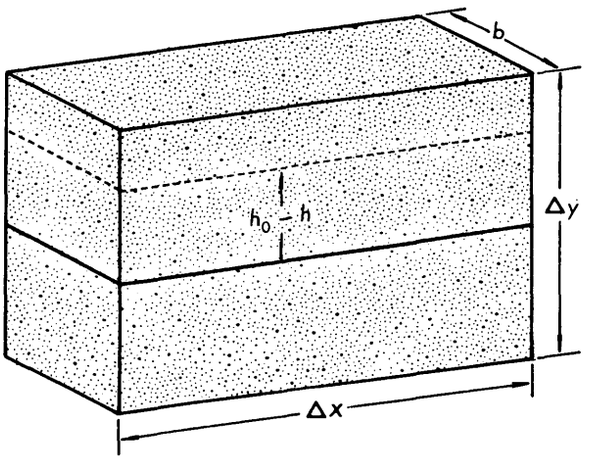

FIGURE 4.—Finite-difference cell.

cell. If this has taken place, the water-table specific yield is transferred to the next lower cell in the column and the transmissivity of the original cell is set equal to zero. This check is made again at the new cell. The check and transfer process is repeated until one is found in which the head is above its center. A similar algorithm could be developed to accomodate an increasing head in the aquifer.

Another useful feature to be included in the modified model is the ability to change constant-head values or add constant-head cells during the simulation. The original model was designed to simulate a number of "pumping periods" or periods in which the stresses on the hydrologic system are assumed to be constant. The modified model is programed to designate new constant-head cells at the start of these pumping periods. This allows the capability of simulating changes in the water level in a trench, deepening an existing trench, or adding a new trench at selected points in time.

Simulations done for this study involved a single partially penetrating trench that was assumed to be instantaneously made and instantaneously deepened at selected times. In a given simulation, a trench was deepened in steps until the entire aquifer thickness was penetrated.

To test the cross-sectional model, a problem involving flow to a fully penetrating trench in an isotropic aquifer was simulated. The same problem was simulated with a plan-view model and the results of the two simulations were compared. In both simulations an initial aquifer thickness of 30 m, a specific yield of 0.2, and a hydraulic conductivity of 4.6 m/d were assumed. An instantaneous head decline of 24 m was assumed to take place at the beginning of the simulation. The same discrete representations for time and distance were used in both simulations. Average values in a vertical were used for comparison with values from the plan-view solution. The computed values from each of the simulations were in agreement to within 1 percent of the initial aquifer thickness. These cross-sectional results were also compared with results obtained from Yeh's solution (fig. 5). Although the difference in this comparison is somewhat greater than was observed in the comparison of the two finite-difference solutions, the results still indicate a close agreement. Values from Yeh's solution indicate more drawdown than the values from the cross-sectional solution. The reason for this slight difference has not been determined; however, probable causes include peculiarities in one or both of the numerical techniques used.

NONDIMENSIONAL SIMULATION

A solution obtained by cross-sectional simulation is applicable only to the problem described by the input parameters. It is desirable, however, to obtain a solution that, for a given set of boundary conditions, is universal with respect to various input parameters. This can be accomplished by nondimensionalizing the basic flow equation (Smith, 1965).

Equation 1 can be transformed to nondimensional form by dividing each quantity with the units of length by some fixed length. For later convenience, the initial aquifer thickness (h_0) is chosen for the fixed length. The resulting variable substitutions are $x^* = x/h_0$, $y^* = y/h_0$, and $h^* = h/h_0$. Equation 1 becomes

$$\frac{K_{xx}b}{h_0}\frac{\partial^2 h^*}{\partial x^{*2}} + \frac{K_{yy}b}{h_0}\frac{\partial^2 h^*}{\partial y^{*2}} = \frac{bS_y h_0}{\Delta y}\frac{\partial h^*}{\partial t}, \qquad (2)$$

where water-table conditions exist. Defining $t^* = \Delta y K_{xx} t/(S_y h^2_o)$, equation 2 is simplified to

$$\frac{\partial^2 h^*}{\partial x^{*2}} + \frac{K_{yy}}{K_{xx}}\frac{\partial^2 h^*}{\partial y^{*2}} = \frac{\partial h^*}{\partial t^*}. \qquad (3)$$

To apply this equation to points other than those on the aquifer surface, it must be assumed that the specific storage is negligible.

To solve equation 3 with a finite-difference model, a value of unity is used for the starting head, values of $\Delta x/h_0$ and $\Delta y/h_0$ are used for cell dimensions, and $\Delta y K_{xx} t/(S_y h^2_o)$ is used for time. Then for a given anisotropy ratio, K_{yy}/K_{xx}, and boundary conditions, the resultant solution will be applicable to aquifers with any starting head, specific yield, and horizontal hydraulic conductivity.

RESULTS OF NONDIMENSIONAL SIMULATIONS

To illustrate nondimensional simulations of flow to a partially penetrating trench, a problem involving a trench that penetrated half of the aquifer's thickness

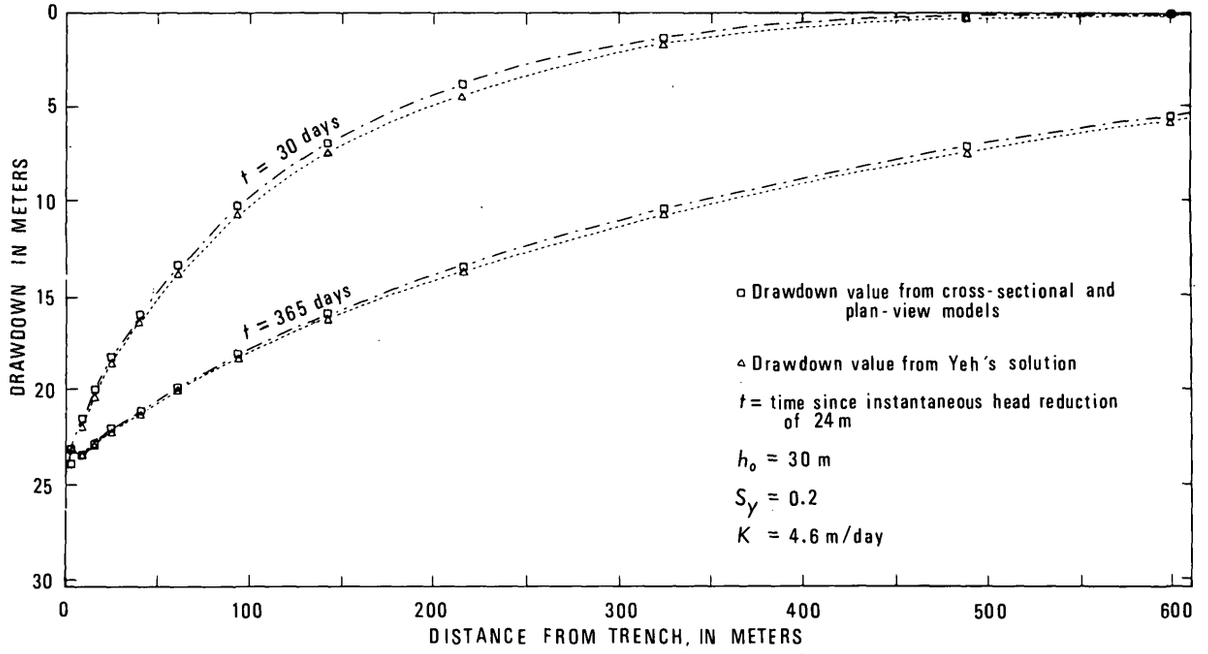

FIGURE 5.—Comparison of results from cross-sectional model with results from other solutions.

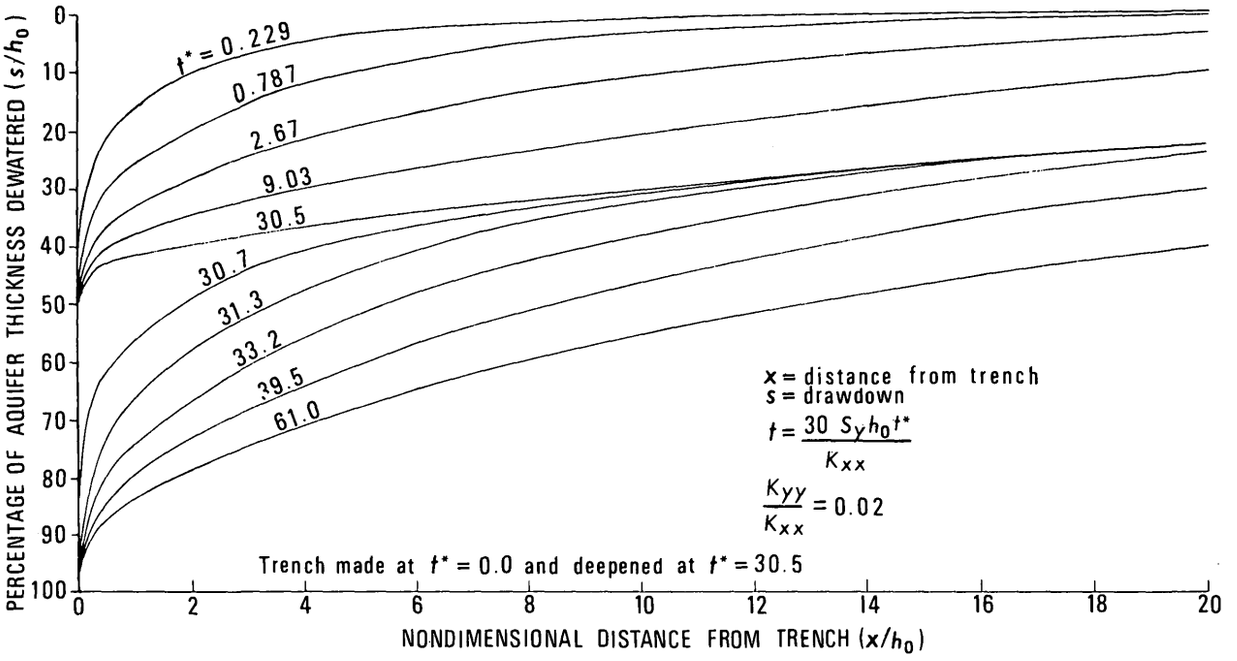

FIGURE 6.—Nondimensional water-surface profiles from sample problem.

at the start of the simulation and then deepened to penetrate the remaining half at some point in nondimensional time was selected for simulation. The point in time was chosen somewhat arbitrarily as $t^* = 30.5$. The ratio of vertical to horizontal hydraulic conductivity was given as 0.02. Drawdown values, as computed by the model at the surface of the aquifer, are the ratio of the aquifer water-level decline to the total aquifer thickness. Their distance from the trench is computed by summing the $\Delta x/h_o$ values. The resultant value is the number of aquifer thicknesses that the point is from the trench. For various nondimensional

times, nondimensional water-surface profiles are represented graphically in figure 6.

SUMMARY

The effects of dewatering by trenching can be evaluated by solving the one-dimensional or two-dimensional ground-water flow equations. If the trench fully penetrates the aquifer and flow in the aquifer can be assumed to be horizontal, then one or more of several published solutions can be used. If the flow cannot be assumed to be horizontal, then the problem can be solved by modifying a two-dimensional digital model to simulate the flow problem in cross section.

In the cross-sectional model finite-difference grid, the upper or water-table cells must drop out when the head declines to a value less than the distance from the base of the aquifer to the center of the cell. Specific yield at the water-table cells must be represented differently because the head decline there is not a function of the area of the cell in the x-y plane as is assumed in a plan-view model. By modifying the model to read in constant-head values at the start of a pumping period, the user can change or add constant-head cells that simulate a trench.

Through variable substitutions made for various input parameters, a problem can be simulated nondimensionally. The resultant solution is universal with respect to various input parameters.

REFERENCES CITED

Glover, R. E., 1973, Ground-water movement: U.S. Bur. Reclamation Eng. Mon. 31, p. 48.

Smith, G. D., 1965, Numerical solutions of partial differential equations: New York, Oxford, p. 9–10.

Trescott, P. C., Pinder, G. F., and Larson, S. P., 1976, Finite-difference model for aquifer simulations in two dimensions with results of numerical experiments: U.S. Geol. Survey Techniques Water-Resources Inv., book 7, chap. C1, 116 p.

Yeh, W. W., 1970, Nonsteady flow to surface reservoir: Am. Soc. Civil Engineers Proc., Hydraulics Div. Jour., v. 96, no. HY3, paper 7137, p. 609–617.

Jour. Research U.S. Geol. Survey
Vol. 5, No. 5, Sept.–Oct. 1977, p. 541–545

A METHOD FOR ADJUSTING VALUES OF MANNING'S ROUGHNESS COEFFICIENT FOR FLOODED URBAN AREAS

By H. R. HEJL, Jr., Lawrence, Kans.

Abstract.—A method is presented for adjusting values of Manning's roughness coefficient for flooded urban areas on the basis of the density of buildings on a flood plain and verified roughness coefficients for natural conditions. An urban roughness coefficient can be calculated to emulate the water-surface profiles to within 0.06 meter for depths of flow less than 0.6 meter and plus or minus 10 percent for depths between 0.6 and 2 meters.

A method is presented here to allow users of the U.S. Geological Survey's step-backwater and floodway analyses, computer program E431 (Shearman, 1976), to adjust values of Manning's roughness coefficient (*n*) for flooded urban areas. Because few, if any, verified values of *n* currently are available for urban areas, users of the step-backwater and floodway analyses program have a choice of either (1) eliminating the portion of the cross section occupied by buildings and selecting a value of *n* for the areas between the buildings, or (2) using the total area of the cross section and estimating a value of *n* that includes the effect of the buildings. The first choice is unsatisfactory because the data requirements are too stringent and the second choice has not been defined adequately by verified values of *n*. The method proposed here is an effort towards the development of a technique for determining values of *n* that include the effects of buildings. The method requires verified values of *n* for natural conditions and estimates of the areas occupied by buildings in a cross section and along the profile parallel to the direction of flow.

DERIVATION

In the technique described below, the hypothesis for adjusting the value of *n* for buildings in a flood plain is based on the assumption that only the portion of a flood plain not occupied by buildings can convey water downstream and that streets are parallel and perpendicular to the direction of flow. The roughness coefficient for a cross section including buildings is derived by letting the total discharge, Q_T, in cubic meters per second, be equal to

$$Q_T = \Sigma \frac{1}{n_o} A_o R_o^{2/3} S_o^{1/2}, \quad (1)$$

where n_o, A_o, R_o and S_o represent Manning's roughness coefficient, area in square meters, hydraulic radius in meters, and friction slope in meters per meter, of the individual openings between the buildings. The total discharge can also be expressed as

$$Q_T = \frac{1}{n_b} A_T R_T^{2/3} S^{1/2}, \quad (2)$$

if the roughness coefficient, n_b, compensates for the area in a cross section occupied by buildings and if A_T and R_T are total area and hydraulic radius, respectively. Equating the right side of equation 1 and equation 2 results in the following:

$$\frac{1}{n_b} A_T R_T^{2/3} S^{1/2} = \Sigma \frac{1}{n_o} A_o R_o^{2/3} S_o^{1/2}. \quad (3)$$

For shallow depths of flow and constant values of n_o, equation 3 can be simplified to

$$\frac{A_T}{n_b} \approx \frac{\Sigma A_o}{n_o}, \quad (4)$$

$$n_b \approx \frac{A_T}{\Sigma A_o} n_o, \quad (5)$$

or

$$n_b \approx \frac{W_T}{\Sigma W_o} n_o, \quad (6)$$

where n_b is the equivalent roughness coefficient for a cross section through a row of buildings perpendicular to the direction of flow and the ratio of total area to summation of the individual areas of the openings is approximated by the substitution of widths as shown in figure 1.

The roughness coefficient for a reach along a profile parallel to the direction of flow is derived by proportioning, on the basis of length, roughness coefficients for cross sections including buildings and roughness coefficients for cross sections without buildings. The portion of the roughness applicable for cross sections including buildings is equal to

$$\Delta n_1 = \frac{L_T - \Sigma L_o}{L_T} n_b, \quad (7)$$

where L_T is the total length of the reach and ΣL_o is the summation of the distances between the rows of buildings parallel to the direction of flow as shown in figure 1. It follows that the portion of the roughness applicable for the cross sections without buildings can be expressed as

$$\Delta n_2 = \frac{\Sigma L_o}{L_T} n_o, \quad (8)$$

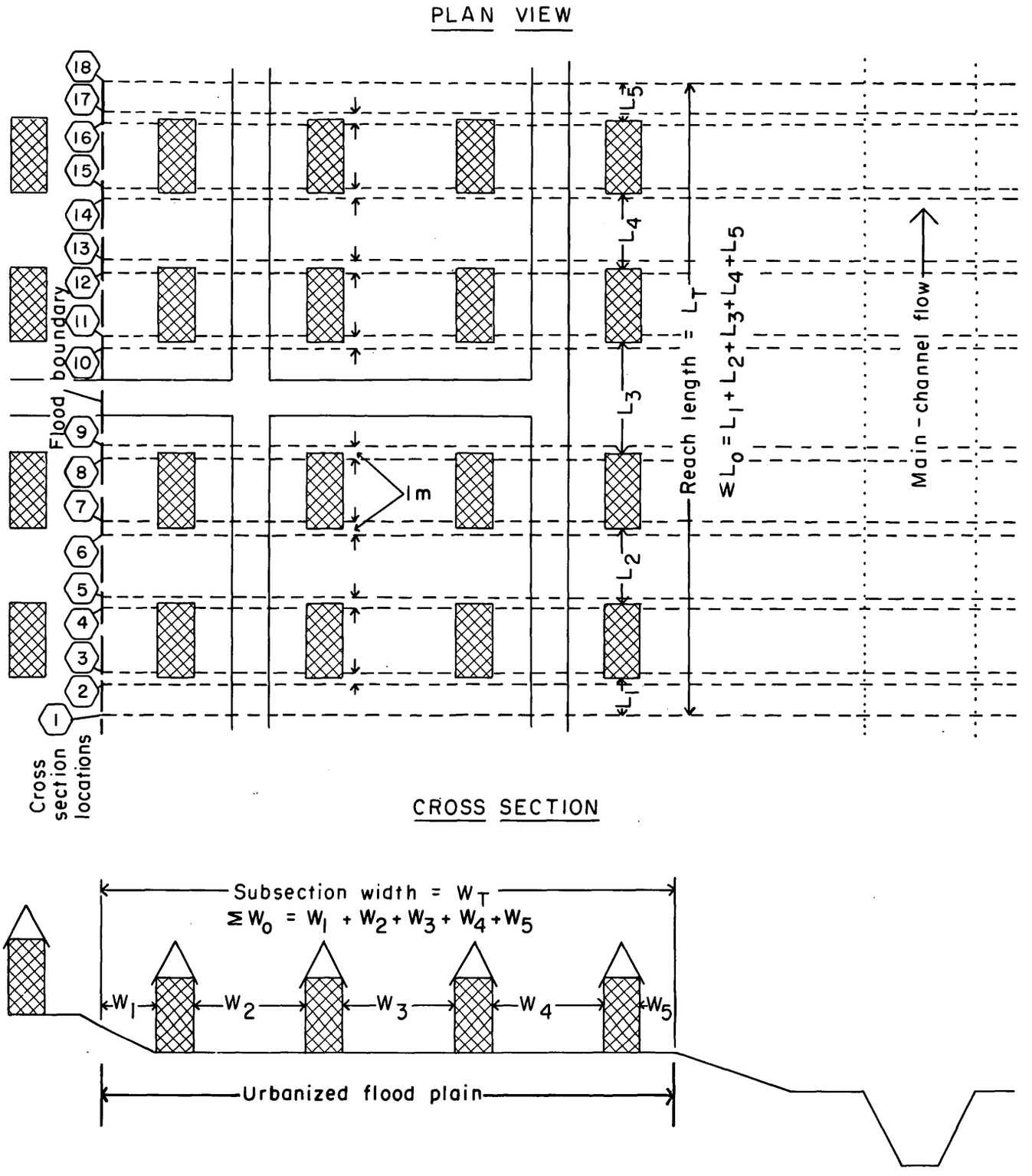

FIGURE 1.—Diagram of idealized urban area where the streets are parallel and perpendicular to the direction of flow.

assuming a constant roughness coefficient between the rows of buildings that is the same as the one found between the buildings in a cross section in equation 6. If it were not for the expansion losses, contraction losses, and effects of the sides of buildings on the hydraulic radius, equations 7 and 8 could be summed to describe the roughness coefficient for urban areas. If cross sections including buildings and cross sections without buildings are located as shown in figure 1, the U.S.

Geological Survey's step-backwater and floodway analyses program, which utilizes Manning's equation, computes the expansion losses as being equal to one-half of the change in velocity head between cross sections in expanding reaches, the contraction losses as being equal to zero, and the hydraulic radius as including the additional wetted perimeter of the sides of the buildings. Using total cross-sectional area, analyses of hypothetical data indicate that the expansion losses and the effect of the sides of the buildings can be approximated by an empirical adjustment of

$$\Delta n_3 = \frac{n_b - n_o}{2}. \quad (9)$$

The summation of roughness coefficients for subreaches including buildings, subreaches without buildings, and the empirical adjustment results in an urban roughness coefficient, n_u, equal to

$$n_u = \Delta n_1 + \Delta n_2 + \Delta n_3, \quad (10)$$

or

$$n_u = \frac{(L_T - \Sigma L_o)}{L_T} n_b + \frac{\Sigma L_o}{L_T} n_o + \frac{n_b - n_o}{2}, \quad (11)$$

where n_u is the adjusted value of Manning's n for urban areas used with total cross-sectional area. If equation 6 is substituted for n_b, equation 11 can be simplified to

$$n_u = n_o \left[\frac{3}{2} \left(\frac{W_T}{\Sigma W_o} \right) + \left(1 - \frac{W_T}{\Sigma W_o} \right) \frac{\Sigma L_o}{L_T} - \frac{1}{2} \right], \quad (12)$$

where n_o is the roughness coefficient for the area between the buildings on a flood plain, $W_T / \Sigma W_o$ is the ratio of total width to the summation of the individual widths between the buildings of a cross section through a row of buildings perpendicular to the direction of flow, and $\Sigma L_o / L_T$ is the ratio of the summation of the distances between rows of buildings to the total length of the reach along a profile parallel to the direction of flow.

APPLICATION OF METHOD

The steps required for applying the method for adjusting values of Manning's n, for urban areas are as follows:

Step 1: Cross-section requirements are basically the same as those for nonurbanized areas. The cross sections are subdivided to separate the main-channel flow from the flow between the buildings in a flood plain. The urban roughness coefficient, n_u, is applied only to the subsections that include buildings; the flood plains on the left and right banks are evaluated independently. A subdivided cross section is shown in figure 1.

Step 2: Estimate the ratio of total width, W_T, to summation of the widths of individual openings, ΣW_o, for a cross section through a row of buildings of average density in the reach of flood plain being evaluated perpendicular to the direction of flow as shown in figure 1. This estimate can be made in the field, by aerial reconnaissance, or from a map.

Step 3: Estimate the ratio of the summation of distances between rows of buildings, ΣL_o, to the total length of reach, L_T, parallel to the direction of flow for the reach in step 2.

Step 4: Select a Manning's roughness coefficient, n_o, for the open area between the buildings. Open areas include features such as fences, trees, shrubbery, and streets.

Step 5: Compute the urban roughness coefficient, n_u, from equation 12 and use the roughness coefficient for the subsections, including buildings, directly in the step-backwater and floodway analyses program; use total area of the cross section.

DESCRIPTION OF URBAN-AREA MODELS

Urban-area models similar to the urbanized flood plain shown in figure 1 consisting of 305-meter channels of uniform depth with vertical walls at sides were used to evaluate the empirical adjustment portion of the urban roughness coefficient, n_u. Nine buildings were spaced on 30-meter centers in rows perpendicular to the direction of flow. The rows of buildings were spaced on 61-meter centers in the reach except for one of the combinations shown in table 1 where the rows were spaced on 30-meter centers. The dimensions of the buildings and slope of the channel were varied for the nine combinations shown in table 1. A constant roughness coefficient value of 0.040 for the area between the buildings was used for all the combinations. Model A was designed to produce the most reliable water-surface profiles available by using cross sections located 1 meter downstream, at downstream edge, at upstream edge, and 1 meter upstream from each row of buildings. Model B is the suggested simplified model using only the cross sections located 1 meter downstream and 1 meter upstream from each row of buildings and adjusting for the area occupied by buildings by applying the method for urban roughness coefficient, n_u.

TABLE 1. — *Urban-area model combinations shown in figure 3*
[Each row includes 9 buildings on 30-meter centers with the rows on 61-meter centers except in combination 4, which was on 30-meter centers]

Combination No.	Ratio of total width to summation of widths of openings in cross section ($\frac{W_T}{\Sigma W_o}$ in fig. 1)	Ratio of summation of distances between rows of buildings to total reach length ($\frac{\Sigma L_o}{L_T}$ in fig. 1)	Flood-plain slope (m/m)	Urban roughness coefficient (n_u)
1	1.33	0.80	0.002	0.050
2	1.67	.80	.002	.058
3	1.67	.60	.002	.064
4	1.67	.40	.002	.069
5	2.00	.80	.001	.068
6	2.00	.80	.002	.068
7	2.00	.80	.004	.068
8	2.00	.60	.002	.076
9	3.33	.80	.002	.105

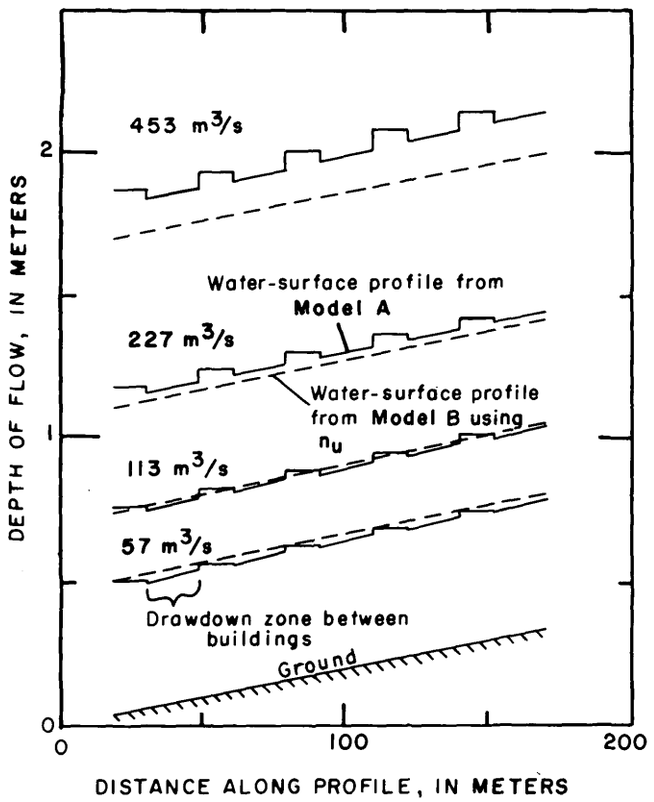

FIGURE 2.—Comparison of water-surface profiles obtained from model A and model B, which used the urban roughness coefficient, n_u.

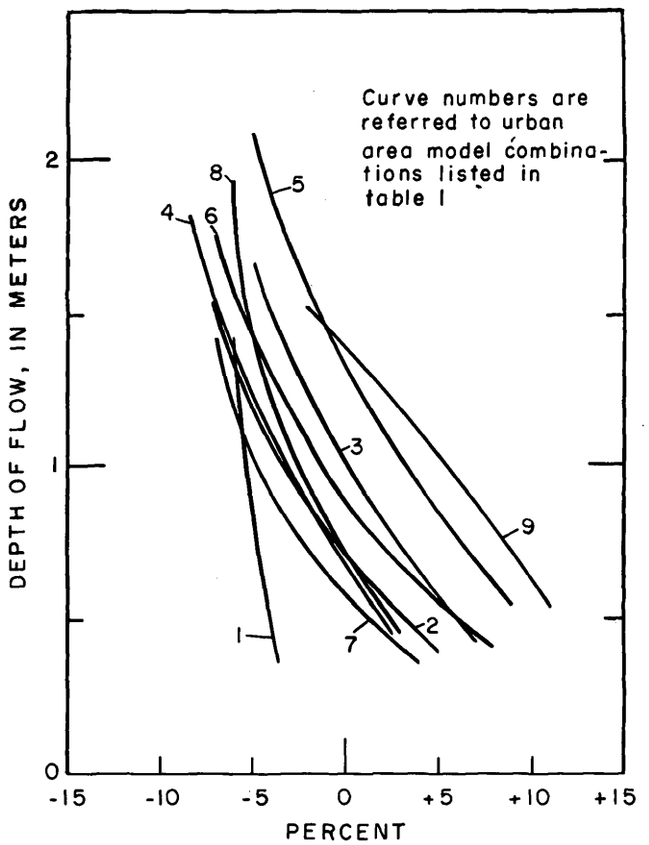

FIGURE 3.—Depth versus percent deviation in depth of flow when comparing the results of model B to model A.

MODEL RESULTS

The computation of water-surface profiles for models A and B were made with the U.S. Geological Survey's step-backwater and floodway analyses, computer program E431. Although the program uses U.S. customary units, the results were converted to SI units for this paper; Manning's n is the same in both systems of units. Because model A used detailed cross-sectional data, it was assumed to produce more reliable water-surface profiles than model B, which used total cross-sectional area and the urban roughness coefficient, n_u. A comparison of the water-surface profiles produced from model A and model B for combination 4 in table 1 is shown in figure 2. Model B most nearly emulates the water-surface profile of model A at a depth of flow of about 0.8 meter, which occurs at 113 m^3/s (cubic meters per second). The resulting comparisons of the nine combinations in table 1 are shown in figure 3 as percent deviation in depths of flow determined by model B as compared with those determined by model A. Figure 3 indicates that the urban roughness coefficient, n_u, increases with increases in depth of flow (except for combination 1, which is consistently 5 percent low), slope (combinations 5,6, and 7), and housing density. The probable reason for this relation is the nonlinear evaluation of the expansion losses in model A where they are computed as one-half of the difference in the velocity heads ($\alpha V^2/2g$, where α is the velocity-head coefficient, V is the mean velocity in the section, and g is the acceleration of gravity), between cross sections in expanding reaches and, to a lesser degree, the effect of the building sides on the hydraulic radius, which is taken to the two-thirds power. Model B produced water-surface profiles to within 0.06 meter of those from model A for depths of flow less than 0.6 meter and plus or minus 10 percent for depths of flow between 0.6 and 2 meters for the combinations tested. This included combination 9 where the reliability of the expansion losses made by computer program E431 are questionable because 70 percent of the cross-sectional area perpendicular to the direction of flow was occupied by buildings.

SUMMARY

The method for adjusting roughness values, n_u, for computing water-surface profiles in flooded urban areas combines the advantages of the two currently available options—(1) eliminating the portion of the cross section occupied by buildings and selecting a value of n for the areas between buildings, and (2) using the total area of the cross section and estimating a value of n that includes the effects of buildings. This method uses a value of n based on verified values for natural conditions and considers the total area of a cross section, thus eliminating the tedious task of delineating the cross-sectional areas occupied by buildings. An urban roughness coefficient, n_u, can be calculated and used with

cross sections required for natural conditions to emulate the water-surface profile computed from a very large number of cross sections to within 0.06 meter for depths of flow less than 0.6 meter and plus or minus 10 percent for depths of flow between 0.6 and 2 meters. The technique presented may be particularly useful in studies made to predict flooding hazards in urban areas. These studies often incorporate valley cross sections obtained by photogrammetric methods or by utilizing surveys made for purposes other than step-backwater analysis. Development of the technique described herein should result in values of Manning's *n* for urban areas that are both realistic and reproducible.

REFERENCES CITED

Bailey, J. F., and Ray, H. A., 1966, Definition of stage-discharge relation in natural channels by step-backwater analyses: U. S. Geol. Survey Water-Supply Paper 1869-A, 24 p.

Barnes, H. H., Jr., 1967, Roughness characteristics of natural channels: U. S. Geol. Survey Water-Supply Paper 1849, 213 p.

Benson, M. A., and Dalrymple, Tate, 1966, General field and office procedures for indirect measurements: U. S. Geol. Survey Techniques Water-Resources Inv., book 3, chap. A1, 30 p.

Dalrymple, Tate, and Benson, M. A., 1966, Measurements of peak discharge by the slope-area method: U.S. Geol. Survey Techniques Water-Resources Inv., book 3, chap. A2, 12 p.

Shearman, J. O., 1976, User's manual for computer program E431, computer applications for step-backwater and floodway analyses: U. S. Geol. Survey Open-File Rept. 76–499. 103 p.

Jour. Research U.S. Geol. Survey
Vol. 5, No. 5, Sept.–Oct. 1977, p. 547–559

PERIPHYTON AND PHYTOPLANKTON IN THE SACRAMENTO RIVER, CALIFORNIA, MAY 1972 TO APRIL 1973

By LINDA J. BRITTON, Denver, Colo.

Prepared in cooperation with California Department of Water Resources

Abstract.—Periphyton and phytoplankton samples were collected monthly at five sites in the Sacramento River between May 1972 and April 1973. Periphyton were analyzed for species identification and biomass, and phytoplankton were analyzed for species identification and concentrations. The results were used to assess biological water-quality conditions in the river and to compare phytoplankton types and concentrations at three sites with those in 1960–61.

Diatoms were the dominant group in both numbers and types of periphyton and phytoplankton. The number of genera and frequency of occurrence of periphyton increased downstream. The periphyton biomass decreased downstream and with succeeding monthly sampling periods. The highest productivity was at site B, below Red Bluff, probably because the Red Bluff Diversion Dam provides optimum conditions for periphyton growth. The decreasing productivity downstream is probably a function of higher sediment concentrations. The periphyton biomass ranged from 0.00 to 0.56 grams per square meter per day throughout the study period.

Phytoplankton concentrations and diversity increased downstream. The highest phytoplankton concentration was 980 organisms per milliliter at site D, above Knights Landing, in September. The diversity indices ranged from 0.95 to 3.88 for all sites throughout the study period. Fewer phytoplankton genera were collected in 1972–73 than in 1960–61, but the generic composition was similar. Total phytoplankton concentrations were nearly always higher in 1960–61 than in 1972–73. Green algal concentrations were significantly higher ($p<0.05$) at site C and diatoms were significantly higher at all three sites in 1960–61. Blue-green algal concentrations were higher in 1972–73, but differences between the two time intervals were not significant.

From May 1972 to April 1973, water quality was studied at five sites on the Sacramento River. The methods and basic data have been presented by Britton and Averett (1974). The purpose of the study was to evaluate the water-quality status of the river, to compare the findings with results obtained in 1960–61 by the California Department of Water Resources (1962a, b, c, d), and to assess water-quality changes that have occurred in the river since 1960–61. Phytoplankton and periphyton were collected for use as indicators of biological water quality. Phytoplankton were analyzed for types and abundance, and periphyton for types and biomass. Samples of phytoplankton and periphyton were collected monthly during the summer when productivity was probably at a maximum. Additional phytoplankton samples were collected at least once during the autumn and spring. High discharges prevented collection of samples during the winter.

This paper presents the methods of data collection and processing, and qualitative and quantitative findings of phytoplankton and periphyton with temperature and sediment data. Because periphyton analysis was not included in the 1960 study, only phytoplankton was used to compare water-quality changes between 1960–61 and 1972–73.

DESCRIPTION OF STUDY AREA

The Sacramento River extends nearly 650 km from the headwaters near Mount Shasta to its mouth at San Francisco Bay. The river drains about 67 340 km^2, principally agricultural land in the northern Central Valley. Five sampling sites were established in a reach of the Sacramento River from a point above Red Bluff downstream to Knights Landing (designated A through E in fig. 1).

At the two upstream sites, above and below Red Bluff (sites A and B), the river channel is approximately 110 m wide, with depths ranging from 1.5 to 6 m. The banks of the river are steep and densely wooded. The river substrate ranges from fist-sized cobbles to sand. Discharge in this reach of the river is largely controlled by releases from Shasta Lake, by inflows from tributary streams, and by inflow of ground water (California Department of Water Resources, 1962a). Because the river is highly regulated, the discharge at these two sites, except during local flooding in the winter, remains fairly constant at about 396 m^3/s. Site A was chosen because it represents a typical reach of the upper river and was one of the sampling

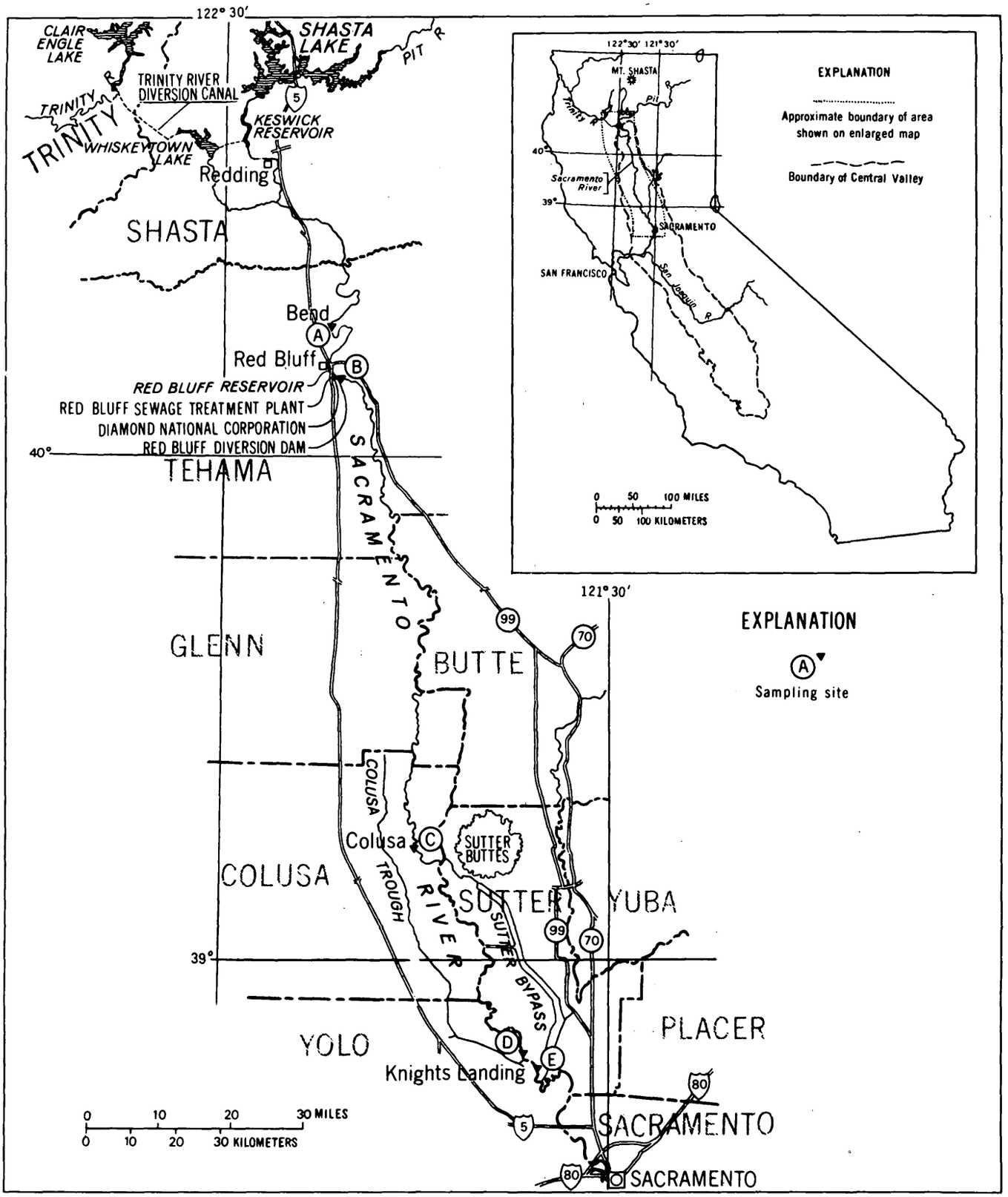

FIGURE 1.—Sacramento Valley showing river sampling sites.

sites in the 1960–61 study. Site B is below the Red Bluff Diversion Dam which impounds water from the river in a 4 830 000-m³ reservoir. This site was chosen to evaluate water-quality effects that might be caused by wastes discharged directly upstream from the dam. Site B was not a sampling site for phytoplankton analysis in the 1960–61 study.

At the three downstream sites (sites C–E, fig. 1), the river channel is narrow and meanders through the valley and flow is extensively controlled by levees and flood-bypass systems. At each of these three sites, the river is about 60 m wide and has substrates of sand, silt, and clay. During the sampling period for phytoplankton and periphyton collection, average depths at the three sites ranged from 3 to 8 m. Sites C and D were chosen because they represent a typical reach of the middle parts of the river, and because they were sampled in the 1960–61 study. Site E is immediately downstream from the entrance of the Colusa Trough (not shown in fig. 1) and was chosen to evaluate possible downstream water-quality changes due to the effects of the trough. Site E was not a sampling site for phytoplankton analysis in the 1960–61 study. A more detailed description of sites and sampling procedures is contained in Britton and Averett (1974).

Discharge, diversions, and control changes in the river must be considered in the comparison of phytoplankton samples collected in 1960–61 and 1972–73. In 1963 the Trinity River diversion canal brought Trinity River water into the Sacramento River for the first time, causing higher average discharges in 1972–73 than in 1960–61. The average discharges for the sampling periods of May 1960 to April 1961 compared to May 1972 to April 1973 are:

Site	Average discharge, in m³/s	
	1960–61	1972–73
A	275.28	402.15
C	267.63	410.65
D	283.21	385.16

The average discharges for each month during the May to April sampling period were almost always higher in 1972–73 than in 1960–61. The discharges were noticeably higher in the summer of 1972 than 1960 not only because of the addition of the Trinity River water but also because of additional controls on the Pit River, (not shown in fig. 1) Trinity River, and upper Sacramento River, which hold excess storage over the winter for release in the summer. Several dams and reservoirs that impound and regulate Sacramento River water did not exist in 1960–61. Therefore, the discharges in 1960–61 were lower in the summer when phytoplankton growth and production were probably at a maximum.

METHODS

In 1972, periphyton were collected on (64×1200-mm) Plexiglas artificial substrates suspended vertically or horizontally in the river. At all sites, except site C, the substrates were positioned parallel to the flow. The substrates were initially attached approximately 150 mm below the surface of the water; although they were nonfloating, the depth of the substrates for an entire sampling period probably did not vary 102 mm. The substrates were placed in the main flow of the channel, and near the banks at all sites, except site B (below Red Bluff). At site B, the substrates were placed near the right bank, in a pool area south of an island which divides the river. Usually, two artificial substrates were placed at each sampling site and removed approximately 4–5 weeks later (table 1). The substrates and attached periphyton were air-dried after removal. For those substrates that were placed vertically in the water, the top-bottom orientation was noted. To compensate for areas where insufficient light caused no growth, only the top areas where maximum growth occurred were scraped. In the laboratory, a measured area of the dried periphyton was removed from the substrates and species identification and periphyton biomass in (g/m²)/d (grams per square meter per day) were determined using the procedures described by Slack and others (1973). The minimum area removed by scraping was 0.0026 m². On most substrates, several 0.0026-m² areas were scraped and species identification and mean daily periphyton biomass were determined on each subsample.

TABLE 1.—*Data on periphyton sample collection in 1972*

[See figure 1 for location of sampling sites]

Sampling site	Colonization period		Scraped Plexiglas strips			
			Species identification		Biomass	
	Date	Number of days	Number of samples	Total area (m²)	Number of samples	Total area (m²)
A	June 8-July 18	40.0	3	0.0075	10	0.025
	July 18-Aug. 22	35.0	2	.0050	4	.010
	Aug. 22-Sept. 27	35.5	2	.0050	3	.0075
	Sept. 27-Nov. 8	41.5	1	.0025	10	.025
B	May 2-June 8	37.0	4	.010	4	.010
	June 8-July 18	40.0	4	.010	10	.025
	July 18-Aug. 23	35.5	2	.0050	4	.010
	Aug. 23-Sept. 27	35.0	2	.0050	4	.010
	Sept. 27-Nov. 8	42.5	2	.0050	10	.025
C	May 3-June 8	36.0	3	.0075	4	.010
	June 8-July 19	40.5	4	.010	10	.025
	July 19-Aug. 23	35.0	2	.0050	2	.0050
	Aug. 23-Sept. 28	36.0	2	.0050	4	.010
	Sept. 28-Nov. 9	42.0	2	.0050	10	.025
D	May 3-June 9	36.5	3	.0075	4	.010
	June 9-July 20	41.0	3	.0075	10	.025
	July 20-Aug. 24	35.0	2	.0050	4	.010
	Aug. 24-Sept. 28	35.5	2	.0050	4	.010
	Sept. 28-Nov. 9	42.0	2	.0050	10	.025
E	June 9-July 20	41.0	3	.0075	10	.025
	July 20-Aug. 24	35.0	2	.0050	4	.010
	Aug. 24-Sept. 28	35.5	2	.0050	4	.010
	Sept. 28-Nov. 9	42.0	2	.0050	10	.025

Periphyton were identified by concentrating the scraped cells in a known volume of distilled water. An aliquot of the concentrated sample was removed and placed in an Utermöhl chamber (Utermöhl, 1958) and settled onto a microscopic cover glass at the bottom of the apparatus. Identification and counts were made at a commercial laboratory by use of an inverted microscope as described by Slack and others (1973).

The dry weight, ash weight, and organic (ash-free) weight of the periphyton were determined for several samples from each artificial substrate using the methods described by Slack and others (1973). The dry weight of periphyton was determined by ovendrying the sample to a constant weight at 105°C. The ash weight was determined by burning the dried residue in a muffle furnace at 500°C for one hour. The organic or ash-free weight of the periphyton was calculated as the difference between ash weight and dry weight. The results, expressed in $(g/m^2)/d$, permit comparison of periphyton from substrates that were placed in the river for varying periods of time. The rate expression $(g/m^2)/d$ is the mean daily periphyton biomass. Actually, the rate expression includes the accumulation of periphyton and other organisms, such as bacteria and fungi. However, the bulk of the organic material is periphyton, and will be referred to as such throughout the report.

The limitations of the biomass method for estimating periphyton productivity have been discussed by Wetzel (1965). Sloughing of organic material and population turnover are two factors which interfere with estimating the productivity. Also, the measurements obtained from the substrates often indicate the environmental conditions affecting the substrate. In this particular study, factors such as current and light availability were not assessed. The results are indicative of the organic material present at the time of removal.

In 1972–73, water samples for phytoplankton analysis were collected with a depth-integrating sampler. Samples were collected on a near monthly basis at the center, right, and left banks of the river and composited for each site. The samples were preserved with Lugol's solution and analyzed for species identification and concentrations by use of an inverted microscope and the methods described by Slack and others (1973).

In 1960–61, water samples for phytoplankton analysis were collected monthly at 22 sites (California Department of Water Resources, 1962a and c). The data from three sites (sites A, C, and D) will be presented here. The water samples were collected in a Kemmerer water bottle at various depths and were composited for each site. The samples were preserved in 40-percent formalin and stored at 5°C until analyzed. Samples were concentrated by means of a centrifuge, and the volume of sample was adjusted to 25 mL and analyzed with a microscope using the Sedgwick-Rafter method described by California Department of Water Resources (1962c).

RESULTS

Periphyton

Occurrence and identification

The qualitative results of periphyton occurrence are in table 2. The diatoms (class, Bacillariophyceae) were the dominant group, having the greatest number of species. Of the diatoms, *Achnanthes lanceolata* and *Melosira varians* occurred at every site and with a high percentage of occurrence during the study period. *M. varians* occurred in every sample collected at the three downstream sites (sites C–E). It is an epipelic-type (living on mud) algae (Hynes, 1970), which probably accounts for its more frequent occurrence at the downstream sites where a silt-clay river-bottom substrate predominates. *Achnanthes lanceolata* occurred in every sample at the two upper sites (sites A and B), and it is considered as either epilithic (living on rocks) or epiphytic (living on plants), which coincides with the conditions in the upper river. *Achnanthes* and *Cocconeis*, which normally grow on mosses and stones, are the first types to colonize and grow on artificial substrates such as glass slides (Hynes, 1970). The green

TABLE 2.—*Occurrence of periphyton in samples, in percent, in 1972*

[See figure 1 for location of sampling sites]

Sampling site	A	B	C	D	E
Number of samples	4	5	5	5	4
Total days in river	152	190	189.5	190	153.5
Total area scraped — m^2	0.0200	0.0350	0.0325	0.0300	0.0225
CHLOROPHYTA					
Chlorophyceae (green algae)					
Cladophora sp.	--	20	40	--	--
FGA (filamentous green algae)	50	60	60	60	75
CHRYSOPHYTA					
Bacillariophyceae (diatoms)					
Achnanthes lanceolata	100	100	80	60	75
Bacillaria paxillifer	--	--	--	20	50
Cocconeis placentula	25	20	60	40	50
Cymbella sp.	--	--	--	20	25
Diatoma vulgare	--	--	80	40	--
Fragilaria virescens	--	--	20	60	75
Gomphonema sp.	--	--	--	20	25
Melosira varians	50	40	100	100	100
Navicula exigua	--	--	20	--	--
Navicula sp.	25	20	--	20	--
Nitzschia palea	50	40	20	--	25
Rhoicosphenia curvata	25	80	60	60	50
CYANOPHYTA					
Myxophyceae (blue-green algae)					
FBGA (filamentous blue-green algae)	--	--	20	--	--
Lyngbya sp.	--	--	20	--	--

and blue-green algal groups were composed mainly of unidentified filamentous forms.

Site C consistently had the greatest number (12) and the highest total percentage of occurrence of periphyton. Four samples were collected at sites A and E, whereas five samples were collected at the other sites, possibly accounting for the lower diversity of types and lower frequency of occurrence of periphyton at sites A and E. Blue-green algae were found only at site C in the May-June and July-Aug. samples (fig. 2). Green algae were found at every site at least twice from May through September, but none were found in the September-November samples. The largest number of genera (7) was found at the three downstream sites in the June-July and July-August samples.

Biomass measurements

Periphyton productivity measurements usually have been limited to the determination of biomass. (Wetzel, 1965). In this study, the dry, ash, and organic weights of biomass were determined to provide an estimate of productivity. The mean daily periphyton biomass for all sites and for each sampling period are shown in figure 3. Biomass measurements are not available for sites A and E in the May-June sampling period because the substrates were lost in the river. Periphyton biomass and mean daily sediment deposition on the substrates and mean daily temperatures are also shown in figure 3. The periphyton biomass generally decreased downstream, and with succeeding monthly sampling periods. The mean periphyton biomass ranged from a high of 0.56 $(g/m^2)/d$ at site B in the June-July period to a low of 0.00 $(g/m^2)/d$ at site E in the September-November period (fig. 3).

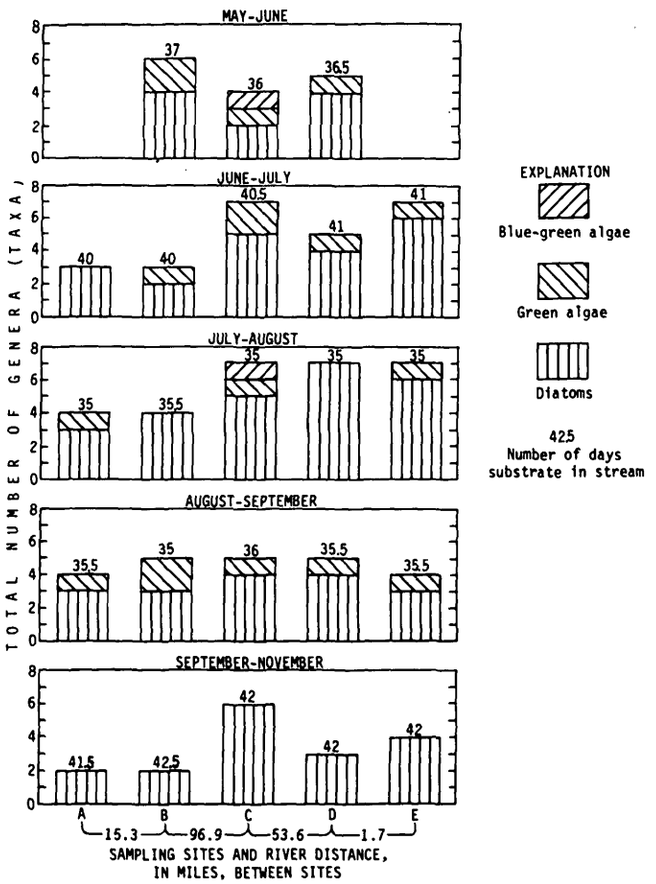

FIGURE 2.—Occurrence of periphyton genera for selected months in 1972.

The mean daily periphyton biomasses, water temperatures, and sediment deposition for all sites were averaged for each monthly sampling interval (fig. 4*A*). The highest mean daily periphyton biomass for all sites was 0.26 $(g/m^2)/d$ in the May-June samples. The lowest mean daily periphyton biomass [0.10 $(g/m^2)/d$] was measured in September-November.

The lowest mean daily sediment deposition [0.73 $(g/m^2)/d$] occurred in May-June, when productivity was highest. If a single high average measurement of sediment deposition at site D in June-July is ignored, the highest average sediment deposition was 0.97 $(g/m^2)/d$ in September-November, when periphyton biomasses were the lowest. Usually, the periphyton biomass decreased from May to September as sediment deposition increased.

Temperature may often affect production of periphyton, but no monthly correspondence of mean temperature with periphyton biomass was found.

Although periphyton biomass appears to decrease from the May-June sampling period to the September-November sampling period, the 95-percent confidence limits show that the September-November period was probably the only period that was significantly different from all others (fig. 4*A*).

Figure 4*B* shows the averages for all sampling intervals of the mean daily periphyton biomass, water temperatures, and sediment deposition at each site. The higher mean periphyton biomass at site B was probably due to the discharge of waste effluent and combined nutrients upstream from the dam. Except at site A, the mean periphyton biomass decreased downstream, with increasing sediment and temperature. It seems that either sedimentation interfered with periphyton colonization or that the types of periphyton selective to a substrate having a higher sediment content did not have sufficient time for colonization. For example, the dominant alga, *Achnanthes lanceolata*, occurred most frequently at the three downstream sites, but apparently not in high enough concentrations to increase the biomass levels at these three sites. There are many factors such as pH, alkalinity, velocity, and

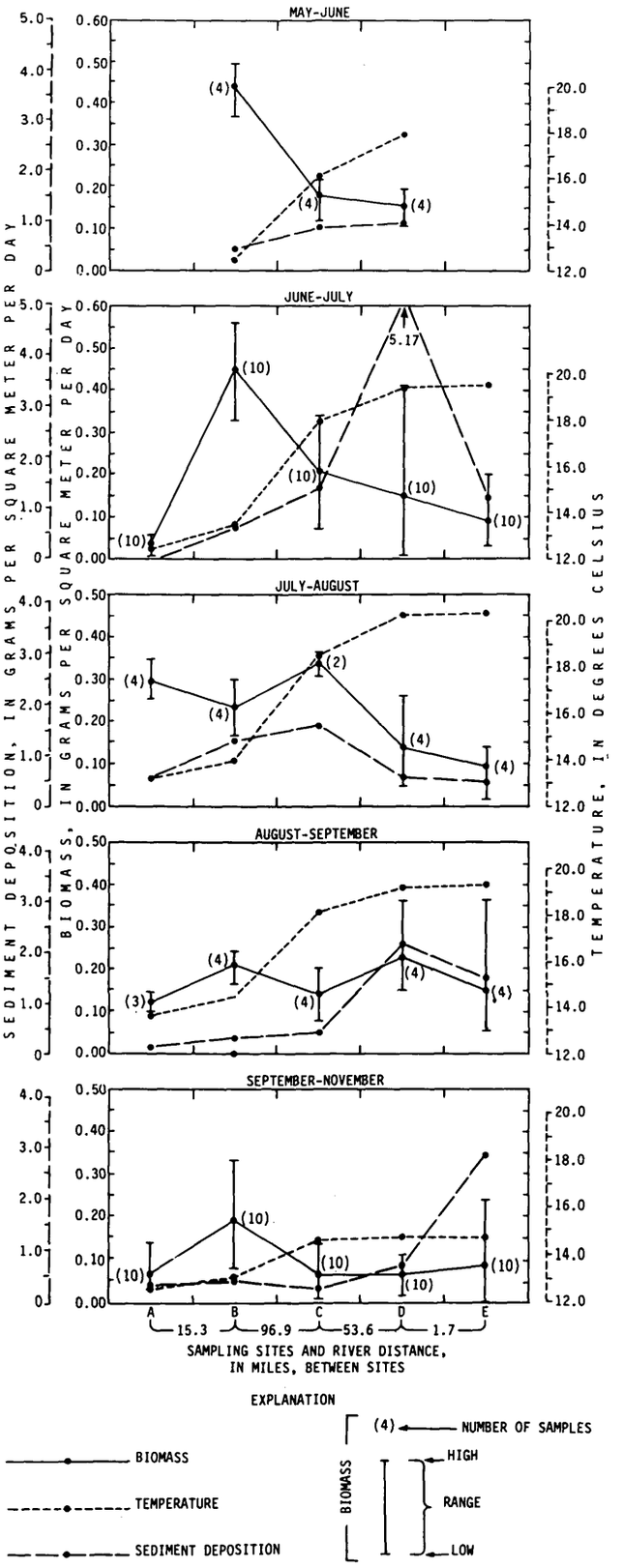

FIGURE 3.—Mean daily periphyton biomass, mean daily sediment deposition, and mean daily temperature, May through November 1972.

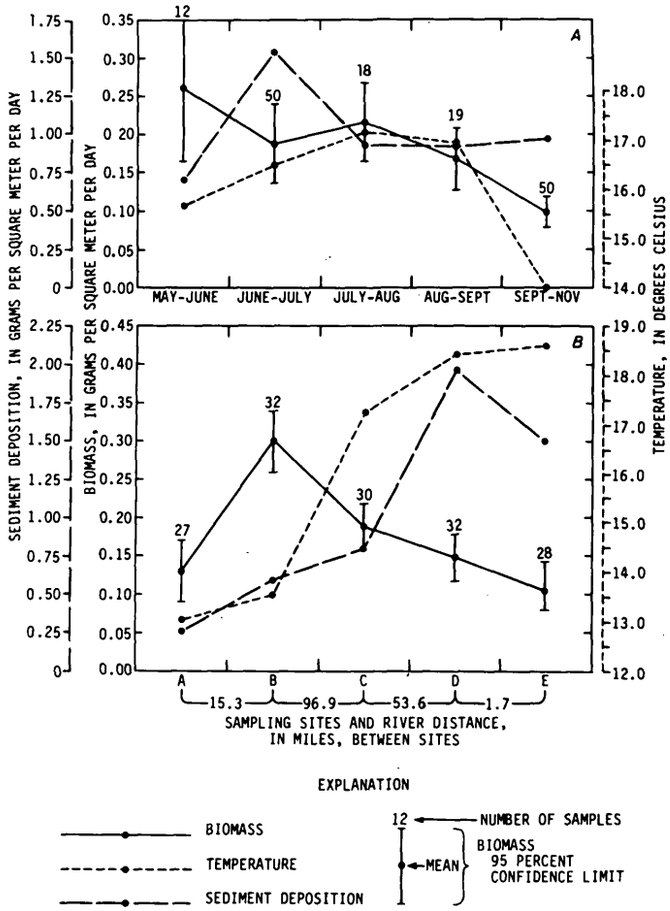

FIGURE 4.—Averages of periphyton biomass, sediment deposition, and temperature, May through November 1972. *A*, For all sites. *B*, For individual sites.

light that control occurrence and growth of periphyton and any one of these may actually be the primary factor for difference in periphyton biomass. Regardless of the biomass differences (fig. 4*B*) the confidence limits show that site B is probably the only site where biomass was significantly different from the other sites.

Phytoplankton

Occurrence and identification

Phytoplankton were represented by 43 species of diatoms, 11 species of green algae, 8 species of blue-green algae, and 1 species of yellow-brown algae, total-63 species (table 3). As with the periphyton, diatoms were the dominant group in number of species, frequency of occurrence, and concentration. Among the diatoms, *Achnanthes lanceolata* and *Melosira varians* occurred most frequently, and in the highest concentrations at all five sites. The diatoms *Fragilaria virescens* and *Nitzschia palea* occurred frequently at every site, but in much higher concentrations at the three down-

TABLE 3.—*Types, concentrations, and occurrence of phytoplankton, May through November 1972*

[Samples were collected monthly for 7 months. Occurrence indicates number of samples in which the species occurred]

Phytoplankton taxa	Sites																			
	A				B				C				D				E			
	Organisms/mL			Occurrence	Organisms/mL			Occurrence	Organisms/mL			Occurrence	Organisms/mL			Occurrence	Organisms/mL			Occurrence
	Mean	High	Low		Mean	High	Low		Mean	High	Low		Mean	High	Low		Mean	High	Low	
CHLOROPHYTA																				
Chlorophyceae (green algae)																				
Actiniastrum hantzschii	--	--	--	--	--	--	--	--	73	73	73	1	92	110	73	2	74	84	64	2
Ankistrodesmus falcatus	--	--	--	--	--	--	--	--	28	42	14	2	59	59	59	1	52	52	52	1
Ankistrodesmus sp.	12	12	12	1	23	23	23	1	--	--	--	--	110	110	110	1	64	64	64	1
Crucigenia quadrata	--	--	--	--	--	--	--	--	--	--	--	--	20	20	20	1	--	--	--	--
Eudorina elegans	--	--	--	--	--	--	--	--	58	58	58	1	42	42	42	1	24	24	24	1
Pandorina morum	12	12	12	1	--	--	--	--	--	--	--	--	--	--	--	--	--	--	--	--
Pediastrum duplex	240	240	240	1	--	--	--	--	--	--	--	--	--	--	--	--	--	--	--	--
Scenedesmus bijuga	40	66	24	3	46	78	24	3	63	89	26	5	130	210	36	7	120	260	56	6
Scenedesmus quadricauda	30	30	30	1	--	--	--	--	--	--	--	--	--	--	--	--	--	--	--	--
Scenedesmus sp.	--	--	--	--	--	--	--	--	--	--	--	--	--	--	--	--	10	10	10	1
Sphaerocystis schroeteri	150	150	150	1	210	210	210	1	--	--	--	--	--	--	--	--	--	--	--	--
CHRYSOPHYTA																				
Bacillariophyceae (diatoms)																				
Achnanthes lanceolata	67	110	41	7	90	140	51	7	84	170	38	7	60	85	22	7	49	100	16	5
Amphora ovalis	--	--	--	--	--	--	--	--	51	51	51	1	--	--	--	--	55	55	55	1
Asterionella formosa	--	--	--	--	--	--	--	--	38	38	38	1	38	38	38	1	40	40	40	1
Cocconeis placentula	--	--	--	--	15	15	15	1	6	6	6	1	4	4	4	1	8	8	8	1
Cyclotella bodanica	--	--	--	--	--	--	--	--	25	36	14	2	34	34	34	1	34	34	34	1
Cyclotella meneghiniana	--	--	--	--	--	--	--	--	--	--	--	--	31	31	31	1	--	--	--	--
Cyclotella sp.	51	51	51	1	36	36	36	1	--	--	--	--	15	15	15	1	130	130	130	1
Cymatopleura solea	--	--	--	--	--	--	--	--	--	--	--	--	--	--	--	--	2	2	2	1
Cymbella sp.	--	--	--	--	--	--	--	--	--	--	--	--	15	15	15	1	16	16	16	1
Cymbella ventricosa	22	25	20	2	24	31	15	3	42	52	31	2	38	44	32	2	34	51	16	2
Diatoma vulgare	40	56	25	2	23	30	14	3	16	24	9	2	6	6	6	1	2	2	2	1
Epithemia sorex	--	--	--	--	--	--	--	--	--	--	--	--	8	8	8	1	4	4	4	1
Epithemia zebra	--	--	--	--	--	--	--	--	4	4	4	1	4	4	4	1	4	4	4	1
Fragilaria crotonensis	25	25	25	1	--	--	--	--	--	--	--	--	--	--	--	--	--	--	--	--
Fragilaria sp.	--	--	--	--	--	--	--	--	--	--	--	--	79	79	79	1	21	21	21	1
Fragilaria virescens	40	55	31	3	40	51	30	4	150	200	85	4	200	430	86	4	120	260	64	4
Gomphonema parvulum	--	--	--	--	--	--	--	--	--	--	--	--	--	--	--	--	18	18	18	1
Gomphonema sp.	--	--	--	--	--	--	--	--	8	8	8	1	14	14	14	1	--	--	--	--
Gyrosigma sp.	--	--	--	--	--	--	--	--	--	--	--	--	2	2	2	1	--	--	--	--
Melosira crenulata	44	44	44	1	--	--	--	--	38	67	8	2	45	61	29	1	120	160	76	2
Melosira granulata	--	--	--	--	--	--	--	--	6	6	6	1	--	--	--	--	--	--	--	--
Melosira sp.	--	--	--	--	69	69	69	1	--	--	--	--	31	31	31	1	--	--	--	--
Melosira varians	42	69	26	6	35	47	24	6	83	200	30	6	75	190	42	5	72	180	26	5
Meridion sp.	16	16	16	1	--	--	--	--	--	--	--	--	--	--	--	--	--	--	--	--
Navicula exigua	--	--	--	--	--	--	--	--	8	8	8	1	36	36	36	1	24	24	24	1
Navicula papula	--	--	--	--	--	--	--	--	2	2	2	1	--	--	--	--	--	--	--	--
Navicula radiosa	--	--	--	--	--	--	--	--	22	22	22	1	--	--	--	--	--	--	--	--
Navicula sp.	--	--	--	--	45	45	45	1	57	57	57	1	22	22	22	1	--	--	--	--
Navicula viridula	--	--	--	--	--	--	--	--	--	--	--	--	--	--	--	--	16	16	16	1
Nitzschia acicularis	--	--	--	--	--	--	--	--	40	40	40	1	69	69	69	1	55	55	55	1
Nitzschia linearis	--	--	--	--	--	--	--	--	4	4	4	1	--	--	--	--	--	--	--	--
Nitzschia palea	62	97	36	4	74	96	55	4	150	180	130	4	140	230	91	4	95	120	64	1
Nitzschia romana	38	54	21	3	45	62	27	2	96	150	43	3	120	120	120	1	79	97	60	2
Nitzschia sigmoidea	--	--	--	--	--	--	--	--	--	--	--	--	6	6	6	1	--	--	--	--
Nitzschia sp.	60	60	60	1	65	65	65	1	43	43	43	1	32	32	32	1	50	50	50	1
Rhoicosphenia curvata	16	16	15	2	65	65	65	1	65	140	24	6	53	77	40	5	49	83	23	5
Surirella angustata	--	--	--	--	--	--	--	--	--	--	--	--	6	6	6	1	--	--	--	--
Surirella arctissima	21	21	21	1	--	--	--	--	--	--	--	--	--	--	--	--	--	--	--	--
Surirella ovata	36	46	21	3	43	68	21	3	38	52	15	4	35	40	30	2	24	26	22	2
Synedra acus var radians	--	--	--	--	--	--	--	--	--	--	--	--	--	--	--	--	10	10	10	1
Synedra sp.	--	--	--	--	--	--	--	--	15	15	15	1	--	--	--	--	--	--	--	--
Synedra ulna	--	--	--	--	--	--	--	--	28	28	27	2	--	--	--	--	130	130	130	1
Tabellaria flocculosa	--	--	--	--	--	--	--	--	--	--	--	--	2	2	2	1	--	--	--	--
Chrysophyceae (yellow-brown algae)																				
Synura uvella	--	--	--	--	--	--	--	--	--	--	--	--	75	130	20	2	--	--	--	--
CYANOPHYTA																				
Myxophyceae (blue-green algae)																				
Agmenellum elegans	--	--	--	--	--	--	--	--	230	230	230	1	--	--	--	--	--	--	--	--
Agmenellum sp.	--	--	--	--	--	--	--	--	--	--	--	--	--	--	--	--	190	190	190	1
Anabaena sp.	--	--	--	--	52	55	50	2	--	--	--	--	120	120	120	1	--	--	--	--
Anacystis rivularis	81	98	64	2	91	91	91	1	--	--	--	--	--	--	--	--	--	--	--	--
Lyngbya sp.	19	19	19	1	260	260	260	1	--	--	--	--	--	--	--	--	--	--	--	--
Oscillatoria sp.	250	250	250	1	--	--	--	--	130	130	130	1	160	160	160	1	--	--	--	--
Oscillatoria tenuis	88	100	75	2	120	210	40	2	--	--	--	--	--	--	--	--	--	--	--	--
Tolypothrix distorta	--	--	--	--	170	170	170	1	--	--	--	--	--	--	--	--	--	--	--	--
TOTALS	25				22				32				38				34			

stream sites. *F. virescens* has been charactrized as occurring most frequently in waters containing high inorganic nutrient concentrations (Lowe, 1974); higher sediment concentrations downstream may have supplied the large nutrient concentrations required for its occurrence. *N. palea* has frequently been found in waters with low oxygen concentrations, high organic content, and temperatures above 15°C. Its presence in water is considered to be an indicator of organic pollution (Lowe, 1974). Palmer (1969) listed *N. palea* second in a list of organic-pollution-tolerant species of algae.

The green algae (class, Chlorophyceae) were the next dominant class in occurrence and concentration. *Scenedesmus bijuga* occurred at every site at least three times. Most of the green algae occurred at the downstream sites, but all in low concentrations. Few numbers of *Scenedesmus quadricauda* and *Ankistrodesmus falcatus* were found in the river, but they are listed by Palmer (1969) as number 4 and 8 (out of 60) as organic-pollution-tolerant species.

The occurrences of blue-green algae were inconsistent, with no type occurring more than twice at each site. *Oscillatoria* sp. occurred at the most sites (three) and in the highest concentrations. *Oscillatoria tenuis*, another blue-green algae, was also listed among the top five pollution-tolerant species (Palmer, 1969), but in our study it was found only at the two upper sites. Most other algae that are regarded as pollution tolerant were found only, or most abundantly, at the downstream sites. Because of the inconsistency in distribution of organic-pollution-tolerant algae, their occurrence does not necessarily indicate the presence of organic pollution. Most algae have wide rather than narrow tolerance ranges and live and reproduce under variable water-quality conditions. A reliable assessment of biological water-quality conditions, based on individual indicator species, cannot be made until, (1) changes in abundance of tolerant and intolerant phytoplankton species, and (2) occurrence and distribution of organic material, are defined with greater precision.

The greatest number of algal species (38) and highest total mean concentration (2,000 organisms per mL) occurred at site D. The highest number of occurrences of all species of algae was 69 at site C. The overall mean concentration (for each site for all sampling periods) was largest at site B (75 organisms per mL). Site B had the smallest number of species (22). However, the average concentration per species was higher than at the other sites.

The total phytoplankton concentration and number of species generally increased downstream (fig. 5). The highest concentration was 980 organisms/mL at site D in September, and the greatest number of species was 23, at site D in May. The concentration of diatoms was almost always highest at site C. The blue-green algae were found predominantly at the two upstream sites, and in all monthly samples, except May. The overall total concentration of phytoplankton for all sites was highest in June (3,900 organisms per mL) and lowest (2,000 organisms per mL) in November. The highest overall total concentration for all months was 5,000 organisms per mL at site D and the lowest was 2,000 organisms per mL at site A. Green algae occurred in nearly every sample, but most frequently and in higher concentrations downstream.

TABLE 4.—*Similarity indices,*[1] *May through November 1972*

[See figure 1 for location of sites]

Compared sites	A	B	C	D	E
A	--	0.72	0.46	0.48	0.47
B	0.72	--	.48	.57	.50
C	.46	.48	--	.69	.70
D	.48	.57	.69	--	.72
E	.47	.50	.70	.72	--

[1] Similarity indices were calculated from phytoplankton species composited for all monthly sampling intervals.

A similarity index (Odum, 1971) was calculated to compare the species of phytoplankton collected at each site for all sample intervals (table 4). The index is expressed as $S=\frac{2C}{A+B}$, where A is the number of species in sample A, B is the number of species in sample B, and C is the number of species common to both samples. The similarity index values lie between 0 and 1; the closer the value to 1, the greater the similarity in the species composition between sites. The species at one site were compared to the species at another, until the similarity in the species composition of all sites was compared.

The greatest similarities (0.72) were between sites A and B, and sites D and E. Sites A and B are close together as are D and E. The similarity of phytoplankton species decreased downstream. A part of the dissimilarity of sites A and B to sites, C, D, and E is due to the infrequency of blue-green algae at the lower three sites, and a greater preponderance of diatom species at the lower three sites. The change in the phytoplankton community downstream is probably a function of the result of changing habitat on reproduction and growth of diatoms, as the downstream sites have a greater volume of flow and slower velocities than up-

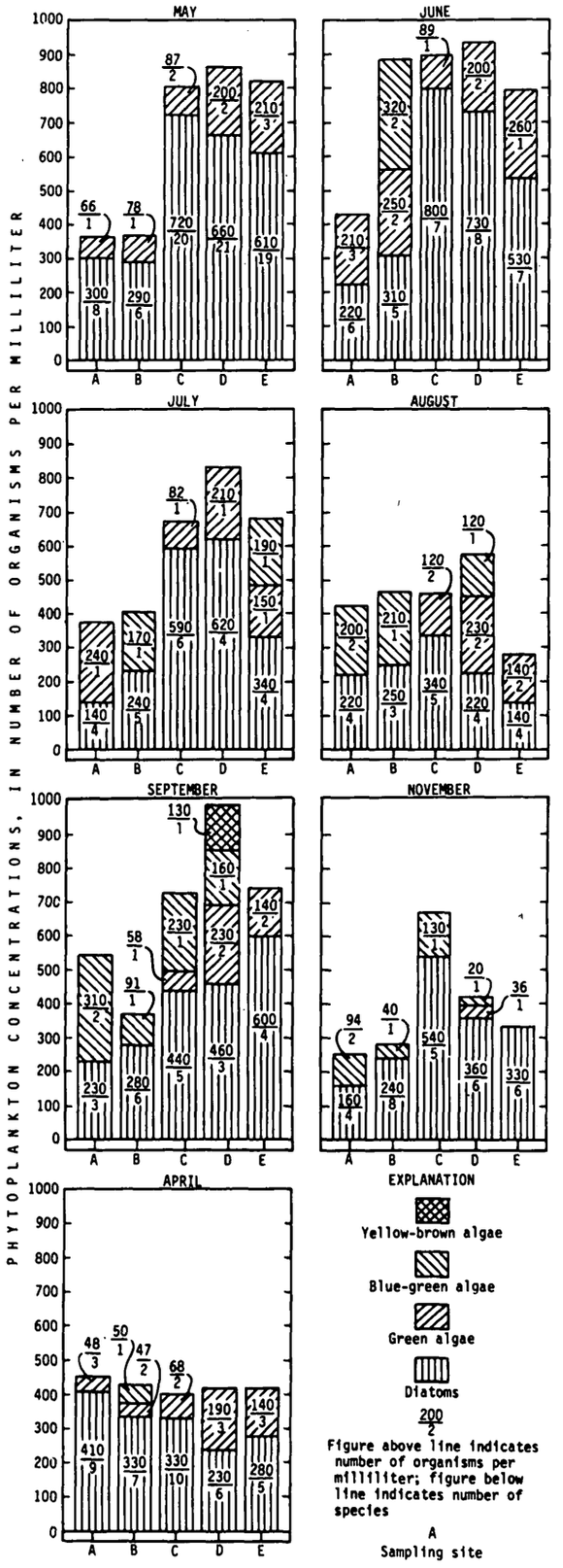

FIGURE 5.—Monthly distribution and concentrations of the major taxa of phytoplankton for selected months in 1972 and April 1973.

stream sites. Changing river conditions downstream may allow for reproduction and growth of more species of phytoplankton while causing the elimination of some species that were found upstream (Patten, 1962).

The diversity index was calculated to quantify phytoplankton community changes in the Sacramento River. The diversity index, as proposed by Wilhm and Dorris (1968, p. 478), considers the diversity per individual (d) as:

$$d = -\sum_{i=1}^{s} \frac{n_i}{n} \log_2 \frac{n_i}{n}$$

where n_i is the number of individuals per taxon, n is the total number of individuals, and s is the total number of taxa in the sample of the community. Logarithms to the base 2 may be obtained by multiplying logarithms to the base 10 by 3.3219. The diversity index values range from 0 to some positive number, with maximum diversity occurring when each individual in the sample belongs to a different species and a minimum diversity occurring when all individuals belong to the same species. Generally, in areas of organic loading, large numbers of individuals and small numbers of species (low diversity) are found; where organic loading or toxic materials are not present, the biotic community consists of large numbers of species.

The phytoplankton diversities that were calculated for each sampling interval for individual sites are shown in figure 6. A two-way analysis of variance test without replication of the diversity indices (Sokal and Rohlf, 1969) showed that there was no significant difference in diversity among sites, but differences in diversity indices owing to sampling period were highly significant ($p<0.001$). The diversity was usually highest for each site in May and April and lowest in July and August. The diversity values ranged from a high

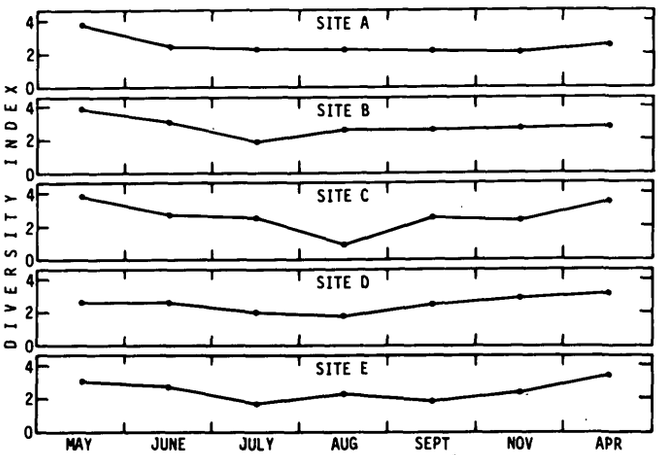

FIGURE 6.—Monthly phytoplankton diversity index values for selected months in 1972 and April 1973.

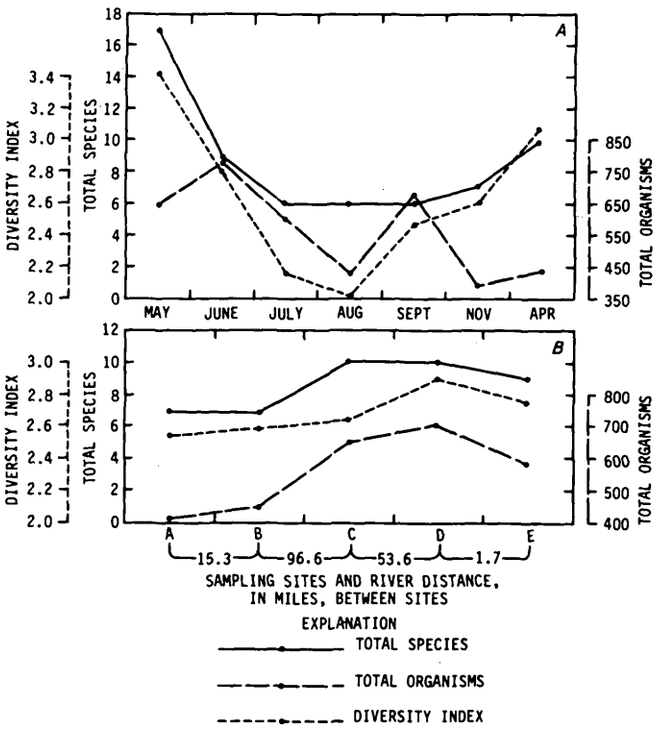

FIGURE 7.—Means of phytoplankton diversity, total organisms, and total species for selected months in 1972 and April 1973. *A*, For each monthly sampling interval for all sites. *B*, For individual sites for all sampling intervals.

of 3.88 at site D in May to a low of 0.95 at site C in August. Figure 7*A* shows the averages for all sites of the diversities, total species, and total organisms for each sampling interval. The mean diversity for all sites decreased from a high of 3.44 in May to a low of 2.04 in August. The diversity index increased again to 3.10 in April. The mean number of species for all sites was also highest in May (17) but decreased to 6 from July to September. The mean number of organisms was highest in June and September and lowest in November.

The averages for all sampling intervals of the diversities, total organisms, and total species for each site are shown in figure 7*B*. The mean diversity for all sampling intervals increased downstream from a low of 2.54 at site A to a high of 2.84 at site D. The mean number of organisms and mean number of species also increased downstream.

Comparison of 1972–73 phytoplankton data with 1960–61 phytoplankton data

The phytoplankton collected during 1972–73 (table 5) and 1960–61 (California Department of Water Resources, 1962c; Greenberg, 1964) were compared at sites A, C, and D. In 1960–61, these sites were characterized by 22 genera of diatoms, 14 genera of green algae, 9 genera of blue-green algae, 3 genera of euglenoids, 1 genus of yellow-brown algae, and 1 genus of dinoflagellates. In 1972–73, phytoplankton from the three sites consisted of 9 genera of diatoms, 8 genera of green algae, 5 genera of blue-green algae, and 1 genus of yellow-brown algae. Of these, 23 genera found in 1960–61 were not found in 1972–73, and 6 genera found in 1972–73 were not found in 1960–61. Most of the variation in generic composition was with the diatoms and green algae, but some green algae collected

TABLE 5.—*Comparison of generic occurrences of phytoplankton, 1972–73 to 1960–61*

[See figure 1 for location of sites]

Genera	Site A		Site C		Site D	
	1972–73	1960–61	1972–73	1960–61	1972–73	1960–61
CHLOROPHYTA						
Chlorophyceae (green algae)						
Actiniastrum	--	--	X	X	X	X
Ankistrodesmus	X	X	X	X	X	X
Cladophora	--	--	--	X	--	--
Closteriopsis	--	--	--	X	--	--
Cosmarium	--	X	--	X	--	X
Crucigenia	--	--	--	--	X	--
Eudorina	--	--	X	--	X	--
Gloecystis	--	X	--	--	--	--
Mougeotia	--	X	--	--	--	--
Oocystis	--	X	--	--	--	X
Pandorina	X	X	--	X	--	X
Pediastrum	X	X	--	X	--	X
Scenedesmus	X	X	X	X	X	X
Sphaerocystis	X	--	--	--	--	--
Stigeoclonium	--	X	--	--	--	--
Tetraedron	--	--	--	--	--	X
UGF (unidentified green flagellates)	--	X	--	X	--	X
Ulothrix	--	X	--	--	--	X
CHRYSOPHYTA						
Bacillariophyceae (diatoms)						
Achnanthes	X	X	X	X	X	X
Amphora	--	X	X	X	--	X
Asterionella	--	X	X	X	X	X
Ceratoneis sp.	--	X	--	X	--	X
Cocconeis	--	X	X	X	X	X
Cyclotella sp.	X	X	X	X	X	X
Cymatopleura	--	--	--	X	--	X
Cymbella	X	X	X	X	X	X
Diatoma sp.	X	X	X	X	X	X
Epithemia	--	--	X	X	X	X
Fragilaria sp.	X	X	X	X	X	X
Gomphonema	--	X	X	X	X	X
Gyrosigma	--	--	--	--	X	X
Melosira	X	X	X	X	X	X
Meridion	X	--	--	--	--	--
Navicula sp.	--	--	X	--	X	X
Nitzschia sp.	X	--	X	X	X	X
Pinnularia sp.	--	--	--	X	--	--
Rhoicosphenia	X	X	X	X	X	X
Rhopalodia	--	--	--	X	--	--
Surirella sp.	X	--	X	X	X	X
Synedra	--	X	X	X	--	X
Tabellaria sp.	--	X	--	X	X	X
Chrysophyceae (yellow-brown algae)						
Dinobryon	--	--	--	--	--	X
Synura	--	--	--	--	X	--
CYANOPHYTA						
Myxophyceae (blue-green algae)						
Agmenellum	--	X	X	--	--	--
Anabaena	--	X	--	X	X	X
Anacystis	X	--	--	--	--	--
Cylindospermum	--	--	--	--	--	X
Entophysalis	--	X	--	--	--	--
Lyngbya	X	X	--	--	--	X
Oscillatoria	X	X	X	X	X	X
Phormidium	--	X	--	--	--	--
Rivularia	--	X	--	--	--	--
Spirulina	--	X	--	X	--	--
EUGLENOPHYTA						
Euglenophyceae (euglenoids)						
Euglena	--	X	--	X	--	X
Strombomonas	--	--	--	X	--	--
Trachelomonas	--	X	--	X	--	X
PYRROPHYTA						
Dinophyceae (dinoflagellates)						
Glenodinium	--	--	--	X	--	--
TOTALS	18	35	22	36	24	37

during 1972–73 were not identified (unidentified green flagellates) and may encompass several of the genera found in 1960–61.

From the data obtained in 1960–61 by the California Department of Water Resources (1962c), the dominant class in both concentration and frequency of occurrence were diatoms, with *Synedra* the most common genus, and *Melosira* and *Cyclotella* next in frequency. The green algae, with *Ankistrodesmus* the most dominant, was the only class other than the diatoms which was frequently found. Of the blue-green algae, *Anabaena* and *Oscillatoria* occurred at all three sites in 1960–61. As mentioned before, *Oscillatoria* was also the dominant blue-green algae collected in 1972–73.

The number of genera increased downstream in 1960–61 from a low of 35 at site A to 37 at site D, a condition similar to that found in 1972–73. However, 40 to 50 percent more genera were collected in 1960–61 than in 1972–73. In the 1960–61 study, the number of genera of blue-green algae decreased downstream, whereas the diatoms increased. In 1972–73, there was no perceptible decrease downstream in blue-green algal genera, but there was a corresponding increase in diatom genera.

In a comparison of the major classes of phytoplankton for sites A, C, and D (fig. 8) for both study periods, the numbers of diatoms and the total phytoplankton concentrations (including some miscellaneous classes) were nearly always higher in 1960–61 than in 1972–73.

Green algal concentrations for both study periods usually peaked in midsummer and decreased to a low in mid-November. The concentrations of green algae were higher in 1960–61 at each site except A. The differences in concentration were not statistically significant ($p>0.05$) at sites A and D, but were significantly larger ($p<0.05$) at site C.

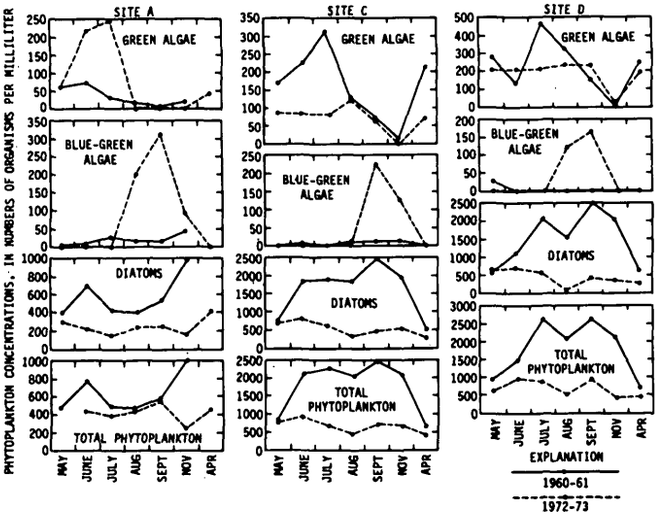

FIGURE 8.—Concentrations of the major groups of phytoplankton, 1960–61 and 1972–73.

The blue-green algal concentrations were nearly always higher in 1972–73 than in 1960–61. Generally, the concentrations during both years decreased downstream. The concentration of blue-green algae increased in 1972–73 throughout the summer, with peaks occurring in September. Concentrations in 1960–61 were always less than 100 organisms per mL at all three sites, and were zero at site D, except in May. However, the higher concentrations in 1972–73 were not significantly different ($p>0.05$) than in 1960–61.

As mentioned previously, the diatom concentrations were larger in 1960–61 than in 1972–73 at all sites and for all sampling intervals, except once each at sites C and D. These higher concentrations at all three sites were significantly different ($p<0.05$). In 1960–61, the diatoms ranged from a low of 410 organisms per mL at site A in May to a high of 2,500 organisms per mL at site D in September. In 1972–73, the diatoms ranged from a low of 150 organisms per mL at site A in July to a high of 800 organisms per mL at site C in June. The mean diatom concentration for all sites, including all samples, was 1,270 organisms per mL in 1960–61 and 420 organisms per mL in 1972–73, which is a 300-percent overall decrease since 1960–61.

The diatoms generally decreased downstream during both study periods. In 1960–61, there were two definite peaks in diatom concentrations. The first peak occurred in June or July, and the second in September or November. In 1972–73, less conspicuous peaks occurred in May or June and in late autumn.

The total phytoplankton concentration at all sites ranged from 450 to 2,700 organisms per mL in 1960–61 and from 250 to 930 organisms per mL in 1972–73. Using the Student's *t*-test, the paired differences for total phytoplankton in 1960–61 and 1972–73 were significantly larger ($p<0.05$) at sites C and D in 1960–61.

SUMMARY AND DISCUSSION

In 1972–73, diatoms were the dominant group in types and occurrence among the periphyton (table 2). The two most common genera were *Achnanthes* and *Melosira* which have been reported as common and often dominant genera in other areas. For example, Douglas (1958) found *Achnanthes* to be the dominant genera in Belle Grange Beck, a small stony stream in England. Cushing (1967) found the autumn-winter periphyton community of the Columbia River to be dominated by diatoms, mainly *Melosira* and *Synedra*, but frequently with high populations of *Achnanthes*.

Butcher (1938) found *Achnanthes* to be a common diatom in alkaline rivers in southern England. Mack (1953) noted that *Achnanthes*, along with several other diatom genera, was common and abundant in the lower and slower-moving reaches of the Liesingsbaches in Vienna Woods, Austria, and Stockner and Armstrong (1971) found *Achnanthes* to be the most common diatom at all sampled depths in the littoral zone of four experimental lakes in northwestern Ontario. *Achnanthes* and *Melosira*, then, are extremely common forms with wide tolerance ranges. *Achnanthes lanceolata* is one of the first taxa to colonize a new stream (McIntire, 1966).

Although differences in types and occurrences of periphyton between sites were small, the number of genera and frequency of occurrence increased downstream from sites A and B. The greatest number of genera and highest percentage of occurrence of periphyton were at site C.

The periphyton biomass decreased downstream with the largest measured mean daily biomass being at site B. The decreased periphyton biomass downstream is probably a function of several factors. First, suspended sediment and sediment deposition on the substrates were probably factors controlling periphyton biomass in the Sacramento River. As sediment deposition increased downstream, the biomass decreased. The sediment deposition probably physically interfered with periphyton colonization and inhibited light penetration through the water. Second, velocity plays an important role in algal distribution and production. In the Sacramento River, the velocity decreased downstream, with increased discharge. The decreased velocity downstream is probably a restrictive factor to periphyton productivity, as others (Hynes, 1970) have observed that attached algae are more abundant in faster moving water and that there is an innate current demand in many species. A current constantly renews materials in solution, such as dissolved gases, to make the water physiologically richer (Hynes, 1970).

The higher mean daily periphyton biomass at site B probably occurred because this site is about 1.6 km downstream from the discharge of sewage and industrial effluents which may provide additional nutrients for periphyton production.

The periphyton biomass decreased throughout succeeding monthly sampling periods, with the highest rate in June-July and the lowest rate in September-November. This decrease probably is a function of increased suspended-sediment deposition produced by higher discharges in September-November.

Periphyton biomass ranged from 0.56 $(g/m^2)/d$ at site B throughout the June-July sampling period to a low of 0.00 $(g/m^2)/d$ at site E throughout the September-November sampling period. Biomass rates in the Sacramento River are higher but comparable to those measured in some other studies. Cushing (1967) measured a high of 0.3 $(g/m^2)/d$ in the Columbia River. However, the measurements made by Cushing were only for 2-week periods; a longer colonization period would probably produce a higher production rate. Stockner and Armstrong (1971) measured 0.027 $(g/m^2)/d$ during the initial colonization period of 30 days in the experimental lakes area of northwestern Ontario, and 0.25 $(g/m^2)/d$ during the most rapid growth phase, 30 days later. Differences in length of colonization period and methods of measurement would have to be considered to determine whether these differences in production rates are significant.

The phytoplankton composition was also dominated by diatoms. Site D had the greatest number of genera collected, but the highest overall mean concentration was at site B. The phytoplankton concentrations increased downstream as the slower reaches of the river provide a longer time for phytoplankton to reproduce (Hynes, 1970). The diversity of phytoplankton increased downstream with a mean high of 2.84 at site D. The diversity indices ranged from 0.95 at site C in August to 3.88 at site D in May. The diversity was lowest in August at all sites and highest in April and May. The wide range of diversity values measured in the Sacramento River reflects a variety of water-quality conditions among the sites throughout the sampling periods. Velocity, temperature, sediments, and many other variables affect the distribution and abundance of phytoplankton.

The phytoplankton composition in 1972–73 was similar to that in 1960–61 at sites A, C, and D, although more genera were collected in 1960–61. The concentrations of total phytoplankton were much higher in 1960–61 than in 1972–73. These differences were the result of higher concentrations of green algae and diatoms in 1960–61. The green algal concentrations were significantly higher at site C in 1960–61 ($p<0.05$) and the diatoms were significantly higher ($p<0.05$) at all three sites in 1960–61. The concentration of blue-green algae was almost always higher in 1972–73 than in 1960–61, but the differences were not significant. However, the higher blue-green algal concentrations in 1972–73 could be biologically significant because blue-green algae often cause nuisance bloom conditions. The blue-green algae in late summer of 1972 peaked to a high of 200 to 300 organisms per mL between the sites, whereas they were near zero at a similar time in 1960.

More frequent sampling should be made on the Sacramento River in the future to determine whether blue-green algal concentrations increase to bloom conditions during the summer.

The decrease in total phytoplankton concentrations from the 1960–61 period to the 1972–73 period was unexpected. Suspended sediment may have increased in the Sacramento River with increased discharge causing a reduction of light penetration and thus a decrease in phytoplankton concentrations. Also, the difference in phytoplankton collection methods may have had an effect on the results between 1960–61 and 1972–73. Further speculation cannot be made without additional and more frequent sampling.

REFERENCES CITED

Britton, L. J., and Averett, R. C., 1974, Water-quality data of the Sacramento River, California, May 1972 to April 1973: U.S. Geol. Survey open-file rept., 59 p.

Butcher, R. W., 1938, The algae of the river: Rep. Avon. Biol. Res., v. 5, p. 47–52.

California Department of Water Resources, 1962a, Sacramento River water pollution survey: California Dept. Water Resources Bull. 111, 112 p.

———1962b, Appendix A—Hydrography, hydrology, and water utilization, *to* Sacramento River water pollution survey: California Dept. Water Resources Bull. 111, 138 p.

———1962c, Appendix B—Water quality, *to* Sacramento River water pollution survey: California Dept. Water Resources Bull. 111, 384 p.

———1962d, Appendix C—Public health aspects, *to* Sacramento River water pollution survey: California Dept. Water Resources Bull. 111, 186 p.

Cushing, C. E., 1967, Periphyton productivity and the radionuclide accumulation in the Columbia River, Washington, U.S.A.: Hydrobiologia, v. 29, p. 125–139.

Douglas, Barbara, 1958, The ecology of the attached diatoms and other algae in a small stony stream: Freshwater Ecology, v. 46, p. 295–322.

Greenberg, A. E., 1964, Plankton of the Sacramento River: Ecology, v. 45, p. 40–49.

Hynes, H. B. N., 1970, The ecology of running waters: Toronto, Univ. Toronto Press, 555 p.

Lowe, R. L., 1974, Environmental requirements and pollution tolerance of freshwater diatoms: U.S. Envirnmental Protection Agency 670/4–74–005, Cincinnati, Ohio, 334 p.

Mack, B., 1953, Zur Algen und Pilzflora des Liesingsbaches: Wett. Leben Sonderh., v. 2, p. 136–149.

McIntire, C. D., 1966, Some effects of current velocity on periphyton communities in laboratory streams: Hydrobiologia, v. 27, p. 559–570.

Odum, E. P., 1971, Fundamentals of ecology (3d ed.): Philadelphia, W. B. Saunders Co., 574 p.

Palmer, C. M., 1969, A composite rating of algae tolerating organic pollution: Jour. Phycology, v. 5, no. 1, p. 78–82.

Patten, B. C., 1962, Species diversity in net phytoplankton of Raritan Bay: Jour. of Marine Research, v. 20, p. 57–75.

Slack, K. V., Averett, R. C., Greeson, P. E., and Lipscomb, R. G., 1973, Methods for collection and analysis of aquatic biolgical and microbiological samples: U.S. Geol. Survey Techniques Water-Resources Inv., book 5, chap. A4, 165 p.

Sokal, R. R., and Rohlf, F. J., 1969, Biometry—The principles and practice of statistics in biological research: San Francisco, W. H. Freeman and Co., 776 p.

Stockner, J. G., and Armstrong, F. A. J., 1971, Periphyton of the experimental lakes area, northwestern Ontario: Jour. Fisheries Research Board, Canada, v. 38, p. 215–229.

Utermöhl, H., 1958, Zur Vervollkommnung der quantitativen Phytoplankton Methodik: Internat. Verein. Limnologie Mitt., no. 9, 38 p.

Wetzel, R. G., 1965, Techniques and problems of primary productivity measurements in higher aquatic plants and periphyton: Mem. Ist. Ital. Idrobiol., 18 suppl., p. 249–267.

Wilhm, J. L., and Dorris, T. C., 1968, Biological parameters for water quality criteria: Bio-science, v. 18, p. 477–481.

Jour. Research U.S. Geol. Survey
Vol. 5, No. 5, Sept.–Oct. 1977, p. 561–563

FEASIBILITY AND TECHNOLOGY FOR MAKING REMOTE MEASUREMENTS OF SOLUTES IN WATER

By MARVIN C. GOLDBERG and EUGENE R. WEINER,
Denver, Colo.

Abstract.—An indepth evaluation of the available technology in the field of laser-Raman spectroscopy indicates that a TV-type detector, a single monochromator with a holographic grating, an entrance slit filter blocking the Rayleigh light, and a pulsed laser coupled to signal averaging electronics is the best combination of commercial equipment that is presently available for building a remote water-quality sensor. The resultant sensor would be capable of measuring oxyanions in water at concentrations from 10 to 50 milligrams per liter at distances from ground level to 30 meters above the sample. The main interferences would be ambient light, bioluminescence, and natural fluorescence, all of which are minimized when taking advantage of the signal generating and readout capability contained in this equipment package.

At present, measurements of dissolved solutes in areally extensive bodies of water are made at a few isolated points and usually with a low sampling frequency. Data from such measurements may not be representative of the entire water body. Of greater importance, such sampling cannot reveal large-scale phenomena that may occur, such as rhythmic changes in the overall concentrations of specific solutes. To explore these large-scale phenomena it is necessary to examine dissolved solutes over areas of several square kilometers in a few hours with a high density of sampling positions or with continuous sampling. A method has been sought to sample these locations simultaneously, or in a very limited time period, to avoid the risk of misinterpreting cyclic or random-event changes that may be of greatest interest to the observer. Only one method at present offers a possibility of making rapid measurements over large areas and that is Raman spectrometry, used in a remote-sensing mode. Theoretical projections of the techniques necessary and the physical limits of Raman spectrometry are given by Goldberg and Weiner (1972). Laboratory measurements to define the parameters that regulate sensitivity and resolution were investigated by Cunningham, Goldberg, and Weiner (1977). The purpose of the present paper is to explore, in depth, some of the ideas postulated by those previous investigations and to project the technological pathway towards development of a remote water-quality sensor.

Even under laboratory conditions, Raman analysis of water solutions is not a highly sensitive technique. Not only is the Raman signal relatively weak (Herzberg, 1945; Sloane, 1971), but water itself scatters a characteristic signal of significant intensity throughout the spectral region where signals from solutes of greatest interest are found (Reeves, 1975; Walrafen, 1962). The signal from a solute in low concentration, therefore, is always superimposed upon a relatively large background signal and must be measured as a small difference between two large numbers. Under these conditions, it is particularly important to minimize all nonrandom signal fluctuations so that the noise part of the signal can be averaged out with high statistical confidence. This problem is more severe in the case of remote sensing by Raman spectrometry because the water background signal generally is increased by photoluminescence and bioluminescence (Goldberg and Devonald, 1973) and by ambient light. In addition, nonrandom laser-intensity fluctuations are increased because of optical variations in the long path of the laser beam through the atmosphere, the air-water interface, and the water sample under observation. Cunningham, Goldberg and Weiner (1977) recommended the use of pulsed laser excitation and TV-type optical multichannel-analyzer detection to alleviate these problems.

The TV-type detector measures a wide wavenumber range of the Raman spectrum in a simultaneous, multichannel fashion and has virtually the same quantum efficiency in the visible spectrum as an ordinary photomultiplier tube. Talmi (1975a, b) recently reviewed the different kinds of TV-type detectors in use and discussed many spectrometric applications. In sequential scanning of a Raman spectrum, nonrandom laser-power fluctuations will affect different parts of the spectrum

by different amounts, in a nonreproducible way which cannot be statistically averaged out. A TV-type detector acquires signals over the entire spectrum simultaneously, much like a photographic plate, so that nonrandom fluctuations affect all parts of the spectrum equally and do not interfere with ratio measurements. All that is needed for accurate measurements is an internal reference signal of known magnitude to calibrate the integrated effect of the signal fluctuations. Cunningham, Goldberg, and Weiner (1977) have shown that the water-bending band at 1650 cm^{-1} (wavenumber) in the water background signal can be used as an internal reference. It appears that an ideal TV-type detector should totally eliminate the problem of nonrandom laser-power fluctuations. Talmi (1975a) has stressed that TV detectors actually available at present have several limitations, such as limited spectral coverage and resolution, low integration capacity, and interchannel crosstalk. Even so, the use of TV-type detectors can reduce the problems of nonrandom Raman signal variations significantly, permitting much longer measuring periods with steady enhancement of signal-to-noise ratios (s/n).

There are further advantages to using TV detectors in Raman remote sensing. The simultaneous acquisition of the entire spectrum changes the total measuring time by a factor equal to the reciprocal of the number of points that must be measured in order to measure a solute peak. As an example, Cunningham, Goldberg, and Weiner (1977) described a three-point method for determining spectral peak parameters. Since the water-reference peak at 1650 cm^{-1} must be measured along with each solute peak, the two peaks require a total of six measurement points, so that the use of a TV detector would reduce the measurement time to one-sixth that of a scanning spectrometer. In addition, observing the whole spectrum continuously has an advantage for qualitative, as well as quantitative, analysis.

The most highly developed TV-type detectors are current-measuring, not photon-counting, devices and therefore have a higher dark-current and random-noise content in their output, a condition that necessitates cooling and an appropriately longer measuring time for the same signal-to-noise ratio. Current-measuring detectors also are more sensitive to small variations in the gain and uniformity of the photosensitive elements. Photon-counting TV detectors, however, are being developed (Talmi, 1975a) and may eventually offer superior performance for Raman remote-sensing purposes.

The problems of background signal intensity arising from detector dark current, sample luminescence, and ambient light can be alleviated by using pulsed laser excitation and gated detection. Laser pulses can be as short as several nanoseconds without decreasing the average power significantly because pulsing the laser permits correspondingly higher peak power levels. When the laser excitation is pulsed, the part of the background signal that arises from the water Raman scattering and from photoluminescent impurities also will be pulsed. Background signal caused by detector dark current, ambient light, and bioluminescence is unaffected by the excitation source and will be continuous. That part of the background signal that is continuous is greatly reduced by using pulsed laser excitation and gating the TV detector to be "on" only while the Raman signal pulse is being received. Because Raman scattering is an instantaneous process, the return signal pulses from the solute are virtually the same width as the excitation pulse. The best signal-to-noise ratio will be achieved if the TV-detector-gate width just matches the signal-pulse width. Detector-gate and laser-pulse widths of 10^{-8} to 10^{-7} seconds are readily obtainable. This can give an overall detector duty cycle of about 10^{-6} with SIT (silicon intensified target) vidicon-type tubes (Talmi, 1975a) when the tube read-out time is taken into account. The continuous background signal will be reduced by a factor equal to the detector duty cycle. Further improvement can be made by using two signal-storage memories so that the continuous part of the background can be measured between pulses and subtracted from the solute Raman signal. Pulsed background-signal intensity due to photoluminescence will be reduced by a factor proportional to the vidicon duty cycle if the photoluminescence lifetime is longer than the detector gating time.

Tobin (1970) has shown that the strong Rayleigh scattering that always accompanies Raman scattering can negate the advantages of optical multichannel detection, if it reaches the detector with too high an intensity. A double monochromator would serve the purpose of rejecting Rayleigh light, but also would severely limit the spectral range displayed on a TV detector and would have less light throughput than a single monochromator. It is common practice to equip single monochromators with an entrance slit band-stop filter or a small "premonochromator" with a wide band pass in order to prevent scattered light from a strong signal from interfering with the measurement of weak signals. As recommended by Cunningham, Goldberg, and Weiner (1977), the best instrumental arrangement for remote sensing by Raman spectrometry might be

one utilizing pulsed laser excitation, TV-type multichannel detection, a single monochromator having some form of Rayleigh light filter, and a holographic diffraction grating, which scatters much less light randomly than the usual ruled or replicated gratings in proportion to the overall light throughout. Present technology indicates that this latter design would be the most fruitful avenue of development and would be most likely to result in a working instrument.

A remote-sensing Raman spectrometer designed as described herein can be made from commercially available components and should be capable of detecting any polyatomic molecule. The evaluation of this proposed Raman sensor as a water-quality monitor was based on the work of Cunningham, Goldberg and Weiner (1977). It was found that the concentrations of nitrate and phosphate in natural water are normally below the predicted instrument sensitivity of 10 to 50 mg/L, whereas sulfate concentrations are normally higher than the predicted sensitivity limits. We believe that a remote sensor capable of measuring sulfate in certain natural waters could be built immediately. Further, it is anticipated that other polyatomic molecules could also be measured, since the Raman detection cross section for sulfate is similar to other molecular Raman cross sections. Additionally, an instrument with these specifications could rapidly map the concentrations of many water solutes, even in water bodies that are difficult to access by ground. With spatially broad and continuous coverage, easily repeated in short-time intervals, the synchronous large-scale distribution patterns of solutes would be revealed, similar to Alain Falconer's macrowaves on the Great Lakes (MacDowell and others, 1972), as well as time variations in the distributions. Information of this kind is unobtainable with present methods.

REFERENCES CITED

Cunningham, K. M., Goldberg, M. C., and Weiner, E. R., 1977, Investigation of detection limits for solutes in water measured by laser Raman spectrometry: Anal. Chemistry, v. 49, no. 1, p. 70–75.

Goldberg, M. C., and Devonald, D. H., III, 1973, Fluorescent spectroscopy, a technique for characterizing surface films: U.S. Geol. Survey Jour. Research, v. 1, no. 6, p. 709–717.

Goldberg, M. C., and Weiner, E. R., 1972, Applications of spectroscopy to remote determination of water quality: Natl. Aeronautical and Space Adm. 4th Ann. Earth Resources Program Rev., v. III, chap. 81, p. 10–14.

Herzberg, Gerhard, 1945, Molecular spectra and molecular structure, II. Infrared and Raman spectra of polyatomic molecules: Princeton, N.J., D. Van Nostrand Co., Inc., 658 p.

MacDowell, J., Falconer, Alain, and Thomson, P. B., 1972, Simulation studies of ERTS–A and B data for hydrologic studies in the Lake Ontario Basin: Natl. Aeronautical and Space Adm. 4th Ann. Earth Resources Program Rev., v. III, chap. 76, p. 1–2.

Reeves, R., ed., 1975, Manual of remote sensing: Falls Church, Va., photogrammetry, v. II, p. 1496–1502.

Sloane, H. J., 1971, The technique of Raman spectroscopy: A state-of-the-art comparison to infrared: Appl. Spectroscopy, v. 25, p. 430–439.

Talmi, Y., 1975a, Applicability of TV-type multichannel detectors to spectroscopy: Anal. Chemistry, v. 47, no. 7, p. 658A–670A.

——— 1975b, TV-type multichannel detcetors: Anal. Chemistry, v. 47, no. 7, p. 697A–709A.

Tobin, M. C., 1970, Theoretical comparison of light amplifier and photomultiplier tube recording of Raman spectra: Appl. Optics, v. 9, p. 502–503.

Walrafen, G. E., 1962, Raman spectral studies of the effects of electrolytes on water: Jour. Chem. Physics, v. 36, p. 1035–1042.

Jour. Research U.S. Geol. Survey
Vol. 5, No. 5, Sept.–Oct. 1977, p. 565–569

CHEMICAL STRUCTURE OF HUMIC ACIDS–PART 1, A GENERALIZED STRUCTURAL MODEL

By R. L. WERSHAW, D. J. PINCKNEY, and S. E. BOOKER, Denver, Colo.

Abstract.—A new model is proposed for the structure of humic acids. In this model humic acid is pictured as being made up of a hierarchy of structural elements. At the lowest level in this hierarchy are simple phenolic, quinoid, and benzene carboxylic acid groups. These groups are bonded covalently into small particles. Particles of similar chemical structure are linked together by weak bonds to form "homogeneous" aggregates. Two or more different types of aggregates may be linked together to form mixed aggregates. Complexes of humic acid and clay minerals are also formed.

The soils, sediments, and surface waters of the Earth's surface constitute a group of interacting systems in which many of the chemical reactions that sustain life on this planet take place. These natural systems consist of both organic and inorganic components. Although the chemistry of the inorganic components has by no means been elucidated completely, a basic theoretical model has been proposed to explain the inorganic reactions that take place in natural waters. (See Garrels, 1960.) The same, however, cannot be said of the organic reactions. One of the main reasons why a model for the organic chemical reactions cannot be formulated is that the chemical structures of the most abundant organic compounds in natural water systems, the humic substances, have not yet been determined.

The humic substances are organic polyelectrolytes which are most commonly identified with the brown organic material in soils (humus). However, humic substances are also present in practically all of the suspended and bottom sediments of rivers, lakes, and estuaries. Their importance in water chemistry is due not only to their ubiquity, but also to their reactivity.

This group of compounds enters into a wide variety of physical and chemical interactions, including sorption, ion exchange, free radical reactions, and solubilization. The water-holding capacity, crumb structure, heat conductivity, exchange capacity, and buffering capacity of soils and the availability of nutrients to plants are controlled to a large extent by the amount of humus in the soil (Kononova, 1966; Paasikallio and others, 1971; Szalay and others, 1970). Humus also interacts with soil minerals; this interaction takes two forms: (1) Humus aids in the weathering and decomposition of silicate and aluminosilicate minerals (Fetzer, 1946), and (2) it is adsorbed by some soil minerals (Schnitzer and Kodama, 1967; Gorbunov and others, 1971).

Both soluble and insoluble organic compounds are sorbed by humus. Ladd and Butler (1971) have shown that the humic and fulvic acid components of soil humus inhibit proteolytic enzymes by binding them. In addition to enzymes, humus strongly binds pesticides and other organic compounds that are found in soils and waters. This sorption reduces the phytotoxicity of herbicides and often inhibits the degradation of pesticides (Wershaw and Goldberg, 1972).

Humic substances are commonly divided into three general categories: Humic acids, fulvic acids, and humin. The definitions for these categories are purely operational in nature. Humic acids are those components of humus which are soluble in strong bases but insoluble in strong acids; fulvic acids are soluble in both acidic and basic solutions; humin is insoluble in both acids and bases. The general belief is that fulvic acids are similar in structure to humic acids but of lower molecular weight. Apparently, however, other groups of compounds such as polysaccharides, proteins, and amino-sugars are also included in many fulvic acid preparations (J. A. Leenheer, oral commun., 1976). Alternate treatment of the humin fraction with strong mineral acids and strong bases generally renders most of the humin soluble in basic solutions (Kononova, 1966). Kononova therefore concluded that humins are humic acids that are bound by the mineral constituents of soils.

In this paper we are proposing a chemical structural model for humic acids. This model will provide a conceptual framework for the further study of humic acids and for interpreting many of the organic inter-

actions that take place in natural water systems. As more information about the chemistry of humic acids is accumulated we should be able to refine the model and to arrive eventually at a detailed understanding of the chemical structure of humic acids. Since the humin and fulvic acid components appear to be related to humic acids, the model that we propose for humic acids should also provide an insight into the chemical structure of these two components as well.

A model of the chemical structure of any polymer material must answer two questions: 1) What are the monomeric units in the polymer? and (2) how are these monomeric units linked together to form the larger macromolecules? We have tried to answer these questions in our model.

The model that we are proposing for humic acid pictures humic acid as being made up of a hierarchy of structural elements. The lowest level in this hierarchy consists of simple phenolic, quinoid, and benzene carboxylic acid groups. These groups are linked together by covalent bonds into relatively small particles with particle weights on the order of a few thousand or less. A small number of more or less chemically distinct particles types can be formed by this process and can be isolated by adsorption chromatography. Groups of similar particles are in turn linked together by weak covalent and noncovalent bonds into aggregates. The degree of aggregation of these "homogeneous" aggregates in solution is a function of pH, the oxidation state of the molecules and of the metal ions present in the system. Different types of "homogeneous" aggregates are linked together in unfractionated humic acids into mixed aggregates. Both mixed and "homogeneous" aggregates can be bonded to mineral particles in soils and sediments to form still larger particles. Other organic compounds can also be incorporated into the humic acid aggregates. Some of these compounds will be weakly bound in the aggregates, whereas others will be chemically bonded to the aromatic network of the particles.

This model is quite different from models that have been proposed previously for humic acid. (See reviews by Schnitzer and Khan, 1972; Flaig, 1971; Kononova, 1966.) In most of the previous proposals it was postulated that humic acids are highly cross-linked aromatic polymers in which covalent bonds such as carbon-carbon, ether, and ester linkages join the monomeric units together into large, high-molecular particles. In addition to the benzene carboxylic acid and phenolic groups that most workers have incorporated into their humic acid modes, some authors have also included fatty acid, protein, and polysaccharide groups in their models.

We will discuss the evidence for this model by starting with the smallest molecular units in the model and then working our way up to the larger structural elements. Chemical degradation has shown that the basic building blocks of humic acids are benezene carboxylic acid groups, substituted phenolic groups, and quinoid groups. A number of relatively drastic chemical degradation procedures have been used for the isolation of the monomeric units of humic acid polymers. Thus, techniques such as sodium-amalgam fusion (Schnitzer and Ortiz de Serra, 1973a; Dormaar, 1969; Stevenson and Mendez, 1967; Burges and others, 1964); oxidation with peracetic acid (Schnitezr and Skinner, 1974); and sequential oxidation with alkaline cupric oxide, alkaline potassium permanganate, and alkaline hydrogen peroxide (Schnitzer and Ortiz de Serra, 1973b) have been used to degrade humic acids. These methods yield single-ring benzene carboxylic acids, simple phenolic acids, aliphatic acids, derivatives of these acids, and single-ring phenols. Potassium permanganate oxidation of methylated humic acid has also yielded a small amount of biphenyl guaiacyl compounds (Schnitzer and Ortiz de Serra, 1973b). Neyroud and Schnitzer (1975a and 1975b) have tried milder techniques for the degradation of humic acids. Using alkaline hydrolysis with 2 *N* sodium hydroxide, they obtained degradation products similar to those mentioned above. Similar products were also isolated after ultrasonic dispersion and hydrolysis with water, but with much lower yield.

Most workers have assumed that humic acids are heterogeneous mixtures of high molecular weight polymers (Kononova, 1966). However, our studies (Wershaw and Pinckney, 1973a, b) have shown that this is not the case but that humic acids are mixtures of a limited number of more or less chemically distinct fractions of relatively low molecular weight that form molecular aggregates in solution. Although some fractions are missing, all the humic acids that we have examined give very similar fractionation patterns when subjected to our standardized fractionation procedure. In addition the same fractions from different humic acids have similar aggregation-disaggregation properties in solutions of different pH. These observations have led us to postulate that any humic acid can be fractionated into a group of fractions, each individual fraction of which is chemically similar to the same fraction from any other humic acid.

Molecular weight of from 700 to over 50 000 has been reported for unfractionated humic acids (Kononova, 1966). We have shown in our previous studies (Wershaw and Pinckney, 1971, 1973b) that the wide range in molecular-weight measurements is due to the fact that humic acids form molecular aggregates in solution,

the size of which is a function of pH and of concentration; thus the measured molecular weight of a particular sample will be a function of the method used for measurement.

In our previous work we attempted to disaggregate the aggregates as much as possible. This was generally achieved by changing the pH of the solutions. Three different types of behavior were detected: (1) Some fractions showed very little change in aggregation at pH values above 3.5, (2) one fraction went through an aggregation minimum at about pH 7 (at pH 7 the system was monodisperse; above and below this pH the system became polydisperse with larger and smaller particles in equilibrium), and (3) in some fractions the aggregates continually decreased in size with increasing pH. Even at pH values as high as 11.5, some larger aggregates were still present in equilibrium with smaller particles. A. R. Monahan, A. F. DeLuca, and R. L. Wershaw (oral presentation, Am. Chem. Soc. Mtg., New York, Aug. 27–Sept. 1, 1972) have also found that the degree of aggregation of some of the fractions is a function of concentration and that at low concentrations the molecules are dissociated. Sipos and others (1972), using ultracentrifugation, have also found that in unfractionated humic acids there is a reduction in size of the aggregates with increasing pH. At the present time it is not possible to give accurate estimates of the molecular weights of the smallest particles that make up the humic acid aggregates.

The smallest particles that we have detected by small angle X-ray scattering in any of the humic acid fractions that we have isolated have radii of gyration of about 0.7 nanometers. A particle of this size could have a molecular weight as high as 1500; however, the molecular weight could be substantially less if the particle swells in solution. Solvation probably does cause some swelling of the humic acid particles so that the molecular weights of the particles are probably considerably less than the maximum values. In some of the other fractions the smallest particles detected are larger, corresponding to a maximum molecular weight of about 10 000.

In those fractions in which disaggregation did not take place when the pH was changed, the smallest particles detected were larger than those in which disaggregation took place. In addition those fractions in which disaggregation did not take place had high clay-mineral concentrations. In these fractions we are apparently dealing with a clay humic acid complex that is not affected by pH change within the range that we have studied.

Up to now we have mainly been discussing aggregation between particles within the same fraction. In unfractionated humic acid preparations, however, association of aggregates of different fractions to form mixed aggregates apparently takes place. Wershaw and Pinckney (1973a) were the first to report evidence for the presence of mixed aggregates in humic acid systems. The evidence for these mixed aggregates is that fractionation of humic acid results in an overall reduction in size of the molecular aggregates in solution.

The bonding mechanisms that account for the aggregation in this model will be the subject of subsequent papers in this series, and therefore we shall only briefly discuss possible bonding mechanisms here. Hydrogen bonding between protons and oxygen atoms on different carboxylic acid groups or between phenolic protons and carboxylic acid oxygen atoms probably accounts for much of the aggregation in humic acid systems (see Wershaw and Pinckney, 1977).

In addition to hydrogen bonding of the humic acid particles there are data that suggest that charge transfer complexes between free radicals are formed in humic acid systems. Steelink and Tollin (1967) and others have detected free radicals in both soils and humic acids isolated from soils. We have also found free radicals in the solutions of the humic acid fractions by electron spin resonance. As Steelink and Tollin have pointed out, the evidence that has been collected strongly suggests that the radicals detected are quinone or phenoxy radicals. Free radicals of this type can enter into charge-transfer complexation reactions, which will result in the formation of dimers and larger aggregates. (See Altwicker, 1967; Szwarc 1972.) Phenoxy radicals can also undergo dimerization in which the monomers are linked together by ether linkages (Becker, 1967; Altwicker, 1967; Mahoney and DaRooge, 1970; Weiner and Mahoney, 1972). Although covalent bonds are formed in these reactions, they are weak in many substituted phenoxy compounds. In solution the dimers or higher polymers are in equilibrium with monomeric free radicals, as shown in the example (Williams and Kreilick, 1967, 1968; Adam and Chiu, 1971) that follows:

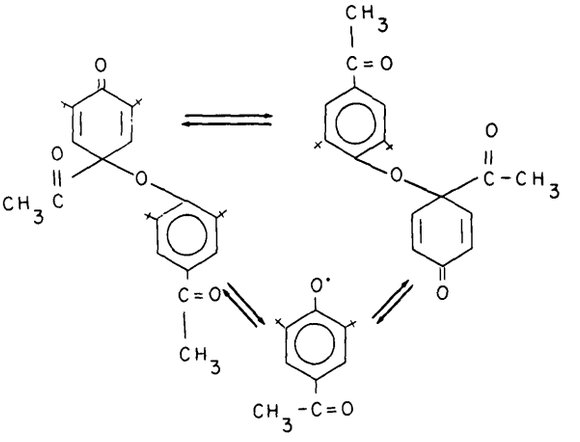

In this example, note that the bonds that are being broken are covalent ones which have been rendered unstable by the presence of bulky groups around them. Also steric hindrance by bulky groups has been found to destablize carbon-carbon bonds in phenoxy dimers (Mahoney and Weiner, 1972; Mahoney and Da Rooge, 1975). This destabilization results in equilibria of the following type:

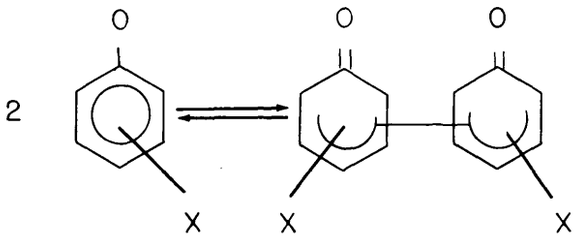

Two other bonding mechanisms possible in humic acid systems are π bonding between planar aromatic-ring structures and metal-ion bridging between humic acid molecules. At the present time there is no direct evidence for the former mechanism; however, from the presence of large numbers of aromatic rings in humic acids, one would expect the mechanism to play some part in the aggregation of humic acid molecules. There is evidence, however, that metal bridging takes place in humic acid systems. Sipos and others (1972) have shown that polyvalent metal ions increase the size of the aggregates in solution; the higher the concentration of metal ions, the larger the aggregates.

CONCLUSIONS

Our proposed model provides a new insight into the structure of humic acid and should be useful in the design of new experiments for further elucidation of its chemical structure. This model should also provide a starting point for the modeling of chemical interactions between humic materials and other organic and inorganic components in natural water systems.

REFERENCES CITED

Adam, Waldemar, and Chiu, Wen Tzong, 1971, The mechanism of a rate-controlled cross-disproportionation between phenoxyl radicals: Am. Chem. Soc. Jour., v. 93, no. 15, p. 3687–3693.

Altwicker, E. R., 1967, The chemistry of stable phenoxy radicals: Chem. Rev., v. 67, p. 475–531.

Becker, Hans-Dieter, 1967, Photochemical reactions with phenols, IV. The benzophenone-sensitized disproportionation of hydroquinone monaryl ethers: Jour. Organic Chemistry, v. 32, p. 2136–2140.

Burges, N. A., Hurst, H. M., and Walkden, Beryl, 1964, The phenolic constituents of humic acid and their relation to the lignin of plant cover: Geochim. et Cosmochim. Acta, v. 28, p. 1547–1554.

Dormaar, J. F., 1969, Reductive cleavage of humic acids of chernozemic soils: Plant and Soil, v. 31, no. 1, p. 182–184.

Fetzer, W. G., 1946, Humic acids and true organic acids as solvents of minerals: Econ. Geology, v. 41, p. 47–56.

Flaig, Wolfgang, 1971, Some physical and chemical properties of humic substances as a basis of their characterization *in* Advances in Organic Geochemistry: Oxford, Pergamon Press, p. 49–67.

Garrels, R. M., 1960, Mineral equilibria at low temperature and pressure: New York, Harper & Bros., 254 p.

Gorbunov, N. I., Yerokhina, G. L., and Shchurina, G. N., 1971, Relationship between soil minerals and humic substances: Soviet Soil Sci.; translated from Pochvovedeniye, no. 7, p. 117–128.

Kononova, M. M., 1966, Soil organic matter, its nature, its role in soil formation and in soil fertility: Oxford, Pergamon Press, 544 p.

Ladd, J. N., and Butler, J. H. A., 1971. Inhibition by soil humic acids of native and acetylated proteolytic enzymes: Soil Biology and Biochemistry, v. 3, p. 157–160.

Mahoney, L. R., and DaRooge, M. A., 1970, Kinetic and thermochemical study of the reaction of 2,4,6-Tri-*t*-butylphenoxy radical with substituted phenols: Am. Chem. Soc. Jour., v. 92, no. 4, p. 890–899.

——— 1975, The kinetic behavior and thermochemical properties of phenoxy radicals: Am. Chem. Soc. Jour., v. 97, no. 16, p. 4722–4731.

Mahoney, L. R., and Weiner, S. A., 1972, A mechanistic study of the dimerization of phenoxyl radicals: Am. Chem. Soc. Jour., v. 94, no. 2, p. 585–590.

Neyroud, J. A., and Schnitzer, Morris, 1975a, The alkaline hydrolysis of humic substances: Geoderma, v. 13, p. 171–188.

———1975b, The mild degradation of humic substances: Agrochimica, v. 19, no. 2, p. 116–126.

Paasikallio, Arja, Hakkinen, Ulla, and Lakanen, Esko, 1971, The effects of soil factors on the uptake of radiostrontium by plants: Annales Agriculturae Fenniae, v. 10, pt. 3, p. 125–130.

Schnitzer, Morris, and Khan, S. V., 1972, Humic substances in the environment: New York, Marcel Dekker, Inc., 327 p.

Schnitzer, Morris, and Kodama, H., 1967, Reactions between a podzol fulvic acid and Na-montmorillonite: Soil Sci. Soc. America Proc., v. 31, no. 5, 632–636.

Schnitzer, Morris, and Ortiz de Serra, M. I., 1973a, The sodium-amalgam reduction of soil and fungal humic substances: Geoderma, v. 9, p. 119–128.

——— 1973b, The chemical degradation of a humic acid: Canadian Jour. Chemistry, v. 51, no. 10, p. 1554–1566.

Schnitzer, Morris, and Skinner, S. I. M., 1974, The peracetic acid oxidation of humic substances: Soil Sci., v. 118, no. 5, p. 322–331.

Sipos, S., Sipos, E., Dekany, I., Szanto, F., Lakatos, B., 1972, Investigation of humic acids and metal humates with analytical ultracentrifuge: Internat. Peat Cong., 4th, Otaniemi, Finland, Proc., v. 4, p. 255–261.

Steelink, Cornelius, and Tollin, Gordon, 1967, Free radicals in soil: Soil Biochemistry, v. 1, p. 147–169.

Stevenson, F. J., and Mendez, J., 1967, Reductive cleavage products of soil humic acids: Soil Sci., v. 103, no. 6, p. 383–388.

Szalay, Sándor, Sámsoni, Z., and Szilágyi, M., 1970, Comparative analyses of the micronutrient content of some plants grown in Hungarian peat and mineral soils: Agrokémia és Taljtan, v. 19, no. 1–2, p. 13–23.

Szwarc, Michael, 1972, Radical anions and carbanions as donors in electron-transfer processes: Accounts Chem. Research, v. 5, p. 169–176.

Weiner, S. A., and Mahoney, L. R., 1972, A mechanistic study of the termination reactions of 2,4,6-trialkylphenoxy radicals: Am. Chem. Soc. Jour., v. 94, no. 14, p. 5029–5033.

Wershaw, R. L., and Goldberg, M. C., 1972, Interaction of organic pesticides with natural organic polyelectrolytes, *in* Advances in Chemistry Series, No. 111, Fate of organic pesticides in the aquatic environment: Am. Chem. Soc., p. 149–158.

Wershaw, R. L., and Pinckney, D. J., 1971, Association and dissociation of a humic acid fraction as a function of pH, *in* Geological Survey research 1971: U.S. Geol. Survey Prof. Paper 750–D, p. D217–D218.

——— 1973a, The fractionation of humic acids from natural water systems: U.S. Geol. Survey Jour. Research, v. 1, no. 3, p. 361–366.

——— 1973b, Determination of the association and dissociation of humic acid fractions by small angle X-ray scattering: U.S. Geol. Survey Jour. Research, v. 1, no. 6, p. 701–707.

——— 1977, Chemical structure of humic acids—Part 2, The molecular aggregation of some humic acid fractions in *N*, *N*-dimethylformamide: U.S. Geol. Survey Jour. Research, v. 5, no. 5, p. 571–577.

Williams, David, Jr., and Kreilick, Robert, 1967, Nuclear magnetic resonance studies of a radical-radical dimerization reaction: Am. Chem. Soc. Jour., v. 89, no. 14, p. 3408–3412.

——— 1968, Nuclear magnetic resonance studies of a series of radical-radical dimerization reactions: Am. Chem. Soc. Jour., v. 90, no. 11, p. 2775–2780.

Jour. Research U.S. Geol. Survey
Vol. 5, No. 5, Sept.–Oct. 1977, p. 571–577

CHEMICAL STRUCTURE OF HUMIC ACIDS–PART 2, THE MOLECULAR AGGREGATION OF SOME HUMIC ACID FRACTIONS IN *N, N*-DIMETHYLFORMAMIDE

By R. L. WERSHAW and D. J. PINCKNEY,
Denver, Colo.

Abstract.—Humic acid fractions form molecular aggregates in solution. In previous studies we have shown by small angle X-ray scattering that the size of these aggregates is a function of pH. In this study we have found that the size of the aggregates of two humic acid fractions in water and buffers and in dimethylformamide solutions can be changed by oxidation with molecular oxygen and air. These results cast new light on the bonding mechanisms that cause aggregation of the humic acid particles in solution. We have interpreted the changes in aggregation sizes as being brought about by changes in intermolecular and intramolecular hydrogen bonding of the humic particles. Solvation of the humic molecules by dimethylformamide interferes with some of the hydrogen bonding reactions between proton donor and acceptor groups on the same humic acid molecules or on different molecules.

Humic acids are highly reactive organic polyelectrolytes that are present in practically all natural water systems. These materials have a unique combination of chemical and physical properties that make them particularly important in natural water chemistry. Humic acids form complexes with metal ions, clays, and other aluminosilicate minerals (Gorbunov and others, 1971; Greenland, 1971). They strongly sorb many organic compounds including pesticides and enzymes (Wershaw and Goldberg, 1972; Ladd and Butler, 1971). Perry and Adams (1971) have shown that peptides such as glycylglylycine are incorporated into humic acid molecules in pH 8.5 solutions. They found that part of the amino nitrogen introduced into the humic acid by this reaction could not be removed by hydrolysis with 6 *N* HCl at 110°C for 24 hours. Anderson (1958) has shown that the hydrolysis products of DNA (deoxyribonucleic acid) are released from humic acid by perchloric acid hydrolysis; he concluded from this that DNA is present in humic acid. The binding of enzymes to humic acids (Ladd and Butler, 1971; Mato and others, 1971) is probably also due in part to the formation of bonds between amino nitrogen groups and reactive sites on the humic acid molecules. Undoubtedly other types of reactions can also take place, some perhaps involving shared metal cations. In natural water systems the soluble salts of humic acid will solubilize insoluble organic compounds and will aid their transport (Wershaw and Goldberg, 1972). Many of these properties are apparently closely related to the fact that humic acids form molecular aggregates that are held together by weak covalent bonds and noncovalent bonds (Wershaw and others, 1977). We have, therefore, undertaken a study of the bonding mechanisms of aggregation of humic acid molecules.

In previous studies (Wershaw and Pinckney, 1973a) we have found that humic acid fractions form molecular aggregates in water solutions. We have shown that the degree of aggregation of some of the fractions is a function of pH. From this work we have proposed a model for the structure of humic acids (Wershaw and others, 1977). In this model we picture the humic particles as forming both homogeneous and heterogenous aggregates. The homogeneous aggregates are composed of chemically similar molecules. The heterogeneous or mixed aggregates, on the other hand, can be composed of different types of molecules or of different homogeneous aggregates.

Slawinska and Slawinski (1975a, b) have studied the effect of air and oxygen on aqueous basic solutions of humic acid by chemiluminescence, visible absorption spectrophotometry, and electron paramagnetic resonance. They have concluded that humic acids in alkaline solutions are oxidized by both air and molecular oxygen. They have suggested that oxidation of phenolic groups and carbonyl groups is taking place along with ring opening and cleavage of other bonds. They have further found that visible radiation stimulates oxidative degradation of humic acids. Riffaldi and Schnitzer (1972) have found that the electron paramagnetic res-

onance spectrum of humic acid in 0.1 *N* NaOH solution is greater in the presence of oxygen than in the absence of oxygen. These results indicate that chemical changes are introduced into humic acids by mild oxidation with molecular oxygen and air in basic solutions. These results on the effect of mild oxidation on the chemistry of humic acid suggest that a further study in this area might provide new insight into the chemistry of humic acids. We have, therefore, decided to continue to examine the aggregation of methylated and unmethylated humic acid fractions in both protic and aprotic solvents as a function of oxidation of the humic acid molecule. Water was chosen as the protic solvent and DMF (dimethylformamide) as the aprotic solvent. An aprotic solvent was desired so that complicating factors resulting from pH changes in protic solvents could be avoided.

The results reported here are the first demonstration that changes in oxidation-reduction potential bring about changes in the aggregation of humic acid fractions in solution. Very little is known about the oxidation states of humic acid fractions; therefore, the data that have been obtained are difficult to interpret, and the interpretations that have been presented must be considered provisional. The value of any study of this nature lies (1) in the stimulation of thought that will lead to the design of new experiments to either prove or disprove the interpretations that have been given to the experimental results and (2) in the refinement of techniques for obtaining more definitive data.

EXPERIMENTAL PROCEDURE

The humic acid fractions were isolated by absorption chromatography on Sephadex as outlined by Wershaw and Pinckney (1973a). This procedure was modified in some instances to exclude dissolved oxygen from the sclutions during all the steps in which the pH was above about 8, including the initial extraction of humic acid from the soil. Oxygen was removed from the solutions by saturating them with nitrogen and carrying out all transfers in a glove bag swept with nitrogen. The methylation was carried out in 2-pyrrolidone using the procedure of Wershaw, Pinckney, and Booker (1975). The methylated products were precipitated by adding an excess of diethyl ether to the pyrrolidone solution. The precipitate was recovered by filtration through fiberglass, washed with diethyl ether, and redissolved in a 1:1 mixture of benzene and methanol. All the solvents used in this work, with the exception of the diethyl ether, were distilled in an all-glass system prior to use and were stored in glass-stoppered bottles. The diethyl ether was Burdick and Jackson "distilled in glass" grade and was used without further treatment. Gas chromatographic and mass-spectrometric analysis indicated that this product was satisfactory for our purposes without further treatment. The pyrrolidone was distilled under vacuum in a Kontes falling-film molecular still.

The two fractions (4A and 4B) discussed in this paper are soluble in DMF and, therefore, some of the samples were also methylated in redistilled DMF.

A detailed description of the small angle X-ray scattering measurements is given by Wershaw and Pinckney (1973b). A sealed quartz-glass capillary cell was used in this work (fig. 1). The sealed cell is a modification of a cell designed by Dr. Travis Presley of Marathon Oil Co.

Two different buffers were used in this study—a pH-5 buffer prepared by adjusting the pH of a 0.1 *M* KH_2PO_4 solution to pH 5 with NaOH, and a pH-9 buffer prepared by adjusting the pH of a 0.2 *M* Na_2HPO_4 solution to pH 9 with HCl. Both of the solutions have relatively low buffer capacities and, therefore, the actual pH of each solution prepared either in the pH-5 or pH-9 buffer was measured; these values are given in the appropriate figures.

DISCUSSION OF RESULTS

Small angle X-ray scattering gives the most direct indication of the effect of various treatments on the aggregation of humic acid fractions. The X-ray scattering data have been analyzed using the methods developed by Guinier (Guinier and Fournet, 1955). Guinier has shown that for an ensemble of randomly oriented identical scattering particles in which there is no long-range order, the scattered intensity, I, may be represented to a close approximation by the equation

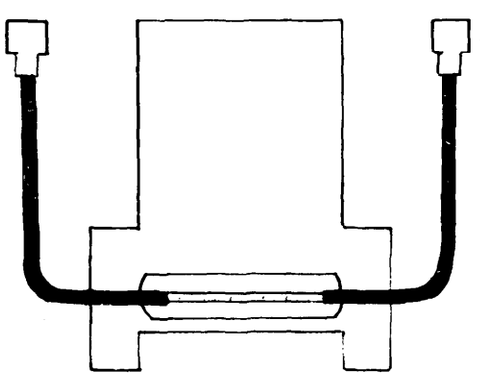

FIGURE 1.—Closed capillary tube used on X-ray scattering camera. The central part of the cell is a quartz-glass capillary; each end member is a bent 18-gage hypodermic needle which is attached to the capillary by a piece of heat-shrinkable Teflon tubing.

$$I = I_e N n^2 e^{(-h^2R^2)/3}, \quad (1)$$

where I_e is the scattered intensity that would result if a single electron were substituted for one of the scattering particles, N is the total number of particles in the ensemble, n is the number of electrons per particle, R is the radius of gyration of one of the particles, and $h = 2\pi \sin 2\theta/\lambda$, where 2θ is the scattering angle and λ is the wavelength of the impinging X-radiation. This equation may be written as

$$\ln I = \frac{-h^2R^2}{3} + \text{constant}. \quad (2)$$

The radius of gyration of the particle, which is defined as the root mean square distance of the electrons in the particle from the center of charge, is a useful general parameter of comparative molecular or particle size.

From equation 2 it is seen that the radius of gyration may be easily calculated from the slope of a plot of ln I versus h^2; this is the so-called Guinier plot or curve. In a system in which all the scattering particles are of equal size the Guinier plot will be a straight line.

In a polydisperse system, the Guinier plot, which is actually a summation of many Guinier plots, is no longer a straight line but is concave up. A Guinier plot of a polydisperse system of particles of uniform electron density will yield the range of particle sizes present in the system.

In this study of the aggregation of humic acid fractions in DMF, we shall use as examples fractions 4A and 4B of the humic acid extracted from the Florida soil described in Wershaw and Pinckney (1973a). These two fractions comprise about 30 to 40 percent of a typical humic acid.

In our discussion of the data obtained in this study we shall be concerned with two different types of hydrogen bonding: (1) Intermolecular hydrogen bonding, which will cause aggregation of the molecules into larger particles, and (2) intramolecular hydrogen bonding, which will result in the molecules assuming a more compact configuration. Thus, an increase in intramolecular hydrogen bonding in a system will lead to a decrease in the radius of gyration of the particles in solution. In our solutions, one would expect that the conditions that favor intermolecular hydrogen bonding may also favor intramolecular hydrogen bonding, so that it is not always possible to differentiate between these two competing effects.

In figure 2 are given the Guinier curves for 0.5 percent solutions of two different preparations of the same humic acid fraction (4A) in DMF. One of the fractions was isolated from a humic acid that had been extracted and fractionated in air (AR extraction) in the usual way and one of the fractions was isolated from a humic acid that was extracted and fractionated in the absence of oxygen (oxygen-free or O-F extraction). The O-F procedure yielded the same fractions in roughly the same proportions as the AR procedure, but the O-F 4A fraction has a larger radius of gyration than the AR 4A fraction.

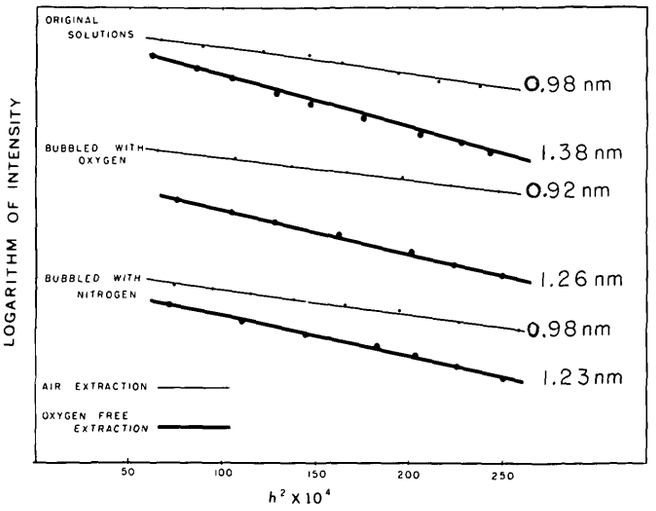

FIGURE 2.—Guinier plots of 0.5-percent solutions of Florida 4A fraction in dimethylformamide, extracted in air and in the absence of oxygen. Plots of the same solutions after bubbling with oxygen and after bubbling with nitrogen. Logarithm of scattered intensity versus h^2. (See text discussion of equations 1 and 2.)

In humic acids there are at least two different groups that can act as proton donors in hydrogen-bonding interactions: (1) carboxylic acid groups and (2) phenolic groups. The carboxylic acid groups are also proton acceptors. Other proton acceptors, such as quinone groups, are probably also present in some humic acid fractions. Stone and Waters (1965) and others have shown that substituted catechols and other phenolic compounds are readily oxidized by air in basic solutions to semiquinones, quinones, and various radical species. Therefore, in the samples extracted with NaOH and fractionated in air, we would expect that most of the phenols would be oxidized and could no longer act as proton donors. However, the quinone groups that are produced could act as proton acceptors. These quinone groups will compete with other proton acceptors for the remaining protons in the system. These protons will also be attracted to the acid carbonyl groups of the humic acid molecules and to the DMF molecules which are basic and can act as proton acceptors, as discussed below. Since there are so many different competitors for the protons in the humic acid particles, a reduction in the number of protons brought about by oxidation should have a net overall effect of

reducing both the intermolecular and intramolecular hydrogen bonding of the humic acid molecules.

In the 0.5-percent solutions, since the measured radius of the AR particles is smaller than that of the O-F particles, the larger effect is that of disaggregation brought about by reduction of the intermolecular hydrogen bonding. Bubbling of oxygen into the O-F sample caused a reduction in the radius of gyration from 1.38 to 1.26 nanometers. This suggests that the humic acid phenolic groups can be oxidized by oxygen in DMF.

The small reduction in particle size of the AR sample after bubbling with oxygen also leads one to the same conclusion. The increase in particle size after bubbling of nitrogen into the AR sample suggests that the effect may be reversible when the oxygen is removed from the AR sample. However, this was not the case with the O-F sample; in fact, a slight further reduction in particle size was noted. This reduction is within the error of measurement and, therefore, suggests that the oxidation of the O-F sample cannot be reversed by removing the oxygen from the system. At this time, it is not clear why in one instance the oxidation appears to be reversible and in the other instance not.

When the concentration of the solution was increased to 1 percent, a reduction in the size of the O-F particles in solution was observed (fig. 3). The particle size measured in this sample is even smaller than the size of the particles in the 0.5-percent solution of the AR sample. This reduction in particle size with an increase in concentration is a puzzling phenomenon that was only observed with the O-F 4A sample. It perhaps indicates that the particles assume a more compact configuration in the more concentrated solution. Grimley (1961) has pointed out that, in a good solvent, the mean square radius of gyration of a flexible polymer molecule should decrease with increasing concentration. This effect, which is independent of the hydrogen-bonding effects discussed above, results when the chains of a flexible polymer assume the configuration of minimum free energy. As the concentration increases, the configuration of minimum free energy becomes more and more compact.

In figure 4 the Guinier plot for a 1-percent solution of methylated O-F Florida 4A fraction is given. The radius of gyration of the particles is about 1 nm. The radius was measured again 64 hours after preparation of the solution, and a small increase in radius to 1.1 nm was noted. Bubbling of oxygen into the solution did not appreciably change the size of the particles. At the present, we have no explanation for the change in radius of gyration with time. However, it is significant that both of the measured radii of the methyl ester are greater than the radius of gyration of the nonmethylated 4A particles in the 1-percent solution in DMF. This is probably due to greater intramolecular hydrogen bonding in the acid. Apparently solvation of the humic acid molecules by DMF prevents intermolecular hydrogen bonding from taking place. Methylation of a humic acid with diazomethane will mainly result in esterification of carboxylic acid groups. However, some acidic phenolic groups may also react (Fieser and Fieser, 1967). The methylated groups can no longer act as proton donors for either intermolecular or intramolecular hydrogen bonding.

In water solutions the sodium salt of O-F Florida 4A fraction disaggregates with increasing pH (fig. 5).

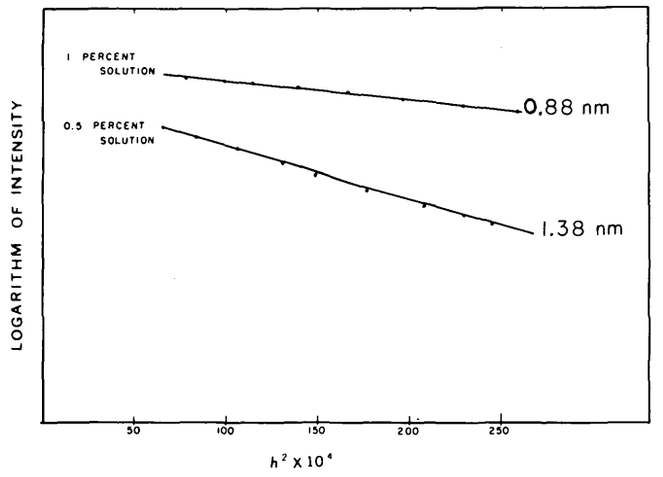

FIGURE 3.—Guinier plots of 0.5- and 1.0-percent solutions of oxygen-free Florida 4A fraction in dimethylformamide. Logarithm of scattered intensity versus h^2. (See text discussion of equations 1 and 2.)

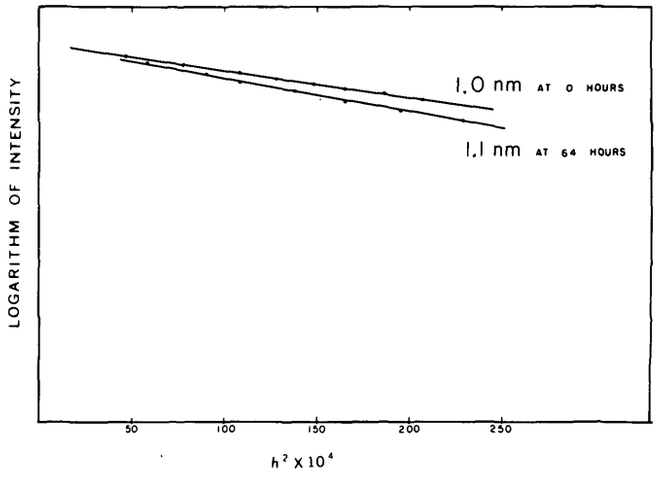

FIGURE 4.—Guinier plot of 1.0-percent solution of methylated oxygen-free Florida 4A fraction in dimethylformamide; the same after 64 hours. Logarithm of scattered intensity versus h^2. (See text discussion of equations 1 and 2.)

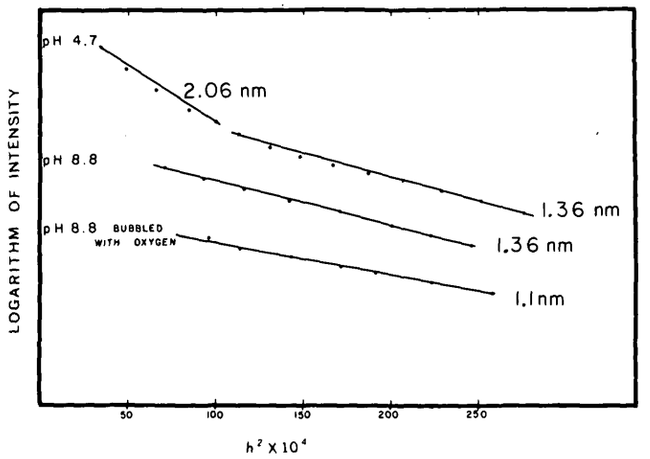

FIGURE 5.—Guinier plots of oxygen-free Florida 4A fraction: 0.5-percent solution in pH-5 buffer (actual solution pH of 4.7) and 1-percent solution in pH-9 buffer (actual solution pH of 8.8). Plot of the 1-percent solution in pH-9 buffer after bubbling with oxygen. Logarithm of scattered intensity versus h^2. (See text discussion of equations 1 and 2.)

Near pH 5 the range of radii of gyration is from 2.06 to 1.36 nm. Near pH 9 the solution is essentially monodisperse with particles of radius of gyration of 1.3 nm. Bubbling of oxygen into this system reduced the radius of the particles to 1.1 nm.

The absence of evidence for larger particles in pH-9 solution indicates that there is less aggregation of the particles in basic solutions. This reduction in aggregation is most likely brought about by the lack of intermolecular hydrogen bonding between acid groups in basic solutions. In acid solutions, the acid groups will be protonated so that hydrogen bonding between the protons and carbonyl oxygens of other acid groups is possible; however, in strongly basic solutions, the acid groups are ionized and cannot act as proton donors. The particles in the pH-9 solution are still substantially larger than those in the 1-percent DMF solution. This indicates that besides hydrogen bonding between acid groups, other aggregation reactions are probably taking place. Another possible mechanism of aggregation is hydrogen bonding of phenolic protons with the carbonyl oxygens of carboxylic acid groups. In general, phenols are much weaker acids than carboxylic acid and in many instances would still be protonated at pH 9. Removal of the phenolic proton would prevent this interaction from taking place and should bring about further disaggregation. We have tried to remove the phenolic protons by oxidation with oxygen and indeed addition of oxygen to the pH-9 solution has caused further disaggregation. As we have pointed out above, Stone and Waters (1965) have shown that substituted catechols are readily oxidized by air in basic solutions to semiquinones, quinones, and various radical species. Therefore, we propose that at least two different hydrogen-bonding mechanisms are bringing about aggregation in humic acids: (1) hydrogen bonding between carboxylic acid protons and carboxyl-oxygen atoms and (2) hydrogen bonding between phenolic protons and carbonyl-oxygen atoms. In solutions of high pH values, the carboxylic acid groups are most likely completely neutralized and, therefore, cannot act as proton donors in hydrogen-bonding reactions. Although it is possible that some of the more acidic phenolic protons have been replaced by sodium ions in the pH-9 buffer solutions that we have used, most of these OH groups are probably still intact and are capable of entering into hydrogen-bonding interactions. Oxidation of these groups by oxygen will convert them to quinone-carbonyl groups that will have no protons for hydrogen bonding, and further disaggregation will take place.

The smaller size of the particles in the DMF solution than in the pH-9 solutions that have not been oxidized indicates that DMF causes more disaggregation of the particles than does the base. In DMF solutions, both the carboxylic acid groups and the phenolic groups will be solvated; therefore, hydrogen bonding between groups in the humic acid molecule will be inhibited.

The mechanism of the interaction of DMF with the humic acid molecules may be better understood by considering some of the solvent properties of DMF. DMF is a basic, aprotic, hydrophilic solvent with a dielectric constant of 36.7 at 25°C. It acts as a hydrogen-bond acceptor in which the oxygen in the DMF molecule is protonated in the presence of proton donors (McClelland and Reynolds, 1974).

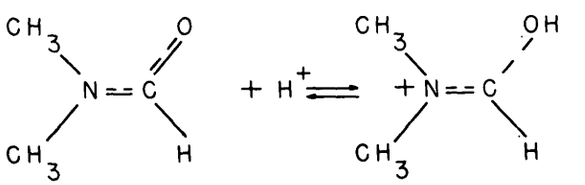

Some authors have also proposed that the proton is attached to the N; however, the work of McClelland and Reynolds (1974), appears to disprove this. Whatever the site of the protonation, the DMF molecules will form hydrogen bonds with the acid and phenolic groups and thereby disrupt some or all of the intermolecular hydrogen bonding between humic acid particles. This in turn will then lead to some disaggregation of the humic acid particles. This inhibition of hydrogen bonding may also reduce the amount of intramolecular hydrogen bonding taking place and may

cause the particles to assume a less compact configuration.

A series of experiments similar to those discussed above for the Florida 4A fraction were performed on the O-F Florida 4B fraction with somewhat different results from those obtained with the O-F 4A fraction (fig. 6). In this regard, little difference in particle size was detected between the 0.5-percent and 1-percent solutions in DMF. The 0.5-percent solution in DMF was run several times, and each time the results were slightly different. Radii of gyration from 0.78 to 0.84 nm were measured for this sample. It is not clear what the variation is due to, but it is likely that two different factors contribute to it. First, the scattering from the sample is very weak and the probable error, therefore, is large. Second, the degree of aggregation in 4B is a function of time; the longer the particles remain in solution, the smaller they get.

Another difference in the properties of the O-F 4B fraction from that of the O-F 4A fraction is that the 4B particles are smaller in pH-9 buffer (fig. 7) than in the fresh DMF (fig. 8). However, 1 month after preparation in the DMF, the measured particle size had diminished from 0.84 to 0.71 nm, which is very close to the size of the particles in the pH-9 buffer (0.69 nm). Bubbling of oxygen into the DMF solution also caused a small reduction in radius of gyration from 0.84 to 0.75 nm. Bubbling of oxygen into the pH-9 solution, on the other hand, brought about a slight increase in radius from 0.69 to 0.73 nm and a decrease in scattered intensity of about 35 percent (not illustrated). The increase in size is within the error of the measurements and is, therefore, probably not

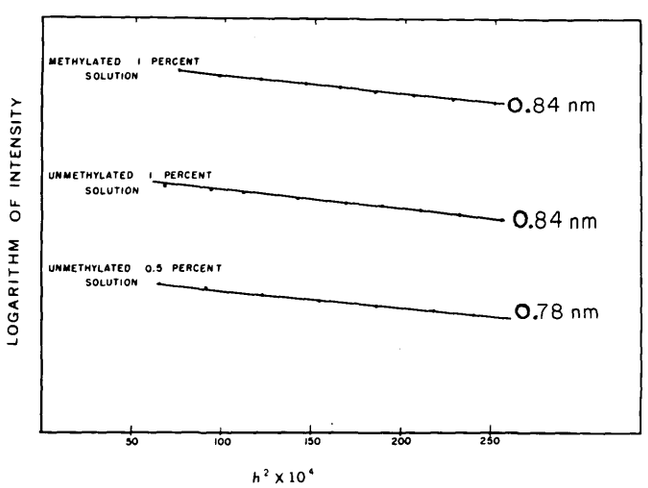

FIGURE 6.—Guinier plots of oxygen-free Florida 4B fraction in dimethylformamide: methylated 1.0-percent solution and unmethylated 1.0- and 0.5-percent solutions. Logarithm of scattered intensity versus h^2. (See text discussion of equations 1 and 2.)

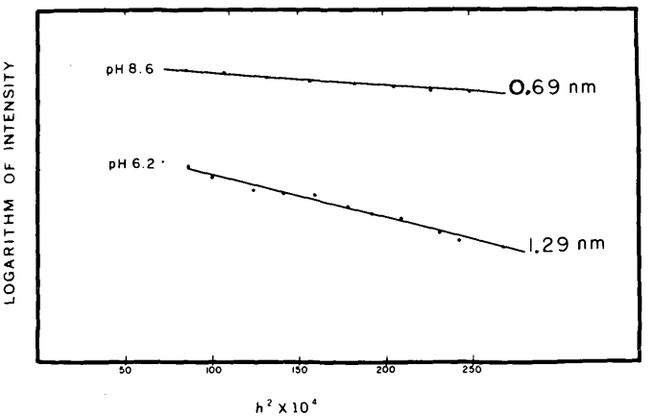

FIGURE 7.—Guinier plots of 1.0-percent solution of oxygen-free Florida 4B fraction in pH-9 buffer (actual solution pH of 8.6) and pH-5 buffer (actual solution pH of 6.2). Logarithm of scattered intensity versus h^2. (See text discussion of equations 1 and 2.)

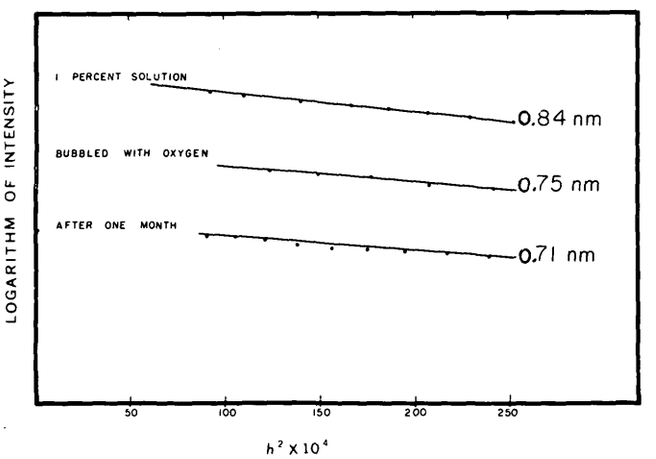

FIGURE 8.—Guinier plots of 1.0-percent solution of oxygen-free Florida 4B fraction in dimethylformamide; the same after bubbling with oxygen. Plot of the same after 1 month. Logarithm of scattered intensity versus h^2. (See text discussion of equations 1 and 2.)

significant. The radius of gyration of the particles of methylated O-F 4B (1 percent in DMF) was 0.84 nm, the same as that for the acid in DMF (not illustrated).

The most conspicuous property of the O-F 4B fraction is the change in size of the particles with time in DMF. This change is probably due to slow oxidation by air of the sample in DMF. This oxidation is accelerated by bubbling oxygen through the sample. The oxidation is apparently complete in the pH-9 solutions. As in the O-F 4A solutions, the oxidation leads to a reduction in intermolecular hydrogen bonding and disaggregation of the particles.

CONCLUSIONS

Humic acids interact with practically all of the other components of natural water systems. Many of these interactions are adsorption interactions in which other molecules are bonded to the surfaces of the humic particles or are incorporated in the humic acid aggregates. In order to understand these adsorption interactions, it is necessary to elucidate the mechanism of weak bonding in humic acids. In this report we have demonstrated that a study of the aggregation of humic acid particles by small angle X-ray scattering can provide information about the bonding of humic acid particles.

As we have shown in the first paper in this series (Wershaw and others, 1977), an understanding of the bonding mechanisms that cause aggregation of the humic acid particles is fundamental to an understanding of their chemical structures. Humic acid molecules form molecular aggregates in solution that appear to be held together by hydrogen bonds and by other weak chemical bonds. The amount of both intermolecular and intramolecular hydrogen bonding that takes place in a given solvent system is a function of the pH, the oxidation state of the humic acid molecules, and the solvation properties of the solvent. Humic acid fractions that have been oxidized by air during extraction or fractionation have fewer proton donor groups per molecule than unoxidized fractions. The oxidized molecules, therefore, enter into few hydrogen-bonding interactions than do the unoxidized molecules.

The molecules of humic acid were susceptible to oxidation by molecular oxygen when dissolved in DMF. It also appears that air oxidation can take place in DMF and leads to a reduction in the amount of hydrogen bonding between the molecules and a disaggregation of the molecular aggregates.

DMF, a basic aprotic solvent, acts as a proton acceptor in hydrogen-bonding interactions with humic acid molecules. This solvation of the humic acid molecules reduces the amount of both intermolecular and intramolecular hydrogen bonding between reactive groups on the humic acid molecules themselves.

REFERENCES CITED

Anderson, George, 1958, Identification of derivatives of deoxyribonucleic acid in humic acid: Soil Sci., v. 86, no. 4, p. 169–174.

Fieser, L. F., and Fieser, Mary, 1967, Reagents for organic synthesis: New York, John Wiley and Sons, Inc., v. 1, 1457 p.

Gorbunov, N. I., Yerokhina, G. L., and Shchurina, G. N., 1971, Relationship between soil minerals and humic substances: Soviet Soil Sci.; translated from Pochvovedeniye, no. 7, p. 117–128.

Greenland, D. J., 1971, Interactions between humic and fulvic acids and clays: Soil Sci., v. 111, p. 34–41.

Grimley, T. B., 1961, Polymer dimensions in solutions of finite concentrations: Faraday Soc. Trans., v. 57, p. 1974–1978.

Guinier, Andre, and Fournet, G., 1955, Small-angle scattering of X-rays: New York, John Wiley and Sons, Inc., 268 p.

Ladd, J. N., and Butler, J. H. A., 1971, Inhibition by soil humic acids of native and acetylated proteolytic enzymes: Soil Biology and Biochemistry, v. 3, p. 157–160.

Mato, M. C., Fabregas, R., and Mendez, J., 1971, Inhibitory effect of soil humic acids on indoleacetic acidoxidase: Soil Biology and Bichemistry, v. 3, p. 285–288.

McClelland, R. A., and Reynolds, W. F., 1974, 13-C nuclear magnetic resonance spectra of *N,N*-dimethylformamide in aqueous acid solution. Evidence for predominant O-protonation at all acidities: Chem. Soc. [London] Jour., p. 824–825.

Perry, D. R., and Adams, W. A., 1971, The incorporation of glycylglycine into humic acid: Biochem. Jour., v. 125, no. 2, p. 29–30.

Riffaldi, R., and Schnitzer, M., 1972, Effects of diverse experimental conditions on ESR spectra of humic substances: Geoderma, p. 1–10.

Slawinska, Danuta, and Slawinski, Janusz, 1975a, Spectroscopic study on mild oxidation of humus acids. Part 1, Oxidation with molecular oxygen: Polish Jour. Soil Sci., v. 8, no. 1, p. 37–47.

——— 1975b, Spectroscopic study on mild oxidation of humus acids. Part 2, Influence of light on oxidation with molecular oxygen: Polish Jour. Soil Sci., v. 8, no. 1, p. 49–58.

Stone, T. J., and Waters, W. A., 1965, Aryloxy-radicals. Part 4, Electron spin resonance spectra of some ortho-Monobenzosemiquinones and secondary radicals derived therefrom: [London] Chem. Soc. Jour., p. 1488–1494.

Wershaw, R. L., and Goldberg, M. C., 1972, Interaction of organic pesticides with natural organic polyelectrolytes, *in* Advances in Chemistry Series, No. 111, Fate of organic pesticides in the aquatic environment: Am. Chem. Soc., p. 149–158.

Wershaw, R. L., and Pinckney, D. J., 1973a, The fractionation of humic acids from natural water systems: U.S. Geol. Survey Jour. Research, v. 1, no. 3, p. 361–366.

——— 1973b, Determination of the association and dissociation of humic acid fractions by small angle X-ray scattering: U.S. Geol. Survey Jour. Research, v. 1, no. 6, p. 701–707.

Wershaw, R. L., Pinckney, D. J., and Booker, S. E., 1975, Pyrrolidone—A new solvent for the methylation of humic acid: U.S. Geol. Survey Jour. Research, v. 3, no. 1, p. 123–126.

——— 1977, Chemical structure of humic acids—Part 1, A generalized structural model: U.S. Geol. Survey Jour. Research, v. 5, no. 5, p. 565–569.

Jour. Research U.S. Geol. Survey
Vol. 5, No. 5, Sept.–Oct. 1977, p. 579–581

THALLIUM CONTENTS OF 16 USGS STANDARD ROCKS

By F. O. SIMON, E. Y. CAMPBELL, and P. J. ARUSCAVAGE,
Reston, Va.

Abstract.—Thallium was determined in 16 USGS standard rocks by atomic absorption spectroscopy in which a heated graphite atomizer was used after extraction as thallium iodide into amyl acetate. Four subsamples from four bottles of each standard sample, except G–1 and W–1, were analyzed in random order, and the average thallium contents in parts per million (as Tl) were AGV–1, 0.41; GSP–1, 1.63; G–2, 1.08; BCR–1, 0.35; SDC–1, 0.80; MAG–1, 0.79; BHVO–1, 0.049; SCo–1, 0.79; SGR–1, 0.34; QLO–1, 0.23; RGM–1, 1.07; STM–1, 0.30; DTS–1, <0.005; and PCC–1, <0.005. The analysis of variance showed that all samples may be considered homogeneous at $F_{0.975}$ and only GSP–1 may be considered heterogeneous at $F_{0.95}$. The Tl contents of G–1 and W–1 are 1.0 and 0.12 ppm, respectively.

Thallium, which shows close geochemical behavior to potassium, is present generally in terrestrial materials in the concentration range of 0.01 to 1.0 $\mu g\ g^{-1}$. A number of analytical techniques have been applied in the determination of thallium in geological materials: neutron activation analysis (Laul and others, 1970; Marowsky and Wedepohl, 1971; Morris and Killick, 1960), emission spectroscopy (De Albuquerque and others, 1972; W. H. Champ in Flanagan, 1969), atomic absorption spectroscopy (Sighinolfi, 1973), and spectrofluorimetry (Schnepfe, 1975). Although most of the authors have analyzed some of the USGS samples, no one has analyzed the entire set for their thallium contents. In the present study, four splits (bottles) of each standard were analyzed four times each (for a total of 16 analyses for each standard) by atomic absorption spectroscopy in which a heated graphite analyzer was used.

The analytical data are compared with those of other authors in table 1, and the statistical estimates are given in table 2. One-way analysis of variance was used to determine whether the mean sum of squares among bottle means for the thallium content was significantly larger than the variation within bottles for any given standard.

ANALYTICAL TECHNIQUE

Samples were decomposed by digestion with HF, HNO_3, and $HClO_4$ in covered Teflon beakers for 16 hours on a hotplate. For samples containing greater than 0.1 $\mu g\ g^{-1}$ Tl, 200 mg of sample was used; for those containing less than 0.1 $\mu g\ g^{-1}$ Tl, 1.000 g was used. After evaporation to dryness, sufficient 0.5 *M* HCl was added to dissolve the salts. In general, 10 mL and 40 mL were adequate for the 200-mg and 1-g samples, respectively. Three milliliters of HI was added, and TlI was extracted into 2 mL of amyl acetate by shaking for 5 minutes in a stoppered test tube. The

TABLE 1.—*Comparison of results, in parts per million of thallium, of this work with those of other works*

[NAA, neutron activation analysis; AAS-HGA, atomic absorption spectroscopy-heated graphite atomizer; ES, emission spectroscopy; ±, within-bottle standard deviation]

Sample	This work (AAS-HGA)	Marowsky and Wedepohl (1971) (NAA)	De Albuquerque and others (1972) (ES)	W. H. Champ *in* Flanagan (1969) (ES)	Wahler (1968) (Polarographic)	Sighinolfi (1973) (AAS-HGA)	Schnepfe (1975) (Spectrofluorimetric)	Laul and others (1970) (NAA)
G-2	1.08±.12	1.22	1.05	1.3	0.85	0.95-1.18	----	0.89
GSP-1	1.63±.14	1.21	1.2	1.6	.71	1.52-1.55	----	1.3
AGV-1	.41±.12	1.63	.28	1.6	.27	.53-.59	----	.34
BCR-1	.35±.05	.35	.27	---	.36	.28-.30	----	.33
PCC-1	<.005	.0008	.005	---	<.05	[1].020	----	.00075
DTS-1	<.005	.0008	.003	---	<.05	[1].011	----	.00051
G-1	1.0	1.20	1.3	1.3	.66	---------	1.09	1.06
W-1	.12	.12	.11	---	<.05	0.11	0.11	.10

[1] Analytical error suspected (Sighinolfi, 1973).

TABLE 2.—*Concentration of thallium in 12 USGS standard rocks*

[S.D., the within-bottle standard deviation; Ns, not significant at $F_{0.95}$]

Standard rock	Bottle (split/position)	Thallium, in parts per million, for indicated subsample 1	2	3	4	Mean (ppm)	S.D.	F
AGV-1---------	2/13	0.43	0.46	0.40	0.44	0.41	0.12	1.053 Ns
	52/21	.43	.35	.40	.38			
	111/14	.39	.45	.39	.38			
	14/18	.35	.48	.45	.42			
GSP-1---------	39/20	1.66	1.50	1.87	1.52	1.63	.14	4.101
	65/11	1.36	1.62	1.74	1.35			
	38/23	1.47	1.54	1.60	1.54			
	55/5	1.78	1.85	1.74	1.92			
G-2----------	56/4	1.17	.97	1.01	1.23	1.08	.12	.510 Ns
	75/8	1.06	1.06	1.24	1.15			
	16/23	1.01	.96	1.13	1.20			
	116/17	.92	.93	1.26	.98			
BCR-1---------	80/7	.36	.34	.36	.38	.35	.05	.534 Ns
	19/29	.34	.30	.30	.38			
	67/32	.42	.38	.43	.25			
	46/18	.34	.33	.33	.38			
SDC-1---------	119/4	.80	.78	.65	.86	.80	.10	.242 Ns
	97/12	.92	.66	.87	.82			
	61/24	.74	.75	.79	.87			
	76/15	.64	.84	.89	.93			
MAG-1---------	26/6	.89	.66	.81	.86	.79	.14	.813 Ns
	38/3	.81	.85	.75	.78			
	31/5	.69	.99	1.01	.70			
	12/27	.46	.90	.70	.74			
BHVO-1--------	12/8	.06	.07	.03	.03	.049	.019	.204 Ns
	4/1	.05	.05	.07	.03			
	31/5	.05	.07	.07	.03			
	50/14	.05	.07	.03	.03			
SCo-1---------	26/3	.78	.80	.80	.85	.79	.07	.413 Ns
	55/23	.83	.82	.90	.68			
	40/15	.81	.78	.69	.89			
	68/3	.76	.84	.72	.72			
SGR-1---------	25/23	.51	.29	.28	.47	.34	.089	.666 Ns
	28/3	.28	.33	.41	.30			
	4/12	.27	.29	.40	.47			
	33/19	.25	.24	.32	.40			
QLO-1---------	9/24	.23	.22	.23	.22	.23	.02	1.412 Ns
	2/20	.23	.23	.19	.19			
	17/23	.25	.23	.27	.18			
	39/15	.23	.23	.27	.25			
RGM-1---------	13/7	1.10	1.18	1.10	1.28	1.07	.11	1.965 Ns
	55/4	.95	.83	1.07	1.15			
	48/31	1.12	.99	1.20	1.08			
	54/5	1.07	1.15	.93	.95			
STM-1---------	45/30	.25	.34	.32	.22	.30	.04	.278 Ns
	21/26	.30	.32	.31	.25			
	21/27	.29	.28	.30	.30			
	41/10	.32	.33	.36	.23			

layers were allowed to separate overnight (several hours standing is essential for phase separation), and the absorbances of 0.01-mL aliquots of the organic phase were determined by the atomic absorption spectroscopy in which a heated graphite atomizer was used.

A Perkin Elmer model 503 atomic absorption spectrophotometer was used that had a model HGA 2100 graphite furnace, model 56 recorder, and a deuterium background corrector. A thallium electrodeless discharge lamp was used at a wavelength of 276.8 nm and

at a spectral band width of 0.7 nm. The variables used for the HGA 2100 graphite atomizer were essentially those recommended by the manufacturer: Drying—110°C for 20 seconds; charring—400°C for 20 seconds; atomizing—2600°C for 5 seconds; gas—argon with gas flow interrupted during atomization. The atomization temperature is slightly higher than the recommended temperature (2600°C versus 2300°C). The higher temperature improved the reproducibility and, therefore, lowered the detection limit.

RESULTS AND DISCUSSION

The thallium contents determined in the present study in those USGS samples for which there are other data available are listed with the results of other investigators in table 1. The results are in reasonable agreement with those reported by other authors.

Table 2 lists the individual results, the mean, the within-bottle standard deviation, and the F ratio for each standard sample. One-way analysis of variance was applied to the data to determine whether the variation among bottles was greater than the variation within bottles. In only one case (GSP-1) was the mean sum of squares for the four bottles significantly greater than the variation within individual bottles at the 5 percent confidence level. Heterogenity for thallium in GSP-1 was demonstrated at the 5-percent level, but not at the 1-percent level. The overall analytical error calculated (12 degrees of freedom) ranged from 8.6 to 39 percent.

Two samples, DTS-1 and PCC-1, were found to contain less than 0.005 ppm Tl. A single datum was obtained for two other samples (G-1 and W-1). One-way analysis of variance was not applied to these samples.

REFERENCES CITED

De Albuquerque, C. A. R., Muysson, J. R., and Shaw, D. M., 1972, Thallium in basalts and related rocks: Chem. Geology, v. 10, no. 1, p. 41–58.

Flanagan, F. J., 1969, U.S. Geological Survey Standards; II, First compilation of data for the new U.S.G.S. rocks: Geochim. et Cosmochim. Acta, v. 33, no. 1, p. 81–120.

Laul, J. C., Pelly, I., and Lipschutz, M. E., 1970, Thallium contents of chondrites: Geochim. et Cosmochim. Acta, v. 34, no. 8, p. 909–920.

Marowsky, G., and Wedepohl, K. H., 1971, General trends in the behavior of Cd, Hg, Tl and Bi in some major rock forming processes: Geochim. et Cosmochim. Acta, v. 35, no. 12, p. 1255–1267.

Morris, D. F. C., and Killick, R. A., 1960, The determination of silver and thallium in rocks by neutron activation analysis: Talanta, v. 4, p. 51–60.

Sighinolfi, G. P., 1973, Determination of thallium in geochemical reference samples by flameless atomic absorption spectroscopy: Atomic Absorption Newsletter, v. 12, p. 136–138.

Schnepfe, M. M., 1975, Spectrofluorimetric determination of thallium in silicate rocks with rhodamine-B in the presence of aluminum chloride: Anal. Chim. Acta, v. 79, p. 101–108.

Wahler, William, 1968, Pulse-polarographische Bestimmung der Spurenelemente Zn, Cd, In, Tl, Pb and Bi in 37 geochemischen Referenzproben nach Voranreicherung durch selektive Verdampfung: Neues Jahrb. Mineralogie Abh., v. 108, no. 1, p. 36–51.

Jour. Research U.S. Geol. Survey
Vol. 5, No. 5, Sept.–Oct. 1977, p. 583–587

A COMBUSTIMETRIC METHOD FOR DETERMINING THE TOTAL CARBON CONTENT OF GEOLOGIC MATERIALS

By JOHN H. TILLMAN, Menlo Park, Calif.

Abstract.—A modified LECO WR–12 carbon determinator is used in a combustimetric determination of total carbon in geologic materials. A thermal conductivity cell is used as the sensing device. International reference samples are analyzed and compared to results previously published. Three new standards from the Canadian Certified Reference Materials Project were received and analyzed for the total carbon content.

The accurate determination of carbon in geologic materials has long been a problem. Data for the carbon content (as CO_2) of International Geochemical Reference Samples (Flanagan, 1972) are mainly average values. Abbey (1972, 1973, 1974) and Abbey, Gillieson, and Perrault (1975) include the total carbon content (as CO_2) of standard reference materials but acknowledge uncertainty in most of the data.

Until recently, the most commonly used method for routine work was gravimetric (Peck, 1964; Frost, 1960; Allison, 1960). This procedure is sufficient for carbonate carbon or acid-evolved carbon dioxide. It should be noted that the carbon content reported for many standard reference materials is acid-evolved carbon dioxide and not total carbon. Methods long used for total carbon include combustion in a train in the presence of a flux, digestion with oxidizing acids, and decomposition in a combustion bomb—all followed by gravimetric determination (Hillebrand and others, 1953).

A gasometric method, using an induction furnace to combust the sample and a calibrated buret containing sulfuric acid, has been adapted to many samples (Foscolos and Barefoot, 1970). A combustion method using a carbon-hydrogen-nitrogen analyzer has been used to determine total carbon on some rock materials (Flanagan and others, 1975).

A method for detecting as little as 2 μg of carbonate carbon that employs a thermal conductivity cell as the sensing device was adopted for rocks and minerals (Marinenko and May, 1970). This procedure, based on gas chromatography, differs from the method reported here in the means of decomposition of the sample.

The combustimetric method is a sensitive, accurate, and rapid method for determining the total carbon content in geologic materials. Carbon content greater than 0.005 percent may be determined with good precision. Results of this method are compared with data obtained using the classical gravimetric method stated above.

Acknowledgments.—Thanks are due Sydney Abbey of the Geological Survey of Canada for providing reference materials for comparative analyses.

METHODS AND MATERIALS

Theory and equipment

The data were obtained by combusting the materials using a LECO model 763–200 induction furnace with a thermal conductivity cell as the sensing device. The cell consists of a pair of matched thermistors in two arms of a Wheatstone bridge. The reference thermistor is kept in an environment of constant gas pressure, gas flow, and temperature, and the measuring thermistor is maintained in the same environment, except that the gas composition varies according to the carbon dioxide content of the sample. The sensitivity of the system is governed by the difference in thermal conductivity between the carrier gas (oxygen) and the carbon dioxide. The thermal conductivities of the gases are 5.7×10^{-2} and 3.3×10^{-2} mcal/cm·s·°C for oxygen and carbon dioxide, respectively.

During combustion, the furnace flow carries the sample gas from the combustion chamber to the molecular sieve trap, which holds carbon dioxide at temperatures below 60°C. The gas flow during the combustion cycle flushes the conductivity cell, and the output signal from the electrical bridge remains close to zero. During the analysis cycle, the furnace flow purges the combustion chamber, and the flow to be measured goes through the molecular sieve, which is

heated to 300°C. At this temperature carbon dioxide is liberated from the trap, and the gas is carried past the measuring thermistor in the conductivity cell, thereby causing the bridge to become unbalanced and resulting in a positive reading at the digital voltmeter.

The Model WR–12 carbon analyzer (LECO Corp., St. Joseph, Mich.) is equipped with a carbon-range switch for either low-range (0.0050–0.2000 percent) or high-range carbon (0.010–5.000 percent). The combustion-time control is modified to permit combustion times up to 700 s. A series of steel standard rings was used to determine linearity and to calibrate the instrument.

Sample preparation and procedure

Samples are prepared for analysis by grinding to −100 mesh and then are reduced in size by rolling and quartering. Synthetic standards were prepared using Sierra quartz and varying amounts of reagents containing carbon.

A crucible containing weighed material is inserted onto a porcelain-pedestal positive-loading-and-locking tray. Then the combustion chamber is purged with oxygen for 30 s to remove moisture and any carbon dioxide that may have been introduced during sample loading. The step-by-step operating procedure is the same as that recommended by the manufacturer.

Accelerators

To achieve complete combustion of geologic samples, it is necessary to use accelerators, which ensure complete combustion by lowering the melting point of the mixture.

The manufacturer recommends using copper chips for best analytical results. Some tests resulted in incomplete burns, however, depending on the density of the sample and the amount of sample used (primarily for samples 1 g or larger). Iron or tin chips allowed faster burns and prevented coating of the sample, allowing the gases to be released, but caused spattering and heavy dust buildup. This heavy buildup resulted in several broken combustion tubes and clogged lances after less than ten trials. Also, iron chips were difficult to burn completely. A 1:10 mixture of tungsten and tin rendered low blanks, was highly viscous, and produced a covering that coated the sample causing slower release of the gases. Iron-tin and iron-copper combinations are recommended for use with nonmetallic materials, high-alloy steels, or other samples that are difficult to burn.

A mixture of iron and copper proved to be the best accelerator for the geologic materials analyzed. Complete burns resulted, and there were fewer problems with dust buildup and less deterioration of the lance and combustion tube. Table 1 shows typical calibration curves using three different accelerators and the standard steel rings with 60-s burns.

TABLE 1.—*Typical calibration curves using copper, iron, and iron and copper accelerators and the LECO standard steel rings*

[Combustion time, 60 seconds; carbon range, 0.0050 - 0.2000 percent]

Accelerator	Standard	DVM Reading
Copper (2.6 g)	Blank	0.0056
	0.0257	.0306
	.044	.0532
	.175	.1834
	.192	.2000
Slope:	1.192	
Standard error:	.0013	
Iron (2.0 g)	Blank	0.0090
	0.0247	.0336
	.044	.0556
	.175	.1878
	.192	.2092
Slope:	1.0119	
Standard error:	.0020	
Iron (1.0 g)	Blank	0.0079
and	0.0247	.0323
Copper (1.3 g)	.044	.0537
	.175	.1830
	.192	.2001
Slope:	0.9991	
Standard error:	.0007	

Crucible treatment

Crucibles were treated in two ways. One group was ignited at 1000°C overnight; another was leached in carbon tetrachloride overnight, rinsed in deionized distilled water, dried at 110°C for 4 hours, and ignited overnight at 1000°C. The results (table 2) show that the treatments made little improvement in detection limit or lowering of blank.

TABLE 2.—*Comparison of digital voltmeter (DVM) readings on treated crucibles and untreated crucibles*

[Combustion time, 60 seconds; carbon scale, 0.005-0.2000 percent; accelerator, 1.3 g copper + 1.0 g iron; sample weight compensator, 1.000 g]

Standard	Unignited crucibles	Ignited crucibles	Leached and ignited crucibles
	DVM reading		
Blank	0.0085	0.0072	0.0077
0.0247	.0336	.0356	.0329
.044	.0591	.0591	.0566
.175	.1949	.1955	.1922
.192	.2078	.2102	.2055
Slope:	1.045	1.054	1.037
Standard error:	.002	.002	.002

RESULTS

GA granite

A standard rock, GA, one of the best established reference granites from France, was selected for tests on sample size, combustion time, and amount of accelerator. In many analytical methods, lack of precision might be due in part to sampling variation, which is harder to control in small samples. Very small aliquots could produce substantial errors in determinations. Kleeman (1967) has statistically determined that deviation becomes significant if less than 10^6 grains of a rock sample is taken for analysis.

Results in table 3 show that total carbon content as carbon dioxide for a 0.10-g sample of GA granite deviates considerably from the results at the larger sample weights. When 0.10 g of the sample is analyzed, the total carbon content less the blank was experimentally determined to be 0.0049 for an average of 20 analyses, which is near the detection limit. The results in table 3 show that for GA granite any aliquot of 250 mg or more may be analyzed with good precision.

Combustion times were varied with the accelerator constant at 1 g of iron and 1.3 g of copper and a sample weight of approximately 1.0 g. Incomplete burns resulted when samples were combusted for less than 60 seconds. When the combustion time was set at 70 seconds, burns were complete, and 0.13 percent total carbon as carbon dioxide resulted for 10 consecutive analyses. At 150 seconds the results ranged from 0.13 to 0.16 percent total carbon as carbon dioxide for 10 consecutive analyses.

TABLE 3.—*Total carbon content as CO_2 of five aliquots of GA granite to show variation due to sample size*

[Combustion time, 60 seconds; carbon range, 0.005-0.2000 percent; accelerator, 1 g iron and 1.3 g copper]

Sample weight (g)	Total carbon as CO_2 (percent)
1.000	0.13
.7583	.14
.5029	.14
.2556	.13
.1007	.16

The amount of accelerator to use was determined to be enough to cover the sample completely thereby allowing the sample to be heated in a field of high-frequency magnetic flux that insures complete combustion.

Synthetic standards

Carbon may exist in geologic materials as carbonate minerals, carbonate groups in certain silicates, organic carbon, carbides, and rarely as graphite (Rankama and Sahama, 1950). The form of carbon has a negligible effect on the determination of amount. Table 4 lists data obtained using Sierra quartz as the matrix and various forms and quantities of carbon. For each form of carbon, individual calibration curves were produced using the standard steel rings. The high scale was utilized for the carbide, graphite, and organic carbon; the low scale was used for the carbonate carbon. Burns were 70 seconds long.

Calcium and lead carbonates were analyzed as synthetic standards for the carbon content. The amount of sample was selected to obtain a digital voltmeter reading approximately midrange. The results are listed below.

Reagent	*Weight*	C *as* CO_2
$CaCO_3$	0.0319	44.8
	.0833	44.0
	.0852	44.0
	.1000	43.5
Average		44.1
Theoretical percent C as CO_2 in $CaCO_3$.		44.0
$PbCO_3$	0.0213	16.6
	.0221	16.6
	.0234	16.7
	.0251	16.9
Average		16.7
Theoretical percent C as CO_2 in $PbCO_3$.		16.5

Standard rocks

A comparative analysis of samples from U.S. Geological Survey rock standards is listed in table 5 to show possible variations within the standard.

The data are values obtained between the two different lots of the specified rocks. Variations of total carbon within each lot and variations between each lot are significantly different for three standards.

Determinations of the carbon content of many reference materials from this report and from Flanagan (1972) and Abbey (1974) are listed in table 6 for comparative purposes. All results stated from Flanagan (1972) are average values except GA granite, which is a recommended value. The data that are un-

TABLE 4.—*Effects of various forms of carbon on the determination of carbon in geologic materials*

Carbon source	Wt of reagent (g)		Experimental total C (percent)
Graphitic carbon	0.0273		99.6
99.99 percent total C	.0249		99.7
(Spec. Pure)	.0257		99.6
	.0262		100.2
	.0268		100.0
		Average:	99.8
Carbide carbon			
Silicon carbide (SiC)	.0255		28.6
National Bureau of Standards	.0268		28.9
112: theoretical 29.10 per-	.0251		30.0
cent total C	.0258		29.4
	.0254		29.2
		Average:	29.2
Organic carbon			
Analyzed reagent sodium	.0255		21.3
tartrate: theoretical	.0263		21.3
21.00 percent total C	.0267		21.0
	.0303		21.3
	.0256		21.3
		Average:	21.2
Carbonate carbon			
Analyzed reagent lead	.0078		4.5
carbonate ($PbCO_2$):	.0213		4.5
theoretical 4.49 percent	.1251		4.6
total C	.0234		4.0
	.0300		4.5
		Average:	4.4

certain, reported by Abbey (1974), are indicated by a question mark. The mode of detection for both published sets of data was the gravimetric method. Three Canadian rock samples for use as new Certified Reference Materials from the Canadian Certified Reference Materials Project were analyzed. SY–2 and SY–3 are syenites from the Bancroft area of eastern Ontario and MRG–1 is a gabbro from Mount Royal in Montreal.

TABLE 5.—*Statistical comparison of splits of various reference materials*

[S, significant; NS, not significant at the fractile of the F distribution. The data represent an average of 20 determinations for each standard analyzed. Statistical calculations were performed according to the method for duplicate determinations given by Youden (1955, p. 50–58) and Flanagan, U. S. Geological Survey, Reston]

Standard reference sample	Average percent total C as CO_2	Standard deviation within splits	Calculated F-value for splits[1]	Assessment of variation
AGV-1				
(Split 7, Pos. 7)	0.027	0.0017	21.6	S
(Split 60, Pos. 9)	.024	.0014		
BCR-1				
(Split 34, Pos. 14)	.025	.0034	7.0	NS
(Split 36, Pos. 16)	.022	.0025		
G-2				
(Split 107, Pos. 20)	.109	.0038	6.5	NS
(Split 92, Pos. 29)	.112	.0012		
GSP-1				
(Split 43, Pos. 25)	.131	.0039	41.6	S
(Split 1, Pos. 8)	.125	.0021		
PCC-1				
(Split 53, Pos. 6)	.196	.0048	46.0	S
(Split 14, Pos. 16)	.187	.0032		
MAG-1				
(Split 57, Pos. 21)	8.282	.0383	1.2	NS
(Split 52, Pos. 20)	8.298	.0395		

[1]Critical F-values: 5 percent = 4.11; 1 percent = 7.40.

TABLE 6.—*Comparative data on total carbon content of various reference materials*

Sample description	Flanagan (1972)	Abbey (1974)	Present work
AGV-1 (USGS analyzed andesite)	0.06	0.01	0.03
BCR-1 (USGS analyzed basalt)	.03	.03 ?	.02
GSP-1 (USGS analyzed granodiorite)	.15	.12	.13
G-2 (USGS analyzed granite)	.08	.08	.11
PCC-1 (USGS analyzed peridotite)	.12	.16	.19
MAG-1 (USGS analyzed mud)			8.29
GA (France granite)	.11	.11	.13
JG-1 (Japan granodiorite)	.09	.09 ?	.11
M2 (U.K. pelitic schist)			.13
W-1 (USGS diabase)	.06	.06	.11
SY-1 (Canadian syenite)	.37		.51
SY-2 (Canadian syenite)		.49 ?	.57
SY-3 (Canadian syenite)		.36 ?	.46
MRG-1 (Canadian gabbro)		1.04	1.11
NBS-120b (Phosphate rock)			3.60

REFERENCES CITED

Abbey, Sydney, 1972, "Standard Samples" of silicate rocks and minerals—A review and compilation: Canada Geol. Survey Paper 72–30, 13 p.

——— 1973, Studies in "Standard Samples" of silicate rocks and minerals, Part 3—1973 extension and revision of "usable" values: Canada Geol. Survey Paper 73–36, 19 p.

——— 1974, Studies in "Standard Samples" of silicate rocks and minerals, Part 4—1974 edition of "usable" values: Canada Geol. Survey Paper 74–41, 19 p.

Abbey, Sydney, Gillieson, A. H., and Perrault, Guy, 1975, SY–2, SY–3, and MRG–1—A report on the collaborative analysis of three Canadian rock samples for use as certified reference materials: Canada Dept. Energy, Mines and Resources Mines Br. Research Rept., 56 p.

Allison, L. E., 1960, Wet-combustion apparatus and procedure for organic and inorganic carbon in soil: Soil Sci. Soc. America Proc., v. 40, p. 36–40.

Flanagan, F. J., 1972, Values for international geochemical reference samples: Geochim. et Cosmochim. Acta, v. 37, p. 1189–1200.

Flanagan, F. J., Chandler, J. C., Breger, I. A., Moore, C. B., and Lewis, C. F., 1975, The carbon contents of USGS volcanic rock standards, *in* Descriptions and analyses of eight new USGS rock standards: U.S. Geol. Survey Prof. Paper 84D, p. 123–126.

Foscolos, A. E., and Barefoot, R. R., 1970, A rapid determination of total organic and inorganic carbon in shale and carbonates: Canada Geol. Survey Paper 70–11, p. 1–8.

Frost, I. C., 1960, Comparison of three methods for the determination of total and organic carbon in geochemical studies, *in* Geological Survey research 1960: U.S. Geol. Survey Prof. Paper 400–B, p. B480–B483.

Hillebrand, W. F., Lundell, G. E. F., Hoffman, J. L., and Bright, H. A., 1953, Applied inorganic analysis: New York, New York, John Wiley and Sons, Inc., p. 768–778.

Kleeman, A. W., 1967, Sampling error in the chemical analysis of rocks: Geol. Soc. Australia Jour., v. 14, p. 43–47.

Marinenko, John, and May, Irving, 1970, Gas chromatographic determination of carbonate carbon in rocks and minerals, *in* Geological Survey research 1970: U.S. Geol. Survey Prof. Paper 700–D, p. D103–D105.

Peck, L. C., 1964, Systematic analysis of silicates: U.S. Geol. Survey Bull. 1170, 89 p.

Rankama, K. K., and Sahama, T. G., 1950, Geochemistry: Chicago, Univ. Chicago Press, p. 532–533.

Youden, W. J., 1951, Statistical methods for chemists: New York, John Wiley and Sons, p. 8–58.

Jour. Research U.S. Geol. Survey
Vol. 5, No. 5, Sept.–Oct. 1977, p. 589–593

AN IMPROVED ION-SELECTIVE ELECTRODE METHOD FOR THE RAPID DETERMINATION OF FLUORINE IN ROCKS AND SOILS

By D. M. HOPKINS, Denver, Colo.

Abstract.—An improved method based on an ion-selective electrode technique for the analysis of fluorine in rocks and soils is presented. Analyses are made by using a sodium carbonate–potassium carbonate fusion and a citric acid dissolution of the fuseate. Prior to determining the fluorine concentration by a standard-addition procedure, sodium citrate buffer is added to the solution. The proposed method yields fluorine values in agreement with known values for standard rocks. Values of this method are also presented for six geochemical exploration rock-and-soil reference samples and compared to those from other ion-selective electrode techniques. Fifty samples can be analyzed in 1 person-day. The sensitivity of the method is 100 parts per million, and samples containing up to 45 percent fluorine have been successfully analyzed.

Fluorine commonly concentrates in residual fluids and vapors during the late stages of magmatic crystallization and consequently enriches granitic and alkalic rocks. This concentration and consequent enrichment probably constitute the main reason why fluorine persists as a trace or in minor and major amounts in almost all types of mineral deposits. Positive primary fluoriferous halos are therefore associated with many deposits, and in recent years considerable work has been done on fluorine migration, the use of fluorine values as an indicator of its deposits and of those in which it is an accessory element (Boyle, 1974). An improved ion-selective electrode method for the analysis of fluorine in rock and soil samples to aid in the exploration for mineral deposits is proposed in this report.

Fluorine is found in nature either as the typical singly charged fluoride ion F^- or occasionally as a component of such complex anions as $(BF_4)^-$, $(AlF_6)^{3-}$, $(SiF_6)^{2-}$, in some of which covalent bonds are present. The customary radius of the fluorine atom or the fluoride ion in minerals is about 0.133 nanometers. The close similarity among the radii of $(OH)^-$, 0.14–0.16 nm; O^{-2}, 0.132 nm; and the fluoride ion makes it clear that substitution is readily possible between the univalent anions F^- and OH^- as in topaz, amphiboles, and micas and that fluoride ions can even replace oxygen in many minerals.

Several methods are available for fluorine determination in geological samples (Edmond, 1969; Ficklin, 1970; Fuge, 1976; Ingram, 1970; Kesler and others, 1973; Oliver and Clayton, 1970; Peters and Ladd, 1971). The classical distillation-titration method (Willard and Winter, 1933) is quite reliable and accurate, but it is time consuming and not satisfactory for geochemical exploration involving large numbers of samples. Most of the recent studies employ an ion-selective electrode that is capable of measuring the fluoride-ion activity in aqueous solutions. These methods are faster than, and as sensitive as, distillation-titration methods. The samples are usually fused to release the fluoride ions from the sample matrix, and the fuseate is dissolved with water, complexing agent, and buffer; then the electrode is immersed in this solution to measure the fluoride-ion activity directly.

The sodium carbonate–potassium carbonate fusion mixture used in the proposed method was reported by Shergold and Selfe (1974) in their determination of fluorine in ores. Citric acid and sodium citrate are used to dissolve the fused sample, adjust the pH, maintain a high ionic strength, and inhibit any metal ion-fluoride complexes. This fusion and ion-electrode detection technique permits the direct determination of fluorine in various geologic rock and soil samples in the concentration range from 100 parts per million to over 45 percent fluorine. Fluorine values of this method for several standard rocks compare favorably with certified, accepted, and reported values.

A modified sodium hydroxide fusion–ion-selective electrode method for fluorine analysis is described also. Concentrations for six geochemical exploration reference samples (Allcott and Lakin, 1975), and for opal glass and fluorspar standards, are presented for this sodium hydroxide fusion method and compared with concentrations from the method proposed herein. The concentrations from the two methods have good agree-

ment, but a comparison of the standard deviation versus mean concentrations for the geochemical exploration reference samples, reported near the average crustal abundance of 625 ppm (Mason, 1966, p. 45), indicates that the sodium carbonate–potassium carbonate fusion technique is more desirable at this concentration level.

ANALYTICAL METHOD

Equipment, reagents,[1] and standards

An Orion specific ion meter, Orion model 407, equipped with a specific ion electrode, Orion model 94–09A, and a reference electrode, Orion model 90–01–00, were used to measure the fluoride ion activity in the sample solutions. An electric muffle furnace was used to fuse the samples. A standard laboratory pH meter was used to adjust the pH of the buffer solution. A magnetic stirrer designed to avoid sample solution heating was used in this study and is recommended.

Standard fluoride solutions are prepared as needed from a stock 10 000 ppm sodium fluoride solution, which is prepared by dissolving 2.21 grams NaF (previously dried at 110°C overnight) in 100 milliliters of water. Solutions of 1000 ppm, 100 ppm, and 10 ppm are prepared monthly by serial dilutions from the stock solution, and all fluoride standard solutions are stored in polypropylene bottles.

Anhydrous Na_2CO_3 and K_2CO_3 (previously oven-dried at 110°C overnight) are ground to pass an 80-mesh sieve, and a 1:1 mixture by weight is prepared for the flux. 1*M* citric acid is prepared by dissolving 210.15 g citric acid monohydrate in 1 liter of water. 1 *M* sodium citrate buffer is prepared by first dissolving 294 g of sodium citrate dihydrate in approximately 800 mL of water, then adjusting the pH to 6.0 with 6 *N* HCl, and finally diluting the solution to 1 L.

A solution of 40 g/L of equal parts of Na_2CO_3 and K_2CO_3 is prepared by dissolving 20 g of each in a sufficient quantity of water to make a volume of 1 L of solution.

Proposed Na_2CO_3–K_2CO_3 fusion method

A 50-mg (minus 80-mesh) sample is fused with 2 g of Na_2CO_3–K_2CO_3 flux in a nickel crucible at 800°C for 15 minutes in a muffle furnace. After cooling, add 15 mL of 1 *M* citric acid to the crucible, and allow the mixture to digest until CO_2 evolution is no longer detected (3–4 hours, or preferably overnight). Add 25 mL of the sodium citrate buffer to the contents of the crucible, and then transfer the entire mixture to a 100-mL polypropylene beaker. Carefully rinse the crucible with distilled water, and add the rinse to the beaker; then dilute the sample solution to 100 mL, and add a Teflon-coated stirring bar.

A standard solution to be used for adjusting the specific ion meter to correct for deviations from the theoretical slope of the electrode is prepared as follows: Add 15 mL of 1 *M* citric acid to 25 mL of the 40 g/L solution of 1:1 Na_2CO_3-K_2CO_3 and 1 mL of a 1000- or 100-ppm NaF working standard in a 100-mL polypropylene beaker. Then add 25 mL of 1 M sodium citrate buffer solution, dilute to 100 mL with distilled water, and add a Teflon-coated stirring bar. Set the instrument slope indicator to 100 percent and the temperature compensator to the temperature of the solution; then place the electrodes in the solution while it is gently stirred on a magnetic stirrer. Turn the calibration control for a center-scale reading, and then add 1 mL of the NaF working standard. The needle should go to 1 on the known-addition scale, or the temperature control is adjusted until the correct reading is obtained. Move the slope control until the sample temperature is read on the temperature scale, and now the percent of theoretical slope can be read on the slope scale. The instrument is now adjusted and ready to read the unknown sample.

Remove the electrodes from the standardizing solution, rinse and blot them with absorbent tissue, and place them in the sample solution. Turn the calibration control until the needle points to midscale. Pipet to the sample no more than 3 mL of one of the working NaF standards, and record the reading on the known-addition scale. Allow approximately 5 min before taking a reading if standard additions total less than 100 micrograms. Allow 3 min for 100- to 500-μg additions and 1–3 min for higher additions. Determine the fluoride concentration in parts per million by using the following formula:

$$F = \frac{1000\ \text{mg}}{\text{g}} \times \frac{\text{known } \mu\text{g added to final solution}}{\text{mg of sample}} \times \text{dilution factor} \times \text{meter reading.}$$

The cutoff or sensitivity of this determination procedure is 100 μg/g (100 ppm). For samples containing 100 000 ppm fluoride or more, the citric acid–fuseate solution should be diluted to 100 mL, and an aliquot of 10 mL or another desirable volume should be added to the 25-mL sodium citrate buffer before final dilution to 100 mL.

[1] All chemicals are of reagent grade.

Modified NaOH fusion method

This method is a modification of the procedure proposed by Kesler, Van Loon, and Bateson (1973). A 50-mg (minus 80-mesh) sample is fused with 15 sodium hydroxide pellets for 10–20 min in a muffle furnace at 620°C. After the crucible is cool, add 20 mL of 1 *M* citric acid to dissolve the fuseate. When dissolution is complete, add 25 mL of 1 *M* sodium citrate that has been adjusted to pH 6 with HCl. The contents of the crucible are now transferred to a 100-mL polypropylene beaker, the crucible is rinsed with distilled water, and the beaker is then diluted to 100 mL. A meter adjustment standard is prepared by dissolving 15 NaOH pellets in 25 mL distilled water, and when the solution is cool, it is added to a 100-mL polypropylene beaker containing 20 mL of 1 *M* citric acid. Cool the beaker, and add 25 mL of 1 M sodium citrate buffer (pH 6) and 1 mL of a NaF working standard solution before diluting to 100 mL. The remainder of the meter adjustment and sample-reading steps are the same as described for the method proposed by this report.

DISCUSSION AND RESULTS

The fluoride-sensitive electrode responds to and develops a potential proportional to the activity of free, unbound, uncomplexed fluoride ions in solution. The potential difference forms between the faces of a LaF_3 single crystal, which separates an internal filling solution from the sample solution. The measured potential, E, is given by the simplified Nernst equation,

$$E = E_e - 2.303\frac{RT}{F}\log_{10} a_F^-, \qquad (1)$$

where E_e is a constant potential characteristic of the electrode; R, the gas constant; F, Faraday's constant; T, the absolute temperature; and a_F^-, the activity of fluoride ions in solution. The relationship between the free fluoride ion concentration and the fluoride ion activity is

$$a_F^- = \gamma f C_t, \qquad (2)$$

where γ is the activity coefficient of the fluoride ion, f is the fraction of the total fluoride ion concentration that is free, and C_t is the total concentration of fluoride ion in all its forms—free, complexed, or bound.

The success of the known-addition method depends on making the addition in such a way that γ and f remain constant. The fluoride ion concentration can then be substituted for the activity in equation 1, and a linear relationship between the logarithm of the fluoride ion concentration and the measured potential can be obtained. The activity coefficient, γ, remains constant if a large amount of a noninterfering salt is added to maintain a high, constant ionic strength. The fraction of the total concentration of fluoride ions that is free, f, is held constant by adding a large excess of a reagent, such as sodium citrate, which releases fluoride ions from any complexes formed with Al^{3+}, Fe^{3+}, Si^{4+}, and Be^{2+} ions. Sodium citrate buffer solution also provides enough noninterfering ions to maintain a high, constant ionic strength background in the methods described above. This buffer adjusts the pH to between 5 and 6 to dissociate any HF formed when the pH is less than 5 and to prevent hydroxide ion interference at pH values above 7. Citric acid dissolution of the fused sample gives additional sodium, potassium, and citrate ions for ionic strength and decomplexing.

Table 1 presents the concentrations determined by the proposed method and other fluoride-selective electrode methods for some standard rock samples.

Fluorine concentrations by the proposed method and other fusion–ion-electrode methods are compared in table 2 for six geochemical exploration reference samples (Allcott and Lakin, 1975). Citrate ions are employed in the buffer-complexing agent of each method. Preliminary tests with citric acid, ammonium citrate, and sodium citrate solutions of the same molarity indicate that each is equally effective in releasing fluoride ions from complexes if the pH range and the ionic strength are held constant.

Results for samples GxR1, GxR3, and GxR4, which range from 0.1 to 0.15, 8.1 to 9.0, and 0.2 to 0.35 percent fluoride, respectively, agree closely except for methods D and E in samples GxR3 and GxR4.

Table 3 compares fluorine values determined by Na_2CO_3–K_2CO_3, NaOH, and Na_2CO_3–KNO_3 fusions of opal glass and fluorspar. These results are significant as they demonstrate that only the Na_2CO_3–K_2CO_3

TABLE 1.—*Comparison of fluorine determined by proposed method with reported concentrations for some standard rocks*

[Fluorine in ppm, except that concentrations with decimal values are reported in percent fluoride]

Sample	Proposed method	Standard deviation	Reported values
G-2 Granite	1,430	105	[1]1,290, [4]1,120, [5]1,480, [6]1,230
AGV-1 Andesite	546	21	[1]435, [4]500, [6]475
BCR-1 Basalt	740	125	[1]470, [4]510, [6]545
NBS 120a Phosphate rock	3.8	(✓)	[2]3.92, [3]3.88, [7] [8]3.87, [7] [9]4.01
NBS 91 Opal glass	5.6	.16	[2]5.72, [5]5.72, [7]5.82
NBS 79 Fluorspar	45.0	(✓)	[2]46.3

✓ Standard deviation not calculated; all replicates were equal.
[1] Reported as the accepted value, Flanagan (1973).
[2] Certificate value calculated as percent F in CaF_2.
[3] Edmond, 1969.
[4] Ficklin, 1970.
[5] Ingram, 1970.
[6] Kesler, Van Loon, and Bateson, 1973.
[7] Peters and Ladd, 1971.
[8] Method of decomposition: HCl only.
[9] Method of decomposition: HCl + fusion.

TABLE 2.—*The ion-selective electrode determination of fluoride in six geochemical exploration reference samples*

[Values shown for ppm of fluorine are the averages of replicate analyses; A, NaOH fusion (H. W. Lakin, oral commun., 1976); B, NaOH fusion (H. W. Lakin, oral commun., 1976); C, NaOH fusion (the modified procedure described in the analytical methods section); D, Na_2CO_3-KNO_3 fusion (W. H. Ficklin, oral commun., 1976); E, Na_2CO_3-KNO_3 fusion, TISAB[1] buffer: results using the method of Crenshaw and Ward (1975)]

Sample		Fluorine, ppm					
Reference No.	Type and location	Proposed method	Other methods				
			A	B	C	D	E
GxR1-----	Jasperoid-Drum Mountains, Juab Co., Utah-	1,000	1,300	1,500	1,200	1,000	1,100
GxR2-----	Soil-Park City, Summit Co., Utah---------	520	218	700	485	510	280
GxR3-----	Fe-Mn-W-rich spring deposit, Humboldt Co., Nevada.	85,000	81,000	87,000	90,000	54,000	31,000
GxR4-----	Porphyry copper mill heads, Utah---------	3,100	2,800	3,450	2,850	2,600	2,000
GxR5-----	Soil-B horizon, Somerset Co., Maine------	340	130	475	286	215	270
GxR6-----	Soil-B horizon, Davidson Co., North Carolina.	340	160	540	286	220	280

[1] TISAB: Total Ionic Strength Adjustment Buffer, prepared by dissolving 57 mL glacial acetic acid, 58 g sodium chloride, and 0.3 g sodium citrate in 500 mL water. Adjust the pH to 5.5 with 5 *M* sodium hydroxide solution, and dilute to 1 L with water.

TABLE 3.—*Fusion–ion-electrode determination of fluorine in opal glass and fluorspar*

Sample	Percent fluorine			
	Proposed method	Certificate value	NaOH fusion[1]	Na_2CO_3-KNO_3 fusion[2]
NBS 91, Opal glass----------	5.6	5.72	5.7	3.3
NBS 79, Fluorspar----------	45.0	[3]46.3	48.0	23.0

[1] Method C, table 2.
[2] Method D, table 2.
[3] Calculated as percent F in CaF_2.

and NaOH fusions decompose these high-fluorine-content minerals completely. The low fluorine values result from an incomplete Na_2CO_3–KNO_3 fusion, which is the same technique used for methods D and E in table 2. TISAB buffer, which has a high acetate ion content, is used in method E, table 2, and is reported to give low fluorine assays in some samples (Shergold and Selfe, 1974). This may explain the considerable difference in the fluorine values of methods D and E for sample GxR3, table 2.

Comparisons of the replicate analyses of the six geochemical exploration reference samples for fluorine by using respective Na_2CO_3–K_2CO_3 and NaOH fusion–ion-selective electrode techniques are shown in table 4.

CONCLUSION

The proposed method is useful to improve accuracy in the rapid analysis of a wide variety of rock and soil samples as an aid in geochemical exploration. A sodium hydroxide fusion technique combined with ion-electrode detection gives fluorine values in good agreement with the proposed method, although a statistical comparison indicates that the proposed Na_2CO_3-K_2CO_3 fusion–ion-electrode technique is more desirable near the crustal and subcrustal abundance concentrations.

TABLE 4.—*Comparisons of replicate fluorine analyses determined by using two methods of sample fusion*

[Fluorine in ppm; leaders (---) indicate all replicates equal]

Na_2CO_3-K_2CO_3 fusion					NaOH fusion				
Sample	Replicates	Mean	Standard deviation	95-percent confidence limits	Sample	Replicates	Mean	Standard deviation	95-percent confidence limits
GxR1	1,000, 1,000, 1,000, 1,300, 1,100	1,080	121	1,019-1,140	GxR1	1,000, 1,200, 1,200, 1,500	1,200	134	984-1,420
GxR2	480, 480, 480, 640	520	70	405- 635	GxR2	380, 440, 520, 600	485	98	327- 643
GxR3	85,000, 85,000, 85,000	85,000	---	---	GxR3	90,000, 90,000, 90,000	90,000	---	---
GxR4	3,000, 3,200, 3,200	3,100	105	2,840-3,360	GxR4	2,800, 3,000, 2,400, 3,100	2,850	310	2,350-3,350
GxR5	360, 360, 320, 400, 380	360	32	320- 400	GxR5	280, 320, 260	286	31	208- 364
GxR6	320, 360, 340	340	20	288- 392	GxR6	200, 260, 400	286	105	26- 546

REFERENCES CITED

Allcott, G. H., and Lakin, H. W., 1975, The homogeneity of six geochemical exploration reference samples, *in* Geochemical exploration 1974, Elliott, I. L., and Fletcher, W. K., eds., Geochemical exploration 1974: New York, Elsevier, Developments in Economic Geology 1, p. 659–681.

Boyle, R. W., 1974, Elemental associations in mineral deposits and indicator elements of interest in geochemical prospecting [revised ed.]: Canada Geol. Survey Paper 74–45, p. 35–36.

Crenshaw, G. L., and Ward, F. N., 1975, Determination of fluorine in soils and rocks by known-increment addition and selective-ion electrode detection: U.S. Geol. Survey Bull. 1408, p. 77–84.

Edmond, C. R., 1969, Direct determination of fluoride in phosphate rock samples using the specific ion electrode: Anal. Chemistry, v. 41, no. 10, p. 1327–1328.

Ficklin, W. H., 1970, A rapid method for the determination of fluoride in rocks and soils, using an ion-selective electrode, *in* Geological Survey research 1970: U.S. Geol. Survey Prof. Paper 700–C, p. C186–C188.

Flanagan, F. J., 1973, 1972 values for international geochemical reference samples: Geochim. et Cosmochim. Acta, v. 37, p. 1189–1200.

Fuge, R., 1976, The automated colorimetric determination of fluorine and chlorine in geological samples: Chem. Geology, v. 17, no. 1, p. 37–43.

Ingram, B. L., 1970, Determination of fluoride in silicate rocks without separation of aluminum using a specific ion electrode: Anal. Chemistry, v. 42, no. 14, p. 1825–1827.

Kesler, S. E., Van Loon, J. C., and Bateson, J. H., 1973, Analysis of fluoride in rocks and an application to exploration: Jour. Geochem. Explor., v. 2, p. 11–17.

Mason, Brian, 1966, Principles of geochemistry [3d ed.]: New York, John Wiley and Sons, Inc., p. 45.

Oliver, R. T., and Clayton, A. G., 1970, Direct determination of fluoride in miscellaneous fluoride materials with the Orion fluoride electrode: Anal. Chim. Acta, v. 51, no. 3, p. 409–415.

Peters, M. A., and Ladd, D. M., 1971, Determination of fluoride in oxides with the fluoride-ion activity electrode: Talanta, v. 18, no. 7, p. 655–664.

Shergold, H. L., and Selfe, F. L., 1974, Determination of fluorine content of ores with the fluoride-ion selective electrode: Inst. Mining and Metallurgy Trans., sec. C, v. 83, p. C256–C257.

Willard, H. H., and Winter, O. B., 1933, Volumetric method for determination of fluorine: Indus. Eng. Chemistry, Anal. Ed., v. 5, no. 1, p. 7–10.

Jour. Research U.S. Geol. Survey
Vol. 5, No. 5, Sept.–Oct. 1977, p. 595–596

PREPARATION OF PYRITE-COATED SAND GRAINS FOR RESEARCH ON ROLL-TYPE URANIUM DEPOSITS

By CAROL A. GENT, Denver, Colo.

Abstract.—Ordinary quartz sand grains can be coated with pyrite for use in laboratory experiments on the genetic geochemistry of roll-type uranium deposits. The sand is first added to a ferric chloride solution. The slow addition of sodium hydroxide to the mixture gives the sand grains an iron oxide coating. This coating is then converted to pyrite by reaction with hydrogen sulfide, thus yielding a product suitable for experimental use.

The localization of uranium into roll-type deposits, such as those found in Wyoming, New Mexico, and Texas, is believed to result from a geochemical process initiated by the oxidation of pyrite.

Granger and Warren (1969) devised a laboratory experiment to mimic this geochemical process. The process involves a reaction between pyrite- or marcasite-bearing sand and oxygenated ground water. In Granger and Warren's experiment, natural iron oxide-coated sand grains were reacted with potassium polysulfide (K_2S_n), in a 2000- by 65-mm glass column, to convert the iron oxide coating to iron sulfide. After the resulting iron sulfide-coated sand was washed, a buffered water solution, in equilibrium with atmospheric oxygen, was percolated through the sand. A sharp redox interface quickly developed and started to migrate through the column. An accident affecting the equipment terminated the 1969 experiment before completion, but even before the accident, there were questions as to whether the reaction in the column was a valid synthesis of roll formation. The reaction between the iron oxide-coated sand and the K_2S had probably formed a variety of iron sulfides, most of which had a composition near that of FeS. It was feared that little or no FeS_2 (pyrite or marcasite) had been formed. Therefore, because the monosulfides are much more reactive than FeS_2 and because the products of the reaction might be different, the validity of the model was questioned. Granger and Warren then suggested that a method be found to produce pyrite-bearing sand grains (at low temperature) for use in succeeding experiments on roll-type deposits. The method described in this report successfully produces such sand, some of which is now being used in experiments similar to the one described by Granger and Warren (1969).

Acknowledgment.—Work was conducted in collaboration with M. B. Goldhaber.

PROCEDURE

Laboratory procedures for the synthesis of pyrite in aqueous solution were summarized by Roberts, Walker, and Buchanan (1969). Their greatest yield of pyrite was obtained from a reaction of hydrated ferric oxide with hydrogen sulfide. Because we wished to produce pyrite adhering directly to quartz sand grains, we needed first to coat the sand with iron oxide (preferably hydrated iron oxide) and then to convert the iron oxide coating to pyrite. The first step, preparing an iron oxide-coated sand, was accomplished by including sand in a modification of a goethite synthesis used by Rickard (1974) in his studies on pyrite formation.

Our reagents were analytical grade, and distilled water was used for all solutions. Quartz beach sand from Texas was obtained from the U.S. Geological Survey milling laboratories, where it is ordinarily used to clean grinding plates.

One hundred grams of sand (<32 to >70 mesh) was added to a solution of 15.15 g $FeCl_3 \cdot 6H_2O$ dissolved in 125 mL water. Sodium hydroxide was added slowly, with gentle hand stirring, bringing the solution to approximately pH 10. The reddish-brown mixture was then heated at 90°C for 5 days (subsequent experiments show this time can be reduced to 1 day), after which the remaining supernatant solution was decanted and the wet sand was returned to the oven and heated for another 2 days. The resulting dry red sand mixture was washed with distilled water to remove excess oxide and salt until the wash water was neutral; then the mixture was air dried.

One hundred milliliters of water in a 125 mL Erhlenmeyer flask was saturated with hydrogen sulfide. Ten grams of the red sand was rapidly added, and the flask was immediately capped. The color of the mixture quickly changed from red to black. After 1 day at room temperature the flask was opened and allowed to stand at room temperature for 3 more days. The solution was decanted and the black sand was washed with hot concentrated hydrochloric acid to remove the monosulfides. The resulting gray sand was rinsed with water and was air dried. The experimental quantities were later increased to produce larger amounts of red and gray sand.

RESULTS AND ANALYSES

Although the iron oxide produced from the reaction of ferric chloride and sodium hydroxide was not well crystallized, X-ray diffraction curves showed the peaks for hematite and goethite. In preparing the iron oxide-coated red sand, the final pH was difficult to control, owing to a continual drift toward lower pH during reaction. Further experiments showed that a pH between 10 and 11 favored the formation of goethite, whereas hematite tended to prevail at lower pH levels. The relative intensities of the hematite and goethite peaks varied in the X-ray patterns of the iron oxide from different batches of red sand, but this variation had no apparent effect on the conversion of the iron oxide to pyrite.

Each conversion of red sand to gray sand produced some iron monosulfides. After sulfidization and removal of the black monsulfide with hot concentrated hydrochloric acid, the remaining gray precipitate was readily dissolved in concentrated nitric acid—a distinguishing test for FeS_2. The gray material that did not adhere to the sand grains during hydrochloric acid washing was identified by X-ray diffraction as pyrite and very minor elemental sulfur. A portion of the gray sand was crushed and allowed to stand in hydrofluoric acid until the sand dissolved. The remaining gray solid was filtered and washed, and it was also identified as pyrite by X-ray methods. Peaks for marcasite were not present. The adhering pyrite was examined under both optical and scanning-electron microscopes, and it was found to be sparsely and sporadically distributed on the surfaces of the sand grains. The scattered aggregates of FeS_2 particles showed poor crystal development, and no well-formed pyrite crystals could be seen. The X-ray patterns of the FeS_2 aggregates, however, showed the pyrite to have a well-developed internal crystal structure.

The pyrite from a weighed portion of gray sand was dissolved in concentrated nitric acid. The solution was diluted and analyzed for iron colorimetrically at 562 nm by the method of Stookey (1970); the iron content was also confirmed by analysis (± 0.01 ppm) on an atomic absorption spectrophotometer. Another portion of the gray sand was analyzed for sulfur by X-ray fluorescence. These analyses result in a formula of $FeS_{2.041}$. From one of the batches of sand, enough excess pyrite was washed off by the hydrochloric acid to allow a test for sulfur by way of $BaSO_4$ precipitation and also to analyze for iron. The resulting formula for this solid was $FeS_{1.984}$. These two formulas are close enough to FeS_2 to be well within the degree of error allowed in the analytical techniques.

In a typical run, 16 percent of the original iron ($FeCl_3$) adhered to the sand in the form of oxides. Eighty-five percent of the iron from the oxides was converted to pyrite, although only about 12 percent of this pyrite adhered to the sand grains. The resulting gray sand was 0.11 percent pyrite by weight.

During the course of the experiments the source of our sand was changed from Texas to Ottawa, Ill. The Ottawa sand grains appeared to have smoother surfaces and did not retain the iron oxide and pyrite as well as the original sand grains. Additional investigation showed that finer grain sizes of Ottawa sand; and HF-etched sand grains retained more of the pyrite. Further experiments would be needed to determine the size, composition, and surface qualities of sand grains most suitable for retaining desired amounts of pyrite.

REFERENCES CITED

Granger, H. C., and Warren, C. G., 1969, Unstable sulfur compounds and the origin of roll-type uranium deposits: Econ. Geology, v. 64, p. 160–171.

Rickard, D. T., 1974, Kinetics and mechanism of the sulfidation of goethite: Am. Jour. Sci., v. 274, p. 941–952.

Roberts, W. M. B., Walker, A. L., and Buchanan, A. S., 1969, The chemistry of pyrite formation in aqueous solution and its relation to the depositional environment: Mineralium Deposita, v. 4, p. 18–29.

Stookey, L. L., 1970, Ferrozine—a new spectrophotometric reagent for iron: Anal. Chemistry, v. 42, no. 7, p. 779–781.

Jour. Research U.S. Geol. Survey
Vol. 5, No. 5, Sept.–Oct. 1977, p. 597–602

A THERMOSTATIC WATER BATH FOR EXPERIMENTAL STUDIES IN AQUEOUS SOLUTIONS

By R. M. SIEBERT,[1] K. A. McGEE, and P. B. HOSTETLER,[2]
Columbia, Mo., Reston, Va., and Columbia, Mo.

Abstract.—A temperature-controlled water bath for the study of ion-pairing equilibria and mineral solubility in aqueous solutions below 100°C is described. The bath is similar to a previously described system (P. B. Hostetler and C. L. Christ, 1968, U.S. Geol. Survey Prof. Paper 600–D, p. D217–D221) but incorporates several significant improvements. Included among these are a more efficient stirring mechanism, a potentially larger solid-to-solution ratio, and improved equilibration of the gas phase with the solution.

The apparatus described herein was developed for the study of ion-pairing equilibria and mineral solubilities in aqueous solutions at constant temperatures below 100°C, at approximately 0.1 MPa (1 atmosphere) total pressure of a chosen gas phase, and in a silica-free environment. The apparatus design is derived from and thus is similar to a water-bath system described by Hostetler and Christ (1968), and it incorporates several significant improvements.

Two requirements of a water-bath system were recognized as being important to successful ion-pairing-equilibria and mineral-solubility studies: (1) the adequate stirring of the solution or mineral suspension and (2) the rapid and thorough equilibration of the chosen gas phase with the solution. In the system described by Hostetler and Christ (1968), stirring was accomplished by Teflon-coated magnets which rested on the bottom of the reaction vessels and which were rotated by magnetic stirrers placed underneath the main bath vessel. This arrangement could accommodate only 10–25 g of relatively fine grained material in a 1500-mL vessel without stopping the stirring bar, and little of this mass was actually in suspension. This led to a very low solid-to-solution ratio and, hence, to relatively slow equilibration rates. Also, mutual grinding of the reaction-vessel bottom, mineral grains, and the Teflon bar resulted in damage to the equipment and, sometimes, in enhanced solubility of the mineral because of the production of hypersoluble fine material. The equilibration of the gas phase with the solution in the previous system was commonly found to be incomplete because of the low gas-flow rates required to minimize the evaporation of water during long-term experiments.

In the new apparatus, the stirring is accomplished by using the chosen gas phase. The gas-distribution system in the new apparatus consists of two independent circuits. A schematic diagram of this system is presented in figure 1. The first gas circuit is an open one in which the gas is drawn from storage tanks, is presaturated with respect to water vapor (at the temperature of the experiment) in a separate vessel, is bubbled into the solution in the reaction vessel, and, finally, is bled off the reaction vessel to the atmosphere. The gas-flow rate is low in this circuit. The second circuit is a closed loop. Gas is drawn from the top of the reaction vessel by a pump and is pumped into a heat exchanger within the main water-bath vessel, where the gas is brought back to the bath temperature. The gas is then routed to the funnel-shaped bottom of the reaction vessel, is passed through a flat gas-dispersing frit, and is fountained up through the solution. The gas-flow rate in this circuit is high—about 1.5 L/min. This rapid fountaining of gas through the experimental solution can maintain large quantities of solid in suspension (as much as 100 g in approximately 1800 mL of solution), provide very effective stirring, and allow very rapid and thorough equilibration between the gaseous and aqueous phases. A silica- and metal-free environment is achieved by using only polyolefin-type plastics in the construction of the apparatus.

To date, two water-bath systems of this type have been constructed, one at the Geology Department, University of Missouri at Columbia, and a later version at the U.S. Geological Survey in Reston, Va. Differences between the two are minor, and, unless otherwise noted, the description given here applies to both.

[1] Department of Geology, University of Missouri; present address: Exploration Research Dept., Continental Oil Co., P.O. Box 1267, Ponca City, Okla.
[2] Department of Geology, University of Missouri; present address: School of Earth Sciences, Macquarie University, North Ryde, N.S.W. 2113, Australia.

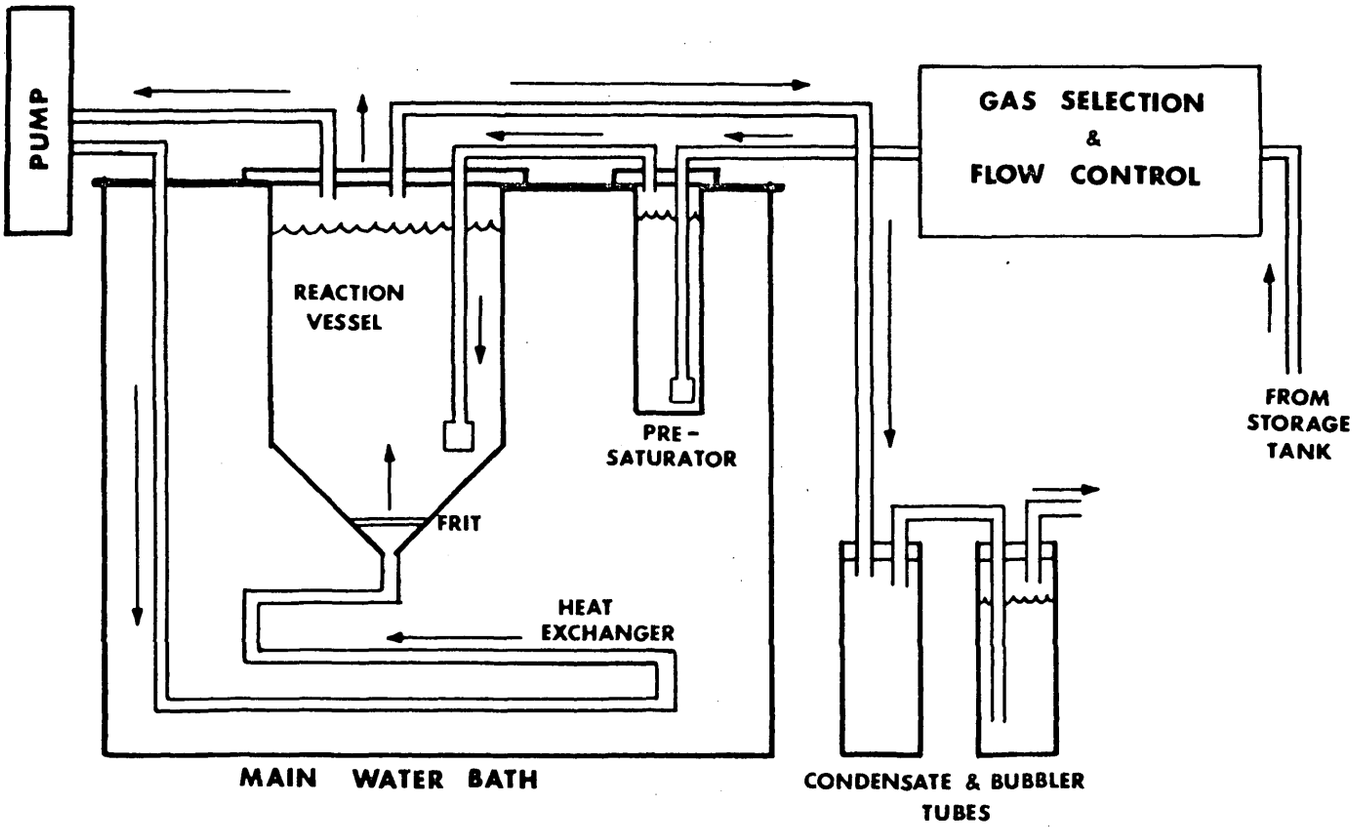

FIGURE 1.—Schematic diagram of the gas-distribution system.

Acknowledgments.—We are grateful to Dennis Kostick, U.S. Geological Survey, for taking the photographs of the baths.

DESCRIPTION

The baths and associated gas- and temperature-controlling apparatus are shown in figure 2. The apparatus consists of a square polypropylene water-bath vessel, in which are suspended five polypropylene reaction vessels, three having a 2000-mL capacity and two having a 500-mL capacity. Auxiliary vessels include a water-presaturation vessel for each reaction vessel, centrifuge tubes to contain pH buffers or other standard solutions, and two 0.95-L (1-qt) jars for aging (presoaking) solids. Water is used for the bath filling, and constant temperature is maintained by an electronic regulating system. Provision is made in the reaction vessels for in situ electrode measurements and for removing solution samples for chemical analysis.

Gases are led from storage cylinders through a series of gas scrubbers (not shown, as they are optional and depend on the type of gas used) to a gas-selector board which consists of five Whitey Micro-Regulating valves (1RS4–A). Each valve controls a vertical row of five Swagelok quick-connect body assemblies. Each row is independent and may be fed by a different gas. The stem parts of the connectors (double end shut-ofi type) are connected by vinyl tubing to one of five (per bath) Nupro fine metering valves (B–4MG) fitted with micrometer knobs. Each of these valves controls the flow rate to one of the five presaturator vessels in the main bath. Each presaturator vessel is made from a 500-mL polypropylene graduate cylinder to which a lid, having a filling port and attached inlet and outlet tubes, is welded. The vessel is welded into the top of the water-bath tank. The gas is bubbled through the water in the presaturator vessel by use of a linear polyethylene frit welded onto a long, 7.9-mm (5/16-in)-diameter[1] polypropylene inlet tube welded to the vessel lid.

The presaturation vessel is attached to the reaction vessel by a short length of polypropylene tubing. Gas is bubbled under the surface of the experimental solution by a linear polyethylene gas-dispersion frit

[1] All tubing used in the construction is 7.9 mm (5/16 in) in diameter. All connections between tubing on or about the water bath are made by using 7.9-mm (5/16-in) polypropylene elbow fittings. Unless specifically mentioned, the tubing and connectors are all of this type.

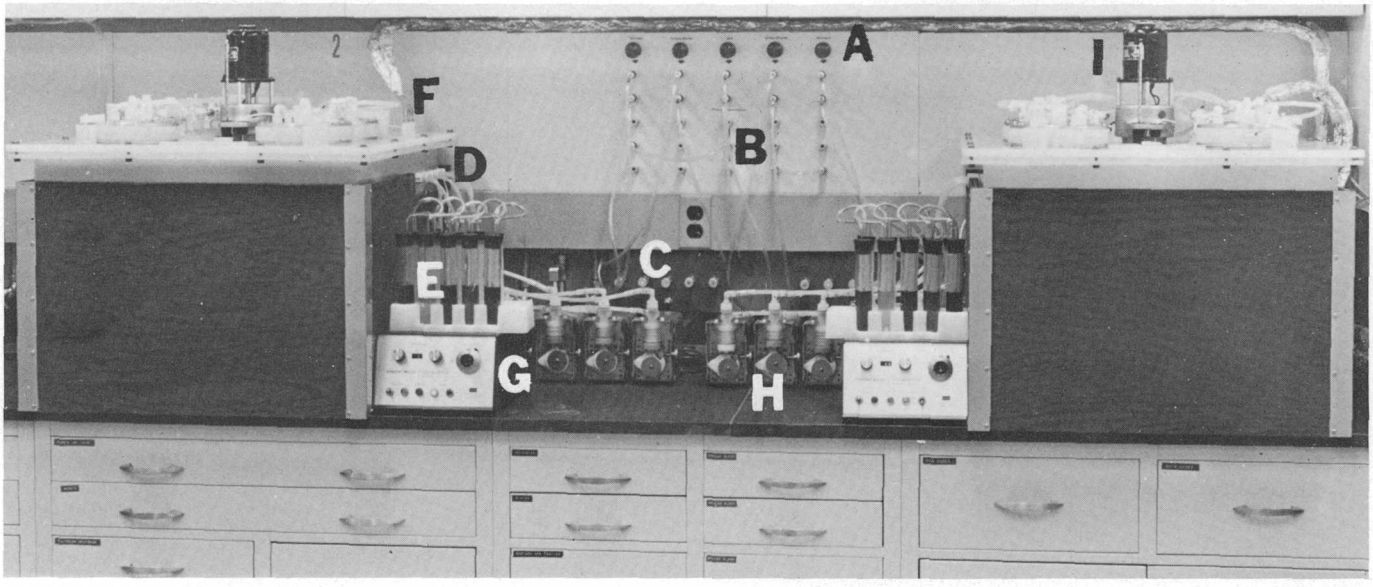

FIGURE 2.—Overall view of bath assembly. *A*, Coarse-valve assembly. *B*, Gas selector board. *C*, Fine metering valves. *D*, Inlet to bath from pumps. *E*, Condensate and bubbler tubes. *F*, External cooling fluid inlet. *G*, Temperature controller. *H*, Pumps. *I*, Heater-stirrer assembly.

welded to a polypropylene tube (protruding 229 mm into the reaction vessel), which in turn is welded to the reaction-vessel lid (fig. 3). The three large reaction vessels are constructed from cylindrical polypropylene plating tanks having a length of 229 mm (9 in) and an outside diameter of 121 mm (4¾ in). The bottom of the tank is cut away, and a shortened heavy-walled polypropylene funnel is welded to the tank (fig. 4). The shortened stem of the funnel is threaded to accept an elbow-tube fitting. A 3.2-mm (⅛-in)-high groove is cut into the inside diameter near the base of the funnel and holds a linear polyethylene frit disc. A 31.75-mm (1¼-in) rim, cut from 12.7-mm (½-in) polypropylene plate, is welded to the top of the vessel. The reaction-vessel lid, also cut from 12.7-mm (½-in) polypropylene plate, has a series of concentric V-shaped grooves machined on the under surface near the perimeter. The protruding crests of these grooves, along with a gasket cut from a sheet of vinyl plastic, form a gas seal when the lid is attached to the vessel rim by six stainless steel screws through two heavy aluminum rings (fig. 4). The metal rings (one under the rim and the other on the lid) provide purchase for the screws and prevent warping of the vessel. In addition to the inlet tube from the presaturator vessel, the reaction-vessel lid has two short lengths of polypropylene tubing welded in place to allow gas connection to the pump and the outside atmosphere. The pump access tube is shielded from splatter by one-half of a small polypropylene funnel (minus the stem) welded to the bottom of the lid so that the funnel half faces the center of the vessel. Electrode and sampling access ports are formed by welding 18- and 50-mL (bottoms cut off) centrifuge tubes onto the center of the lid. These ports are capped by rubber stoppers or polyethylene penny-stoppers.

The gas pumps for the bath system can take one of two forms. In the early version of this apparatus, the pumps were constructed of polyethylene bellows and two check valves. The pumps were mounted on a rack and were driven by a cam-rocker arm assembly. The later version uses commercially available bellows pumps (Gorman-Rupp Bel O Just Model). The flow rate for both is 1–2 L/min, and the rate can be increased by operating two or more pumps in parallel. From the pump, the gas is routed through the side of the main bath assembly (through a bulkhead-type fitting) to 15.24 m (50 ft) of polypropylene tubing within the bath (for heat exchange), and finally to the bottoms of the respective reaction vessels.

The main water-bath vessel is a commercially available polypropylene tank having 12.7-mm (½-in)-thick walls. The tank has internal dimensions of 609.6 × 609.6 ×457.2 mm (24 × 24 × 18 in) and a fluid capacity of 170 L. The tank is fitted into a box made of 12.7 mm (½-in)-thick plywood. The box provides structural support to the tank, and at high temperature the box also provides thermal insulation. The bath lid, which is cut from 12.7-mm (½-in) polypropylene plate, is mated to the tank by means of

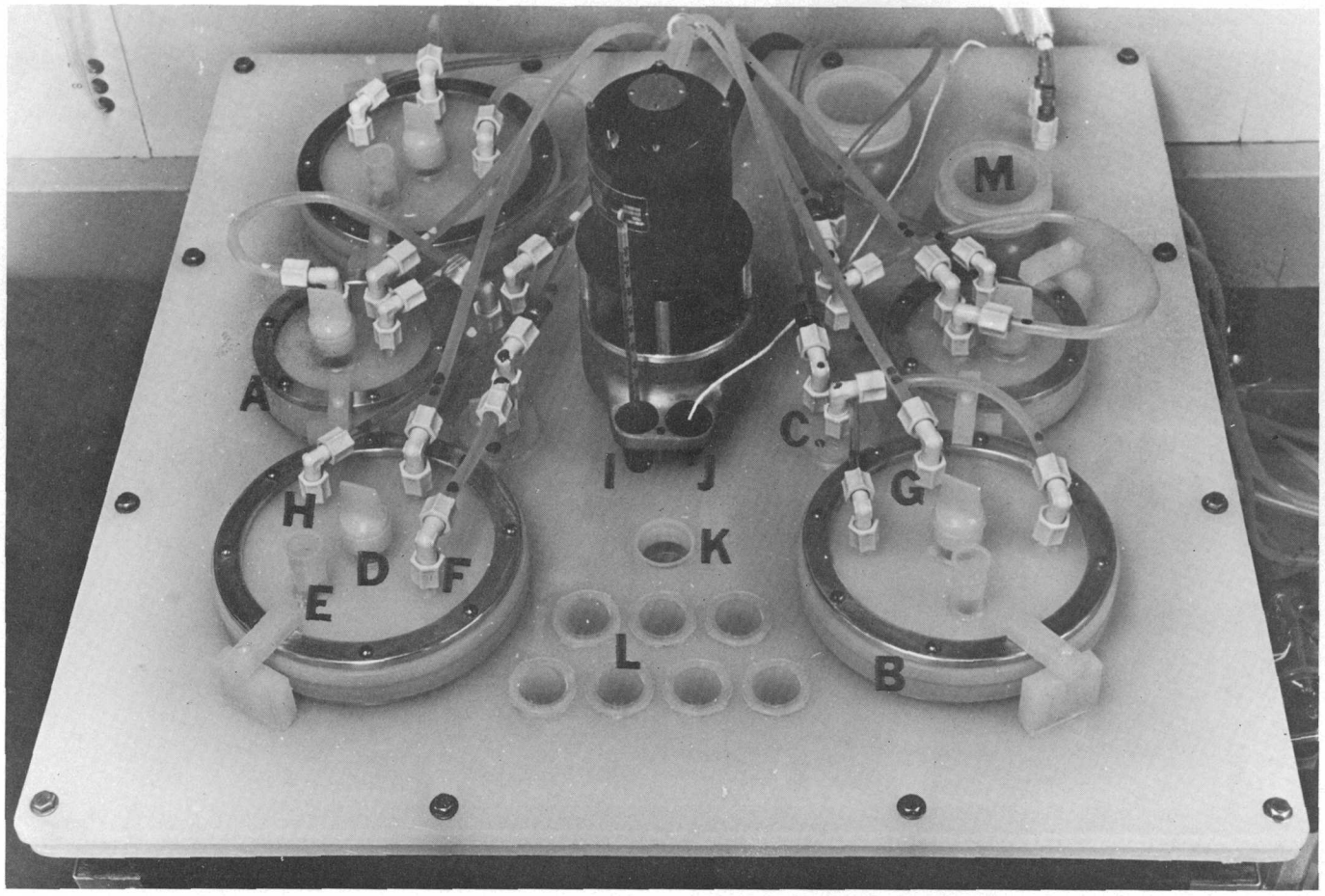

FIGURE 3.—Details of the water bath. *A*, Small reaction vessel. *B*, Large reaction vessel. *C*, Presaturator. *D*, Electrode port. *E*, Sampling port. *F*, Gas inlet tube. *G*, Gas outlet to pump. *H*, Gas outlet to bubbler. *I*, Thermometer. *J*, Thermistor. *K*, Bath-filling hole. *L*, Buffer tubes. *M*, Solution storage jar.

stainless steel nuts and bolts and a gasket of silicone-rubber caulking compound. Six holes are cut in the lid to accommodate the five reaction vessels and the heater-stirrer unit. The reaction vessels are not welded to the lid (in order to facilitate removal for cleaning) but are held down by two swing-aside clamps. Seven 100-mL centrifuge tubes are welded into the lid (fig. 3) and serve as pH-buffer and standard-solution containers. Two 0.95-L (1-qt) polypropylene mason jars are welded into the lid to provide a place to store solutions or to presoak solid phases at the bath temperature. Also, three 25.4-mm (1-in)-diameter holes are bored in the bath lid to provide access for the temperature-sensing element, a thermometer, and bath filling. Provisions have been made in the later water baths for bubbling a gas directly into the bath water, if desired, by welding to the bath top a polypropylene tube which has an attached gas-dispersing frit.

The gas bled off of the reaction vessels is led to two 100-mL polycarbonate centrifuge tubes. The first tube in line is for retaining the condensed water that is removed from the reaction vessel by the gas. The second tube is partially filled with water, and the inlet tube extends below the surface. This acts as a bubbling tube and allows visual monitoring of the gas-flow rate.

The heater-stirrer assembly (Sargent P–6495) sits on the top of the water bath (fig. 2) and is composed of a propeller-type stirrer and three 500-watt heating elements enclosed in a perforated stainless steel cylinder extending down into the bath. The stirring motor assembly was modified to allow the motor to sit (on spacers) 50.8 mm above its collar. The resulting air space prevents hot water vapor from entering the motor. Temperature is controlled by a Sargent (Model ST) Thermonitor unit and a thermistor sensing element. To operate the water bath at room temperature or below, a 15.24-m (50-ft) copper heat-exchanger coil is provided in the main bath vessel. Cool tap water or a refrigerated solution can be circulated

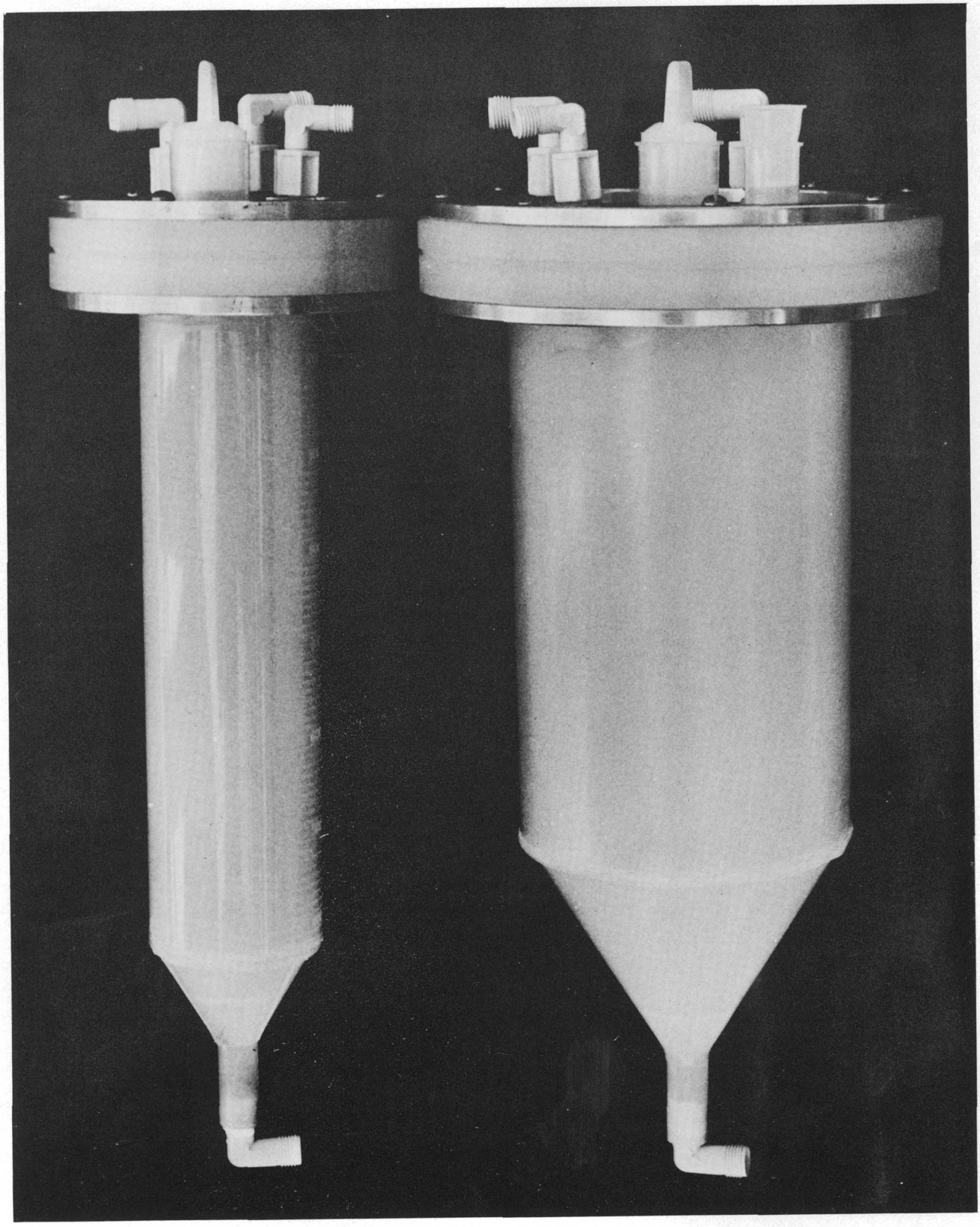

FIGURE 4.—Close-up of both a large and small reaction vessel.

in this coil, depending on the desired operating temperature.

OPERATION OF THE BATHS

Two of these water baths were operated extensively at the University of Missouri at Columbia during bicarbonate ion-pairing studies (W. R. Almon, J. E. Bauman, Jr., P. B. Hostetler, D. L. Leach, and R. M. Siebert, unpub. data, 1976; Siebert and Hostetler, 1977). For this type of short-term experimental work, the main bath temperature was found to vary by approximately ±0.02°C in 24 h. Unfortunately, the temperature of the solution within the reaction vessel was a few tenths of a degree lower than the main bath temperature because of the thermal resistance of the vessel walls. Also, the temperature varied because of additions of reagents. Because the temperature control in ion-pair-equilibria work must be precise, a small immersion heater (and heat-exchange coil), having its own thermistor and regulator, was added to the reaction-vessel lid. This unit maintained the reaction-vessel temperature to within ±0.05°C of the desired value. Experience indicates that the long-term variation in temperature within the reaction vessel is approximately ±0.2°C, less with occasional monitoring and adjustments.

The gas system of this apparatus allows extremely rapid equilibration between the gaseous and aqueous phases. In addition, if the system is perfectly gas tight, the equilibrium activity of the gas is very constant. As an experiment, several grams of solid potassium bicarbonate were added to 1800 mL of distilled water in a large reaction vessel. Then, pH electrodes were sealed into the system, the pumps were started, and the flow of pure CO_2 gas was begun. The measured pH stabilized within 5 min. This time is more indicative of the time required to displace air from the gas system. Subsequent additions of potassium bicarbonate (in aqueous solution injected into the reaction vessel by syringe) required less than 30 s for the pH to stabilize. After one addition, the pH was monitored for 18 h, and it remained constant within ±0.005 pH units during that time interval.

REFERENCES CITED

Hostetler, P. B., and Christ, C. L., 1968, A temperature-controlled water bath for mineral solubility studies: U.S. Geol. Survey Prof. Paper 600–D, p. D217–D221.

Siebert, R. M., and Hostetler, P. B., 1977, The stability of the magnesium bicarbonate ion pair from 10°C to 90°C: Am. Jour. Sci. (In press.)

Jour. Research U.S. Geol. Survey
Vol. 5, No. 5, Sept.–Oct. 1977, p. 603–607

PRESSURE CORRECTIONS FOR FLUID-INCLUSION HOMOGENIZATION TEMPERATURES BASED ON THE VOLUMETRIC PROPERTIES OF THE SYSTEM NaCl–H_2O

By ROBERT W. POTTER II, Menlo Park, Calif.

Abstract.—A series of pressure correction diagrams for 1-, 5-, 10-, 15-, 20-, and 25-percent NaCl solutions has been generated from the volumetric data for NaCl by R. W. Potter II and D. L. Brown in 1975. The diagrams cover the temperature range from 20° to 400°C at pressures up to 200 megapascals (2000 bars). These data can be used to correct fluid-inclusion homogenization temperatures for pressures greater than the liquid-vapor pressure-temperature curve.

Studies of fluid inclusion homogenization temperatures have yielded valuable information with respect to the temperature of many geologic processes, in particular formation temperatures of ore deposits. Homogenization temperatures have long been recognized as representing the true temperature of entrapment of the fluid inclusion, provided the pressure did not exceed the equilibrium vapor pressure of the solution (Ingerson, 1947). If the pressure at the time of entrapment is higher than the equilibrium vapor pressure, then an appropriate temperature correction based on the volumetric properties of the solution in the fluid inclusion is required to obtain the true temperature of entrapment. The resulting corrections can be several hundred degrees; hence, volumetric data for inclusion solutions are of great practical significance.

Prior to this study, there were two major sources of data for making pressure corrections. The data of Lemmlein and Klevtsov (1961) are for sodium chloride solutions up to 30 percent NaCl at temperatures from 150° to 500°C and pressures of 1750 atm. The other source is the presentation by Fisher (1976) of the volumetric data of water in a graphical form for temperatures up to 1000°C and pressures as high as 1000 MPa (10 000 bars). Both of these data sets have some inherent difficulties that preclude their use in certain temperature, pressure, and composition ranges. This paper therefore presents a consistent set of graphical data that will allow for the correction of homogenization temperatures up to 400°C and confining pressures as high as 200 MPa (2000 bars).

The volumetric data for aqueous sodium chloride solutions have been compiled (Potter and others, 1975) and evaluated by a weighted least-squares regression (Potter and Brown, 1975). These data were used to generate graphs of temperature correction (ΔT) versus homogenization temperature for aqueous NaCl solutions (figs. 1–6). During the regression of the data, it was noted that the data of Lemmlein and Klevtsov (1961) were inconsistent with much more precise volumetric data below 200°C as well as being inconsistent with the precise P-T data for the vapor-saturated liquid. The uncertainties of the NaCl density data (Potter and Brown, 1975) are such that the ΔT values have an uncertainty of ± 3°C.

The graphs (figs. 1–6) can be used to correct homogenization temperatures, provided that the composition of the fluid inclusions and the pressure at the time of entrapment can be estimated. Fluid inclusions generally do not contain only NaCl but also various salts in solution (Roedder, 1972). However, a reasonable approximation of the equivalent NaCl content can be obtained from the freezing temperatures, and this approximate composition can be used as an estimate of the composition for the purposes of correcting the homogenization temperatures (Haas, 1971).

Table 1 compares several points from the two previous data sets for pressure corrections and the data set used to generate figures 1–6. Lemmlein and Klevtsov (1961) represent their data in a graphical form of ΔT versus homogenization temperature, which can only be read with a precision of ± 10°C; therefore, the data in table 1 were generated from least-squares regression of their smoothed tabulated data. The discrepancies at 150°C result from a systematic error below 200°C in the data of Lemmlein and and Klevtsov (1961). The discrepancies between Lemmlein and

TABLE 1.—*Comparison of pressure corrections from different publications*

[ΔT, correction in temperature; H. T., homogenization temperature]

Percent NaCl	ΔT(°C) for H.T. = 150°C P = 1,000 bars[a]		ΔT(°C) for H.T. = 250°C P = 1,000 bars[a]		ΔT(°C) for H.T. = 400°C P = 1,000 bars[a]	
b_0	b_{56}		b_{71}		---	
1	---	84	---	84	---	130
5	79	85	86	83	154	121
10	74	90	92	90	104	102
15	87	97	92	94	91	99
20	87	100	96	99	87	93
25	87	91	89	94	86	103

[a]Left-hand column from Lemmlein and Klevtsov (1961); right-hand column, this study.

[b]Data for pure water from Fisher (1976).

Klevtsov and this study at 400°C and 5 percent NaCl are due to the closeness of the critical point, 428°C (Marshall and Jones, 1974), where Lemmlein and Klevtsov's experimental technique becomes imprecise. The differences in the data at 15, 20, and 25 percent NaCl are due to extrapolations of imprecise data by Lemmlein and Klevtsov. Using the water data of Fisher (1976) for concentrated brines would result in corrections that are too low (table 1).

Therefore, considering the difficulties in the previous data sets, such as data only for pure H_2O (Fisher, 1976), systematic errors in the NaCl–H_2O density data, lack of data below 150°C, and an uncertainty in the data presentation of ±10°C (Lemmlein and Klevtsov, 1961), the graphical portrayal of ΔT versus homogenization temperature of NaCl solutions presented in this paper are the most reliable and extensive data set available for pressure corrections. The graphical presentation of Fisher (1976) for pure water and the NaCl solution data given here provide a complete set of diagrams for correcting fluid inclusion homogenization temperatures for compositions ranging from 0 to 25 percent NaCl up to 400°C and 200 MPa.

REFERENCES CITED

Fisher, J. R., 1976, The volumetric properties of H_2O—A graphical portrayal: U.S. Geol. Survey Jour. Research, v. 4, no. 2, p. 189–194.

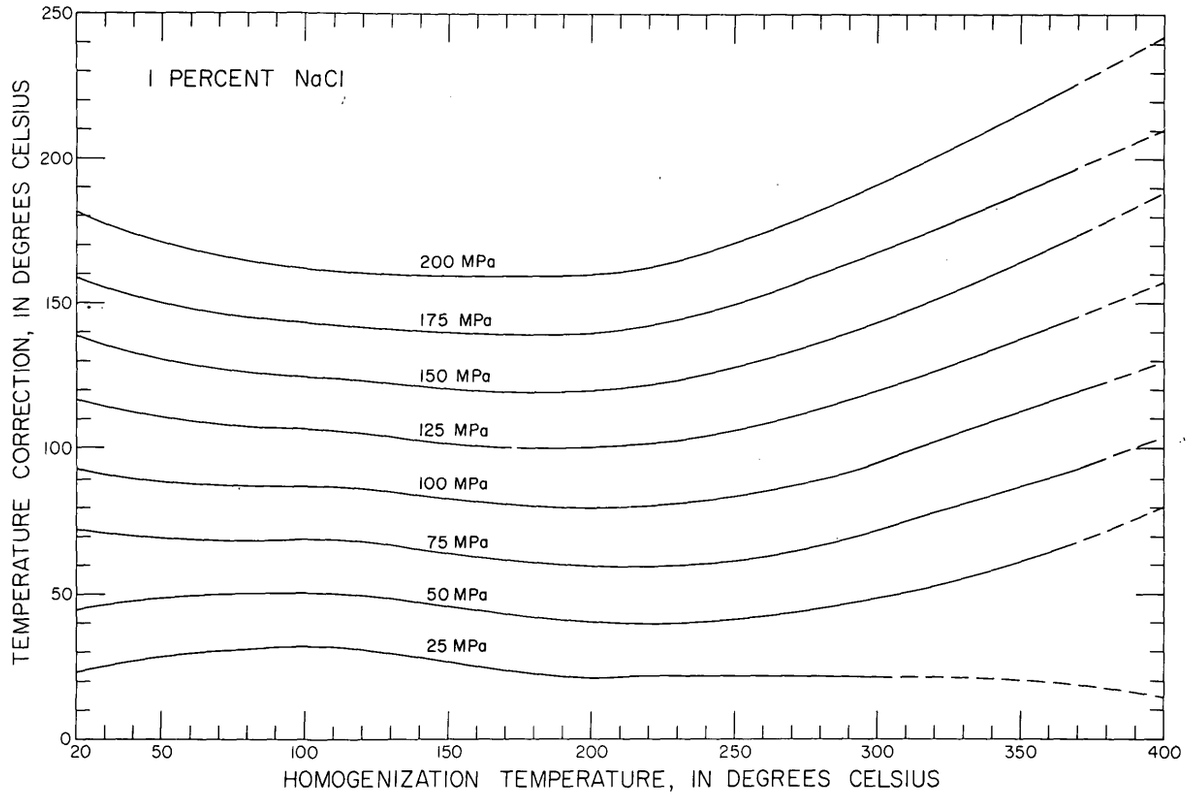

FIGURE 1.—Temperature correction for a 1-percent NaCl solution as a function of homogenization temperature and pressure.

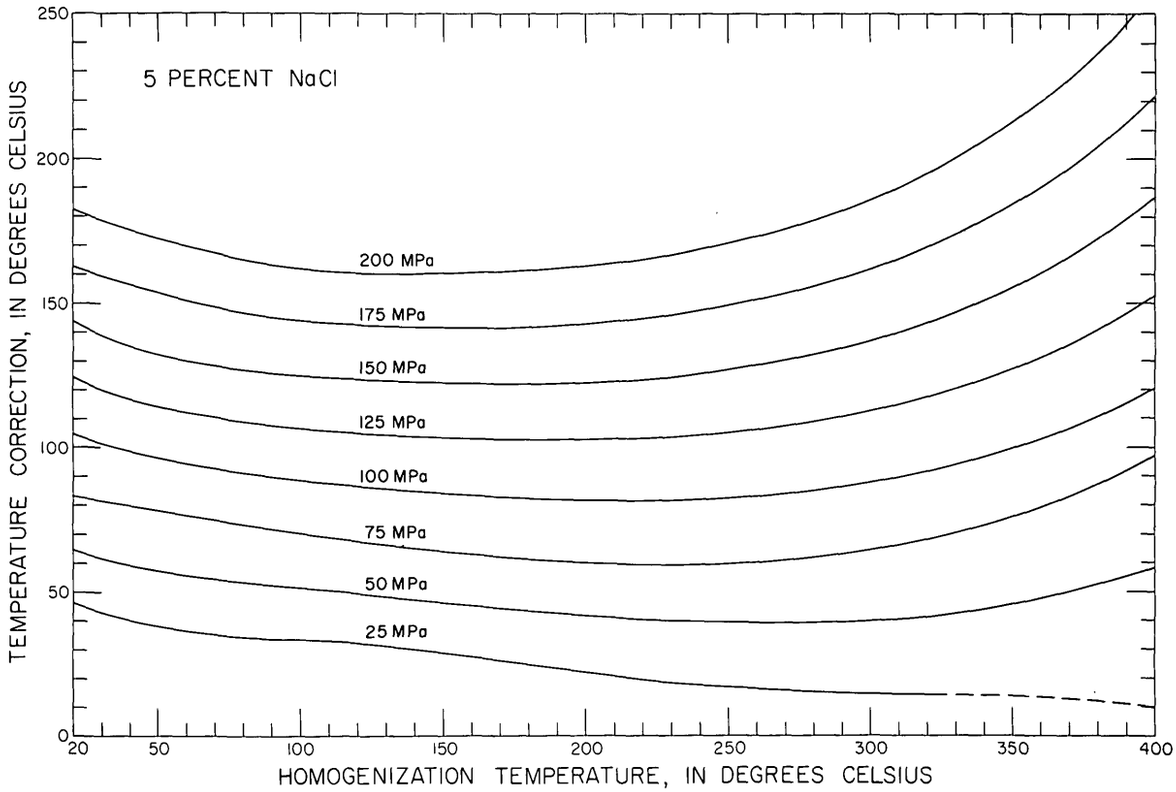

FIGURE 2.—Temperature correction for a 5-percent NaCl solution as a function of homogenization temperature and pressure.

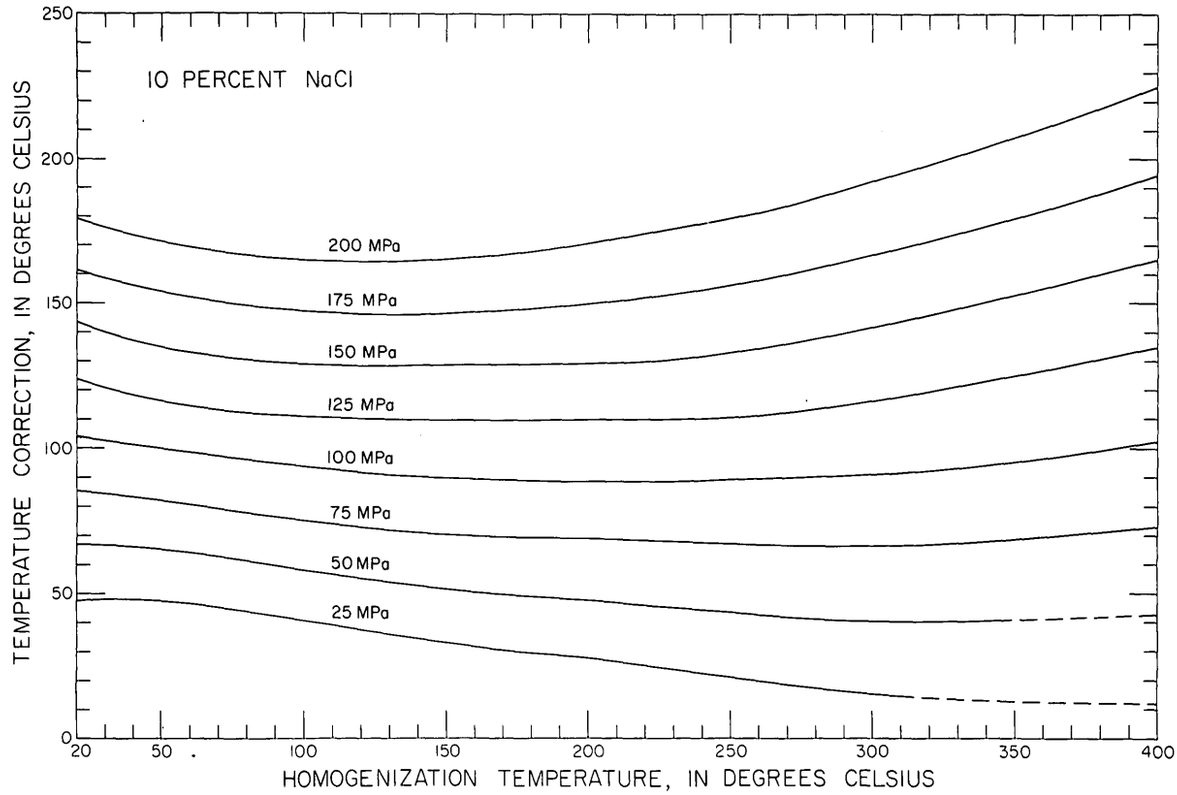

FIGURE 3.—Temperature correction for a 10-percent NaCl solution as a function of homogenization temperature and pressure.

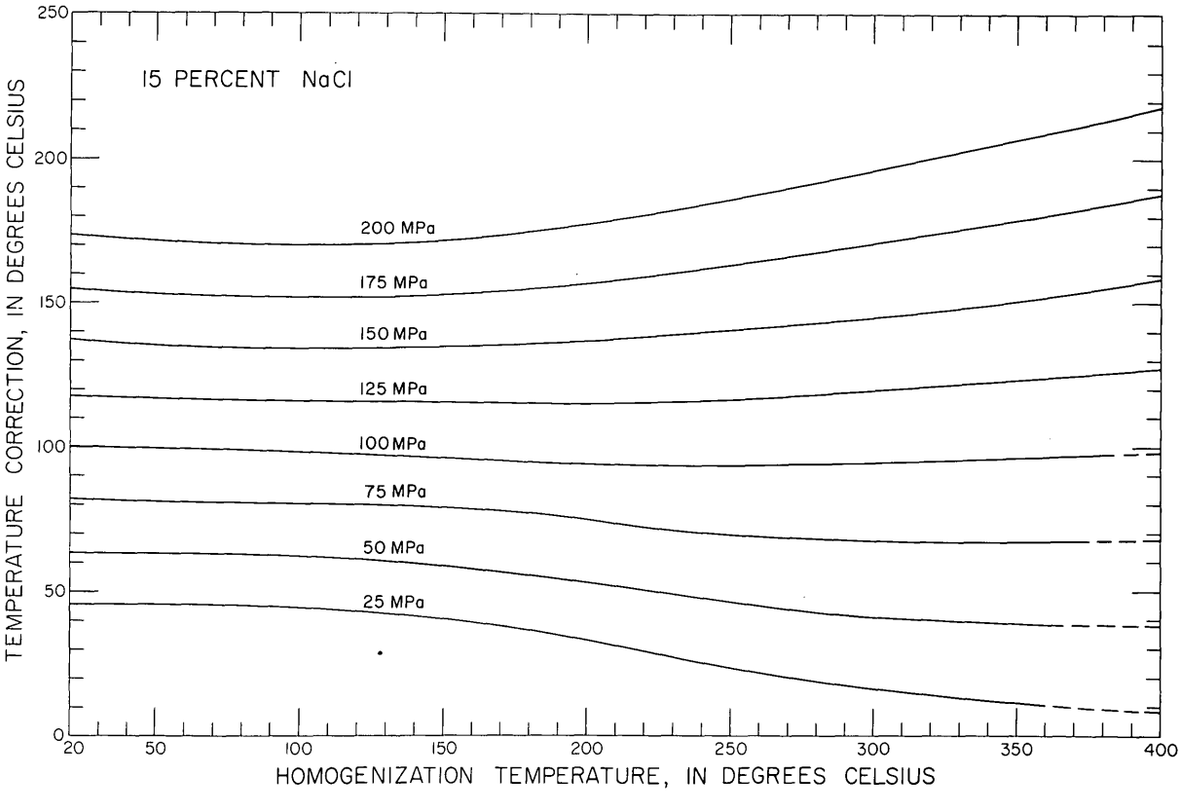

FIGURE 4.—Temperature correction for a 15-percent NaCl solution as a function of homogenization temperature and pressure.

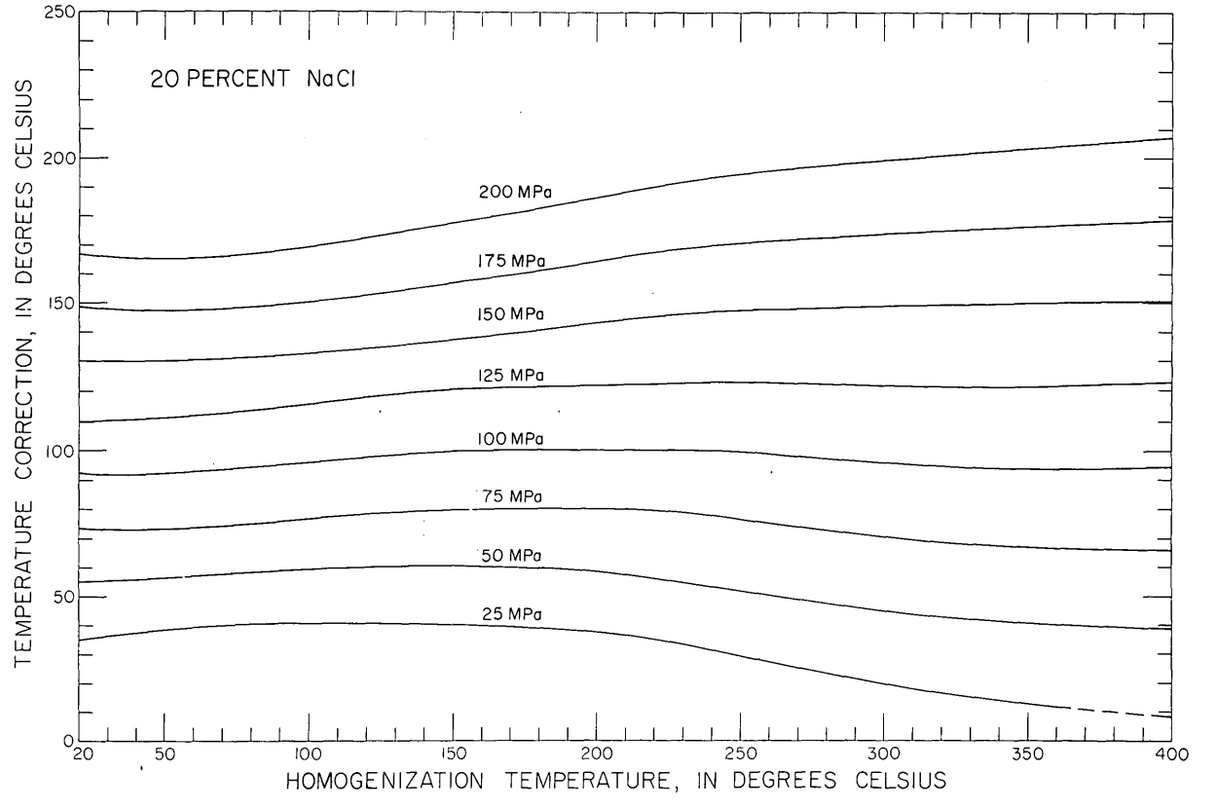

FIGURE 5.—Temperature correction for a 20-percent NaCl solution as a function of homogenization temperature and pressure.

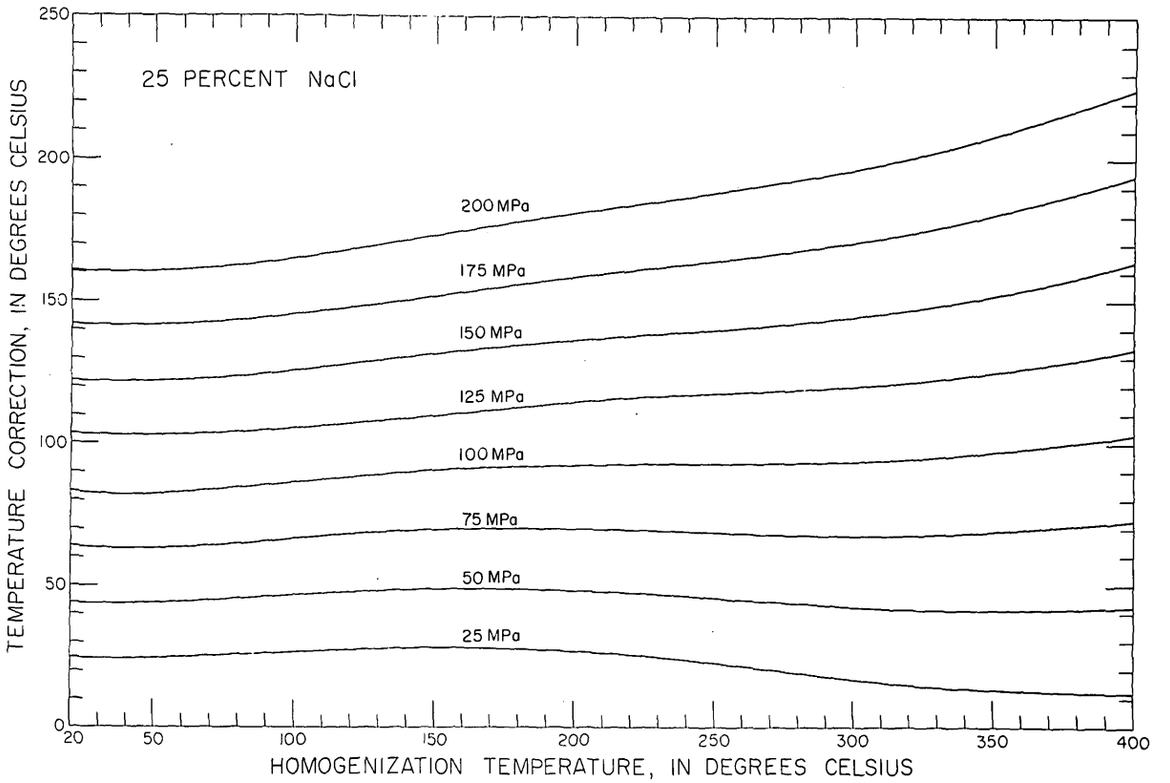

FIGURE 6.—Temperature correction for a 25-percent NaCl solution as a function of homogenization temperature and pressure.

Haas, J. L., Jr., 1971, The effect of salinity on the maximum thermal gradient of a hydrothermal system at hydrostatic pressure: Econ. Geology, v. 66, p. 940–946.

Ingerson ,Earl, 1947, Liquid inclusions in geologic thermometry: Am. Mineralogist, v. 32, p. 375–388.

Lemmlein, G. G., and Klevtsov, P. V., 1961, Relations among the principal thermodynamic parameters in a part of the system H_2O–NaCl (in Russian): Geokhimiya, 1961, p. 133–142.

Marshall, W. L., and Jones, E. V., 1974, Liquid-vapor critical temperatures of aqueous electrolyte solutions: Jour. Inorganic and Nuclear Chemistry, v. 36, p. 2313–2318.

Potter, R. W., II, and Brown, D. L., 1975, The volumetric properties of aqueous sodium chloride solutions from 0° to 500°C at pressures up to 2000 bars based on a regression of the available literature data: U.S. Geol. Survey open-file report, 31 p.

Potter, R. W., II, Shaw, D. R., and Haas, J. L., Jr., 1975, Annotated bibliography of studies on the density and other volumetric properties for major components in geothermal waters 1928–74: U.S. Geol. Survey Bull. 1417, 78 p.

Roedder, Edwin, 1972, Composition of fluid inclusions: U.S. Geol. Survey Prof. Paper 440–JJ, 164 p.

Jour. Research U.S. Geol. Survey
Vol. 5, No. 5, Sept.–Oct. 1977, p. 609–621

EXPLORATION GEOCHEMICAL STUDIES OF SOME SANDSTONE COPPER-URANIUM DEPOSITS, BRADFORD, COLUMBIA, AND LYCOMING COUNTIES, PENNSYLVANIA

By F. G. LESURE, J. M. MOTOOKA, and P. L. WEIS,
Reston, Va., Denver, Colo., Reston, Va.

Abstract.—Semiquantitative spectrographic analyses of mineralized and unmineralized sandstone, siltstone, and claystone from the Catskill Formation of Devonian age in Bradford, Columbia, and Lycoming Counties, Pa., suggest that copper, silver, and uranium are the principal metallic elements concentrated in the mineralized rock. Lead, mercury, and molybdenum may be concentrated slightly in mineralized rock but values are too low to be of use in exploration. The deposits are too small to make large anomalies in stream sediments except in drainage basins of less than a few acres. However, if a large deposit were exposed to weathering, it would probably be detectable by stream sediment sampling. Analyses of oxalic acid leachates of the minus 80-mesh fraction of the stream-sediment samples gave more useful values than analyses of the minus 80-mesh samples in separating drainage basins that have copper deposits from those that have no known copper deposits.

Small deposits of copper minerals in the Catskill Formation of Devonian age in Pennsylvania have been known, and some have been worked since the middle of the 19th Century (Weed, 1911, p. 59). Renewed interest in the deposits because of their uranium content led to studies by the Pennsylvania State Geological Survey in 1956–57 (McCauley, 1961) and the U.S. Geological Survey in 1953–54 (Klemic, 1962). On October 1 and 2, 1974, we made a reconnaissance of a few of the more easily accessible deposits in the New Albany, Beaver Lake and Grassmere Park areas, Bradford, Columbia, and Lycoming Counties, Pa. (fig. 1) as orientation studies for a mineral-resource evaluation of a proposed wilderness area in Virginia that contains rocks of the Hampshire Formation of Devonian age. The Hampshire and Catskill Formations are correlative lithologic and stratigraphic units. Both contain red and greenish-gray sandstones and shales, but only the Catskill has any known copper mineralization. Our reconnaissance was an attempt to find out what trace elements are associated with the copper in the Catskill and what metals are contributed by small sandstone copper deposits to stream sediments in order to evaluate geochemical sampling in the Hampshire Formation (Lesure and others, 1977).

Twenty-one samples (table 1) of mineralized and unmineralized rock from 8 prospect areas and 30 stream-sediment samples (table 2) from nearby streams were collected (figures 2, 3, and 4). All the samples were analyzed in the laboratories of the U.S. Geological Survey in Denver, Colo., and the results are reported here as an example of what trace elements are associated with this type of sandstone copper-uranium deposit. In addition to analyzing the normal minus 30-mesh fraction of the stream sediments, we also analyzed an oxalic acid leachate of the minus 80-mesh material. These leachate samples provide a more selective look at metals tied up in iron and manganese oxide coatings on sediment grains.

The stream-sediment sampling near and at a distance from eight known mineral occurrences indicates that mineral deposits of the size investigated do not contribute anomalously large quantities of copper to stream sediments more than a few tens of meters from the outcrop. The occurrences sampled are believed to contain only a few hundred pounds of copper, but nevertheless in this environment they add small but detectable amounts of copper to stream sediments. We infer that large deposits exposed to surface weathering are likely to produce anomalies of sufficient size to be readily detected in stream sediments. The leachate samples appear to be better than the normal minus 80-mesh fractions in distinguishing drainages that contain copper deposits from those that do not.

GEOLOGY

The copper deposits are in the lower part of the Catskill Formation of Devonian age (McCauley, 1961, p. 17–18). The rocks are nearly flat lying, interlayered red and greenish-gray sandstones, siltstones, and mud-

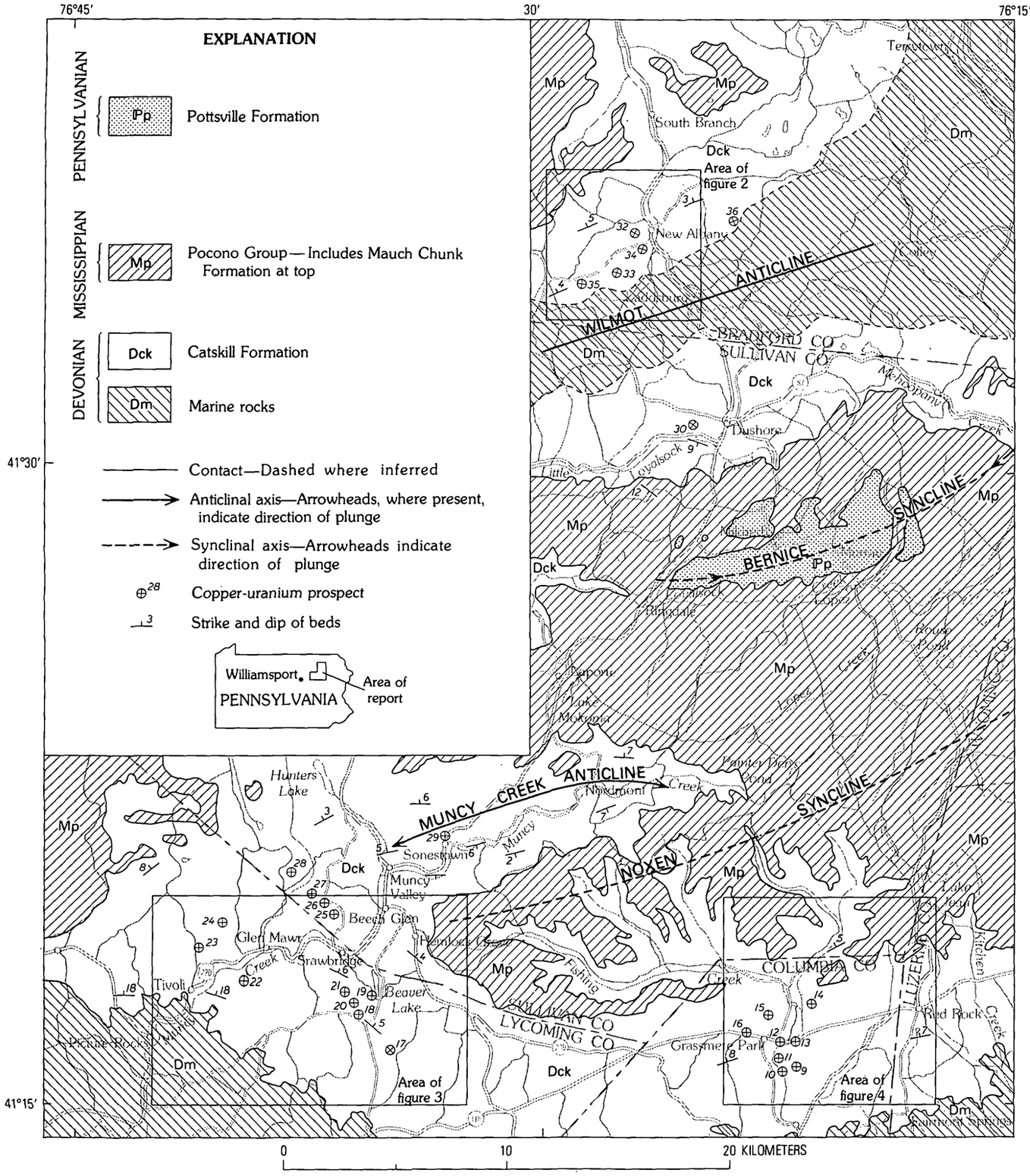

FIGURE 1.—Geologic map of New Albany, Beaver Lake, and Grassmere Park areas. Modified from McCauley (1961, fig. 7).

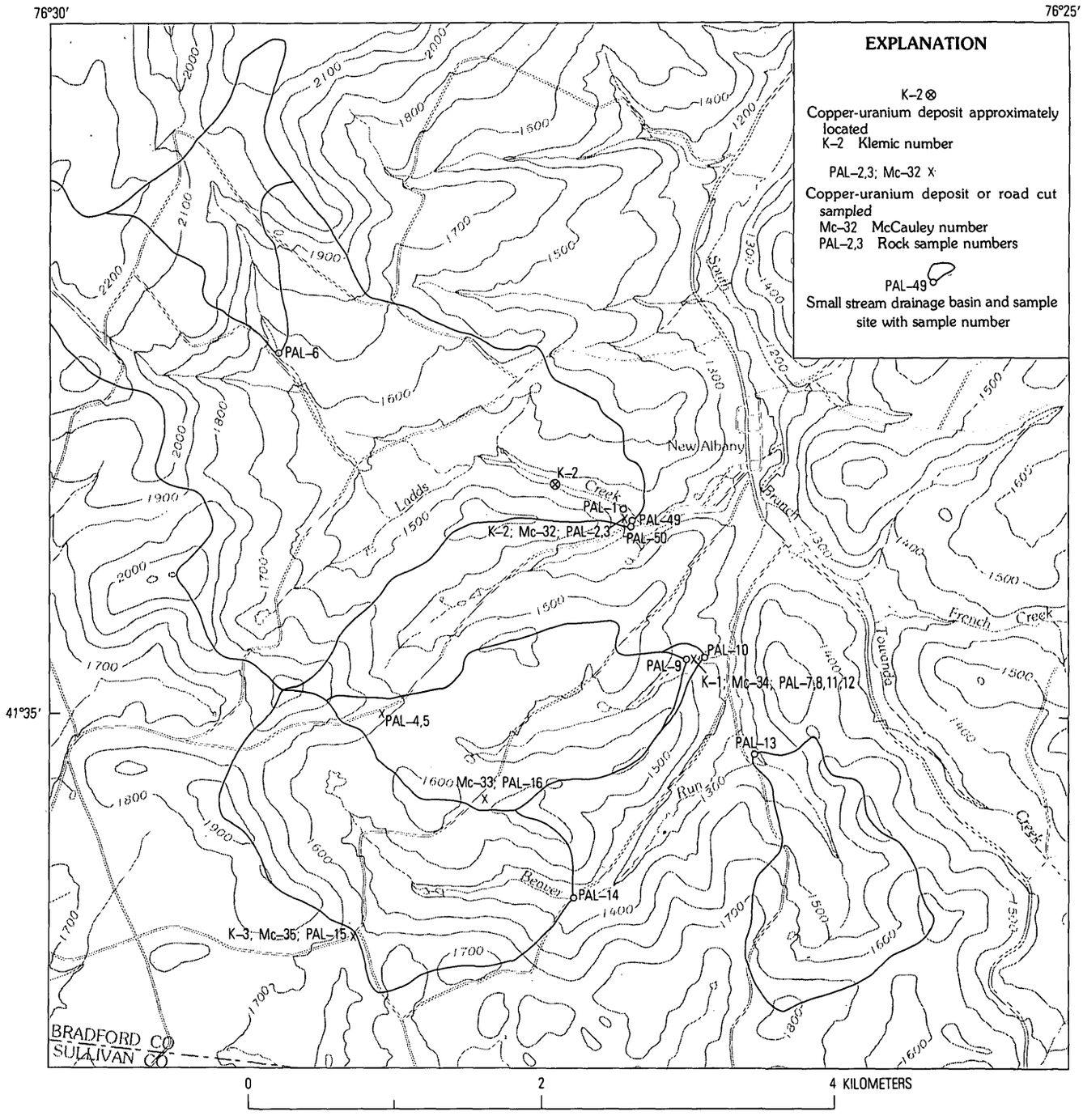

FIGURE 2.—Sample location map of New Albany area, Bradford County, Pa. Contours given in feet (1 foot=0.3048 meter).

stones. The sandstones are fine- to medium-grained mixtures of quartz, feldspar, and mica. Some red shaly beds contain small crystals of gypsum. Calcite is a minor accessory mineral or cement. The mica is generally muscovite, and the flakes are bent around sand grains indicating that the mica is of detrital origin. Greenish-gray beds generally contain recognizable stems and other plant fragments. Some of the plant material is now thin coaly seams; some is represented by impressions only, the organic material having been completely removed during diagenesis.

The area is in the Allegheny Plateau where geologic structures are broad and of low relief. A series of northeast-trending anticlines and synclines is in the vicinity of the three prospect areas (fig. 1). Bedding dips gently to the north or south, commonly less than

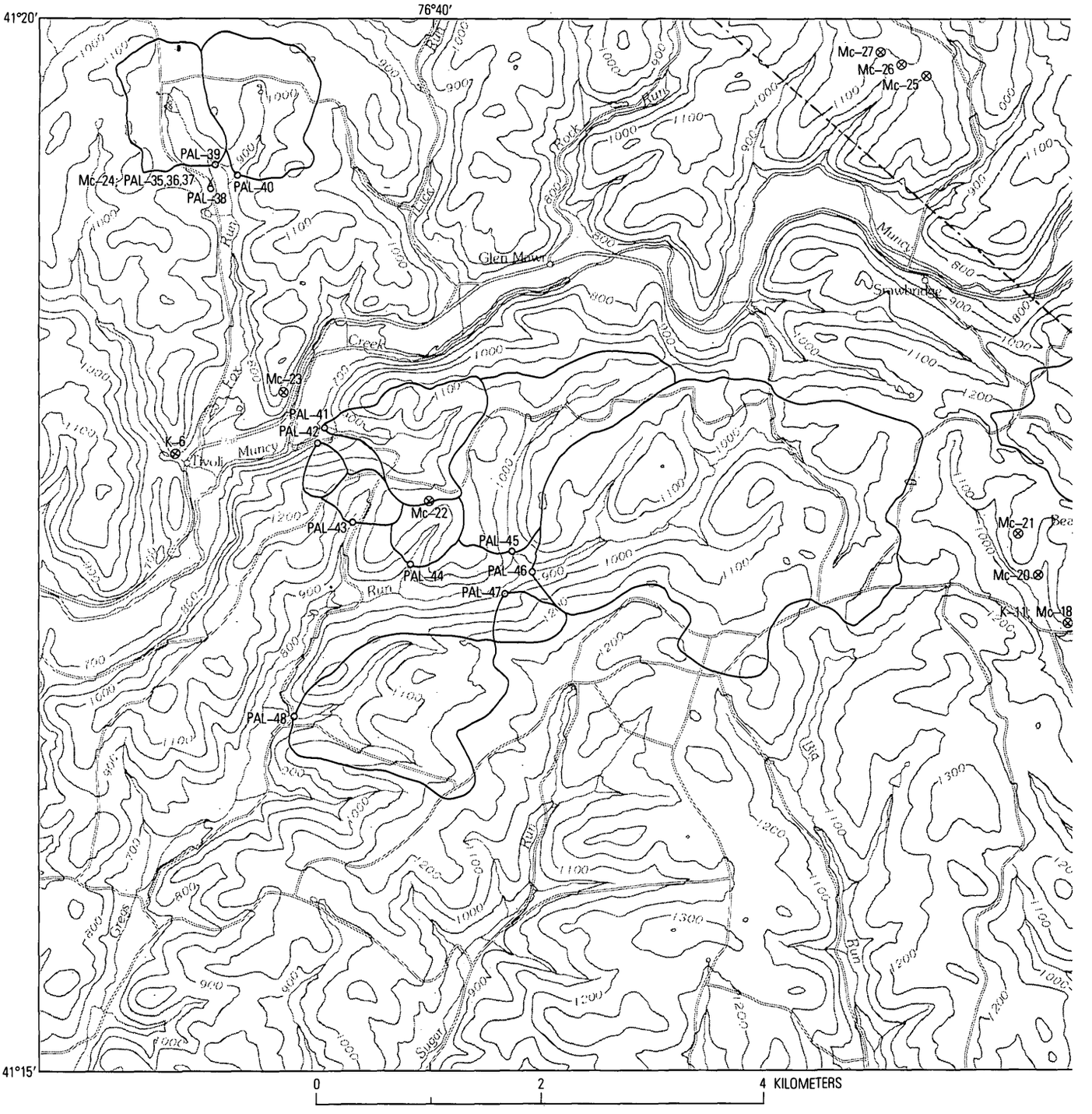

FIGURE 3.—Sample location map of Beaver Lake area, Lycoming

10 degrees. No major faulting is known in the prospect areas (McCauley, 1961, p. 20–23).

Copper minerals are found in the greenish-gray beds in lens-shaped or tabular mineralized zones that are probably only a meter or so thick and generally less than 50 meters in length. Malachite and azurite are common on surfaces and cracks in the rock. Copper sulfide minerals including chalcocite, bornite, and chalcopyrite are scattered through the rock as small grains. Red beds contain no visible copper sulfides and only traces of copper as compared with the mineralized greenish-gray beds.

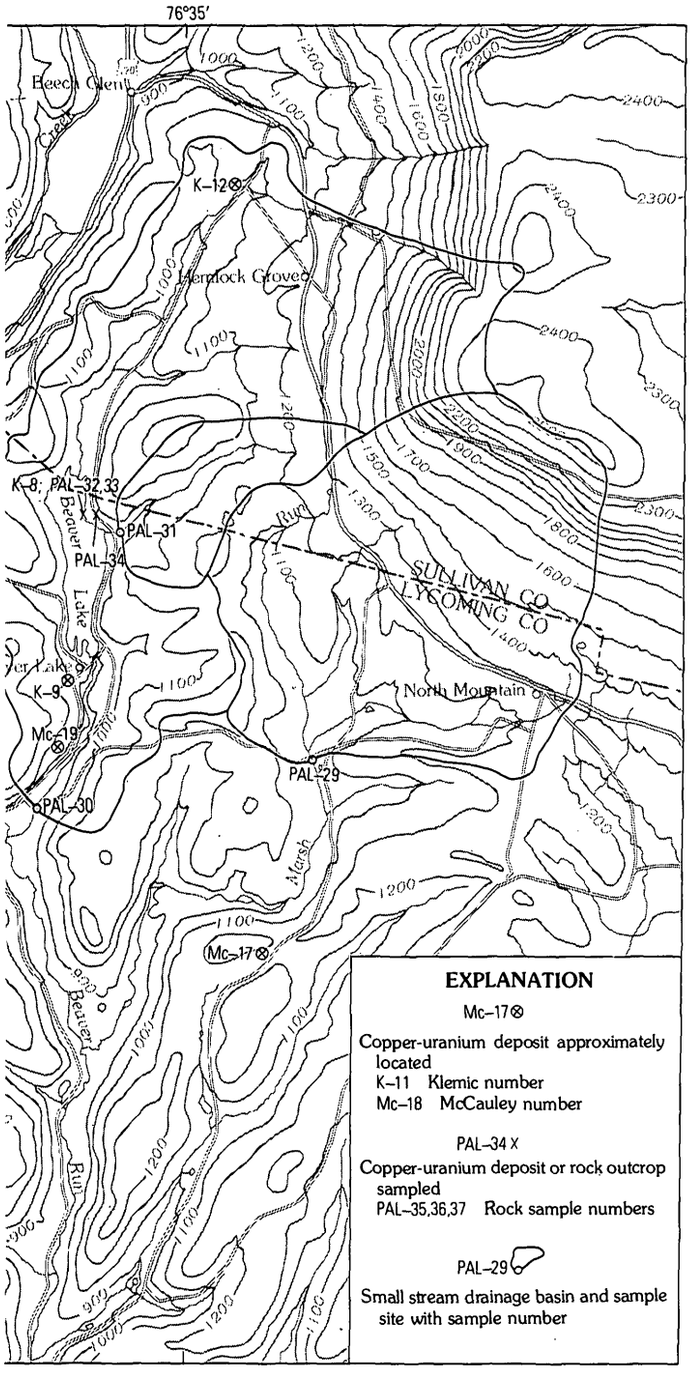

County, Pa. Contours given in feet (1 foot=0.3048 meter).

Uranium in these deposits is associated with carbonaceous material (McCauley, 1961, p. 23), but few of the uranium minerals are visible. McCauley (1961, p. 59) reported the secondary uranium minerals, metazeunerite and uranospinite, from one prospect (Mc 12, fig. 4) and Klemic (1962, p. 278–179) reported traces of yellow and green radioactive minerals from several prospects (K 11, fig. 3; K 14 and K 16, fig. 4).

Trace-element analyses for the greenish-gray and red sandstones and siltstone-mudstones are given in table 1. Silver is present in all copper-rich rock in amounts ranging from 0.5 to 20 parts per million. Gold was not detected in any samples. Mercury is present as a trace (0.02–0.09 ppm) in some of the rocks that are mineralized but is not detected in any of the red beds. Zinc content (32–86 ppm) is low in all samples, but gray rock tends to have a little more zinc (56–86 ppm) than red rock (32–86 ppm). Lead content of the mineralized gray rock is quite variable (20–7000 ppm) but is generally greater than in the unmineralized red beds (10–30 ppm). All seven samples that have detectable molybdenum (7–150 ppm) also have high copper (200–3000 ppm), but five samples that have high copper (500 to more than 20 000 ppm) have no detectable molybdenum. Red beds tend to have no more iron than greenish-gray beds but the finer grained rocks, mudstone-siltstone, appear to have more iron (3–5 percent) than the sandstones (1–3 percent).

STREAM-SEDIMENT SAMPLES

Thirty stream-sediment samples were collected; one is from as near as 3 m from a mineralized zone, nine are 15–2000 m from mineralized zones in the drainage area, and the rest are from drainage areas that have no known mineralized zones. The drainage basins range in size from about 0.4 to 875 hectares. The samples were collected from flowing streams and consist of several handfuls of the finest sediment that we could get, either from the bed of the stream or from recent overflow material along the bank of the stream.

Samples were air dried and screened to minus 80-mesh. Part of the minus 80-mesh fraction was analyzed by semiquantitative spectrographic methods for 30 elements, by atomic absorption methods for gold and zinc, and by instrument for equivalent uranium (eU). A split of the minus 80-mesh fraction was treated with oxalic acid, and the leachate was analyzed by semiquantitative spectrographic methods. The results of these analyses are reported in table 2.

The copper content of the minus 80-mesh fraction of the stream sediment samples ranges from less than 5 to 150 ppm. The distribution of copper values in the 30 samples is bimodal (fig. 5). The streams that drain areas of known copper occurrences contain 7 to 150 ppm copper (table 2). The two highest copper values are in sediments from exceptionally small drainages, about 0.4 ha, that include known copper prospects. Sample 38 is from a drainage ditch about 15 m from

TABLE 1.—*Trace-element analyses of rock samples from copper-uranium deposits and several nearby outcrops*

[For sample localities, see figures 2, 3 and 4. Chemical analyses by atomic absorption were made by G. L. Crenshaw; eU, equivalent uranium, instrumentation by Z. C. Stephenson. Uranium and thorium on five samples by delayed neutron methods by H. T. Millard and D. A. Bickford. Semiquantitative spectrographic analyses were made by J. M. Motooka. Results are reported to the nearest number in the series 1, 0.7, 0.5, 0.3, 0.2, 0.15, 0.1, which represent approximate midpoints of grouped data on a geometric scale. The assigned groups for the series will include the quantitative value about 30 percent of the time. The data should not

Sample	Semiquantitative spectrographic analyses																	
	Fe	Mg	Ca	Ti	Mn	Ag	B	Ba	Be	Co	Cr	Cu	La	Mo	Nb	Ni	Pb	Sc
Greenish-gray sandstone																		
[1]2	2	1.5	0.1	0.7	700	20	30	700	1.5	30	100	7000	50	N(5)	20	50	30	15
5	2	1	5	.7	5000	N(0.5)	20	500	1	15	50	20	30	N(5)	20	30	15	10
[3]15	2	.7	.1	.7	700	1.5	30	300	1	20	70	700	50	N(5)	L(20)	20	3000	10
23	1	.7	1	1	1500	N(0.5)	70	300	L(1)	15	70	30	70	N(5)	30	30	30	10
25	1.5	.7	1	1	1500	10	20	1000	L(1)	15	100	>20000	70	N(5)	L(20)	30	70	15
32	3	1	.1	1	500	3	50	500	1.5	20	100	200	70	15	20	50	700	15
35	1.5	.5	.07	.7	200	3	50	200	1.5	15	100	3000	50	150	20	30	2000	10
37	1.5	.7	1	.7	1500	7	50	200	1.5	15	70	3000	50	10	20	30	300	15
Grayish-red sandstone																		
3	2	1	0.5	0.7	2000	L(0.5)	30	2000	1	20	70	100	30	N(5)	20	30	10	10
24	1.5	.7	1	1	1500	N(0.5)	20	1000	N(1)	15	50	50	50	N(5)	20	20	20	7
26	3	.7	.2	1	1000	N(0.5)	50	300	L(1)	15	70	70	50	N(5)	20	50	10	10
36	2	.7	.5	1	1500	N(0.5)	30	1500	L(1)	15	50	50	50	N(5)	20	30	15	10
Greenish-gray claystone or siltstone																		
7	3	2	0.1	0.7	700	3	50	2000	1.5	20	150	3000	30	N(5)	20	70	50	20
8	3	2	.1	.7	700	3	50	700	1.5	30	150	3000	50	10	20	70	70	20
11	5	2	.1	.5	700	5	30	700	1.5	30	150	500	50	N(5)	L(20)	70	20	20
[3]16	3	1.5	.07	.7	700	10	30	500	1.5	30	100	2000	50	15	L(20)	50	7000	15
[4]28	3	1.5	3	.7	2000	7	30	500	1	30	70	5000	30	70	L(20)	50	7000	15
33	3	2	15	.5	3000	7	30	700	1.5	30	150	3000	70	7	L(20)	70	70	20
Grayish-red claystone or siltstone																		
4	3	1.5	10	0.5	1000	N(0.5)	30	700	1.5	20	100	20	50	N(5)	L(20)	50	20	15
12	5	1.5	.5	.7	700	N(0.5)	30	700	1	20	100	30	30	N(5)	L(20)	50	20	15
34	5	1.5	.5	.7	1500	N(0.5)	50	700	1.5	20	100	50	50	N(5)	20	70	20	15

[1] L(200) As. [2] 700 ppm As. [3] L(200) As. [4] 300 ppm As.

in the New Albany, Beaver Lake, and Grassmere Park areas, Bradford, Columbia and Lycoming Counties, Pa.

be quoted without stating these limitations. Letter symbols: L, detected but below limit of determination; N, not detected. Values in parts per million except for Fe, Mg, Ca, and Ti, which are given in percent. Elements looked for spectrographically but not found and their lower limits of determination; As (200) except as noted, Au(10), Bi(10), Cd(20), Sb(100), Sn(10), Zn(200). Gold was looked for by atomic absorption methods but not detected in any sample at 0.05 ppm limit of determination]

Semiquantitative spectrographic analyses—Con.					Chemical analyses					Sample description
Sr	V	W	Y	Zn	Hg	eU	Th	Zn	U	
Greenish-gray sandstone—Continued										
L(100)	300	N(50)	30	300	N(0.02)	30	--	71	---	Composite of small chips from dump, some have malachite stains.
100	100	L(50)	30	300	N(0.02)	L(30)	9	38	2	Composite chip sample of 30 cm in lower part of unmineralized crossbedded unit, 1 m thick above sample 4.
L(100)	500	L(50)	30	500	.02	140	45	74	134	Composite, 60 cm, malachite-stained, crossbedded.
N(100)	150	N(50)	70	700	.02	40	--	48	---	Composite, 30 cm, bleached, crossbedded, below sample 24.
150	300	N(50)	50	300	.04	110	28	56	74	Composite scattered chips from high grade pile.
L(100)	150	L(50)	30	500	N(0.02)	80	29	85	74	Composite chip sample of 15 cm mineralized rock from back of adit. 6 m from portal K8.
L(100)	100	L(50)	20	300	.02	L(30)	--	41	---	Composite chip sample of 30 cm, malachite-stained, abundant coaly remains.
L(100)	150	N(50)	30	300	.09	40	--	78	---	Composite chip sample of 60 cm, malachite-stained, organic-rich, scattered chalcocite grains, northside of portal.
Grayish-red sandstone—Continued										
L(100)	100	N(50)	20	500	N(0.02)	30	--	44	---	Composite 90 cm, no visible copper minerals.
N(100)	100	L(50)	20	500	N(0.02)	40	--	32	---	Composite, 60 cm, crossbedded, above sample 23.
N(100)	100	L(50)	20	500	N(0.02)	40	--	44	---	Composite, 30 cm, barren, crossbedded, 6 m below prospect pit K 15.
L(100)	100	L(50)	20	300	N(0.02)	L(30)	--	42	---	Composite, 60 cm, crossbedded, above ore horizon.
Greenish-gray claystone or siltstone—Continued										
100	200	L(50)	30	300	0.04	40	--	72	---	Composite, 30, cm, malachite-stained, plant remains, samples from near back on west wall of short adit, 2 m from portal K 1.
100	300	L(50)	30	300	.02	40	23	78	8	Composite, 30 cm, minor plant remains, below sample 7, K 1.
100	200	L(50)	30	200	N(0.02)	30	--	86	---	Composite, 1.2 m, mixed gray and red claystone, east edge of pillar in stoped area, western adit, K 1.
N(100)	200	L(50)	30	200	N(0.02)	30	--	72	---	Composite 15 cm, abundant plant remains.
L(100)	150	L(50)	30	200	N(0.02)	40	19	73	28	Composite scattered chips from dump, organic remains, pyrite, copper sulfides, malachite, azurite.
200	200	L(50)	70	200	.02	30	--	59	---	Composite 30 cm, middle of south wall of adit, 6 m from portal K 8.
Grayish-red claystone or siltstone—Continued										
150	150	L(50)	50	150	N(0.02)	L(30)	--	56	---	Composite, 60 cm, crossbedded, below sample 5.
100	150	L(50)	30	200	N(0.02)	30	--	70	---	Composite, 60 cm, above ore horizon and between two adits. K 1 project.
L(100)	200	L(50)	50	300	N(0.02)	40	--	63	---	Composite, 60 cm, road cut near prospect K 8.

TABLE 2.—*Analyses of stream sediments from New Albany, Beaver Lake,*

[For sample localities see figures 2, 3, and 4. Semiquantitative spectrographic analyses by J. M. Motooka of the minus 80-mesh fraction of stream sediment (R) and of the oxalic acid leachate of the minus 80-mesh fraction (O). All data in parts per million except for Fe, Mg, Ca, and Ti which are given in percent. Lower limit of determination given in parentheses below element symbol. Results of the semiquantitative analyses are reported to the nearest number in the series 1, 0.7, 0.5, 0.3, 0.2, 0.15, 0.1, which represent approximate midpoints of group data in a geometric scale. The assigned groups for the series will include the quantitative value about 30 percent of the time. The data should not be quoted without stating these limitations. Letter symbols: L, detected but below limit of determination; N, not detected; ND, not determined. Elements looked for spectrographically in the minus 80-mesh frac-

Sample	R Fe (0.05)	O Fe (0.1)	R Mg (0.02)	R Ca (0.05)	R Ti (0.002)	R Mn (10)	O Mn (20)	R B (10)	O B (20)	R Ba (20)	O Ba (50)	R Be (1)	O Be (2)	R Co (5)	O Co (10)	R Cr (10)	O Cr (20)	R Cu (5)
Stream drainage area contains mineralized zone																		
PAL- 1	1.5	30	0.2	0.05	0.3	700	>10 000	20	200	150	1500	L(1)	5	10	100	20	500	7
9	1.5	30	.15	.05	.5	500	10 000	20	200	150	1000	L(1)	7	10	100	15	500	7
10	1.5	30	.15	.05	.5	500	>10 000	20	200	150	1500	L(1)	7	10	100	30	500	10
14	1.5	30	.3	.07	.5	1000	>10 000	20	150	200	2000	1	5	15	100	30	300	15
27	1	30	.3	.07	.5	1500	>10 000	20	100	300	3000	1	15	10	150	70	500	30
30	1.5	30	.3	.05	.5	700	>10 000	20	700	150	3000	1	15	10	100	20	500	10
38	1.5	50	.5	7	.3	700	10 000	30	200	200	3000	1	5	15	150	50	700	150
41	.3	30	.5	.05	.5	1000	>10 000	30	100	300	3000	1	10	10	150	70	700	20
49	1.5	30	.2	.05	.5	200	10 000	30	50	150	1500	L(1)	7	10	70	50	300	15
50	1.5	30	.3	.07	.5	700	>10 000	30	50	150	1500	1	5	15	70	50	300	20
Stream drainage area contains no known mineralized zone																		
PAL-13	2	30	0.5	0.1	.05	700	>10 000	30	150	500	2000	1	7	15	100	70	300	15
22	.7	30	.15	L(0.05)	.3	300	>10 000	30	700	150	3000	L(1)	20	7	200	15	700	7
29	2	30	.5	.07	.5	500	10 000	30	150	200	1500	1	10	15	100	70	300	15
31	1.5	30	.3	.07	.5	700	>10 000	30	200	200	3000	1	15	10	150	30	500	15
39	1.5	30	.3	.05	.3	700	>10 000	50	200	150	3000	1	7	15	150	20	500	15
40	.7	30	.15	L(0.05)	.2	500	>10 000	20	500	100	3000	L(1)	15	7	100	15	500	5
42	.2	30	.3	.07	.5	500	10 000	30	100	200	2000	1	7	20	150	70	700	20
43	1.5	30	.2	.05	.5	500	>10 000	30	100	150	3000	1	10	15	150	50	700	15
44	1.5	50	.3	.07	.5	1000	>10 000	30	50	200	7000	1	10	15	300	50	1000	15
45	1.5	30	.3	.05	.3	700	>10 000	30	50	150	5000	1	7	10	300	50	700	15
46	1.5	30	.2	L(0.05)	.5	700	>10 000	30	50	150	3000	1	7	10	200	30	500	15
47	1.5	30	.3	.1	.5	1000	>10 000	30	50	500	7000	1	7	15	300	70	700	15
48	2	30	.5	.7	.7	1000	>10 000	50	50	500	2000	1.5	5	15	200	70	300	15
51	1.5	50	.2	L(0.05)	.2	1500	>10 000	20	20	150	1500	1.5	7	15	500	50	500	15
Stream drainage area stratigraphically above mineralized section																		
PAL- 6	1.5	30	0.3	0.07	0.3	1500	>10 000	50	200	200	1500	1.5	15	15	200	50	700	15
17	.7	30	.1	L(0.05)	.5	200	10 000	30	500	150	1500	L(1)	30	5	100	15	700	5
18	.7	30	.07	L(0.05)	.5	700	>10 000	50	1000	100	2000	L(1)	20	5	150	10	700	L(5)
19	.7	30	.1	L(0.05)	.7	500	>10 000	30	700	150	2000	L(1)	20	5	150	20	700	5
20	.7	30	.1	L(0.05)	.3	700	>10 000	20	300	150	2000	1	30	5	200	15	700	7
21	.7	30	.1	L(0.05)	.5	700	>10 000	30	500	150	2000	1	20	7	150	15	500	5

a prospect, and sample 27 is from a spring less than 3 m from a prospect pit. In two places where sample pairs upstream and downstream from nearby copper prospects could be collected (samples 1, 49, and 50; 9 and 10, fig. 2), the downstream sample was slightly higher in copper than the upstream sample of that pair. Of the nine samples that contained less than 10 ppm copper, five were from watersheds largely or entirely within rocks lithologically identical but stratigraphically higher than the part of the formation that contains the known copper occurrences.

OXALIC ACID LEACH

Oxides in soils and stream sediments have long been recognized as strong scavenging agents for heavy-metal ions (Canney, 1966). When associated with an ore body, these oxides may be enriched with trace metals as a result of surface- and ground-water movements (Carpenter and others, 1975; Whitney, 1975). In an attempt to define the copper anomalies better, the minus 80-mesh fraction of each stream sediment was leached with oxalic acid in order to concentrate the metal ions bound in the iron and manganese oxides. The ease of extraction of these oxides provides a leachate sample, enriched with metal ions, that can readily be analyzed by the six-step semiquantitative spectrographic method (Grimes and Marranzino, 1968). The oxalic acid leaching procedure is described by Alminas and Mosier (1976). Analysis of the leachates (table 2) suggests that most of the heavy-metal concentration is about 10 times that of the minus 80-mesh fraction.

Comparison of copper concentrations for the minus 80-mesh with leachate sets of analyses, after excluding the one high value in each set (fig. 5), discloses that the analytical results from the leached samples have a

and Grassmere Park areas, Bradford, Columbia, and Lycoming Counties, Pa.

tion but not found and their lower limits of determination: Ag(0.5), As(200), Au(10), Bi(10), Cd(20), Mo(5), Sb(100), Sn(10), Zn(200). Those looked for but not found in the leachate: Ag(1), As(500), Au(20), Bi(20), Cd(50), Nb(50), Sb(200). Elements found in some but below the limit of determination were: Nb reported as L(20) for all samples of the minus 80-mesh fraction except 6, 20, 21, 27, 38, 40, and 51, which are reported as N(20), and W reported as L(50) in samples 13 and 14, minus 80-mesh fraction, and as L(100) in all samples of leachate except 6, and 44 thru 51 which are reported as N(100). Atomic absorption analyses for zinc and gold by George Crenshaw. Gold was not detected in any sample at a lower limit of determination of 0.05 ppm. In addition, all samples except Nos. 30 and 41, which were too small to test, contain L(30) eU determined by instrument by Z. C. Stephenson]

O Cu (10)	R La (20)	O Mo (10)	R Ni (5)	O Ni (10)	R Pb (10)	O Pb (20)	R Sc (5)	O Sn (20)	R Sr (100)	O Sr (200)	R V (10)	R Y (10)	R Zn[1] (5)	O Zn (500)	R Zr (10)	Area[2] (hectares)	Distance[3] (meters)
Stream drainage area contains mineralized zone—Continued																	
100	30	15	15	200	N(10)	200	7	L(20)	N(100)	L(200)	70	30	43	700	300	750	450
100	30	L(10)	10	200	N(10)	150	7	N(20)	L(100)	L(200)	50	20	40	L(500)	700	175	1650
150	30	10	15	200	N(10)	200	7	N(20)	N(100)	L(200)	50	20	42	L(500)	700	180	30
100	30	10	15	150	L(10)	200	10	N(20)	L(100)	500	70	30	70	L(500)	300	260	1500
300	20	20	15	150	20	500	7	N(20)	N(100)	L(200)	70	15	130	1000	300	0.4	3
150	20	15	15	150	10	500	5	300	N(100)	300	50	15	74	1500	200	875	450
2000	20	50	20	150	50	150	7	L(20)	200	700	70	20	126	1500	300	0.4	15
100	50	10	20	200	20	200	10	N(20)	L(100)	200	100	30	110	700	200	90	1250
200	50	N(10)	15	200	10	200	5	N(20)	N(100)	ND	70	20	55	500	700	750	30
150	30	N(10)	20	150	15	300	7	N(20)	N(100)	ND	70	30	60	N(500)	300	750	50
Stream drainage area contains no known mineralized zone—Contiued																	
100	30	10	20	200	15	200	10	N(20)	N(100)	200	100	20	60	700	500	140	
150	20	10	10	300	10	500	5	L(20)	N(100)	L(200)	50	20	52	1500	700	245	
100	30	15	20	150	15	300	10	20	N(100)	L(200)	70	20	62	700	300	545	
150	50	15	15	150	15	500	7	L(20)	N(100)	300	70	20	73	1000	300	105	
150	20	15	15	150	10	300	5	N(20)	N(100)	200	50	20	58	500	200	80	
100	L(20)	10	10	150	N(10)	200	L(5)	N(20)	N(100)	L(200)	30	15	46	700	150	100	
150	20	15	20	200	15	150	7	N(20)	N(100)	300	70	20	61	500	300	10	
100	30	15	20	200	15	200	7	N(20)	N(100)	300	70	20	74	500	300	20	
200	20	20	20	500	20	500	7	L(20)	N(100)	ND	70	20	92	1500	200	30	
150	20	20	20	300	10	300	10	L(20)	N(100)	ND	100	15	106	1500	300	170	
150	20	15	15	200	10	300	7	L(20)	N(100)	ND	70	20	77	1000	300	595	
150	30	20	20	300	20	300	10	N(20)	N(100)	ND	100	20	178	700	300	20	
150	30	15	20	200	20	150	10	L(20)	100	ND	70	20	91	700	300	180	
200	30	20	20	200	15	700	7	N(20)	N(100)	ND	70	15	100	1000	150	35	
Stream drainage area stratigraphically above mineralized section—Continued																	
150	30	10	30	300	20	300	10	N(20)	N(100)	L(200)	70	20	72	1000	300	100	
100	20	10	10	200	L(10)	700	5	20	N(100)	300	50	10	33	700	700	100	
150	N(20)	15	7	300	N(10)	700	5	L(20)	N(100)	200	30	10	43	1500	500	170	
150	100	15	10	300	N(10)	500	5	20	N(100)	L(200)	50	15	47	1000	300	195	
100	N(20)	15	10	300	10	700	5	70	N(100)	300	30	20	42	1000	200	180	
70	20	20	10	200	N(10)	300	5	L(20)	N(100)	200	50	10	59	1000	500	105	

[1] By atomic absorption methods.
[2] Stream drainage area.
[3] Distance between sample site and known copper mineralized area upstream.

noticeable reduction in relative dispersion. Leachates of samples from large streams in unmineralized areas (samples 17–22) have about as much copper as the leachates of samples from streams in areas of known mineralization. In an effort to distinguish between the two sets of samples, various combinations of elemental ratios were made (table 3), but only the copper to zinc ratios of the leachate data provide a clear separation of samples from streams that have copper deposits in the drainage basin from samples from streams that have no known copper deposits in the basin (figs. 6 and 7). Out of a total of 30 samples, nine of the leached samples (Nos. 9, 10, 14, 27, 38, 39, 42, 49, and 50) have copper to zinc ratios equal to or greater than 0.3, but only three (Nos. 38, 42, and 50) of the minus 80-mesh samples have copper to zinc ratios greater than 0.3. The mean ratio in both sets of samples is approximately 0.2, but the relative dispersion is greater for the leachate samples than for the minus 80-mesh samples. Values of 0.3 or larger for the copper to zinc ratio appear slightly anomalous (figs. 6 and 7) in both sets of data.

Samples 1, 9, 10, 14, 27, 30, 38, 41, 49, and 50 were collected downstream from copper-prospect areas; the leachate histogram (fig. 6) graphically shows a clear separation of most of these samples from the other groups. Only samples 1, 30, and 41 do not have anomalous copper to zinc ratios. Sample 1 is from a large stream-drainage area and is 450 m from the nearest known copper deposit (fig. 2); sample 30 is also from a large drainage area, is downstream from a dammed lake, and is also 450 m from the nearest deposit (fig. 3). Sample 41, which is from a smaller drainage area, is 1250 m from the nearest copper prospect (fig. 3). Samples 39 and 42 have anomously high copper to zinc ratios but have no known copper deposits in their

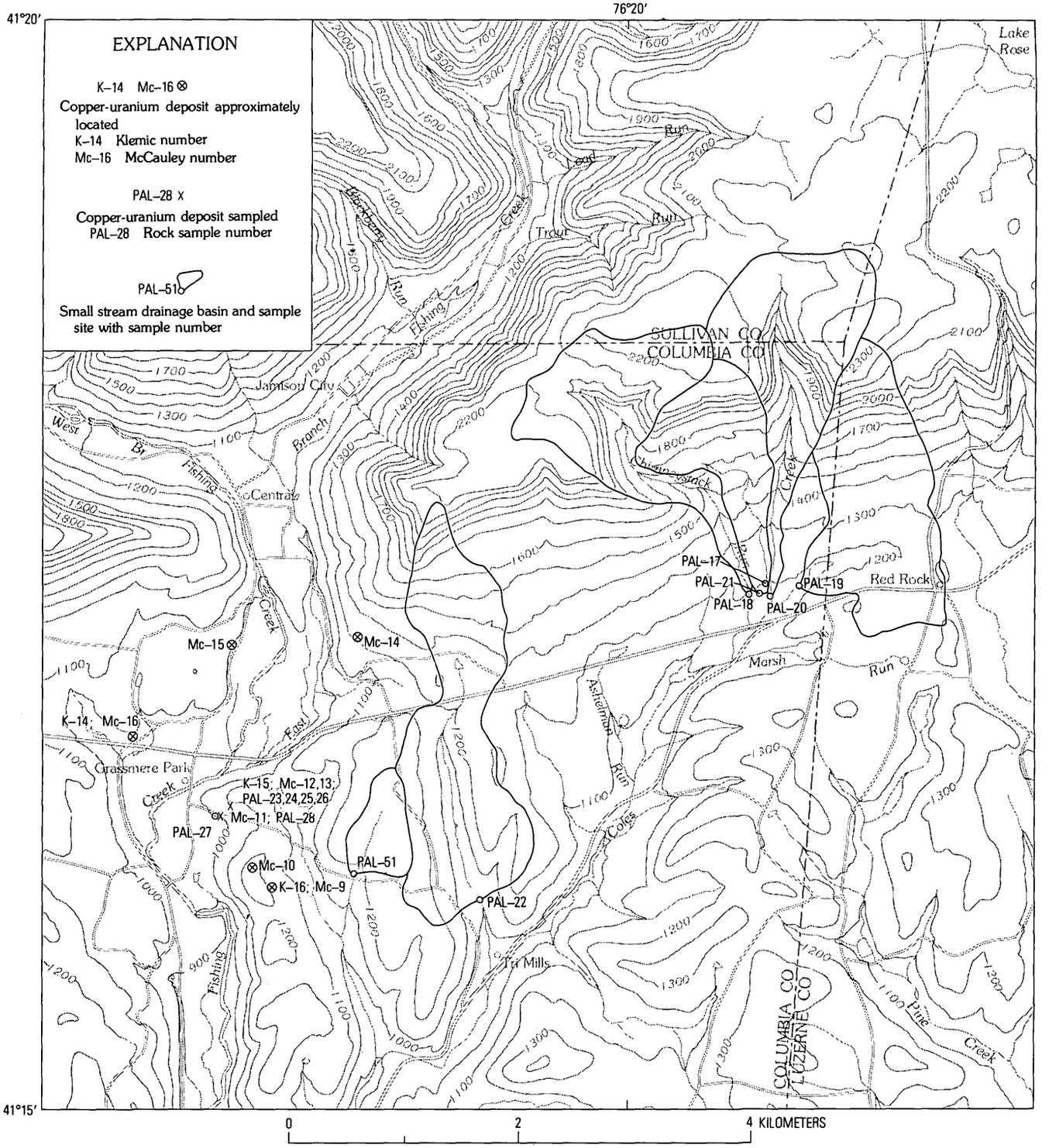

FIGURE 4.—Sample location map of Grassmere Park area, Columbia County, Pa. Contours given in feet (1 foot=0.3048 meter).

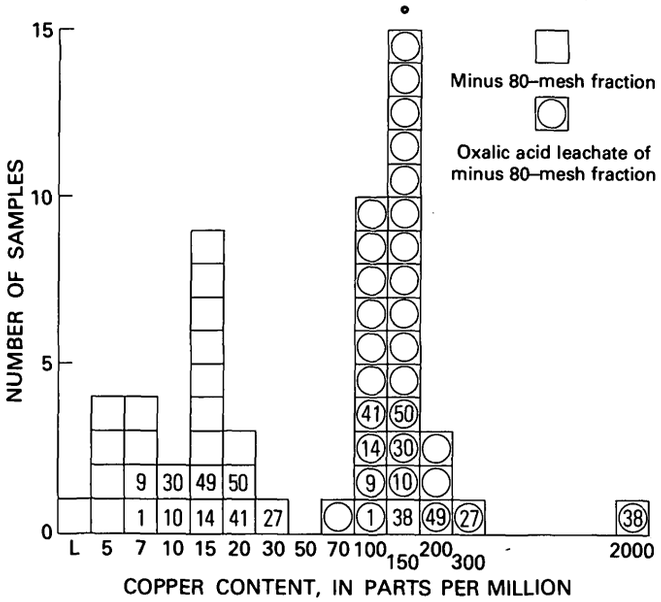

FIGURE 5.—Histogram showing distribution of copper in minus 80-mesh fraction of stream-sediment samples compared with distribution of copper in oxalic acid leachate of minus 80-mesh fraction. Sample number in frame is for stream-draining area containing a known copper deposit. L, detected but below limit of determination.

drainage areas. Both areas, however, are close to known deposits and include areas that are within the favorable stratigraphic interval. These two drainage areas may possibly contain unknown copper deposits.

The oxalic acid leachate technique clearly shows other element patterns which are not apparent in the minus 80-mesh fraction. In addition to enhancing zinc considerably above the detectable level, the leachate also provides for detection of molybdenum, tin, and strontium, elements that were previously undetermined or only recognized at their limits of detection. Molybdenum and strontium do not appear to be concentrated in streams with copper deposits in the drainage basin; tin may actually be slightly more abundant in streams with no copper deposits in the drainage basin. The one sample (No. 30) that has the highest value of tin (300 ppm) is downstream from a dammed lake and small community; the high tin value may be a result of contamination.

The routine six-step semiquantitative spectrographic analysis of stream sediments only provides total trace-metal concentrations without indicating their geochemical significance. Enhancement of the copper values in the oxalic acid leachate suggests a majority of the copper is readily soluble and is coprecipitated from solutions of manganese and iron oxides. Copper transported and redeposited in a system of this sort will produce a sediment whose copper content reflects

TABLE 3.—*Comparison of* Cu/Zn, Cu/Mn *and* (Cu+Pb+Zn)/(Fe+Mn) *ratios for analyses of the minus 80-mesh fraction and the oxalic acid leachate of stream-sediment samples*

Sample	Cu/Zn		Cu/Mn		Cu+Pb+Zn / Fe+Mn (Minus 80 mesh)
	Minus 80 mesh	Oxalic leachate	Minus 80 mesh	Oxalic leachate	
Stream drainage area contains mineralized zone					
1	0.16	0.14	0.010	0.14	0.0031
9	.17	[1].33	.014	.2	.0030
10	.24	[1].50	.020	.3	.0033
14	.21	[1].33	.015	.1	.0053
27	.23	.30	.020	.2	.0156
30	.13	.10	.014	.2	.0059
38	1.2	1.33	.214	2.9	.0207
41	.18	.14	.020	.1	.0375
49	.27	.40	.075	1.5	.0052
50	.33	[2]75	.078	.2	.0060
Stream drainage area contains no known mineralized zone					
13	0.25	0.14	0.021	0.1	0.0043
22	.13	.10	.023	.5	.0094
29	.24	.14	.030	.2	.0044
31	.20	.15	.021	.2	.0065
39	.26	.30	.021	.2	.0052
40	.11	.14	.040	.2	.0088
42	.33	.30	.040	.3	.0384
43	.20	.20	.030	.2	.0067
44	.16	.13	.015	.2	.0079
45	.14	.10	.021	.2	.0083
46	.19	.15	.021	.2	.0064
47	.08	.21	.015	.15	.0133
48	.16	.21	.015	.15	.0060
51	.15	.20	.010	.13	.0078
Stream drainage area stratigraphically above mineralized section					
6	0.21	0.15	0.010	0.1	0.0064
17	.15	.14	.025	.5	.0052
18	[3].07	.10	[3].004	.2	.0055
19	.11	.15	.010	.3	.0069
20	.17	.10	.010	.1	.0076
21	.08	.07	.007	.1	.0083

[1] Zn reported as present but below determination limit (assumed 300 ppm).
[2] Zn reported as not detected at determination limit (assumed 200 ppm).
[3] Cu reported as present but below determination limit (assumed 3 ppm).

both supergene and primary processes. Most of the copper to zinc ratios of the oxalic acid leachate from known mineralized areas are noticeably higher than those from unmineralized areas (figs. 6 and 7), and the determination of ratios may provide a method of normalizing the copper values by eliminating or reducing chemical variations introduced from secondary sources.

The leaching method should prove useful in the interpretation of data from areas where the trace metals present are those introduced by hydromorphic processes in weathering environments. An important advantage of the leaching method is the ability to enhance the concentration of most of the elements determined in the six-step spectrographic method. This, in certain

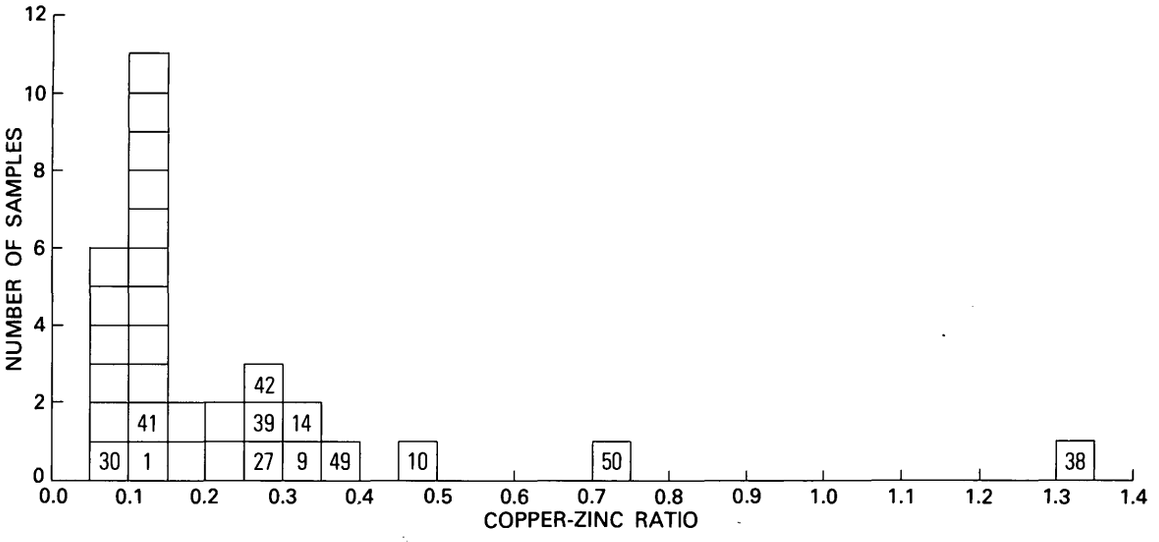

FIGURE 6.—Histogram of copper to zinc ratio in leachate. Sample number in frame.

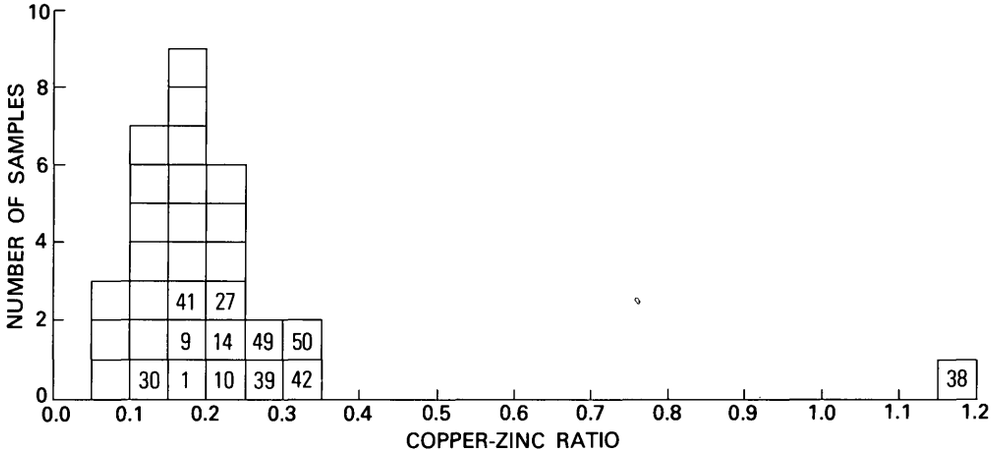

FIGURE 7.—Histogram of copper to zinc ratio in minus 80-mesh fraction. Sample number in frame.

instances, can reduce the problems of interpreting data at or near the detection limits where most analytical methods lose considerable precision.

CONCLUSIONS

Thirty samples are probably not enough to provide strongly supported conclusions, and the results are open to several interpretations. Our interpretations, which follow, could be adequately tested with additional sampling.

1. McCauley (1961, p. 21) points out that the known copper concentrations appear to be stratigraphically controlled and are in the lower part of the Catskill Formation about 600–750 m below the base of the Pocono Group of Mississippian age. The geochemical data are consistent with this hypothesis. Only two rock samples (Nos. 4 and 5) were collected about 100 m above the section that is mineralized. Both samples are similar in trace-element content to unmineralized rock from within the mineralized zone (samples 12, 23, 24, 26, 34, and 36). Five of the nine stream-sediment samples of minus 80-mesh fraction that have less than 10 ppm copper (Nos. 17–21) are from streams draining a stratigraphic interval above the mineralized zone, but one sample from the higher zone (No. 6) contains 15 ppm copper. This higher stratigraphic interval, however, was sampled in only two areas, and four samples from streams draining the favorable stratigraphic interval contained only 5–7 ppm copper.
2. Areas and stratigraphic intervals where copper concentrations are known can be delineated effec-

tively by stream-sediment sampling by using the oxalic acid leachate method and "normalizing" the data. This method, however, needs testing in larger areas and our method of "normalizing" (that is, using copper to zinc ratios) may not be valid in other areas.

3. The known mineralized occurrences in the study area probably contain only a few hundred kilograms of metal but appear to produce recognizable anomalies in drainage basins of less than one hectare in area (samples 27 and 38). If a deposit that contains several orders of magnitude more of metal was exposed to weathering, in this or a similar environment, it would likely produce a recognizable anomaly in the larger drainage basins we sampled, that is, ones of 100–750 hectares; dilution of copper in the stream sediment would be of the same relative amount as present in the smaller drainage area containing a smaller deposit. Our sampling does not suggest the presence of large unknown deposits in the region sampled.
4. The analyses of the leachates suggest that a majority of the metals, resulting from both supergene and primary processes, are tied up in the iron and manganese oxides. The leachate provides a more selective look at the oxides and, in turn, results in a more positive contrast between certain elements when a system of "normalization" is applied.

REFERENCES CITED

Alminas, H. V., and Mosier, E. L., 1976, Oxalic acid leaching of rock, soil, and stream-sediment samples as an anomaly-accentuation technique: U.S. Geol. Survey Open-File Rept. 76–275, 14 p.

Canney, F. C., 1966, Hydrous manganese–iron oxide scavenging—Its effect on stream sediment survey [abs.]: Canada Geol. Survey Paper 66–54, p. 11–12.

Carpenter, R. H., Pope, T. A., and Smith, R. L., 1975, Fe-Mn oxide coatings in stream sediment geochemical surveys: Jour. Geochem. Explor., v. 4, no. 3, p. 349–363.

Grimes, D. J., and Marranzino, A. P., 1968, Direct-current arc and alternating-current spark emission spectrographic field methods for semiquantitative analysis of geologic material: U.S. Geol. Survey Circ 591, 6 p.

Klemic, Harry, 1962, Uranium occurrences in sedimentary rocks of Pennsylvania: U.S. Geol. Survey Bull. 1107–D, p. 243–288.

Lesure, F. G., Geraci, P. J., Mory, P. C., and Williams, B. B., 1977, Mineral resources of the Ramseys Draft Wilderness Study Area, Augusta County, Virginia: U.S. Geol. Survey Bull. 1397–C. (In press.)

McCauley, J. F., 1961, Uranium in Pennsylvania: Pennsylvania Geol. Survey, 4th ser., Bull. M43, 71 p.

Weed W. H., 1911, Copper deposits of the Appalachian States: U.S. Geol. Survey Bull. 455, 166 p.

Whitney, P. R., 1975, Relationship of manganese–iron oxides and associated heavy metals to grain size in stream sediments: Jour. Geochem. Explor., v. 4, no. 2, p. 251–263.

Jour. Research U.S. Geol. Survey
Vol. 5, No. 5, Sept.–Oct. 1977, p. 623–628

RARE EARTHS, THORIUM, AND OTHER MINOR ELEMENTS IN SPHENE FROM SOME PLUTONIC ROCKS IN WEST-CENTRAL ALASKA

By MORTIMER H. STAATZ, NANCY M. CONKLIN,
and ISABELLE K. BROWNFIELD, Denver, Colo.

Abstract.—Sphene is an abundant accessory mineral in some abnormally radioactive plutonic rocks in west-central Alaska. Seven samples of sphene from four different areas in west-central Alaska contained from 20 350 to 39 180 parts per million total rare earths and 390 to 2000 ppm thorium. The lanthanide content in six of the seven sphenes is chiefly the light rare earths and is similar to that of crustal abundance; a seventh sphene from the Darby Mountains, however, contains above average amounts of the heavy rare earths. A comparison of the lanthanide distribution in sphene from several areas indicates that the structure of sphene will accommodate whatever lanthanides are available when the mineral crystallizes. The amount of thorium and rare earths in sphene is also affected by the presence of other accessory minerals. Sphene in rocks containing either allanite or zircon has a lower thorium content than in rocks that do not contain allanite or zircon. Sphene, because of its abundance, may contain the greater part of the rare earths and thorium in some of the plutonic rocks of west-central Alaska.

Rare earths and thorium occur in silicic igneous rocks, especially those associated with alkalic complexes. These elements commonly occur in accessory minerals such as sphene, zircon, allanite, garnet, epidote, thorite, apatite, thorianite, and monazite. Thorium and the rare-earth elements are major constituents of allanite, monazite, thorite, and thorianite, but proxy for major constituents in sphene, zircon, apatite, epidote, and garnet. This last group of accessory minerals is commonly much more abundant than the primary thorium- and rare-earth-bearing minerals and thus may contain most of these elements in some rocks.

Recent studies in the southeastern Seward Peninsula have shown that some of the plutonic rocks in the area contain above-average amounts of thorium and uranium when compared to the averages for these elements in similar plutonic rocks of Alaska (Miller and Bunker, 1975; Miller and Bunker, 1976, p. 373). Further sampling of granitic rocks in west-central Alaska by T. P. Miller and the senior author found that some of them also have above-average rare-earth contents. For the present studies of Alaskan rocks, six samples were chosen from plutonic bodies having an above-average radioactive-mineral content for this type of igneous rock. These samples consist of quartz monzonite from the Darby Mountains, syenite from the Selawik Hills, nepheline syenite and garnet-bearing syenite from Granite Mountain, and two samples of gneissic monzonite from the Zane Hills (fig. 1). Examination of heavy-mineral separates showed that sphene was the only mineral that was common in all samples. Sphene was selected for a detailed study of its minor-element content because of the abundance of this mineral. It was also collected from a placer deposit that lay a few kilometers downstream from the gneissic monzonite in the Zane Hills.

We also analyzed for comparison sphene from three other areas of silicic rocks in the United States. These sphenes came from granitic pegmatite near Kingman, Ariz., syenite near Hamilton, Mont., and a thorite vein in the Hall Mountain district of northernmost Idaho. Sphene and other accessory minerals (table 1) were separated using heavy liquids and a magnetic separator.

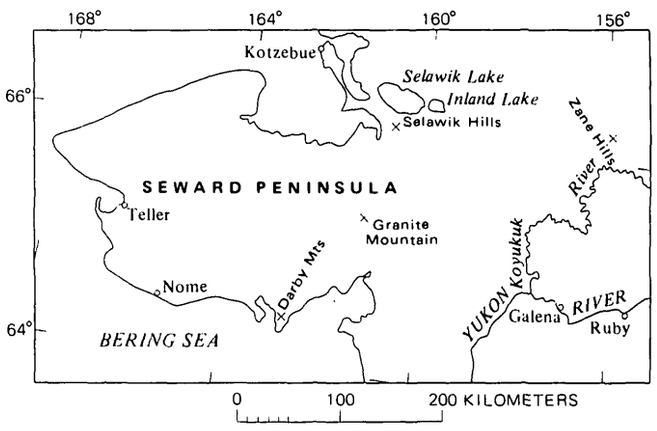

FIGURE 1.—Index map showing the areas (×) from which the sphene was collected in Alaska.

TABLE 1.—*Relative amounts of accessory minerals in plutonic rocks from and adjacent to the Seward Peninsula, Alaska*

Sample No.	Area	Rock type	Relative amounts of mineral in each sample: Moderate	Small	Scarce
M113705	Darby Mountains	Quartz monzonite	Sphene Allanite	----------	----------
A-1-s	Selawik Hills	Syenite	Sphene	----------	Epidote Thorianite
A-9-74	Granite Mountain	Nepheline syenite	Garnet Sphene	----------	Bastnaesite Synchisite
A-11-74	---do---	Garnet syenite	Garnet Sphene	----------	----------
A-3-74	Zane Hills	Gneissic monzonite	Sphene	Zircon Allanite	----------
A-5-74	---do---	---do---	Garnet Sphene	Thorite Urano-thorianite	----------
A-6-74	---do---	Placer on Bear Creek	Zircon Urano-thorianite	Sphene Garnet	Epidote

Among the accessory minerals separated from the six Alaskan plutonic samples are: allanite, thorite, thorianite, bastnaesite, and synchisite (table 1). These minerals contain major amounts of thorium, rare earths, or both, but with one exception, these minerals are much less abundant than sphene in these samples. In one sample (M113705) from the Darby Mountains, allanite, although somewhat less abundant than sphene, contains most of this sample's thorium and rare earths (table 3).

The abundance of sphene makes it an important contributing source of thorium and rare earths in the sampled rocks. Furthermore, sphene generally contains more rare earths than the next most common accessories, zircon and melanite garnet. The zircon in plutonic rocks, however, generally contains more thorium than does the sphene (Hurley and Fairbairn, 1957, p. 940–941).

MINOR ELEMENTS IN SPHENE

The thorium content of analyzed sphene from west-central Alaska (table 2) ranges from 390 to 2000 parts per million. In comparison, 25 sphenes from plutonic

TABLE 2.—*Quantitative and semiquantitative spectrographic analyses in parts per million of minor elements of various sphene samples*

[Semiquantitative spectrographic analysis indicated by underlining; N.D., not detected; N.A., no analysis; N. M. Conklin, analyst]

Area	Darby Mountains, Alaska	Selawik Hills, Alaska	Granite Mountain, Alaska		Zane Hills, Alaska			Kingman, Ariz.	Hamilton, Mont.	Hall Mountain, Idaho
Field No.	M113705	A-1-s	A-9-74	A-11-74	A-3-74	A-5-74	A-6-74	Az	RM-6-61	PH-26-70
Type of sample	Quartz monzonite	Syenite	Nepheline syenite	Garnet-bearing syenite	Gneissic monzonite		Placer	Pegmatite	Syenite	Thorite vein
Th	<700	2,000	460	1,000	760	390	1,400	<500	<500	2,100
La	1,500	3,600	4,600	4,800	6,400	5,000	5,500	940	1,400	N.D.
Ce	5,000	9,300	9,700	9,500	13,000	10,000	10,000	2,800	3,800	N.D.
Pr	1,000	500	1,500	1,500	2,000	1,500	1,500	700	500	N.D.
Nd	4,800	4,100	5,600	5,700	9,600	5,100	6,500	3,300	2,100	N.D.
Sm	1,500	1,000	1,500	1,000	3,000	1,500	1,500	1,500	<1,000	N.D.
Eu	<300	100	300	<200	300	<200	200	300	200	200
Gd	870	400	700	700	700	700	700	1,500	700	510
Tb	<500	N.D.	<200	<200	<200	<200	<200	<200	<200	N.A.
Dy	1,350	200	500	300	700	500	300	2,000	200	670
Ho	160	<200	150	70	200	150	<200	700	<100	150
Er	500	<300	<200	<200	<200	200	<200	1,000	<200	480
Tm	120	N.D.	30	<50	50	50	<100	100	<100	100
Yb	840	50	90	60	200	320	150	1,400	80	440
Lu	37	N.D.	<50	<50	30	70	<100	300	<50	50
Total lanthanides.	17,680	19,250	24,670	23,630	36,180	25,090	26,350	16,540	8,980	2,600
Y	7,600	1,100	1,200	800	3,000	2,800	2,100	10,000	1,500	4,300
Total rare earths.	25,280	20,350	25,870	24,430	39,180	27,890	28,450	26,540	10,480	6,900
Mn	4,100	490	400	300	1,400	2,100	780	830	630	400
Nb	9,400	6,000	3,300	4,100	5,000	6,300	4,600	1,600	2,400	11,000
Zr	1,300	4,400	4,600	3,800	7,800	7,400	11,000	700	1,900	560
Sn	2,800	260	120	120	125	390	260	420	110	50
Sr	17	1,800	160	140	70	80	<200	20	1,300	20
Ba	50	80	100	900	60	80	225	60	80	150
V	310	300	680	640	400	480	N.A.	680	820	600
Cu	13,000	N.A.	<50	<50	N.A.	<50	<10	N.A.	<10	<50
Pb	160	100	30	30	N.A.	70	<150	N.A.	<20	70
U	<700	<700	<700	<700	<700	<700	<700	<700	<700	<700

rocks in the United States and Canada were found by Hurley and Fairbairn (1957, p. 941) to contain from 20 to 3150 ppm thorium. Sphene from the thorite vein on Hall Mountain in Idaho (table 2) contained 2100 ppm thorium. The vein from which this sample was taken yielded 6500 ppm thorium, most of it in the mineral thorite. The maximum amount of thorium that will fit into the structure of sphene does not appear to be more than about 3000 ppm.

The total rare-earth content of the seven analyzed Alaska sphenes (table 2) ranged from 20 350 to 39 180 ppm. Only one of the three non-Alaskan sphenes analyzed—the one from the pegmatite near Kingman, Ariz., containing 26 540 ppm—had a similar total rare-earth content. Sphene from near Hamilton, Mont., and Hall Mountain, Idaho, contained less than half that amount of total rare earths. Lee, Mays, Van Loenen, and Rose (1969, p. B45) analyzed 14 sphenes from granodiorite and quartz monzonite in the Mount Wheeler area, Nevada, and found them to contain from 5920 to 29 630 ppm total rare earths. Thus, sphene in Alaska and elsewhere is commonly one of the principal minerals containing rare earths in plutonic rocks.

The distribution of the individual rare earths can be best seen by making plots of the lanthanide (rare earths having atomic numbers 57 to 71) content after the manner of Semenov and Barinskii (1958, p. 407–408). The plot of the distribution of the lanthanides

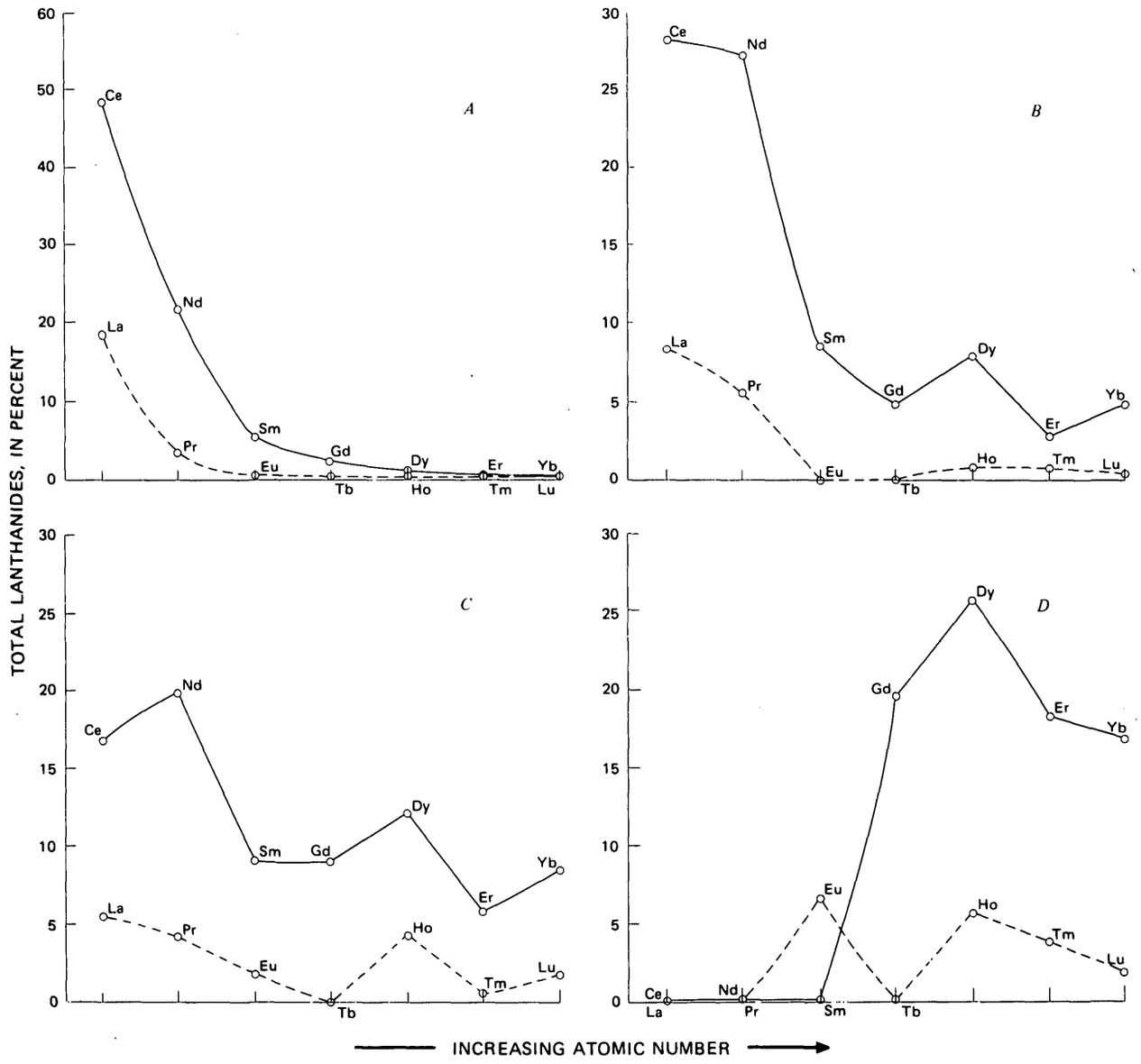

FIGURE 2.—Distribution of lanthanides in four sphenes. *A*, Sample A–1–s from the Selawik Hills, Alaska. *B*. Sample M113705 from the Darby Mountains, Alaska. *C*, Sample Az from near Kingman, Ariz. *D*, Sample PH–26–70 from Hall Mountain, Idaho. Solid line, even atomic-numbered lanthanides; dashed line, odd atomic-numbered lanthanides.

in the sphene from the Selawik Hills (fig. 2*A*) might be called a normal one, because it is similar to the plot of crustal abundance (Staatz and others, 1974, p. 681) as well as to that of many analyzed minerals. The lanthanide distributions in sphenes from Granite Mountain and the Zane Hills (fig. 1) are almost identical. The distribution of the lanthanides and yttrium in the sphene (sample M113705) from the Darby Mountains (fig. 2*B*) is somewhat different, as it has a greater proportion of the heavy lanthanides (atomic number greater than 63) and a high yttrium content. The lanthanide distribution in the sphene from near Hamilton, Mont., follows the normal pattern but those in the two from Arizona and Idaho are widely divergent, both from the normal plot and from each other. The Arizona sphene (fig. 2*C*) has almost as much heavy as light lanthanides, and yttrium makes up 38 percent of the total rare earths. The Idaho sphene (fig. 2*D*) has practically no light rare earths, and yttrium makes up 62 percent of the total rare earths. This unusual lanthanide distribution in the Idaho sphene is similar to that in the various veins in this area (Staatz and others, 1974, p. 680).

Thus, the plots of the lanthanide distribution in the six sphenes from Alaska and in the sphene from near Hamilton, Mont., resemble each other and that of crustal abundance (table 2, fig. 2), but the plots of the lanthanide distribution in the other Alaskan sphene and the sphenes from Arizona and Idaho differ greatly from the norm and from each other.

What is the significance of the variation in the lanthanide patterns? The differences in the patterns can reflect the structure of the mineral, how the lanthanides are distributed in the magmatic fluids from which the mineral is formed, or both. The structure of some minerals, such as bastnaesite and monazite, does not easily accommodate heavy rare earths, and the lanthanide patterns of these minerals are similar to that of crustal abundance or of the pattern shown in figure 2*A*. A few minerals, like xenotime and cenosite, accommodate principally the heavy rare earths, and the patterns of these minerals are similar to those illustrated in figure 2*C* and *D*. The structure of some other minerals, including thorite and sphene, will accommodate whatever rare earths are available when these minerals crystallize.

In addition to thorium and rare earths, a number of other minor elements may be concentrated in sphene (table 2). These include niobium, zirconium, uranium, strontium, barium, vanadium, copper, lead, manganese, and tin. In sphenes from west-central Alaska, niobium (3300–9400 ppm) and zirconium (1300–11 000 ppm) are two of the most common minor elements. The uranium content of all analyzed sphene appears to be less than 700 ppm. Uranium was analyzed by using semiquantitative spectrographic methods, and in all of four samples it was below the limit of sensitivity (700 ppm); we, therefore, do not know how the uranium content of the sphene varies from sample to sample. The only mineral that contained measurable uranium was the zircon from the Zane Hills, which yielded 3000 ppm uranium. Uranium fits more easily into the lattice of zircon than into the lattice of sphene. Hurley and Fairbairn (1957, p. 943) found in four granitic rock samples from New England and Nova Scotia that approximately seven times as much uranium occurred in zircon as in sphene. Hence, any uranium in a magma that forms zircon will be concentrated in zircon in preference to sphene. Minor elements such as strontium, barium, copper, and lead are relatively abundant in some sphenes and relatively sparse in others. Copper in all but one of the analyzed sphenes was below the limit of detectability. The sphene from the Darby Mountains, however, contained 13 000 ppm copper. Only minor amounts of copper are found in the magma of most plutonic rocks, but it was evidently available in the magma of the quartz monzonite from the Darby Mountains. Thus, the quantity of some minor elements in sphene may reflect the availability of that particular element in the magma during the formation of the sphene.

ACCOMMODATION OF MINOR ELEMENTS IN SPHENE

Sphene having a formula of $CaTiSiO_5$ is made up ideally of four elements, but actually it may contain trace amounts of a large number of elements. Zabavnikova (1957, p. 273) reported that 40 elements have been found in sphene. In 18 samples from the U.S.S.R. she (1957, p. 274–275) found that 2.18 to 12.79 percent of the sphene was oxides of elements not included in the ideal formula. The amount of extraneous elements found in sphene depends to some degree on the types of rock in which this mineral is found. The sphene found in mafic rocks fairly closely approximates the idealized formula and lacks thorium, niobium, zirconium, rare earths, and strontium (Zabavnikova, 1957, p. 278). These elements, however, are concentrated in the alkalic rocks, and sphene from these rocks is richer in total minor elements.

The minor elements that occur in sphene are chiefly those whose ionic radii are most similar to calcium, titanium, or silicon. To fit into the sphene structure the minor element must have the same charge as the element it replaced or some other substitution must have been made to balance out the charges. Thus manganese,

strontium, and barium, elements having a plus two charge, directly replace calcium, and zirconium and tin, elements having a plus four charge, directly replace titanium. Thorium, uranium, rare earths, and niobium replacements are somewhat more complex and occur in the following manner:

Th^{+4} or U^{+4} replaces Ca^{+2} and simultaneously Fe^{+2} replaces Ti^{+4} or Th^{+4}, or U^{+4} replaces Ca^{+2} and simultaneously Fe^{+3} replaces Ti^{+4} and F^{-1} replaces O^{-2}. (Rare earths)$^{+3}$ replace Ca^{+2} and simultaneously Fe^{+3} replaces Ti^{+4}. Nb^{+5} replaces Ti^{+4} and simultaneously Na^{+1} replaces Ca^{+2}.

If the charges are the same, the nearer in size the ionic radii are to one another, the easier will be the substitution and the more will be the replacement of one element by the other. The ionic radius of strontium (1.12 A or 0.112 nm) is much closer to that of calcium (0.99 A or 0.099 mm) than it is to barium (1.34 A or 0.134 nm). Thus, where strontium is present, it will replace calcium in preference to barium. Barium, however, is a much more abundant element than strontium in plutonic magmas. These two factors affect the amount of each found in any sphene and are the probable cause for the large variance in the strontium to barium ratio (0.13 to 23) in the 10 sphenes we analyzed (table 2).

DISTRIBUTION OF MINOR ELEMENTS BETWEEN SPHENE AND ASSOCIATED ACCESSORY MINERALS

When thorium, rare earths, or other elements reach a certain concentration in a magma, minerals may form in which these elements are primary components. Thus, the formation of monazite or allanite depletes the amounts of thorium and rare earths in the magmatic fluid, and therefore smaller amounts of them are available during the formation of sphene. Similarly, other accessory minerals such as zircon, garnet, or apatite compete with sphene for various minor elements. A comparison can be made of minor elements present in three sphenes from Alaska with those in another accessory mineral occurring in the same sample (table 3). Allanite occurs with sphene that came from the Darby Mountains, melanite garnet occurs with sphene in the sample from Granite Mountain, and zircon occurs with sphene in the sample from the Zane Hills. The thorium contents of the sphene and associated melanite garnet from Granite Mountain are about equal. The thorium content of the sphene is much less than that of the associated allanite from the Darby Mountains and of the zircon from the Zane Hills. The total rare-earth content of all sphene analyzed is high and greatly exceeds that of the associated garnet and zircon, but it is less than that of allanite in which the rare earths are a major component. Some relatively low amounts of other minor elements in the sphene may be due to their removal from the magmatic fluids prior to the formation of this mineral. For instance, melanite garnet, which crystallized early, is relatively abundant in the sample from Granite Mountain. The garnet contained 6400 ppm manganese, yet the sphene had only 300 ppm, which is one of the lower values found for this element (table 3). Similarly, allanite from the Darby Mountains yielded 330 ppm strontium, but the associated sphene had only 17 ppm, one of the lower values for this element (table 3). Thus, in both magmas a minor element was depleted by crystallization of an earlier forming accessory mineral that contains this element. On the other hand, the amounts of niobium and tin in the sphene are much greater than those found in al-

TABLE 3.—*Quantitative and semiquantitative spectrographic analyses of minor elements in parts per million of three sphenes and an associated accessory mineral, west-central Alaska*

[Semiquantitative spectrographic analysis indicated by underlining; N. M. Conklin, analyst]

Sample No. and area	Mineral	Th	Total rare earths	Mn	Nb	Zr	Sn	Sr	Ba	V	U
M113705, Darby Mountains.	Sphene	<700	25,280	4,100	9,400	1,300	2,800	17	50	310	<700
	Allanite	12,000	172,560	8,700	230	1,100	150	330	210	380	<700
A-11-74, Granite Mountain.	Sphene	1,000	24,430	300	4,100	3,800	120	140	900	640	<700
	Garnet	950	5,250	6,400	160	2,700	<70	<50	<50	1,270	<700
A-3-74, Zane Hills.	Sphene	760	39,180	1,400	5,000	7,800	125	70	60	400	<700
	Zircon	5,200	1,980	<20	<50	<100,000	<50	<20	<100	<50	3,000

lanite, garnet, or zircon from the same sample (table 3). This abundance is undoubtedly because the ionic radii of niobium and tin are similar to that of titanium.

CONCLUSION

Sphene, where abundant in the plutons of west-central Alaska, may be one of the principal sources of thorium and rare earths in these rocks. The amounts of these elements present in sphene depend not only on their amount in the original magma, but also on the abundance of other accessory minerals that may preferentially contain these elements.

REFERENCES CITED

Hurley, P. M., and Fairbairn, H. W., 1957, Abundance and distribution of uranium and thorium in zircon, sphene, apatite, epidote, and monazite in granitic rocks: Am. Geophys. Union Trans., v. 38, no. 6, p. 939–944.

Lee, D. E., Mays, R. E., Van Loenen, R. E., and Rose, H. J., Jr., 1969, Accessory sphene from hybrid rocks of the Mount Wheeler mine area, Nevada, *in* Geological Survey research 1969: U.S. Geol. Survey Prof. Paper 650–B, p. B41–B46.

Miller, T. P., and Bunker, C. M., 1975, U, Th, and K analyses of selected plutonic rocks from west-central Alaska: U.S. Geol. Survey Open-File Rept. 75–216, 5 p.

——— 1976, A reconnaissance study of the uranium and thorium contents of plutonic rocks of the southeastern Seward Peninsula, Alaska: U.S. Geol. Survey Jour. Research, v. 4, no. 3, p. 367–377.

Semenov, E. I., and Barinskii, R. L., 1958, The composition characteristics of the rare earths in minerals [in Russian]: Geokhimiya 1958, no. 4, p. 314–333; translated in Geochemistry 1958, no. 4, p. 398–419.

Staatz, M. H., Shaw, V. E., and Wahlberg, J. S., 1974, Distribution and occurrence of rare earths in the thorium veins on Hall Mountain, Idaho: U.S. Geol. Survey Jour. Research, v. 2, no. 6, p. 677–683.

Zabavnikova, I. I., 1957, Diadochic substitutions in sphene [In Russia]: Geokhimiya 1957, no. 3, p. 226–232; translated in Geochemistry 1957, no. 3, p. 271–278.

Jour. Research U.S. Geol. Survey
Vol. 5, No. 5, Sept.–Oct. 1977, p. 629–636

PLATINUM, PALLADIUM, AND RHODIUM IN VOLCANIC AND PLUTONIC ROCKS FROM THE GRAVINA-NUTZOTIN BELT, ALASKA

By NORMAN J PAGE, HENRY C. BERG; and JOSEPH HAFFTY,
Menlo Park, Calif.; Denver, Colo.

Abstract.—The Gravina-Nutzotin belt of Middle(?) Jurassic to middle Cretaceous sedimentary and volcanic rocks in south and southeastern Alaska includes concentrically zoned ultramafic complexes known to contain platinum-group metals. Previous isotopic, petrologic, and geologic studies suggested a close relation in time and space between the volcanic rocks and the ultramafic complexes. Interpretation of 40 analyses for platinum, palladium, and rhodium in volcanic and plutonic rocks of the belt indicates a strong geochemical correlation between the two groups of rocks and is in support of their being cogenetic either from directly connected magma chambers and flows or indirectly by selective concentration processes from similar mantle material.

The Gravina-Nutzotin belt of Middle(?) Jurassic to middle Cretaceous sedimentary and volcanic rocks in southern and southeastern Alaska (Berg and others, 1972) contains or adjoins at least 25 identified concentrically zoned ultramafic complexes. At least six of them are known to be platinum and palladium bearing (Clark and Greenwood, 1972), but only the Salt Chuck ultramafic mass (which may not be a concentrically zoned complex) on Prince of Wales Island has produced appreciable amounts of platinum metals. Recently, the concentrically zoned ultramafic bodies have been interpreted as the crystallization products of floored magma chambers that produced the volcanic rocks in the belt (Irvine, 1973; Berg and others, 1972). Evidence to support this hypothesis includes (1) contemporaneity in age of the complexes and volcanic rocks shown by potassium-argon and stratigraphic studies (Lanphere and Eberlein, 1966; Berg and others, 1972), (2) strontium-rubidium-potassium isotopic similarities (Lanphere, 1968), and (3) petrologic analysis of mineral compositions and their derivation in the volcanic rocks by Irvine (1967, 1973, 1974). Demonstration of this close correlation between volcanic rocks and their probable plutonic equivalents offers an opportunity to examine the geochemical cycle of the platinum-group metals through the volcanic stage. As a corollary, the geochemistry of the platinum-group metals may be used as additional evidence of the correlation between the volcanic rocks and the products from probable magma chambers.

Most basaltic rocks that have been analyzed by modern methods for platinum-group metals contain relatively low concentrations of these metals (Crocket and Skippen, 1964), and the fire assay–spectrochemical method of Haffty and Riley (1968) lacks the sensitivity to examine platinum, palladium, and rhodium concentrations in them. Because volcanic rocks from the Gravina-Nutzotin belt have slightly higher levels of platinum and palladium than most volcanic rocks studied to date, the analytical methods of Haffty and Riley are applicable.

This report (1) presents platinum, palladium, and rhodium analyses of volcanic rocks in the Gravina-Nutzotin belt for comparison with mafic volcanic and ultramafic rocks in other areas, (2) evaluates the geochemical distribution of platinum, palladium, and rhodium in these rocks, and (3) examines the relation between the volcanic rocks and the concentrically zoned ultramafic bodies or masses.

LOCATION OF SAMPLES AND DESCRIPTION OF ROCK TYPES

Forty samples were selected from rocks previously analyzed for major elements (Berg and others, 1972). Criteria for selection were to analyze the greatest variety of rock types and to obtain the widest possible distribution within the Gravina-Nutzotin belt. Figure 1 shows the approximate locations of the samples analyzed; table 1 gives the exact location by latitude and longitude and the analytical results.

PLATINUM, PALLADIUM, AND RHODIUM ANALYSES

The analyses given in table 1 were performed by the method of Haffty and Riley (1968). Sixty percent

TABLE 1.—*Palladium, platinum, and rhodium analyses, rock descriptions, and locations of rock samples from the Gravina-Nutzotin belt, southern and southeastern Alaska*

[Textures range from massive and nonfoliated to phyllitic or schistose; metamorphosed, but relatively nonschistose rocks are termed "recrystallized." Relict ferromagnesian (fm) phenocrysts may be clinopyroxene, hornblende, or actinolite; pl, relict plagioclase phenocrysts; <, less than, means that element was not detected at the stated level of sensitivity; tr, trace, means that element was detected in amount below level of determinability. Analysts: Joseph Haffty and W. D. Goss]

Map	Sample	Parts per billion			Location		Rock descriptions
		Pd	Pt	Rh	Latitude	Longitude	
1	67ABg208A	24	<10	<5	55°11'41"	131°22'53"	Porphyritic metatuff (pl).
2	68ABg656A	<4	<10	<5	55°12'50"	131°25'19"	Porphyritic crystal-lithic metatuff (fm).
3	67ABg535	19	14	<5	55°14'15"	131°10'28"	Metadiorite, Anvil Mountain pluton.
4	67ABg537	tr	21	<10	55°15'06"	131°11'03"	Metadiorite, Anvil Mountain pluton.
5	68ABg315	<8	<19	<10	55°15'18"	131°14'11"	Recrystallized porphyritic phase of Anvil Mountain pluton.
6	68ABg574A	tr	<10	<5	55°15'50"	131°12'53"	Porphyritic crystal-lithic metatuff (pl) or volcanic breccia.
7	66ABg258A	<4	<10	<5	55°16'11"	131°13'49"	Metatuff, relict lithic clasts.
8	67ABg247	18	<10	<5	55°17'07"	131°13'52"	Porphyritic crystal-lithic metatuff (pl).
9	70ABg220	5	<10	<5	55°14'47"	131°43'04"	Recrystallized porphyritic tuff (pl, fm).
10	70ABg219	11	14	<5	55°15'36"	131°42'43"	Recrystallized porphyritic tuff (fm).
11	69ABg671C	<4	<10	<5	55°15'58"	131°40'11"	Recrystallized porphyritic volcanic conglomerate (pl, fm).
12	70ABg218	9	tr	<5	55°16'12"	131°44'07"	Recrystallized porphyritic tuff (pl, fm).
13	69ABg753	<4	<10	<5	55°17'17"	131°36'42"	Fine-grained schist with relict phenocrysts (pl, fm).
14	70ABg221	10	<10	<5	55°17'58"	131°43'18"	Recrystallized porphyritic tuff (pl, fm).
15	70ABg217	<4	<10	<5	55°18'03"	131°46'04"	Recrystallized porphyritic tuff (pl, fm).
16	69ABg656B	tr	<10	<5	55°18'36"	131°41'31"	Actinolite-hornblende-epidote schist.
17	70ABg215	tr	<10	<5	55°19'29"	131°46'15"	Recrystallized volcanic sandstone or crystal-lithic tuff; relict fm and pl phenocrysts, lithic fragments.
18	70ABg222	<4	<10	<5	55°19'42"	131°45'50"	Recrystallized porphyritic tuff (pl, fm).
19	70ABg214	<4	<10	<5	55°20'24"	131°46'32"	Recrystallized porphyry (pl, fm).
20	70ABg223	6	<10	<5	55°21'09"	131°46'43"	Recrystallized porphyritic crystal-lithic tuff (fm, pl).
21	69ABg735	10	<10	<5	55°21'31"	131°42'40"	Actinolite-epidote-chlorite-calcite schist; relict fm phenocrysts.
22	70ABg224	9	tr	<5	55°21'42"	131°47'41"	Recrystallized volcanic siltstone or crystal-lithic tuff; relict fm and pl phenocrysts, lithic fragments.
23	70ABg212	6	<10	<5	55°22'02"	131°47'12"	Recrystallized porphyritic crystal tuff (pl, fm).
24	70ABg213	14	<10	<5	55°22'12"	131°46'42"	Semischist; relict fm and pl phenocrysts.
25	69ABg612A	11	19	<5	55°25'36"	131°51'00"	Recrystallized crystal-lithic tuff (pl, fm).
26	69ABg606	tr	<10	<5	55°26'41"	131°52'39"	Recrystallized porphyritic crystal-lithic tuff (pl, fm).
27	71ABg296	8	<10	<5	55°44'08"	132°12'41"	Recrystallized agglomerate or flow breccia.
28	71ABg295	12	<10	<5	55°44'12"	132°12'35"	Phyllite; probably derived from fm-porphyritic tuff and agglomerate.

TABLE 1.—*Palladium, platinum, and rhodium analyses, rock descriptions, and locations of rock samples from the Gravina-Nutzotin belt, southern and southeastern Alaska*—Continued

Map	Sample	Parts per billion			Location		Rock descriptions
		Pd	Pt	Rh	Latitude	Longitude	
29	71AEr66	12	<10	<5	55°52'29"	132°20'45"	Recrystallized porphyritic tuff and flow(?) breccia (fm).
30	71ABg286	18	tr	<5	55°53'21"	132°19'52"	Phyllite derived from fm-porphyritic tuff (fm) and agglomerate.
31	71ABg242	<4	<10	<5	56°06'02"	132°41'41"	Porphyritic dike (pl, fm) cutting mid-Cretaceous graywacke and argillite.
32	71ABg229	11	11	<5	56°06'31"	132°42'10"	Recrystallized porphyritic sill (pl, fm) cutting mid-Cretaceous graywacke and argillite.
33	71ABg230	<4	<10	<5	56°06'58"	132°42'02"	Recrystallized tuff and agglomerate interbedded with argillite and tuffaceous graywacke.
34	71ABg231	tr	<10	<5	56°07'25"	132°42'13"	Recrystallized porphyritic flows (pl, fm), flow breccia crystal-lithic tuff, and tuffaceous graywacke.
35	71ABg232	8	<10	<5	56°11'16"	132°42'20"	Recrystallized tuff and agglomerate.
36	71ABg247	9	12	<5	56°12'20"	132°45'49"	Recrystallized porphyritic breccia (pl, fm) and tuff.
37	71ABg256	16	<10	<5	56°27'28"	132°34'37"	Recrystallized tuff and volcanic breccia.
38	71Abg260	7	19	<5	56°38'05"	132°56'47"	Phyllite derived from porphyritic tuff (fm) and agglomerate.
39	71ABg276	15	tr	<5	57°17'24"	133°26'29"	Schist derived from tuff and fine-grained agglomerate.
40	71ABg277	9	<10	<5	57°17'52"	133°26'55"	Phyllite derived from porphyritic tuff (fm, pl) and volcanic breccia.

of the samples contain palladium at levels above 4 ppb (parts per billion), 17.5 percent of the samples contain platinum at levels above 10 ppb, and no samples contain rhodium at levels above 5 ppb. Palladium concentrations range from less than 4 to 24 ppb and average 11.5 ppb for the unqualified determinations, and platinum concentrations range from less than 10 to 21 ppb and average 15.7 ppb. The average platinum-palladium ratio is 1.37 and ranges from 0.74 to 2.71. These values may be compared with results from 305 other volcanic rocks from the Columbia River Basalt Group (8 samples), andesite from Silver Peak, Nev. (6), ankaramite from Maui, Hawaii (15), Ordovician greenstone from Nevada (2), basinite from Hawaii (4), and Cambrian greenstone and other rocks from Iron Canyon, Nev. (270), which were analyzed by similar methods. Of the 305 samples, 20 percent contained palladium above 4 ppb and 1.9 percent contained platinum above 10 ppb. These relations suggest that the rocks of the Gravina-Nutzotin belt are relatively enriched in palladium and platinum compared to other volcanic rocks. For comparison, the average palladium content of samples from Iron Canyon is 3.4 ppb (137), and the average platinum content is 6.7 ppb (13) (Theodore and others, 1976).

Another comparison can be made with data given by Crocket and Skippen (1964) on rocks they called continental plateau-building and nonorogenic oceanic basalts. They analyzed 13 plateau-building basalts and 10 nonorogenic oceanic basalts from various localities. From these data they suggested that each continental plateau-building basalt province is characterized by a particular range of palladium contents and that these variations were related to the platinum-group metal content of the source materials, although differences in crystallization and generation of the magmas probably are also part of the process. Figure 2 shows that palladium concentrations from the Gravina-Nutzotin belt have a spread as wide as those found by Crocket and Skippen (1964) for all basaltic provinces and wider than those they found for a single province, but with a large proportion of the concentrations in the range between 5 and 24 ppb palladium. This suggests that the Gravina-Nutzotin rocks are relatively enriched in palladium compared to other single provinces of volcanic rocks. The source, mantle or

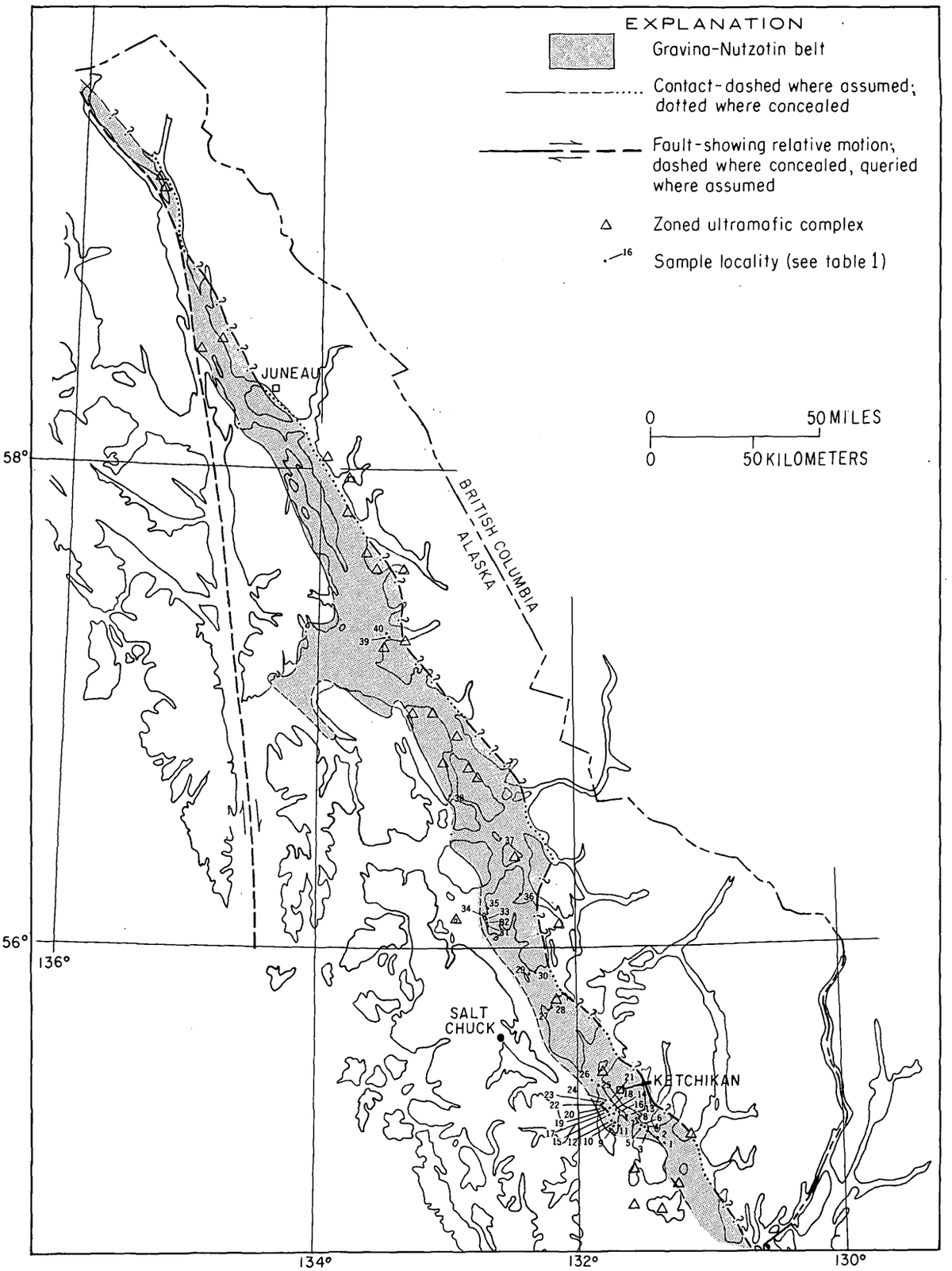

FIGURE 1.—Index map of southeastern Alaska showing Gravina-Nutzotin belt, zoned ultramafic complexes, and locations of metamorphosed volcanic and plutonic rocks sampled for platinum-group metal content. Compiled in part from Berg and others (1972) and Taylor and Noble (1969).

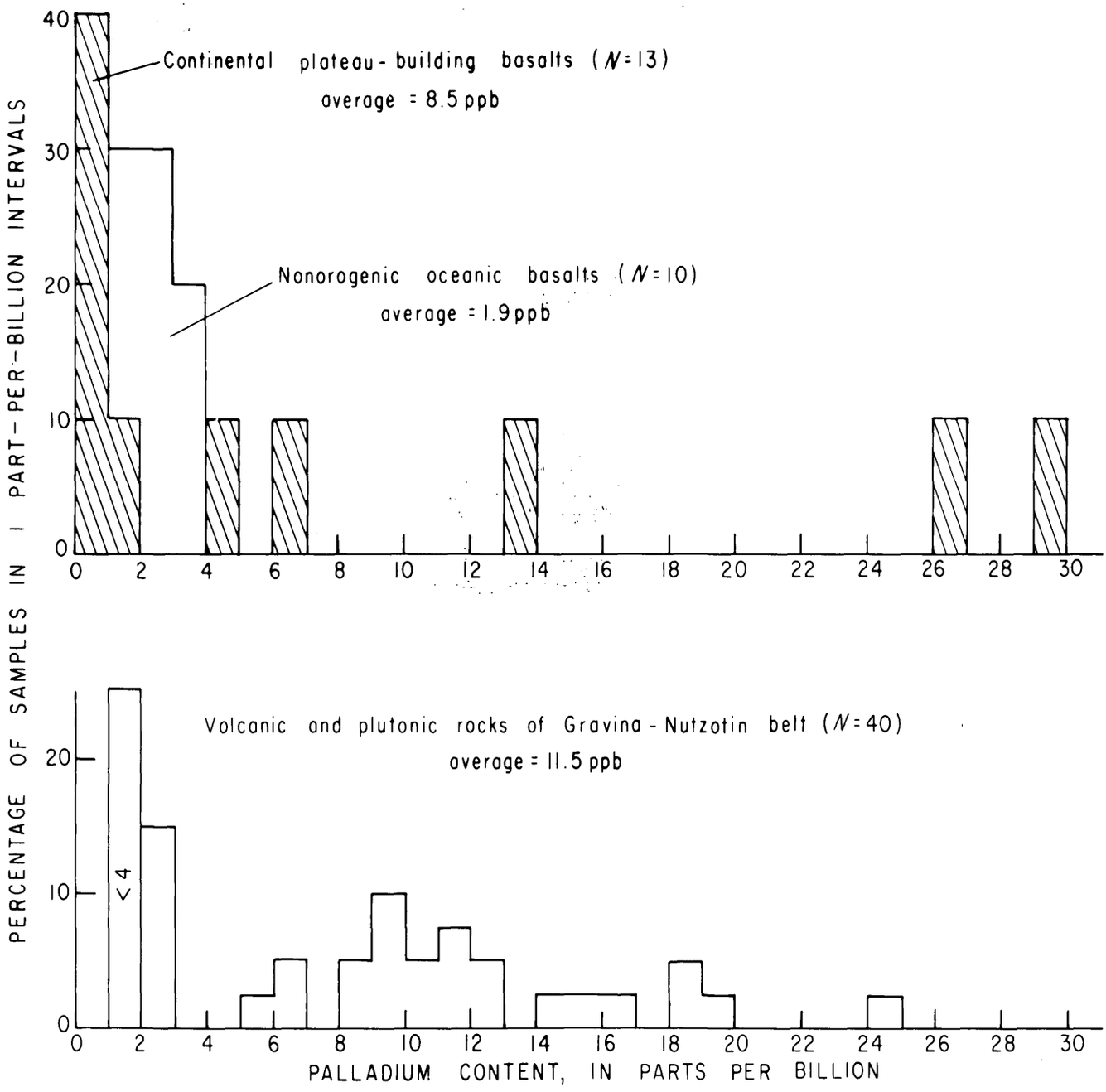

FIGURE 2.—Histograms showing percentage of samples in 1-ppb intervals of palladium comparing samples from the Gravina-Nutzotin belt with those of Crocket and Skippen (1964). *N*=number of samples.

other, must have been extremely variable over relatively short distances in the Gravina-Nutzotin belt if Crocket and Skippen's (1964) model applies. In addition, the data suggest that the geochemical cycle of rhodium must be different from that of platinum and palladium. Also, the data in table 1 demonstrate that these Gravina-Nutzotin rocks contain relatively low amounts (below detection limits) of rhodium, as is true of other rocks analyzed to date (Theodore and others, 1976).

COMPARISON OF PLATINUM-GROUP METAL DISTRIBUTIONS IN THE GRAVINA-NUTZOTIN BELT WITH THOSE IN ULTRAMAFIC COMPLEXES

Relatively sparse and variable quality data on platinum-group metal distributions determined previously

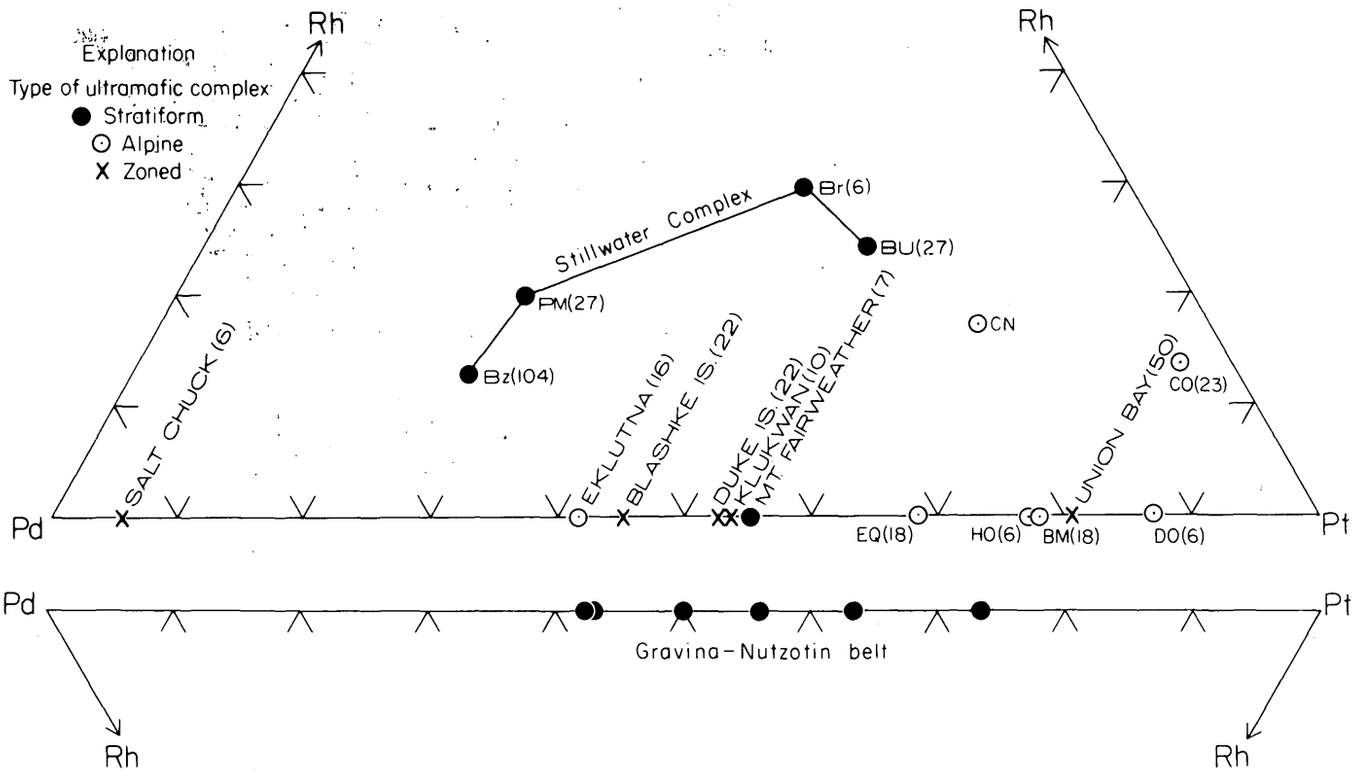

FIGURE 3.—Triangular diagram comparing platinum-palladium-rhodium ratios for ultramafic rocks from stratiform, alpine, and concentrically zoned complexes with rocks from the Gravina-Nutzotin belt. Number of samples analyzed upon which the ratio of the average is based is shown in parentheses. Bz, norites, gabbros, and cumulates from the Basal zone; PM, silicate cumulates from the Peridotite member of the Ultramafic zone; Br, cumulates from the Bronzitite member of the Ultramafic zone; BU, Banded and Upper zone cumulates; CO, chromitites from southwestern Oregon; HO, harzburgites from southwestern Oregon; DO, dunites from southwestern Oregon; CN, chromitites from New Idria and Red Mountain, Calif.; BM, dunites and hartzburgites from Burro Mountain, Calif.; EQ, serpentinized and partially serpentinized ultramafic rocks from the Eagle quadrangle, Alaska.

in different groups of rocks summarized by Crocket (1969) prevent detailed comparisons among different provinces. However, the limited numbers of modern platinum, palladium, and rhodium analyses from stratiform, alpine, and concentrically zoned ultramafic complexes allow a provisional comparison between some ultramafic complexes and rocks from the Gravina-Nutzotin belt. Analyses of rocks are available for (1) the stratiform, mafic, and ultramafic Stillwater Complex, southwestern Montana (Page, Riley, and Haffty, 1969, 1972; Page, Rowe, and Haffty, 1976), (2) the alpine ultramafic complexes of southwestern Oregon (Page and others, 1975), (3) some alpine ultramafic complexes in California (Page, 1969; Loney and others, 1971), (4) alpine ultramafic rocks from the Eagle quadrangle, east-central Alaska (Keith and Foster, 1973), and (5) concentrically zoned complexes of southern and southeastern Alaska (Clark and Greenwood, 1972). Analyses from each type of complex show a wide range of concentrations and ratios within groups of individual samples, but each type of complex appears to have a characteristic average content of platinum-group metals or a characteristic ratio of two or more of the metals.

Within this apparent framework of distinctive contents and ratios, similarities of the platinum, palladium, and rhodium distributions in the rocks from the Gravina-Nutzotin belt and in concentrically zoned ultramafic complexes are illustrated in figure 3. The similarities are lack of detectable rhodium concentrations and a moderate range of Pt/Pt+Pd ratios for individual samples with an average ratio of 57.8 for the Gravina-Nutzotin belt and 53.4 for the concentrically zoned complexes. A major dissimilarity is, of course, the levels of concentration of the two groups of rocks; the Gravina-Nutzotin belt has a much lower level than the concentrically zoned ultramafic complexes. The ratios of Pt/Pt+Pd in the Gravina-Nutzotin belt appear to have little similarity to those in alpine or stratiform complexes.

INTERPRETATION

The similarities in platinum, palladium, and rhodium distributions between the volcanic and ultramafic rocks in the Gravina-Nutzotin belt can be explained in several ways. One possibility is that different magmas derived from the same homogeneous mantle material independently formed both groups of rocks. Most of the geologic and geochemical evidence cited previously, however, suggests that this hypothesis is not tenable. Another explanation is that the same magma formed both groups of rocks and that the products of the process simply represent the extrusive and intrusive phases. If so, then the process by which the intrusive rocks accumulated throughout the belt lacked the ability to change the overall Pt/Pt+Pd ratios of the extrusive magma but did have the capacity to concentrate metals. Locally, then, the extrusive rocks should (and do) differ from their cogenetic ultramafic intrusion rocks in Pt/Pt+Pd ratio as well as in amount of platinum-group metals. A third explanation is that after extrusion and crystallization, the volcanic rocks in the Gravina-Nutzotin belt underwent changes—regional metamorphism or deuteric hydrothermal alteration—that brought their original Pt/Pt+Pd ratios close to those in the zoned ultramafic complexes. Widespread low-grade regional metamorphism did occur in the belt after or during the emplacement of the ultramafic and the volcanic rocks (Berg and others, 1972), but there is no evidence of significant metasomatism or of mobilization of metallic elements into or out of the volcanic rocks during this event (H. C. Berg, unpub. data, 1977). Therefore, this hypothesis seems unlikely.

Other interpretations involve the nature of the source material. If upper Mesozoic alpine-type ultramafic rocks in southern and southeastern Alaska (Jones and others, 1976; Plafker and others, 1976; Berg and Jones, 1974) represent the same mantle material from which the volcanic rocks and zoned complexes were generated—perhaps by fractional crystallization or fractional melting of mantle in a different tectonic setting (Berg and others, 1972)—then the moderate Pt/Pt+Pd ratios of the Gravina-Nutzotin belt and zoned ultramafic complexes reflect a selective concentration of palladium over platinum with little or no concentration of rhodium during magma generation.

REFERENCES CITED

Berg, H. C., Jones, D. L., and Richter, D. H., 1972, Gravina-Nutzotin belt-tectonic significance of an upper Mesozoic sedimentary and volcanic sequence in southern and southeastern Alaska, *in* Geological Survey research 1972: U.S. Geol. Survey Prof. Paper 800–D, p. D1–D24.

Berg, H. C., and Jones, D. L., 1974, Ophiolite in southeastern Alaska: Geol. Soc. America Abs. with Programs, v. 6, no. 3, p. 144.

Clark, A. L., and Greenwood, W. R., 1972, Geochemistry and distribution of platinum-group metals in mafic to ultramafic complexes of southern and southeastern Alaska, *in* Geological Survey research 1972: U.S. Geol. Survey Prof. Paper 800–C, p. C157–C160.

Crocket, J. H., 1969, Platinum metals, *in* Wedepohl, K. H., executive ed., Handbook of geochemistry, v. II/1: Berlin, Springer-Verlag, p. 78-B–78-0.

Crocket, J. H., and Skippen, G. B., 1964, Palladium in basaltic and ultramafic rocks: Internat. Upper Mantle Proj., Canadian Prog. Rept. (June 1963–64), p. 103.

Haffty, Joseph, and Riley, L. B., 1968, Determination of palladium, platinum, and rhodium in geologic materials by fire-assay and emission spectrography: Talanta, v. 15, p. 111–117.

Irvine, T. N., 1967, The Duke Island ultramafic complex, southeastern Alaska, *in* Wyllie, P. J., ed., Ultramafic and related rocks: New York, John Wiley & Sons, Inc., p. 84–96.

——— 1973, Bridget Cove volcanics, Juneau area, Alaska—possible parental magma of Alaskan-type ultramafic complexes: Carnegie Inst. Yearbook 72, p. 478–491.

——— 1974, Petrology of the Duke Island ultramafic complex, southeastern Alaska: Geol. Soc. America Mem. 138, 240 p.

Jones, D. L., Pessagno, E. A., Jr., and Csejtey, Bela, Jr., 1976, Significance of the upper Chulitna ophiolite for the Late Mesozoic evolution of southern Alaska: Geol. Soc. America Abs. with Programs, v. 8, no. 3, p. 385.

Keith, T. E. C., and Foster, H. L., 1973, Basic data on the ultramafic rocks of the Eagle quadrangle, east-central Alaska: U.S. Geol. Survey Open-File Rept. 581, 4 sheets.

Lanphere, M. A., 1968, Sr-Rb-K and Sr isotopic relationships in ultramafic rocks, southeastern Alaska: Earth and Planetary Sci. Letters, no. 4, p. 185–190.

Lanphere, M. A., and Eberlein, G. D., 1966, Potassium-argon ages of magnetite-bearing ultramafic complexes in southeastern Alaska: Geol. Soc. America Spec. Paper 87, p. 94.

Loney, R. A., Himmelberg, G. R., and Coleman, R. G., 1971, Structure and petrology of the Alpine-type peridotite at Burro Mountain, California, U.S.A.: Jour. Petrology, v. 12, no. 2, p. 245–309.

Naldrett, A. J., and Cabri, L. J., 1975, Ultramafic and related rocks—their classification and genesis with special reference to the occurrence of nickel sulfides and platinum-group elements: Soc. Econ. Geologists Internat. Platinum Symposium Program and Abs., p. 12–14.

Page, N. J, 1969, Platinum content of ultramafic rocks, *in* U.S. Geological Survey heavy metals program progress report 1968—topical studies: U.S. Geol. Survey Circ. 622, p. 5.

Page, N. J, Johnson, M. G., Haffty, Joseph, and Ramp, Len, 1975, Occurrence of platinum group metals in ultramafic rocks of the Medford-Coos 2° quadrangles, southwestern Oregon: U.S. Geol. Survey Misc. Field Studies Map MF-694, scale 1:250 000.

Page, N. J, Riley, L. B., and Haffty, Joseph, 1969. Platinum, palladium, and rhodium analyses of ultramafic and mafic rocks from the Stillwater Complex, Montana: U.S. Geol. Survey Circ. 624, 12 p.

——— 1972, Vertical and lateral variation of platinum, palladium, and rhodium in the Stillwater Complex, Montana: Econ. Geology, v. 67, no. 7, p. 915–924.

Page, N. J, Rowe, J. J., and Haffty, Joseph, 1976, Platinum metals in the Stillwater Complex, Montana: Econ. Geology, v. 71, p. 1352–1363.

Plafker, George, Hudson, Travis, Jones, D. L., and Berg, H. C., 1976, The Border Ranges fault system in the Saint Elias Mountains and Alexander Archipelago, Alaska: U.S. Geol. Survey Circ. 733, p. 14–16.

Taylor, H. P., Jr., and Noble, J. A., 1969, Origin of magnetite in the zoned ultramafic complexes of southeastern Alaska, *in* Wilson, H. D. B., ed., Magmatic ore deposits: Econ. Geology Mon. 4, p. 209–230.

Theodore, T. G., Venuti, P. E., Page, N. J, and Carlson, R. R., 1976, Maps showing geochemical distribution of palladium and other elements in rocks at Iron Canyon, Lander County, Nevada: U.S. Geol. Survey Misc. Field Studies Map MF–790.

Jour. Research U.S. Geol. Survey
Vol. 5, No. 5, Sept.–Oct. 1977, p. 637–642

OCCURRENCE OF BLOEDITE AND RELATED MINERALS IN MARINE SHALE OF DIABLO AND TEMBLOR RANGES, CALIFORNIA

By K. J. MURATA, Menlo Park, Calif.

Abstract.—Bloedite, epsomite, and related minerals occur in small amounts throughout the arid eastern foothills of the Diablo and Temblor Ranges, as efflorescences on siliceous shale and as deposits around small springs and a brine pond. These minerals ultimately are products of weathering of underlying organic shale, and they are reminders that the chemistry of weathering of reduced organic shale is largely a reversal of the chemistry of its early diagenesis.

Bloedite, $Na_2Mg(SO_4)_2 \cdot 4H_2O$, has been found as a widespread efflorescent mineral in Miocene Monterey Shale and other siliceous formations in the arid Temblor and Diablo Ranges of California. The presence of the mineral was first noted incidentally in whole-rock X-ray diffraction patterns of shales prepared during a recent study of diagenetic silica minerals (Murata and Larson, 1975).

Previously, bloedite was known in California only as a saline deposit in desert playas (Murdoch and Webb, 1966), and the large crystals recovered from the mud of Soda Lake (Schaller, 1913; Gale, 1914) immediately to the west of Temblor Range (fig. 1, loc. 9) are examples of this mode of occurrence. Arnold and Johnson (1909) early surmised that the salts of Soda Lake had been leached out of the marine sedimentary formations of the surrounding ranges. This report confirms the presence and describes the characteristics of bloedite and related minerals in some of these formations.

The presence of minor bloedite in caliche such as that of the Chilean nitrate deposits is well known (Wetzel, 1928; Palache and others, 1951). J. F. McAllister of the U.S. Geological Survey, Menlo Park, Calif., has called attention (written commun., June 1976) to an undescribed occurrence of efflorescent bloedite that he found in the Pliocene continental Furnace Creek Formation (McAllister, 1970) of Death Valley, Calif.

The treeless eastern foothills of the Temblor and Diablo Ranges, where bloedite occurs, have an annual rainfall of 250 mm or less, most of which occurs during the winter (December through March). Runoff is brief

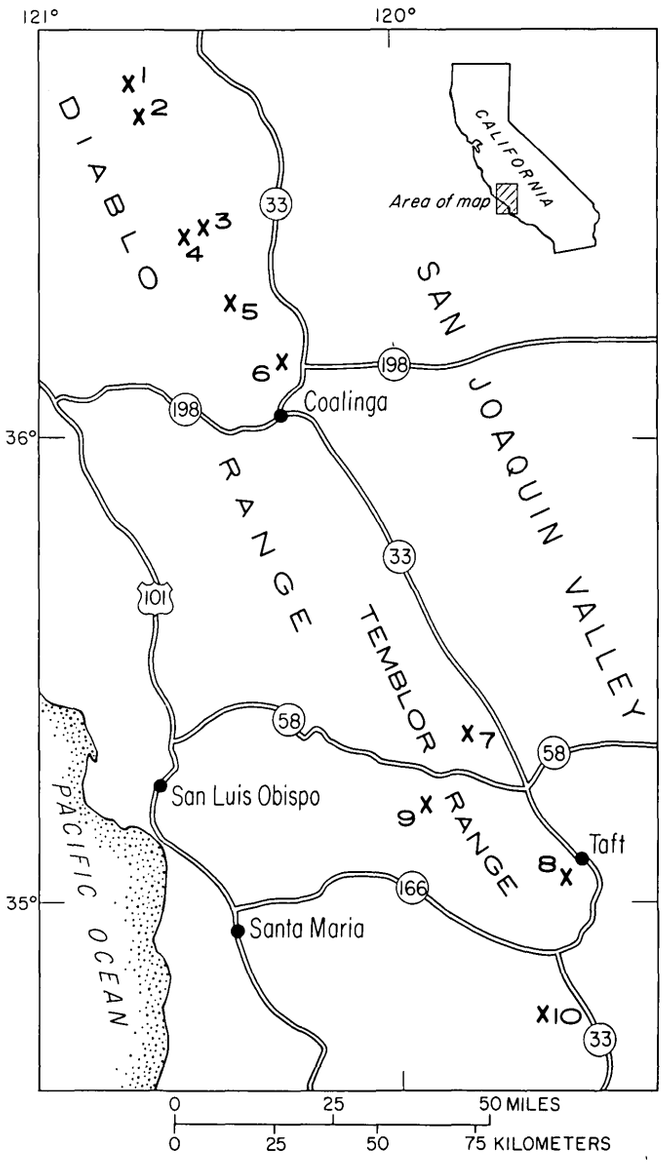

FIGURE 1.—Index map of part of California showing localities of bloedite and related minerals. The particulars of the localities are given in table 1. The apparent absence of the minerals between localities 6 and 7 is largely due to the fact that this interval was not studied in detail.

and rapid and accumulates as ephemeral lakes or disappears into the alluvium of San Joaquin Valley. Part of the rainfall penetrates a meter or so into the sedimentary rocks, especially porous, siliceous shale, of the foothills; it then slowly returns to the surface as a diffuse capillary flow in response to surface evaporation during the dry season or as a rare localized discharge in the form of a small spring (Richards and Richards, 1957; Wood and Dale, 1964).

During its subterranean migration, this vadose water dissolves various constituents from the rocks and eventually deposits them at or near the surface as evaporite minerals, such as gypsum, calcite, halite, bloedite, and epsomite. Valuable surficial deposits of gypsite have formed in this way on Monterey Shale and related rocks of the region and have been mined extensively (Ver Planck. 1952). The minor amount of bloedite present in the outcropping rocks seems worthy of attention because of the novelty of this mode of occurrence for the mineral and because of the significance of bloedite in the geochemistry of interstitial water of marine shales.

Acknowledgments.—I thank colleagues J. H. Feth, J. F. Poland, and G. I. Smith for valuable advice regarding the hydrology of arid regions and D. W. Brown for chemical analysis of the brines.

LOCALITIES AND MODES OF OCCURRENCE OF BLOEDITE AND RELATED MINERALS

Only a few patches of efflorescent bloedite and (or) epsomite ($MgSO_4 \cdot 7H_2O$) were found at most of the localities shown in figure 1 and table 1, but bloedite occurs along a section of Monterey Shale 3 km thick at locality 7 and along a section 0.5 km thick at locality 8. These two localities were sampled in much detail in an earlier study (Murata and Larson, 1975), and it is likely that more bloedite would be found at the other localities if they were sampled as intensively.

The general mode of occurrence of bloedite is illustrated by means of samples (fig. 2) from locality 7. The mineral forms small globular clusters within porous, siliceous shale (fig. 2*A*) or grows as efflorescent rosettes and dendrites on surfaces of fractures (fig. 2*B*, *C*). The generally dark color of the aggregates may result from the hygroscopic nature of bloedite or of an accompanying saline mineral. The efflorescent epsomite of locality 6 closely resembles bloedite. Springs at localities 5 and 10 deposit crusts of bloedite and (or) epsomite along margins of a small discharge that, during the dry season, evaporates completely within a distance of a few tens of meters.

A small (about 15-m-diameter) pond of dense brine at locality 4 seems to be a miniature of the previously mentioned Soda Lake. To date, only mirabilite, thenardite, hydroglauberite, and halite have been found in the pond, but the pond brine deposits much bloedite as well when allowed to evaporate in the laboratory at 25°C. Halite is present in samples from all localities but will not be discussed further.

TABLE 1.—*Data on localities of bloedite and related minerals shown on figure 1*

Locality	Lat N., long W.	Nature of occurrence
	Merced County	
1. Unnamed arroyo 1 km south of Laguna Seca Creek.	36°53', 120°48'	Bloedite efflorescence on Eocene and Oligocene Kreyenhagen Shale.
	Fresno County	
2. Unnamed arroyo 1.5 km north of Wildcat Canyon.	36°50',120°47'	Bloedite efflorescence on Upper Cretaceous and Paleocene Moreno Shale.
3. Tumey Gulch - - - - - - - -	36°34', 120°37'	Bloedite efflorescence on Eocene and Oligocene Kreyenhagen Shale.
4. Tumey Gulch - - - - - - - -	36°33', 120°38'	Brine pond fed by a small spring in middle Eocene Domengine Formation.
5. Cantua Creek - - - - - - -	36°25', 120°34'	Bloedite deposited from a small spring in Upper Cretaceous and Paleocene Moreno Shale.
6. Oil City area - - - - - -	36°15',120°22'	Epsomite efflorescence on shale of Oligocene and Miocene Temblor Formation.
	Kern County	
7. Chico Martinez Creek - - -	35°26', 119°47'	Bloedite efflorescence on Miocene Monterey Shale.
8. Taft area - - - - - - - - -	35°06',119°31'	Do.
	San Luis Obispo County	
9. Soda Lake - - - - - - - - -	35°13', 119°53'	Large crystals of bloedite in playa mud (Schaller, 1913).
	Santa Barbara County	
10. Alamo Canyon - - - - - - -	34°46', 119°35'	Epsomite and bloedite deposited from a small spring in Miocene Monterey Shale.

IDENTIFICATION OF BLOEDITE AND EPSOMITE

The X-ray powder diffraction data obtained on bloedite from the several localities are identical to those published for the mineral by the Joint Committee on Powder Diffraction Standards (Berry, 1974), so they are not presented here. A chemical analysis (table 2, sample 1) of a water extract of the crystals shown in figure 2*C*, when corrected for minor amounts of chloride and bicarbonate, yields molecular ratios of $Na:Mg:SO_4$ of 1.83:1.02:2.00, which agree moderately well with the theoretical ratios of 2.00:1.00:2.00. A small amount of a magnesium sulfate mineral (such as hexahydrite, $MgSO_4 \cdot 6H_2O$), undetectable through X-ray diffraction, may be present to cause an apparent deficiency in sodium, but the chemical analysis adequately supports the X-ray identification of bloedite.

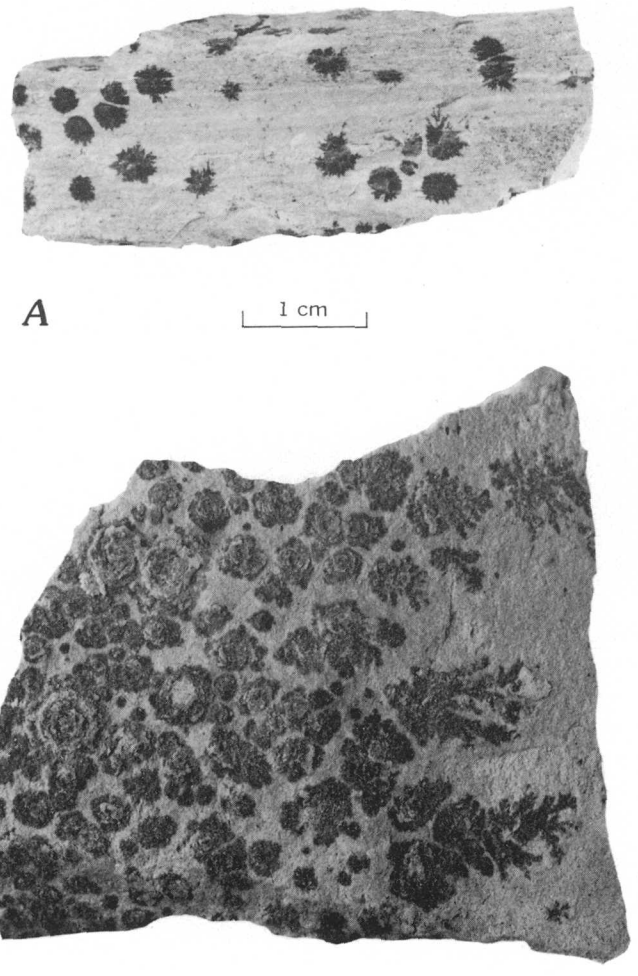

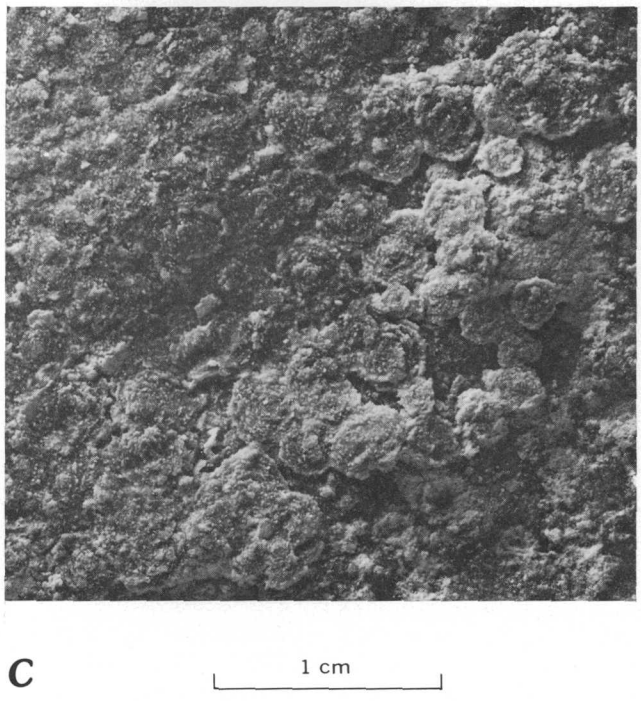

FIGURE 2.—Modes of occurrence of bloedite in Monterey Shale of Chico Martinez Creek. *A*, Section perpendicular to the bedding, showing stellated globules of bloedite within porcelanite. *B*, Rosettes and dendrites developed on a parting in diatomaceous mudstone. *C*, Coalescing thin rosettes forming a virtually continuous crust about 2 mm thick on a parting surface in diatomaceous mudstone.

Only an aggregate refractive index of 1.485 could be measured on the tiny crystals of bloedite, which were generally much contaminated with clays, diatoms, and other components of siliceous shale.

Epsomite was identified by its X-ray diffraction pattern (Berry, 1974) and by its characteristic alteration to hexahydrite upon exposure to dry air for a few days.

SODIUM SULFATE WATERS OF THE REGION AND ORIGIN OF BLOEDITE

Sodium sulfate waters ranging in salinity from 500 to 7000 ppm represent the most common type of water in streams, springs, and wells of the region, especially as drainage out of marine sedimentary rocks of Tertiary age (Wood and Davis, 1959). The composition of such a water from a spring in Miocene Monterey Shale is shown in analysis 4 of table 2 and in figure 3*E*. During evaporation of this water, the moderate amounts of calcium and bicarbonate could be largely eliminated through precipitation as calcite. In sulfate waters poor in bicarbonate, calcium could also be removed as gypsum, resulting eventually in a sodium-magnesium-sulfate brine that could deposit bloedite.

Brines containing very different proportions of sodium, magnesium, and sulfate can deposit bloedite (Wood, 1975). One such brine could theoretically be generated through isothermal evaporation of seawater (fig. 3*A*) at 25°–40°C, in absence of reaction at transition points (Borchert, 1940; Stewart, 1963; Braitsch, 1971). At 25°C, a small amount of bloedite would deposit along with halite from the brine (fig. 3*B*) that was left after 98 percent of the original water was evaporated and after virtually all calcium and about 90 percent of the original sodium chloride had precipitated (Braitsch, 1971, p. 86). If there is complete reaction at the transition points, no bloedite is obtained, the only magnesium-bearing sulfate produced being kieserite, $MgSO_4 \cdot H_2O$. In fact, primary bloedite is rare in deposits of oceanic salts.

The compositions of the bloedite-depositing pond brine (analysis 3, table 2) and spring water (analysis 2, table 2) are shown in figures 3*C* and 3*F*, respectively. These waters contain smaller percentages of magnesium than the residual seawater brine (fig. 3*B*) but are as rich in sodium and much richer in sulfate. These

TABLE 2.—*Chemical analyses of a water leachate of crude bloedite and of sodium-magnesium-sulfate spring and pond waters*

[ppm, parts per million; epm, equivalents per million. Analyst for 1-3: D.W. Brown; analysis 4: Wood and Davis (1959).]

	1		2		3		4	
	ppm	epm	ppm	epm	ppm	epm	ppm	epm
Ca	0	0.0	720	35.9	315	15.7	230	11.5
Mg	1,130	92.9	660	54.3	16,200	1,330	181	14.9
Na	2,120	92.2	3,300	143.5	80,800	3,510	430	18.7
K	10	0.2	43	1.1	1,500	38.4	10	.3
HCO_3	16	0.3	750	12.3	5,360	87.8	337	5.5
CO_3	0	0.0	3	.1	12	0.4	0	0.0
SO_4	8,740	181.9	10,100	210.2	134,000	2,790	1,560	32.5
Total	12,300	- -	16,100	- -	305,000	- -	2,830	- -
	1		2		3		4	
pH	6.60		7.88		7.67		7.7	
Density at 20°C (g/mL)	1.03		1.01		1.30		- -	
Date collected	- -		11-18-75		9-7-75		11-8-55	

1. Water leachate of bloedite crystals that were scraped off specimen shown in figure 2C, from locality 7 of table 1.
2. Water of bloedite-depositing spring at locality 5 of table 1.
3. Water of a small brine pond at locality 4 of table 1.
4. Water of spring 29-21-33E issuing from Monterey Shale in the area of locality 8 of table 1.

compositional differences largely explain the frequent occurrence of mirabilite and thenardite and their association with bloedite in continental but not in oceanic salt deposits.

Rather early in postdepositional history, marine sediments rich in organic matter undergo microbial and inorganic reactions that increase bicarbonate and decrease sulfate and magnesium in the pore water (White, 1965; Presley and Kaplan, 1968; Sayles and Manheim, 1975; among others). Dissolved sulfate is reduced to sulfide that is immobilized and accumulated in the sediment as pyrite. Magnesium is depleted through formation of dolomite or montmorillonite (Braitsch, 1971; Gieskes and others, 1975). Altered seawater of this kind is widely represented among brines of oil fields of the region shown in figure 1 (Weddle, 1968; Sullivan, 1971), and the brine (fig. 3*D*) produced from Monterey Shale (Antelope Member of local usage) in the Buena Vista Hills field (Weddle, 1968, table 1) is typical. The low content of sulfate and magnesium precludes such a pore water having a direct role in the formation of bloedite in the surface rocks.

When orogenic movements raise the reduced sediments out of the sea, oxygenated meteoric waters flush out the altered pore water and decompose the diagenetic minerals that had formed under reducing conditions. Oxidation of pyrite produces sulfuric acid and a limonite oxidate. The sulfuric acid decomposes dolomite or montmorillonite to bring magnesium back into solution. Calcium derived from dolomite could be precipitated as gypsum or calcite or fixed in sodium-montmorillonite through cation exchange.

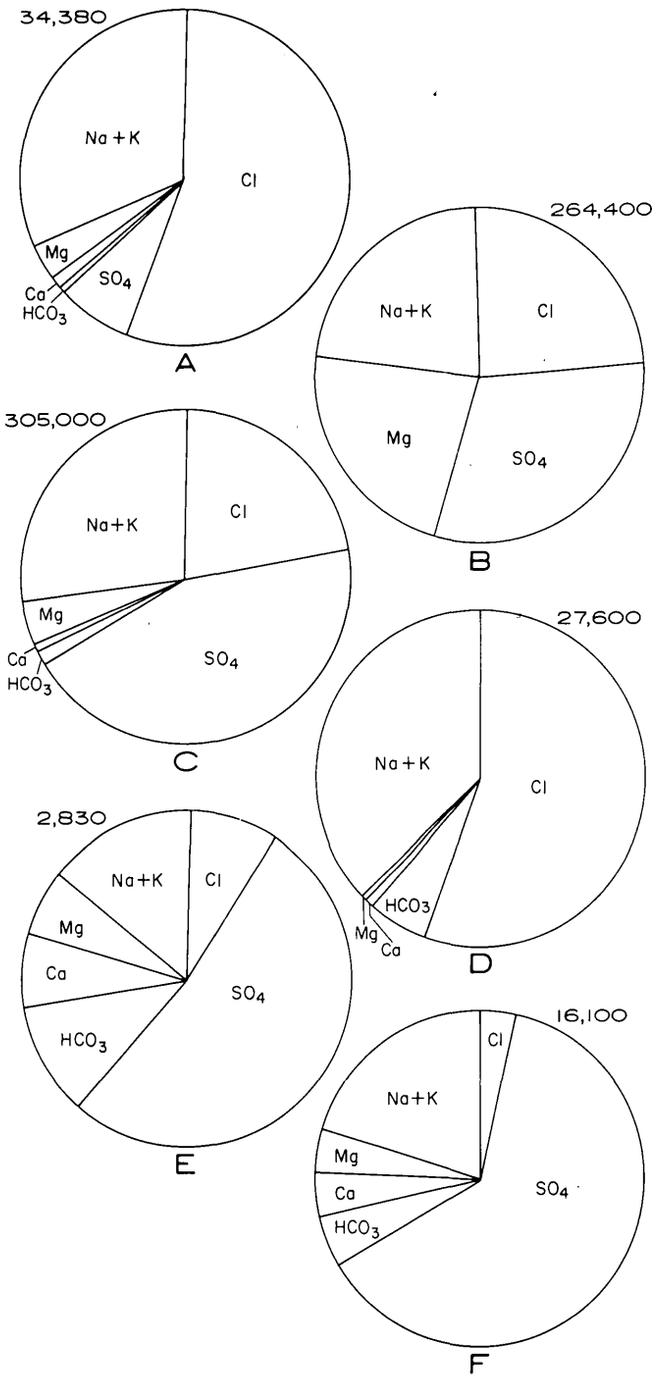

FIGURE 3.—Composition (weight percent of total dissolved matter) of bloedite-depositing brines and of comparison waters. The number over each diagram gives the total dissolved matter (ppm) in the particular water. *A*, Seawater. *B*, Residual brine from evaporation of seawater, which could deposit bloedite. *C*, Bloedite-depositing brine of pond; analysis 3 of table 2. *D*, Typical oil-field brine from the Monterey Shale of Buena Vista Hills field (Weddle, 1968). *E*, Spring water; analysis 4 of table 2. *F*, Bloedite-depositing spring water; analysis 2 of table 2.

The excess of sodium chloride would be precipitated during prolonged evaporation at or near the surface, and a bittern rich in sulfate of magnesium and sodium would separate by moving away from the precipitated halite. Fractional crystallization of this sort, repeated through a series of wet and dry seasons, could separate bloedite and epsomite from most other salts.

Bloedite and related minerals thus appear to be mainly products of weathering of reduced organic shale, taking place in a land of little rain. These minor minerals are reminders that the chemistry of weathering of organic shale is largely a reversal of the chemistry of early diagenesis of this shale.

REFERENCES CITED

Arnold, Ralph, and Johnson, H. R., 1909, Sodium sulphate in Soda Lake, Carrizo Plain, San Luis Obispo County, California: U.S. Geol. Survey Bull. 380, p. 369–371.

Berry, L. G., ed., 1974, Selected powder diffraction data for minerals: Swarthmore, Pa., Joint Comm. Powder Diffraction Standards, 833 p.

Borchert, Hermann, 1940, Die Salzlagerstaetten des deutschen Zechsteins [Salt deposits of the German Zechstein]: Archiv fuer Lagerstaettenforschung, no. 67, 196 p.

Braitsch, Otto, 1971, Salt deposits, their origin and composition: New York, Springer-Verlag, 297 p.

Gale, H. S., 1914, Sodium sulphate in the Carrizo Plain, San Luis Obispo County, California: U.S. Geol. Survey Bull. 540, p. 428–433.

Gieskes, J. M., Kastner, Miriam, and Warner, T. B., 1975, Evidence for extensive diagenesis, Madagascar Basin, Deep Sea Drilling site 245: Geochim. et Cosmochim. Acta, v. 39, no. 10, p. 1385–1393.

McAllister, J. F., 1970, Geology of the Furnace Creek borate area, Death Valley, Inyo County, California: California Div. Mines and Geology, map sheet 14.

Murata, K. J., and Larson, R. R., 1975, Diagenesis of Miocene siliceous shales, Temblor Range, California: U.S. Geol. Survey Jour. Research, v. 3, no. 5, p. 553–566.

Murdoch, Joseph, and Webb, R. W., 1966, Minerals of California—Centennial volume (1866–1966): California Div. Mines and Geology Bull. 189, 559 p.

Palache, Charles, Berman, Harry, and Frondel, Clifford, 1951, The system of mineralogy of James Dwight Dana and Edward Salisbury Dana, v. 2: New York, John Wiley & Sons, 1124 p.

Presley, B. J., and Kaplan, I. R., 1968, Changes in dissolved sulfate, calcium, and carbonate from interstitial water of near-shore sediments: Geochim. et Cosmochim. Acta, v. 32, no. 10, p. 1037–1048.

Richards, L. A., and Richards, S. J., 1957, Soil moisture, *in* Soil, the yearbook of agriculture, 1957: U.S. Dept. Agriculture, p. 49–60.

Sayles, F. L., and Manheim, F. T., 1975, Insterstitial solutions and diagenesis in deeply buried marine sediments: results from the Deep Sea Drilling Project: Geochim. et Cosmochim. Acta. v. 39, no. 2, p. 103–127.

Schaller, W. T., 1913, Immense bloedite crystals: Washington Acad. Sci. Jour., v. 3, no. 3, p. 75–76.

Stewart, F. H., 1963, Marine evaporites, *in* Fleischer, Michael, ed., Data of geochemistry: U.S. Geol. Survey Prof. Paper 440–Y, 53 p.

Sullivan, J. C., 1971, Oil and gas field waters in central San Joaquin Valley, Fresno, Kings, and Madera Counties, California: California Div. Oil and Gas, Summ. Operations, California Oil Fields, v. 57, no. 1, p. 29–43.

Ver Planck, W. E., Jr., 1952, Gypsum in California: California Div. Mines and Geology Bull. 163, 151 p.

Weddle, J. R., 1968, Oilfield waters in southwestern San Joaquin Valley, Kern County, California, *in* Guidebook: Am. Assoc. Petroleum Geologists–Soc. Econ. Geophysicists–Soc. Econ. Paleontologists and Mineralogists, Pacific Secs., 43d Ann. Mtg. 1968, p. 25–32.

Wetzel, W., 1928, Die Salzbildungen der Chilenischen Wueste [Salt formations of the Chilean desert]: Chemie der Erde, v. 3, p. 375–436.

White, D. E., 1965, Saline waters of sedimentary rocks, *in* Fluids in subsurface environment—A symposium: Am. Assoc. Petroleum Geologists Mem. 4, p. 342–366.

Wood, J. R., 1975, Thermodynamics of brine-salt equilibria—I. The systems NaCl–KCl–$MgCl_2$–$CaCl_2$–H_2O and NaCl–$MgSO_4$–H_2O at 25°C: Geochim. et Cosmochim. Acta, v. 39, no. 8, p. 1147–1163.

Wood, P. R., and Dale, R. H., 1964, Geology and ground-water features of the Edison-Maricopa area, Kern County, California: U.S. Geol. Survey Water-Supply Paper 1656, 108 p.

Wood, P. R., and Davis, G. H., 1959, Groundwater conditions in the Avenal-McKittrick area, Kings and Kern Counties, California: U.S. Geol. Survey Water-Supply Paper 1457, 141 p.

Jour. Research U.S. Geol. Survey
Vol. 5, No. 5, Sept.–Oct. 1977, p. 643–649

COMPARISON OF GRANITIC INTRUSIONS IN THE PELONA AND OROCOPIA SCHISTS, SOUTHERN CALIFORNIA

By FRED K. MILLER and DOUGLAS M. MORTON, Menlo Park, Calif.

Abstract.—Dating of some small plutons in the San Gabriel and Chocolate Mountains, southern California, yields Miocene K-Ar ages. A single granodiorite pluton that has been segmented by branches of the San Jacinto fault intrudes the Pelona Schist and yields ages of 14.0 to 18.6 million years. Several quartz monzonite plutons in the Chocolate Mountains, 235 kilometers to the southeast and on the opposite side of the San Andreas fault, yield ages ranging from 20.0 to 23.4 m.y. At least one pluton in the Chocolate Mountains intrudes the Orocopia Schist, a probable equivalent of the Pelona Schist. Chemical, modal, textural, mineralogical, and apparent K-Ar age differences suggest that the two groups of plutons are not offset parts of a single body, but the differences do not preclude the two groups from being related in a general way.

Granitic plutons yielding Miocene K-Ar ages include the Pelona Schist in the eastern San Gabriel Mountains and the Orocopia Schist about 235 km to the southeast in the southern Chocolate Mountains. The Miocene ages are unusually young for plutonic rocks in the southern California region if previously reported ages are representative. A middle Miocene pluton intrudes the Pelona Schist in the San Gabriel Mountains and has been segmented into several separated bodies by strike-slip faults. Several early Miocene plutons are distinguishable from one another in the Chocolate Mountains. Textural and compositional comparisons, in addition to the age difference, suggest, but not unequivocally so, that the plutons in the San Gabriel and Chocolate Mountains are not offset equivalents along the San Andreas fault.

THE PELONA-OROCOPIA AGE PROBLEM

The Pelona-Orocopia-type rocks are lowgrade but pervasively metamorphosed schist, greenstone, quartzite, and carbonate rocks that are exposed as large isolated bodies at widely separated localities on both sides of the San Andreas and Garlock faults (fig. 1). Other schist units, the Rand Schist in the Rand Mountains and the Catalina Schist, shown in figure 11, have been proposed as Pelona equivalents by Hershey (1912) and Shoellhamer and Woodford (1951), respectively. Although the Rand is generally accepted as correlative with the Pelona, the correlation between the Catalina Schist and the Pelona is open to considerable question.

The original intent in dating the plutonic rocks that intrude the schists was to establish a minimum age for the schists. The problem of correlating the various schist bodies that have different names at different places has occupied the attention of many geologists over the past six decades, primarily because the schist units offer potential as indicators of offset along the San Andreas fault and secondarily because they represent a major, apparently widespread, but poorly understood, period of depositional and metamorphic history. Attempts at positive correlation, however, have been frustrated by the destruction of sedimentary features by metamorphism and the lack of fossils or reliable isotopic age data. Without fossil evidence, distinctive marker beds or zones, or other unique features within the schists, it has been impossible to match presumed offset bodies of schist on opposite sides of the San Andreas fault (for example, Hill and Dibblee, 1953, and Crowell, 1962).

Although the Miocene ages establish only a very young minimum age for the schists, they provide the only reliable isotopically determined upper limit obtained to date. The Pelona-Orocopia type rocks occur in a region where large and numerous Mesozoic plutons are found, although there is no documented intrusive relation between the schists and a Mesozoic pluton. Even though only Tertiary plutonic rocks are known to intrude the schists, this does not preclude the possibility that the schist or schist protolith is older than the Mesozoic plutonic activity in the region because the contacts between the schists and all pre-Tertiary rocks are faults (Ehlig, 1968; Dillon,

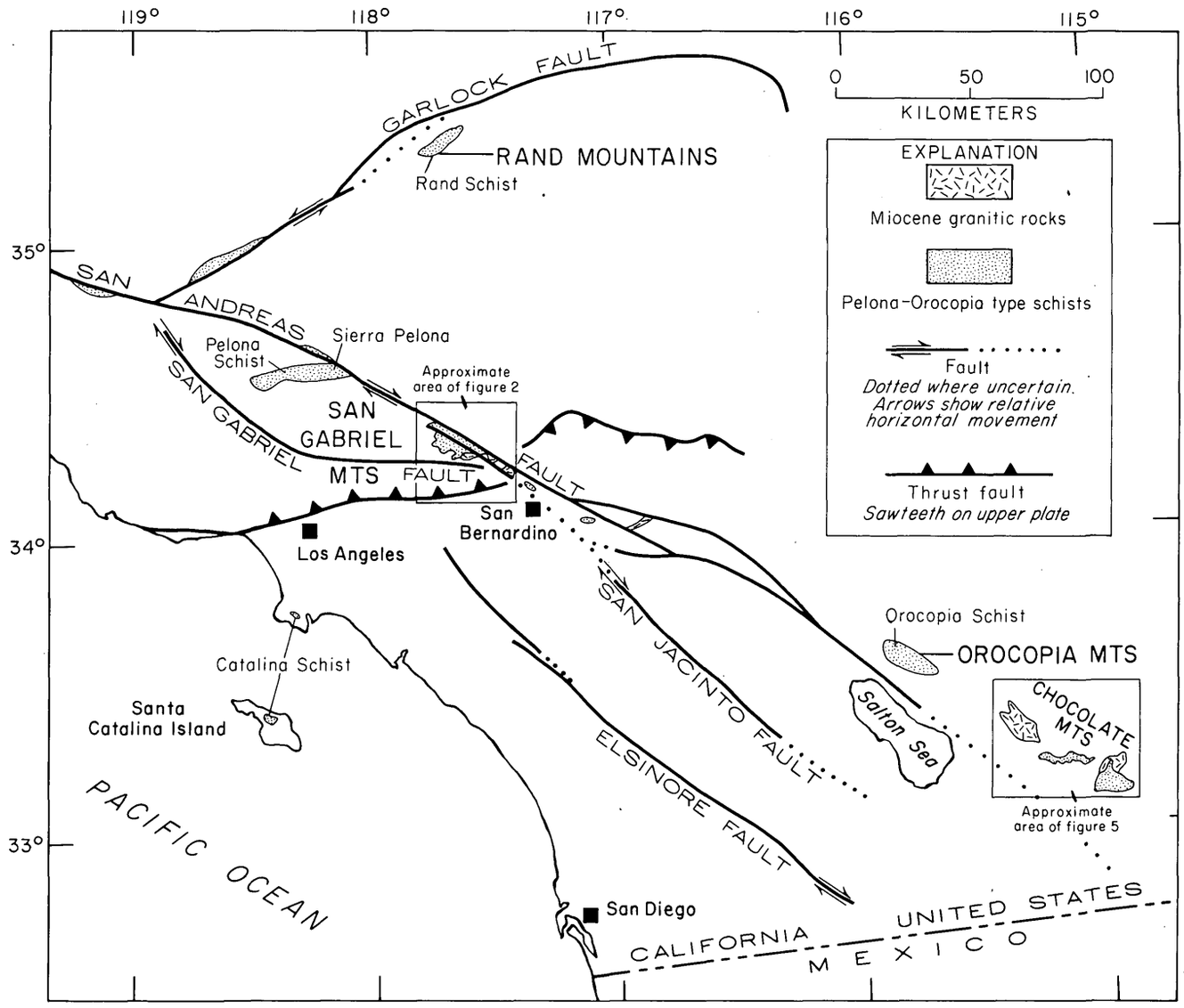

FIGURE 1.—Location of Pelona-Orocopia-type rocks in southern California. Size of smaller occurrences is exaggerated to show on map.

1975).[1] The protolith could have been deposited before, during, or after emplacement of the Mesozoic plutons, and the two subsequently were juxtaposed by thrust faulting to their present relative positions. The dating of the Miocene pluton also puts an upper age limit on the time of thrusting that placed the pre-Tertiary crystalline rocks over the Pelona Schist in the eastern San Gabriel Mountains. The thrust fault is clearly cut by the pluton, and the pluton displays none of the fabric developed in the rocks above or below the fault or in the mylonite zone that separates them.

[1] R. W Kistler (oral commun., 1976) has obtained a K–Ar date of 18.2 m.y. on biotite and 74.2 m.y. on coexisting hornblende from a plutonic rock intrusive into the Rand Schist collected about 1 km south of Randsburg in the Rand Mountains. He considers the biotite date to be a reset age and the hornblende date to be a minimum age.

PLUTONIC ROCK IN THE EASTERN SAN GABRIEL MOUNTAINS

The Miocene pluton in the eastern San Gabriel Mountains underlies 20 km² between Telegraph Peak and Cajon Canyon. It has been segmented into three sparate bodies by branches of the San Jacinto fault (fig. 2). The rock is a distinctive uniform-appearing medium- to coarse-grained biotite granodiorite; apparent textural variations are noticeable only along parts of the intrusive margins where finer grained porphyritic textures are developed in the outermost 30 m. The rock is conspicuously nonfoliate in contrast to the host rocks and other nearby plutonic and gneissic rocks.

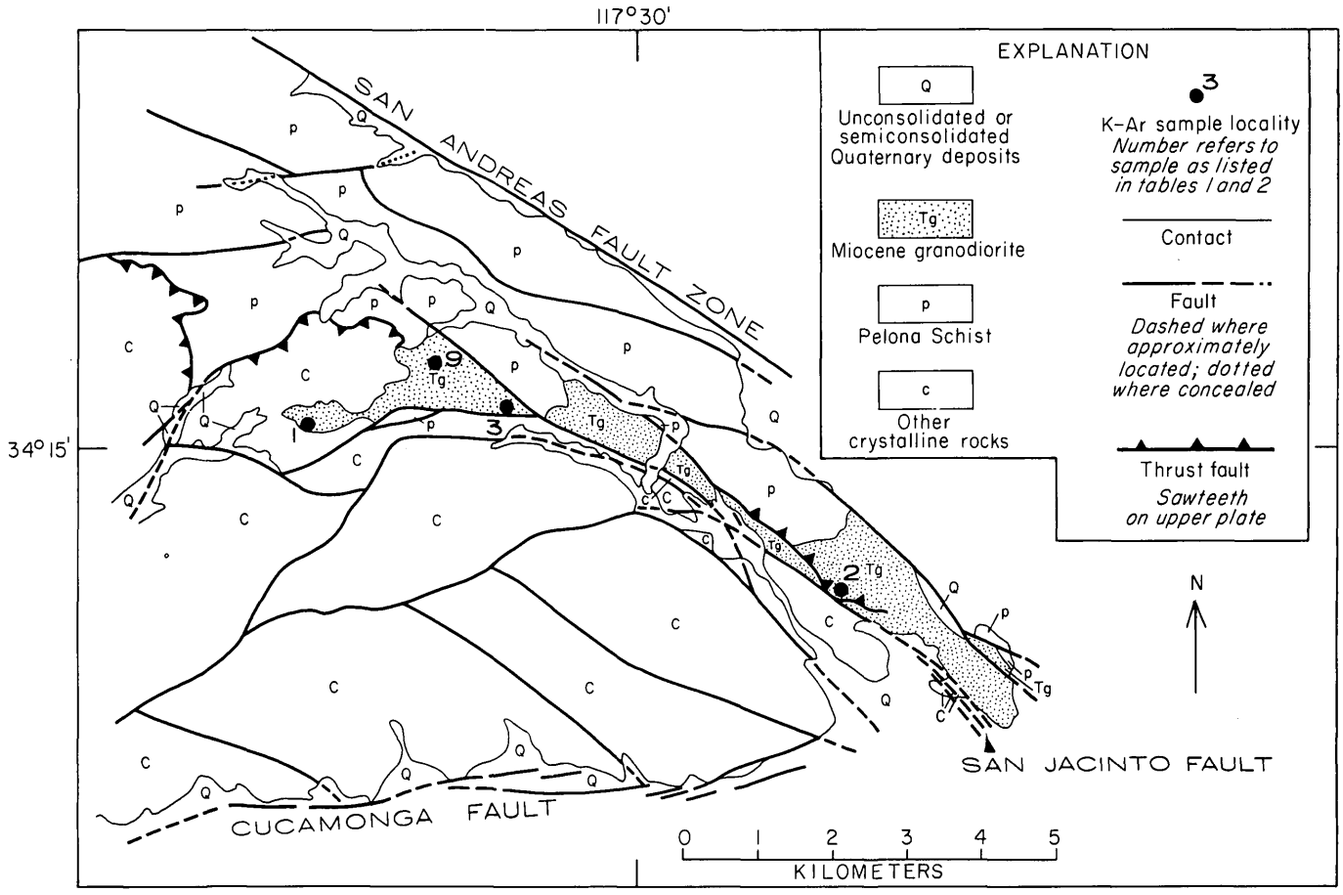

FIGURE 2.—Simplified geologic map of the eastern part of the San Gabriel Mountains showing K-Ar sample localities.

The compositional uniformity of the pluton is reflected in a small field defined by the modes in figure 3. Small-scale (25-mm-thick) irregularly shaped plagioclase (An_{25})-rich zones and potassium-feldspar (microcline)-rich zones are noticeable on stained slabs, however, and necessitate that large areas be counted. Except for some rock at the pluton margin, the granodiorite has a normal granitic texture. It is nonporphyritic but is characterized by semiround quartz crystals or crystal aggregates slightly larger than the other minerals and suggestive of beta quartz. Biotite, the only mafic mineral, averages about 8 percent of the rock. Accessory minerals are zircon, apatite, sphene, opaque minerals, and sparse garnet. Figure 4*A* illustrates the typical texture of this rock and shows the difference between it and the typical Chocolate Mountains rock (fig. 4*B*).

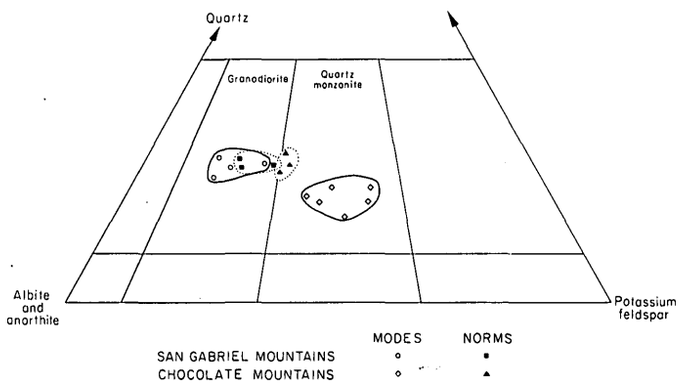

FIGURE 3.—Modes and norms of rocks from Chocolate and San Gabriel Mountains.

Analyses 1, 2, and 3 in table 1 show the chemical variation within the parts of the pluton sampled. Of all the major constituents, only K_2O and Na_2O show any particular variation from one sample to another. This variation may be a function of the inhomogeneity of feldspar distribution as shown in the stained slabs. In all samples, however, the ratio of Na_2O to K_2O is greater than 1.

PLUTONIC ROCKS IN THE CHOCOLATE MOUNTAINS

Plutonic rocks are exposed over about 100 km² in the central and southern Chocolate Mountains; probably most are Miocene in age (fig. 5). Only 13 km² of

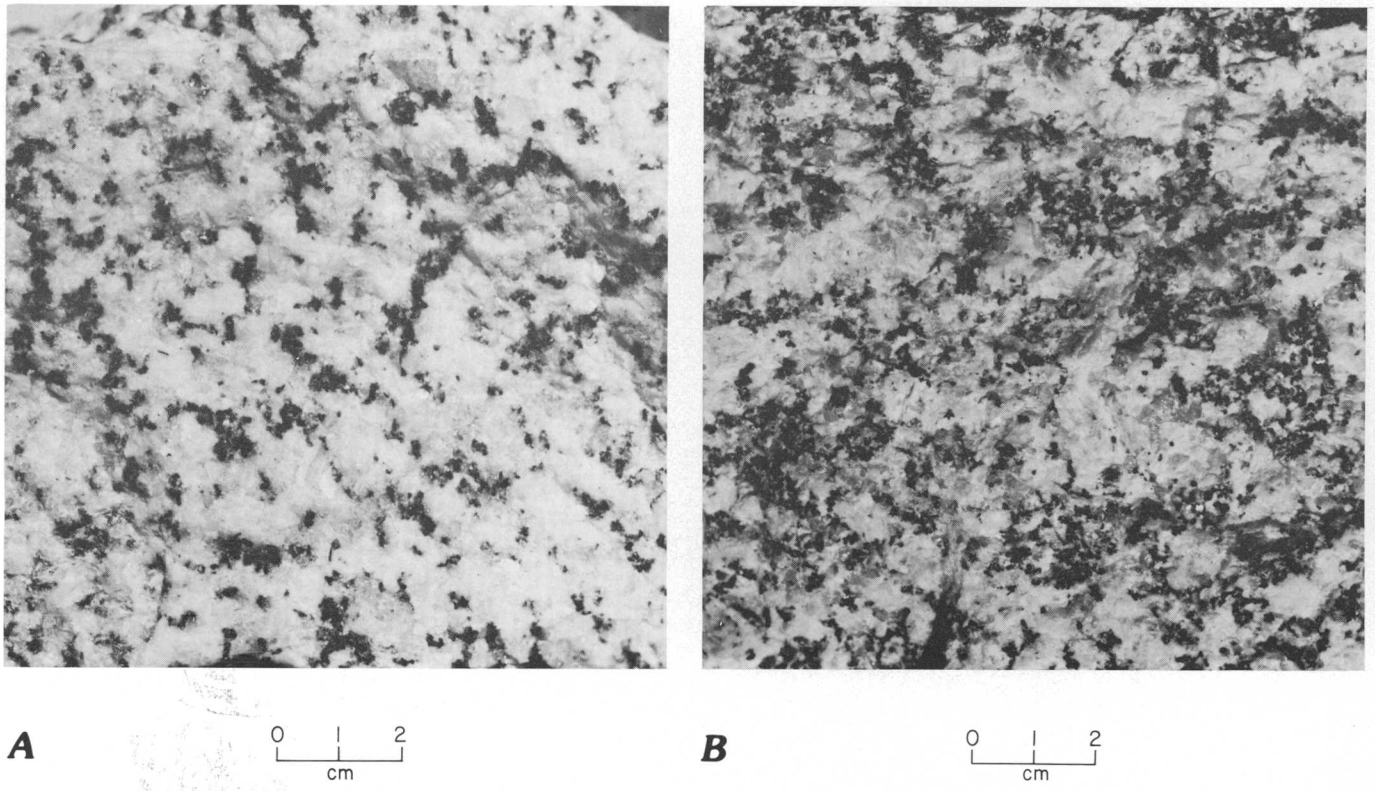

FIGURE 4.—Typical texture of Miocene plutonic rock. *A*, San Gabriel Mountains. *B*, Chocolate Mountains. Feldspar phenocrysts are present but do not show well in the photograph. Note finer grained "salt-and-pepper" texture of mafic and felsic minerals compared to San Gabriel Mountains sample.

these rocks in the central part of the range has been mapped in detail, but most of the rest has been examined in reconnaissance. Five individual plutons have been identified, and probably several more are present. All but one, a leucocratic biotite quartz monzonite, are porphyritic medium- to fine-grained quartz monzonite bodies that probably were emplaced at a relatively shallow depth. Groundmass textures are hypidiomorphic granular, and, although most rocks have some hypabyssal characteristics such as myrolitic cavities, in general they more closely resemble plutonic rocks than hypabyssal rocks.

These plutons contain plagioclase or potassium feldspar phenocrysts up to 40 mm long; the average length is about 20 mm. Plagioclase composition averages An_{20}. Potassium feldspar shows no triclinic twinning, but its structural state was not checked with X-rays. All the plutonic rocks contain hornblende and biotite and have an average color index of 8. Modal analyses of these rocks are shown in figure 3.

The single nonporphyritic pluton mentioned previously contains only biotite, has a color index of about 5, and is coarser grained than the porphyritic rock. This rock does not have the hypabyssal texture of the porphyritic rocks but has characteristics similar to the widespread Cretaceous plutonic rocks in southern California. This rock has not been dated and may be Tertiary or Cretaceous. It occurs just north of Salvation Pass and is included with the Tertiary granitic rocks in figure 5.

The dated Miocene rocks intrude the Orocopia Schist, the nonporphyritic leucocratic quartz monzonite, and a highly deformed polymetamorphic complex of mixed metaigneous and metasedimentary rocks. Chilled margins of fine-grained porphyritic quartz monzonite are common within the outermost 60 m of individual plutons. Dikes of porphyritic quartz monzonite are present in the host rocks near contacts but are not common. Stoped blocks of country rocks within the quartz monzonite are locally abundant in the outer 30 to 90 m of plutons.

Analyses 4, 5, and 6 (table 1) are considered representative of the Miocene plutonic rocks in the Chocolate Mountains. Samples 4 and 5 are from different parts of the same pluton (about 5 km apart); number 6 is from a coarser grained pluton in the southernmost part of Chocolate Mountains (fig. 5). The variation of any particular constituent of the analyses is very slight, and, although two plutons are represented, the analyses suggest that they almost certainly are genetically related.

TABLE 1.—*Chemical analyses and CIPW norms of samples from the San Gabriel and Chocolate Mountains*

[Numbers 1-6 correspond to sample localities on figures 2 and 5. Sample 1 analyzed by B. P. Fabbi, X-ray spectroscopy; samples 2-6 analyzed by S. Botts, rapid-rock method (Shapiro, 1967)].

	Biotite granodiorite, eastern San Gabriel Mountains			Hornblende-biotite quartz monzonite, Chocolate Mountains			Average of analyses 1-3	Average of analyses 4-6
	1	2	3	4	5	6	7	8
SiO_2	70.2	70.7	70.4	69.0	70.6	70.4	70.4	70.0
Al_2O_3	16.0	15.8	15.8	14.8	14.3	15.0	15.9	14.7
Fe_2O_3	.15	.50	.40	.80	.70	.50	.35	.67
FeO	1.4	1.4	1.2	2.2	2.1	2.1	1.3	2.1
MgO	.65	1.0	1.0	.90	.70	1.1	.88	.90
CaO	2.5	2.7	2.3	2.1	1.9	2.6	2.5	2.2
Na_2O	4.4	4.5	3.9	3.9	3.8	3.3	4.2	3.7
K_2O	2.7	2.8	3.8	4.0	4.2	3.9	3.1	4.0
H_2O^+	.53	.43	.50	.61	.56	.74	.48	.63
H_2O^-	.07	.14	.07	.19	.15	.22	.09	.19
TiO_2	.34	.37	.31	.43	.45	.47	.34	.45
P_2O_5	.12	.09	.07	.08	.10	.11	.09	.10
MnO	.04	.00	.00	.03	.02	.02	.01	.02
CO_2	.05	.02	.01	.01	.01	.01	.03	.01
Total	99.15	100.45	99.76	99.05	99.59	100.47	99.67	99.67
	CIPW norms							
q	27.7	26.0	26.4	24.4	26.6	28.1		
c	1.6	0.7	1.3	0.4	0.3	0.9		
or	16.2	16.5	22.5	23.9	25.0	23.0		
ab	37.4	38.0	33.1	33.4	32.3	27.8		
an	11.9	12.8	11.0	10.0	8.8	12.2		
en	1.6	2.5	2.5	2.3	1.8	2.7		
fs	2.0	1.5	1.4	2.8	2.6	2.7		
mt	0.2	0.7	0.6	1.2	1.0	0.7		
il	0.6	0.7	0.6	0.8	0.9	0.9		
ap	0.3	0.2	0.2	0.2	0.2	0.3		
Total	99.5	99.6	99.6	94.4	99.5	99.3		

The modes for rocks from the Chocolate Mountains shown in figure 3 represent samples from three different plutons. They define a relatively small field in the quartz monzonite region of the diagram.

K-Ar AGES OF THE PLUTONIC ROCKS

Biotite from four samples in the eastern San Gabriel Mountains and coexisting hornblende-biotite pairs from three rocks in the Chocolate Mountains were dated. The analytical data and calculated ages are given in table 2. All mineral separates were examined in immersion oils hornblende separates contained no biotite, and biotite separates, with one exception, were more than 99 percent pure. The single exception is the biotite with 7.87 K_2O from sample 6, which contained a small amount of chlorite and a few grains of hornblende. A second determination, made on a purified separate, is also given.

TABLE 2.—*Analytical data for dated samples*

[Samples 1-3, 9 from the San Gabriel Mountains; samples 4-6 Chocolate Mountains. All sample numbers except for 9 correspond to numbers in figures 2 and 5 and table 1. Constants used to calculate ages are: $\lambda\beta = 4.72 \times 10^{-10}$ yr^{-1}; $\lambda\varepsilon = 0.584 \times 10^{-10}$ yr^{-1}; $K^{40}/K = 1.19 \times 10^{-4}$]

Sample	Mineral	K_2O	^{40}Ar rad (mol/g)	Radiogenic Ar(%)	Age (m.y.)
1	Biotite	8.54, 8.51	2.353×10^{-10}	81	18.6±0.6
2	Biotite	8.75, 8.81	1.886×10^{-10}	56	14.5±0.4
3	Biotite	8.90, 8.98	1.855×10^{-10}	74	14.0±0.4
9	Biotite	8.79, 8.97	1.850×10^{-10}	45	14.0±0.6
4	Hornblende	.906, .912	2.814×10^{-11}	36	20.8±1.7
	Biotite	7.95, 7.98	2.744×10^{-10}	79	23.2±0.8
5	Hornblende	.945, .954	3.064×10^{-11}	49	21.7±1.3
	Biotite	7.76, 7.75	2.698×10^{-10}	84	23.4±0.7
6	Hornblende	.529, .525	1.563×10^{-11}	25	20.0±0.6
	Biotite	7.87, 7.87	2.377×10^{-10}	80	20.3±0.6
	Biotite	8.34, 8.38	2.611×10^{-10}	69	21.0±0.6

Three samples from the San Gabriel Mountains yielded middle Miocene ages of about 14 m.y., and samples from the Chocolate Mountains yielded early Miocene ages between 20 and 23 m.y. Sample 1, from the San Gabriel Mountains, yielded an age of 18.6 m.y., more than 25 percent higher than the others from that area. This sample was collected within the contact zone adjacent to older crystalline rocks that yielded K-Ar ages of about 70 m.y., and it was finer grained than most of the pluton, showing obvious marginal chill effects. The older apparent age yielded by this rock may result from argon retained by partly assimilated biotite from the host rock. The consistency of the 14-m.y. ages obtained on representative rocks from different parts of the pluton suggests that this is an emplacement age. An alternative interpretation, however, is that the 18.6-m.y. age of the chilled margin rock more closely represents the time of emplacement and that the 14-m.y. ages of the coarser grained interior rocks indicate an extended cooling history for the inner part of the pluton.

Rock from the westernmost part of the Miocene pluton in the San Gabriel Mountains has been previously dated, yielding 17±5-m.y. and 26±3-m.y. K-Ar dates and 25±15-m.y. and 19±15-m.y. Rb-Sr dates on biotite (Hsü and others, 1963). We redated this body in order to reduce the large plus-minus values reported by Hsü and to eliminate possible interlaboratory differences in comparing dates from the San

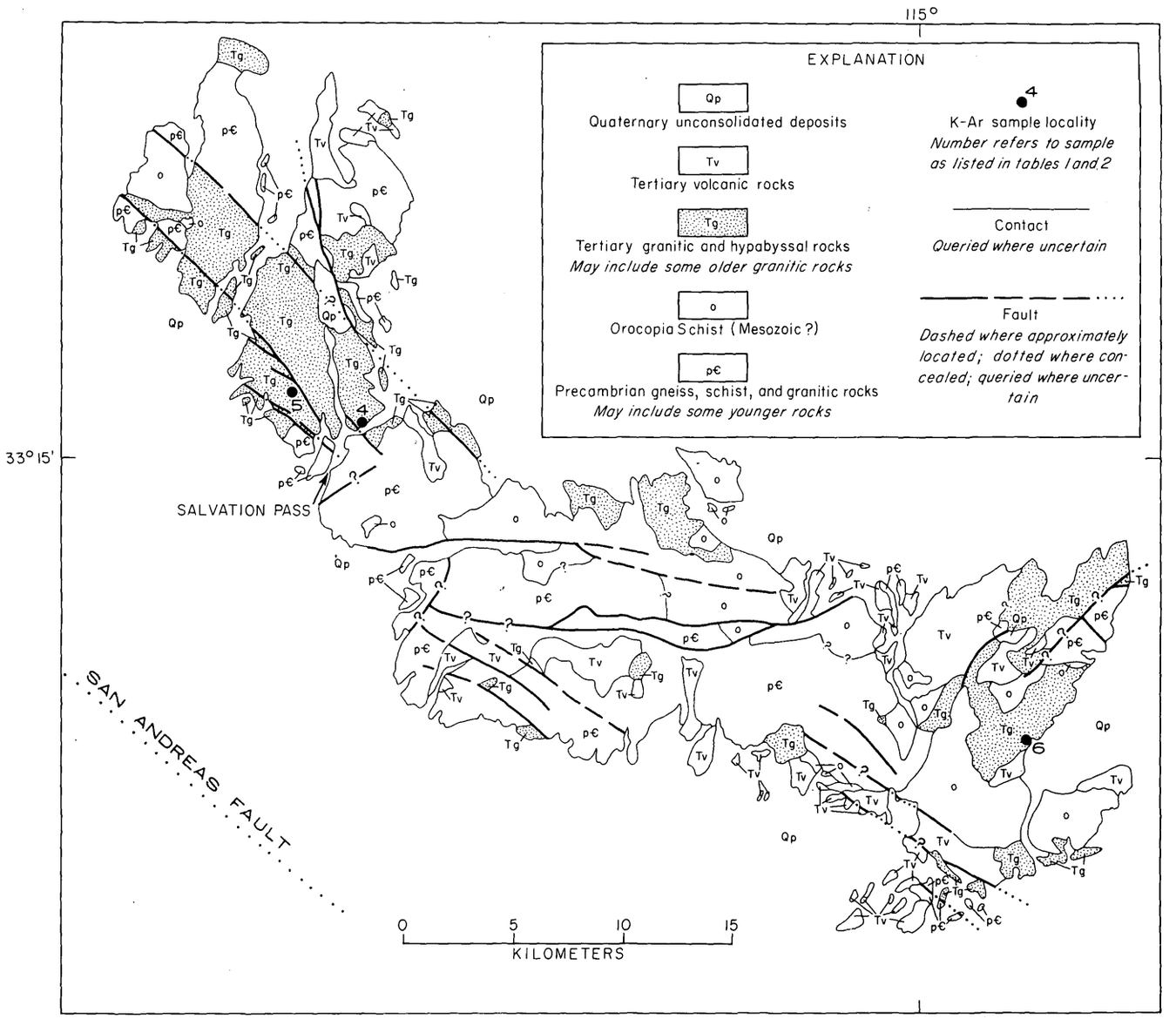

FIGURE 5.—Simplified geologic map of the southern part of the Chocolate Mountains showing K-Ar sample localities. Geology modified from Jennings (1967).

Gabriel Mountains with those from the Chocolate Mountains.

The coexisting hornblende-biotite pairs from the Chocolate Mountains rocks yielded concordant ages within the analytical precision of the dating. It is unusual that in all analyses the hornblende gave slightly younger ages than the coexisting biotite. This is exactly opposite of most coexisting hornblende-biotite pairs from other localities (Hart, 1961, 1964; Miller, 1975). The significance of this apparent reversal is not understood.

SUMMARY AND DISCUSSION

Miocene plutonic rocks intrude the Pelona and Orocopia Schists but are found on opposite sides of the San Andreas fault, about 235 km apart. The Pelona and Orocopia Schists are lithologically similar and probably equivalent units. Plutonic rocks in the San Gabriel Mountains, intrusive into the Pelona Schist, are biotite granodiorite and yield K-Ar ages ranging from 18.6 to 14.0 m.y. Plutonic rocks in the Chocolate Mountains, intrusive into the Orocopia Schist, are hornblende-biotite quartz monzonite and yield K-Ar

ages ranging from 20.0 to 23.4 m.y. The difference in ages and modal composition suggests that the plutons are separate and probably unrelated bodies despite their similar geologic occurrence. However, chemically the two plutons are quite similar, and the modal difference may only reflect different crystallization histories. In addition, even though the age of rocks from the Chocolate Mountains is well established on the basis of concordant hornblende-biotite pairs, the age of the pluton in the San Gabriel Mountains could be 13.4 to 19.2 m.y. if the maximum analytical error is considered. The upper limit brings the possible age of the pluton in the San Gabriel Mountains within the lower age limit of those in the Chocolate Mountains.

The means of the age data, however, indicate different ages for the two plutonic groups. This difference, in addition to the different textures, mineral compositions, modal compositions, and slight, but important, chemical differences in Al_2O_3 and total iron tend to suggest that the two plutonic groups are unrelated or at best are related only in a very general way.

REFERENCES CITED

Crowell, J. C., 1962, Displacement along the San Andreas fault, California: Geol. Soc. America Spec. Paper 71, 61 p.

Dillon, John, 1975, The Chocolate Mountain-Orocopia-Vincent thrust system as a tectonic element of late Mesozoic California: Geol. Soc. America Abs. with Programs, v. 7, no. 3, p. 311.

Ehlig, P. L., 1968, Causes of distribution of Pelona, Rand, and Orocopia Schists along the San Andreas and Garlock faults, *in* Dickinson, W. R., and Grantz, Arthur, eds., Proceedings of the conference on geologic problems of the San Andreas fault system: Stanford Univ. Pubs. Geol. Sci., v. 11, p. 294–306.

Hart, S. R., 1961, Mineral ages and metamorphism, *in* Kulp, J. L., ed., Geochronology of rock systems: New York Acad. Sci. Annals v. 91, art. 2, p. 192–197.

——— 1964, The petrology and isotopic-mineral age relations of a contact zone in the Front Range, Colorado: Jour. Geology, v. 72, no. 5, p. 493–525.

Hershey, O. H., 1912, The Belt and Pelona series: Am. Jour. Sci., ser. 4, v. 34, p. 263–273.

Hill, M. L., and Dibblee, T. W., Jr., 1953, San Andreas, Garlock and Big Pine faults, California: Geol. Soc. America Bull., v. 64, p. 443–458.

Hsü, K. J., Edwards, G., and McLaughlin, W. A., 1963, Age of the intrusive rocks of the southeastern San Gabriel Mountains, California: Geol. Soc. America Bull., v. 74, no. 4, p. 507–512.

Jennings, C. W., 1967, Geologic map of California, Olaf P. Jenkins edition, Salton Sea sheet: California Div. Mines and Geology, scale 1:250 000.

Miller, F. K., 1975, Distribution and trends of discordant ages of the plutonic rocks of northeastern Washington and northern Idaho: Geol. Soc. America Bull., v. 86, p. 517–528.

Shapiro, Leonard, 1967, Rapid analysis of rocks and minerals by a single solution method: U.S. Geol Survey Prof. Paper 575–B, p. B187–B191.

Schoellhamer, J. E., and Woodford, A. O., 1951, The floor of the Los Angeles basin, Los Angeles, Orange, and San Bernardino Counties, California: U.S. Geol. Survey Oil and Gas Inv. Map OM–117.

Jour. Research U.S. Geol. Survey
Vol. 5, No. 5, Sept.–Oct. 1977, p. 651–661

USE OF A HYBRID COMPUTER IN ENGINEERING-SEISMOLOGY RESEARCH

By ROBERT B. PARK and WALTER W. HAYS, Denver, Colo.

Abstract.—A hybrid computer is an important tool in the seismological research conducted by the U.S. Geological Survey in support of the Energy Research and Development Administration nuclear explosion testing program at the Nevada Test Site and the U.S. Geological Survey Earthquake Hazard Reduction Program. The hybrid computer system, which employs both digital and analog computational techniques, facilitates efficient seismic data processing. Standard data processing operations include: (1) preview of dubbed magnetic tapes of data; (2) correction of data for instrument response; (3) derivation of displacement and acceleration time histories from velocity recordings; (4) extraction of peak-amplitude data; (5) digitization of time histories; (6) rotation of instrumental axes; (7) derivation of response spectra; and (8) derivation of relative transfer functions between recording sites. Catalog of time histories and response spectra of ground motion from nuclear explosions and earthquakes that have been processed by the hybrid computer are used in the Earthquake Hazard Research Program to evaluate the effects of source, propagation path, and site effects on recorded ground motion; to assess seismic risk; to predict system response; and to solve system design problems.

In April, 1974, the U.S. Geological Survey assumed the responsibility for operation and management of a medium-sized hybrid computer system under an interagency agreement with the Nevada Operations Office, Energy Research and Development Administration (ERDA). This particular system (Frock, 1968) had been developed specifically for processing and analyzing the ground-motion and structural response data from nuclear explosions detonated in ERDA's testing program at the Nevada Test Site. The system, which is operated by the U.S. Geological Survey, is located on the campus of the Colorado School of Mines in Golden, Colo., and supports ERDA's ground-motion and structural response program and the U.S. Geological Survey's Earthquake Hazards Reduction Program.

HYBRID COMPUTER SYSTEMS

A hybrid computer may be defined as a computational system which employs both digital and analog computational techniques. The modern hybrid computer system is designed to take advantage of the best features of the analog and digital computer and is much more than just the tying together of a digital and analog computer through an analog to digital converter. It is an integrated system containing many interactive control and data-transfer functions.

The hybrid computer is especially efficient for processing seismic data because of its dual analog and digital capabilities. For mass storage of time-history data, analog format is efficient because data can be densely packed. For example, a 1-inch 14-track analog tape can hold the equivalent of more than 10^9 data points. In contrast, the same data would require about 150 standard digital tapes, if one assumes a rate of 100 samples per second and a word length of 16 bits. The digital computer has greater flexibility in random storage and retrieval of large quantities of data and virtually unlimited precision.

The hybrid system allows efficient combination of time and frequency-domain analyses. It offers ease of input and output, speed of operation, and relatively simple computation of transfer functions. It may be used for mathematical simulation or for processing operations which involve amplification, integration, differentiation, summation, and filtering (Bekey and Karplus, 1968).

U.S. GEOLOGICAL SURVEY HYBRID SYSTEM

The hybrid computer system operated by the U.S. Geological Survey is medium sized. It is fully integrated with direct instructions for the analog components exercised by the digital section (fig. 1). The functions of the analog tape units and strip-chart recorders may also be controlled by the digital section, making possible the automated searching of tapes and the generation of edited time histories.

The major components of the hybrid system are: (1) an EAI (Electronics Associates, Inc.) 690 hybrid

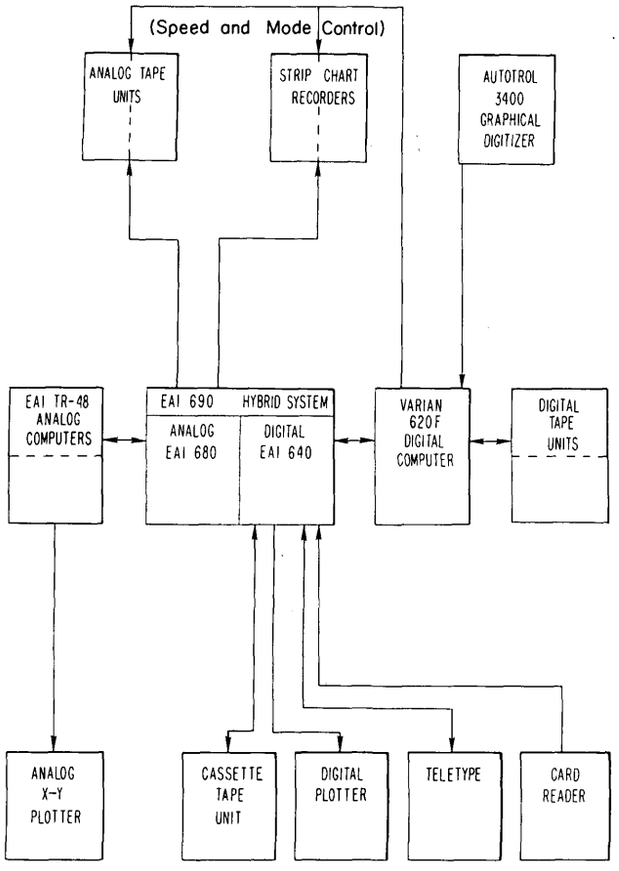

FIGURE 1.—Block diagram of hybrid computer system operated by the U.S. Geological Survey.

computer, (2) a Varian 620F digital computer having a total memory of 20 000 16-bit words, and (3) two EAI TR–48 analog computers. The associated peripheral equipment consists of two analog tape units, two 8-channel strip-chart recorders, two digital tape units, a digital cassette tape unit, a card reader, and a digital plotter. At the present time, an interface is being built to PDP–11 computer.

In a well-scaled hybrid computer problem, an accuracy of 0.1 to 1 percent is readily realized. This level of accuracy is adequate for practically all engineering-seismology research problems.

RESEARCH APPLICATIONS

Most of the research on earthquake studies currently in progress within the U.S. Geological Survey is directed toward the multifaceted earthquake-hazard-reduction problem (Wallace, 1974). There are four approaches to the reduction of earthquake hazards that are currently being investigated: (1) seismic-risk assessment for improved land use and building codes, (2) engineering to resist earthquakes, (3) earthquake prediction, and (4) earthquake control and modification. Research related to the first two approaches encompasses a number of interrelated elements (fig. 2). An important part of the research program is the acquisition of catalogs of ground-motion time histories and spectra for a wide range of earthquakes and recording sites. These data are analyzed in terms of the source, path, and site elements of the wave-propagation system and are applied in risk assessment and system-design problems.

Data Processing

The data processing operations which are performed on the hybrid computer system during the analysis of seismic data include:

1. Preview of dubbed tape,
2. Correction of data for instrument response,
3. Derivation of displacement and acceleration time histories from, the velocity recording,
4. Extraction of peak amplitudes of ground motion,
5. Digitization of time histories,
6. Rotation of instrumental axes,
7. Derivation of pseudorelative velocity (PSRV) response spectra, and
8. Derivation of relative transfer functions between recording sites.

These operations are shown in a generalized block diagram in figure 3, using the earthquake aftershock sequence as a frame of reference. Each operation will be described below.

Preview

The preview program is the first operation performed on the velocity signal recorded on the L–7 velocity system. The L–7 system (King, 1969) is an accurately calibrated, portable seismograph system which records ground velocity on analog magnetic tape. It has a flat response to ground velocity over a

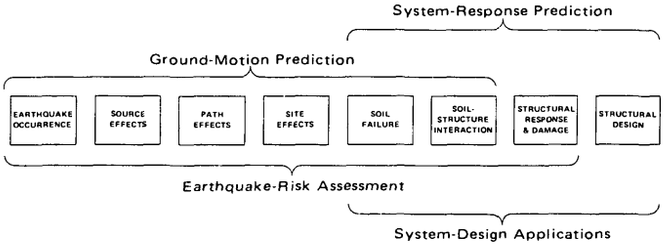

FIGURE 2.—Schematic Illustration of elements in research related to seismic-risk assessment and earthquake-resistant engineering.

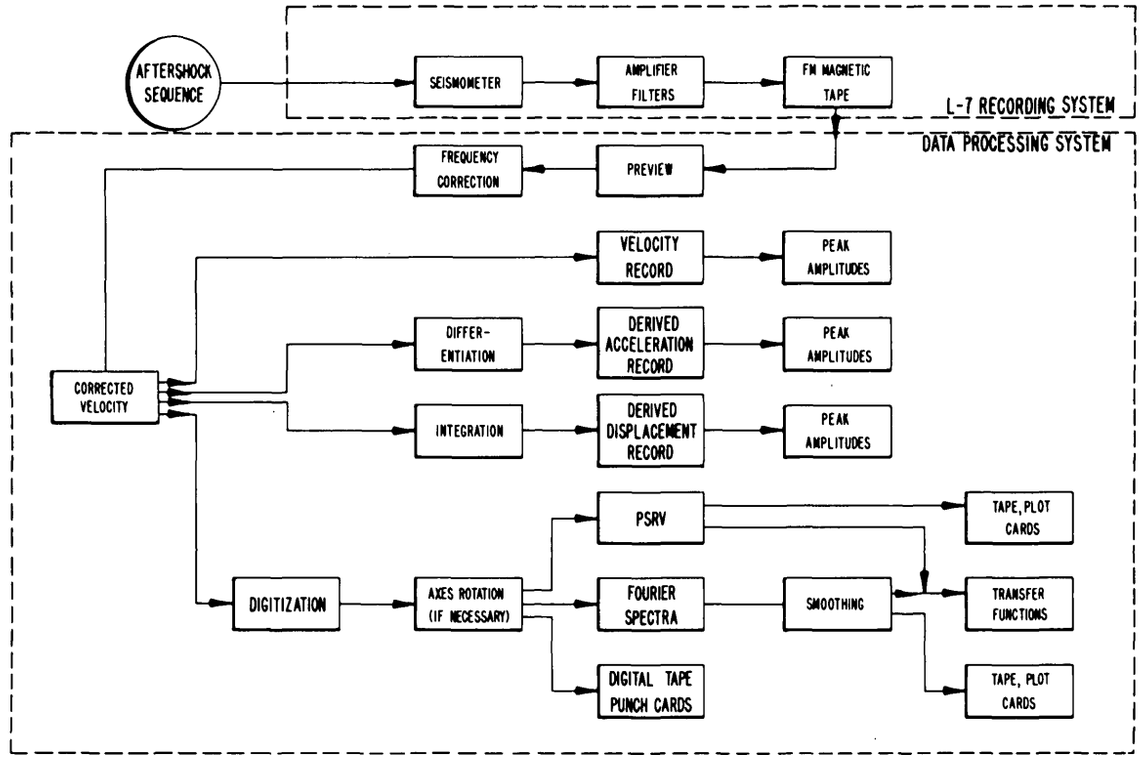

FIGURE 3.—Block diagram showing the general sequence followed in processing seismic data on the hybrid computer system.

broad frequency range (fig. 4) which makes it useful in engineering-seismology studies. In preview, a paper strip chart of the time history is made for each of two recording levels. The charts are then visually examined to determine problems associated with high-frequency noise, overranged signals, or the quality of the calibration signal. The best data channel is then selected to be processed. The strip charts are also checked against the data logs made in the field to verify the instrument-gain settings.

Correction

The frequency response of the L–7 system is flat from 0.1 to 35 Hz (see fig. 4); therefore, it is generally not necessary to correct for the frequency response of the L–7 instrument. For other velocity recording systems, this might not be the case. The correction routine for the L–7 velocity system involves filtering the signal through a high-pass filter in order to obtain a more accurate zero signal without affecting the event or calibration signals. The corner frequency of the filter is set at 0.03 Hz, well below the natural low-frequency corner of the seismic recording system.

Derived motions

The acceleration and displacement time histories are derived, respectively, by differentiation and integration of the corrected velocity signal with respect to time. These signals are derived through an analog circuit where the corner frequencies are set to suppress noise, low-frequency drift, and other undesirable characteristics of the input signal.

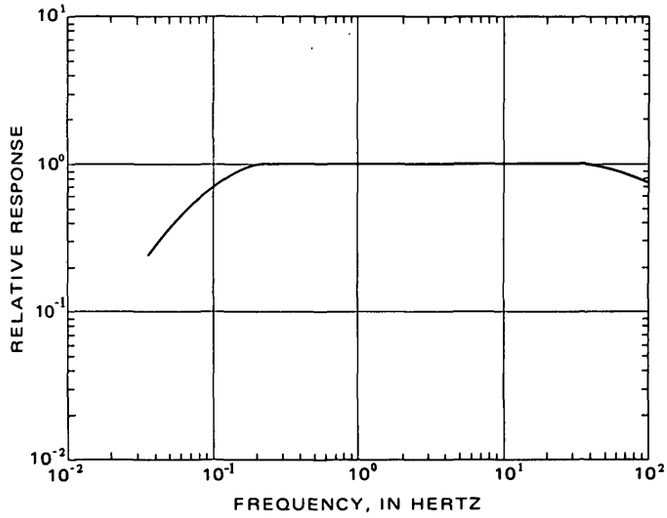

FIGURE 4.—Frequency-response curve for the L–7 seismograph velocity system (King, 1969).

The analog transfer function used in the derivation of the acceleration signal is given by:

$$H_a = \frac{-10^5 K_a \omega_1 S}{(S^2 + 2h\omega_1 S + \omega_1^2)(S + \omega_1)}, \quad (1)$$

where H_a = acceleration transfer function,
S = Laplace complex variable,
K_a = gain setting,
h = 0.707
ω_1 = $2\pi f$ = 220 radians per second, and
f = 35 Hz.

The frequency-response curve for the acceleration transfer function is shown in figure 5. It has a peak response of +12 db (decibels) at a frequency of 30 Hz.

The transfer function used to derive the displacement is given by:

$$H_d = \frac{-100 K_d S^2}{(S + \omega_1)(S^2 + 2h\omega_1 S + \omega_1^2)}, \quad (2)$$

where H_d = displacement transfer function,
S = Laplace complex variable,
K_d = gain setting,
h = 0.707,
ω_1 = $2\pi f$ = 0.6283 radians per second, and
f = 0.1 Hz.

The frequency-response curve for the displacement transfer function is shown in figure 6. It has a peak response of 14 db at a frequency of 0.12 Hz.

An example of an acceleration and displacement time history derived from a corrected velocity signal is shown in figure 7.

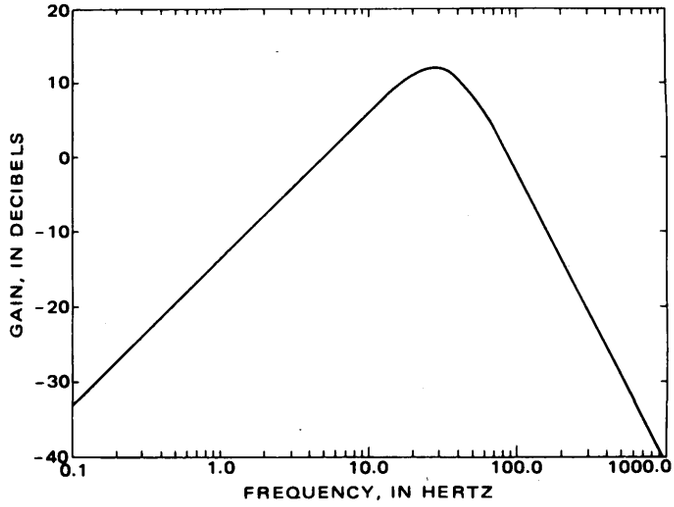

FIGURE 5.—Frequency response of the acceleration transfer function.

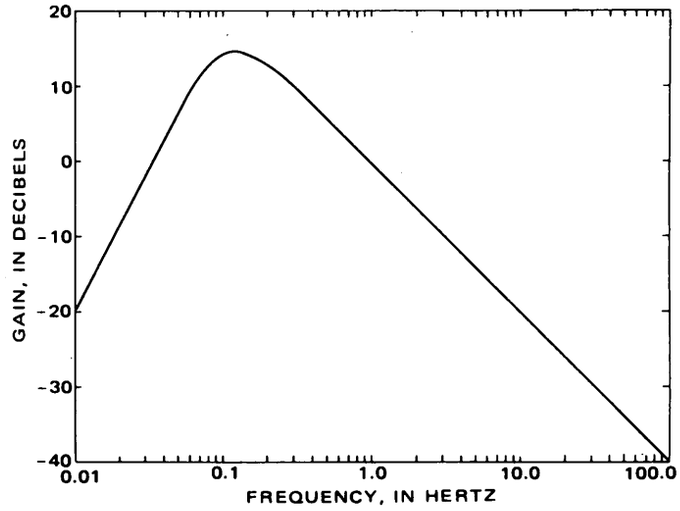

FIGURE 6.—Frequency response of the displacement transfer function.

Peak-amplitude scaling

In order to obtain the peak ground motion from a time history it is necessary to determine the instrument scale factor. The general formula for obtaining the peak value is implemented in the digital section at the time the data are digitized and is:

$$\text{Peak amplitude} = \frac{KV_c}{P_v} \times \frac{D_v}{D_p}, \quad (3)$$

where V_c is the calculated instrument scale factor,
D_v/D_p is the ratio of the peak amplitude to the peak to peak value of the calibration signal, and
K, P_v are constants dependent upon the type of ground motion under consideration.

The units of the peak amplitude are cm/s, g, and cm for velocity, acceleration, and displacement. The values of the constant K are 1.0, 0.0032, 0.1 for velocity, acceleration, and displacement, respectively. The value of P_v is always 1.0 for velocity. The value of P_v varies from recording to recording for acceleration and displacement. This value represents a factor to be applied to these traces in order to provide for a full-scale amplitude on the output plots. Figure 8 gives a graphic display of the calculation of the peak amplitude.

Digitization of velocity signals

The corrected velocity signal is passed through an analog to digital converter at a specified sample rate, (generally 160 samples per second for seismic signals measured in the near field). Control of the analog tape units by the digital sector facilitates making several passes through the data set to optimize the amplitude and timeframe and to select the best channels before digitization. The digitized signal is then written on a digital tape so that the option of making additional analyses on a digital computer can be exercised. The digitized signal is also passed through a digital-to-

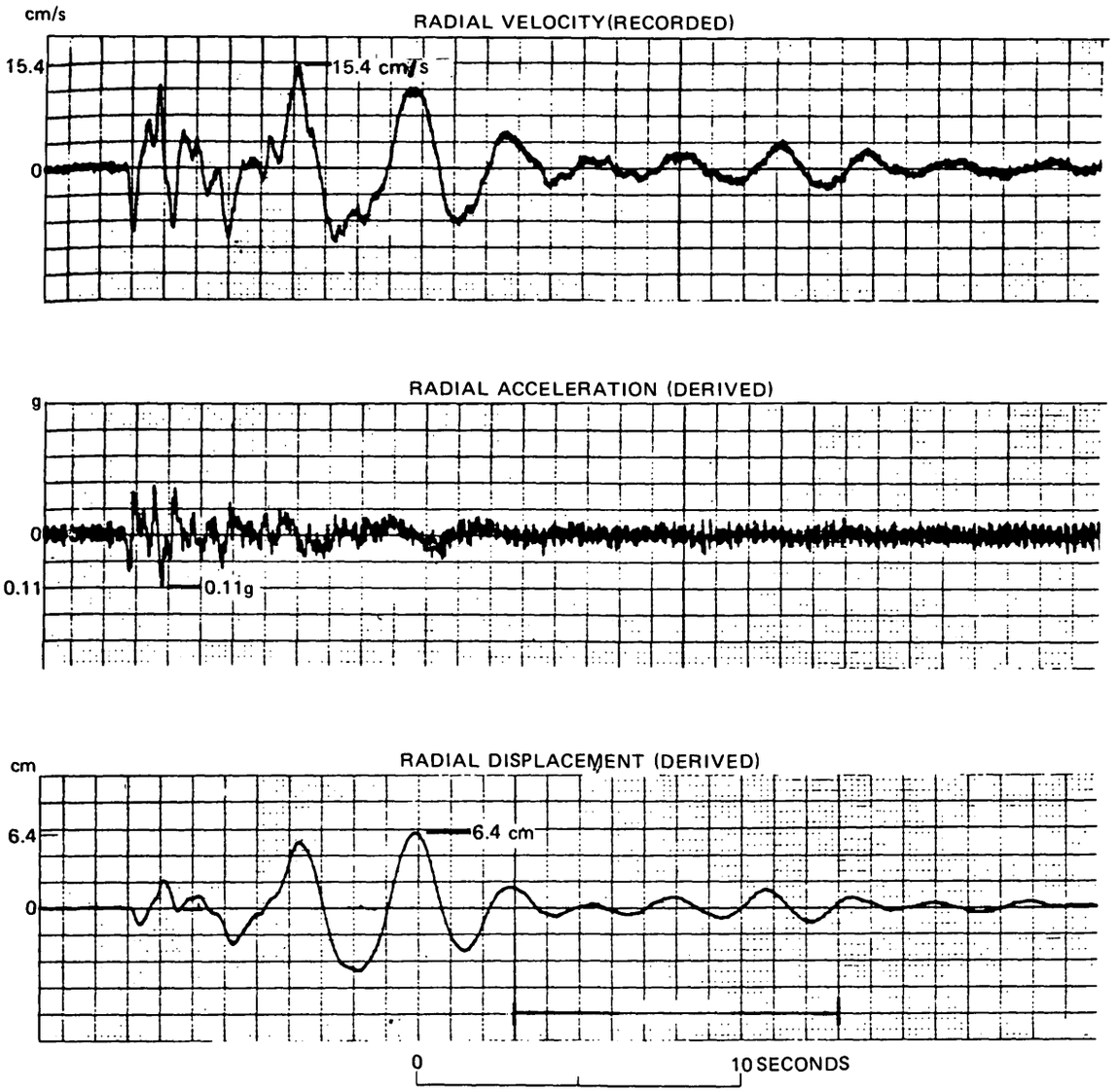

FIGURE 7.—Recorded velocity and derived acceleration and displacement time histories.

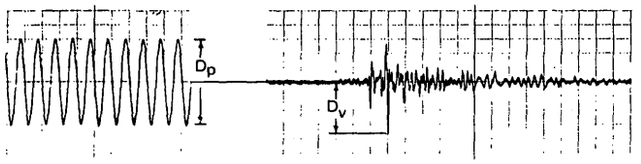

FIGURE 8.—Graphic display of peak-amplitude scaling. Graph on left is the calibration signal of the seismometer and on right is a recorded earth movement. D_p is peak amplitude and D_v is peak value of calibration signal.

analog converter so that the output signal, written on the digital tape, can be compared with the original recordings to verify the accuracy of the digitization procedure.

Rotation of axes

It is sometimes necessary for analysis purposes to rotate the axes of the horizontal components of ground motion in order to align them with instrumental components recorded at other locations. The technique used to rotate the components is the conventional transformation for rectangular coordinates. The rotation of axes with fixed origin is defined as:

$$x'(t) = x(t)\cos\Theta + y(t)\sin\Theta$$
$$y'(t) = y(t)\cos\Theta - x(t)\sin\Theta \qquad (4)$$

where Θ is the angle of rotation,
$x(t), y(t)$ are the time histories along the original axes, and
$x'(t), y'(t)$ are the rotated components.

An example of a time history rotated by use of the above procedure is shown in figure 9.

Derivation of pseudo-relative velocity (PSRV) spectra

The hybrid system is well suited for the derivation of PSRV spectra. The velocity time history is passed through a set of low-damped, band-pass filters. The peak value of each of the filter time-history outputs comprises the spectrum and is plotted on logarithmic tripartite paper.

The PSRV filter is described by the equation

$$y''(t)+2h\omega_n y'(t)+\omega_n{}^2 y(t)=\omega_n x'(t), \qquad (5)$$

where $y(t)$ = the relative motion of the mass of the single-degree-of-freedom system representing the PSRV filter,

$'$ = differentiation with respect to time,

h = critical damping,

$\omega = 2\pi f$ = center frequency of filter in radians, and

$x(t)$ = absolute particle velocity of the ground.

The filter may also be expressed in Laplace transform notation as a transfer function

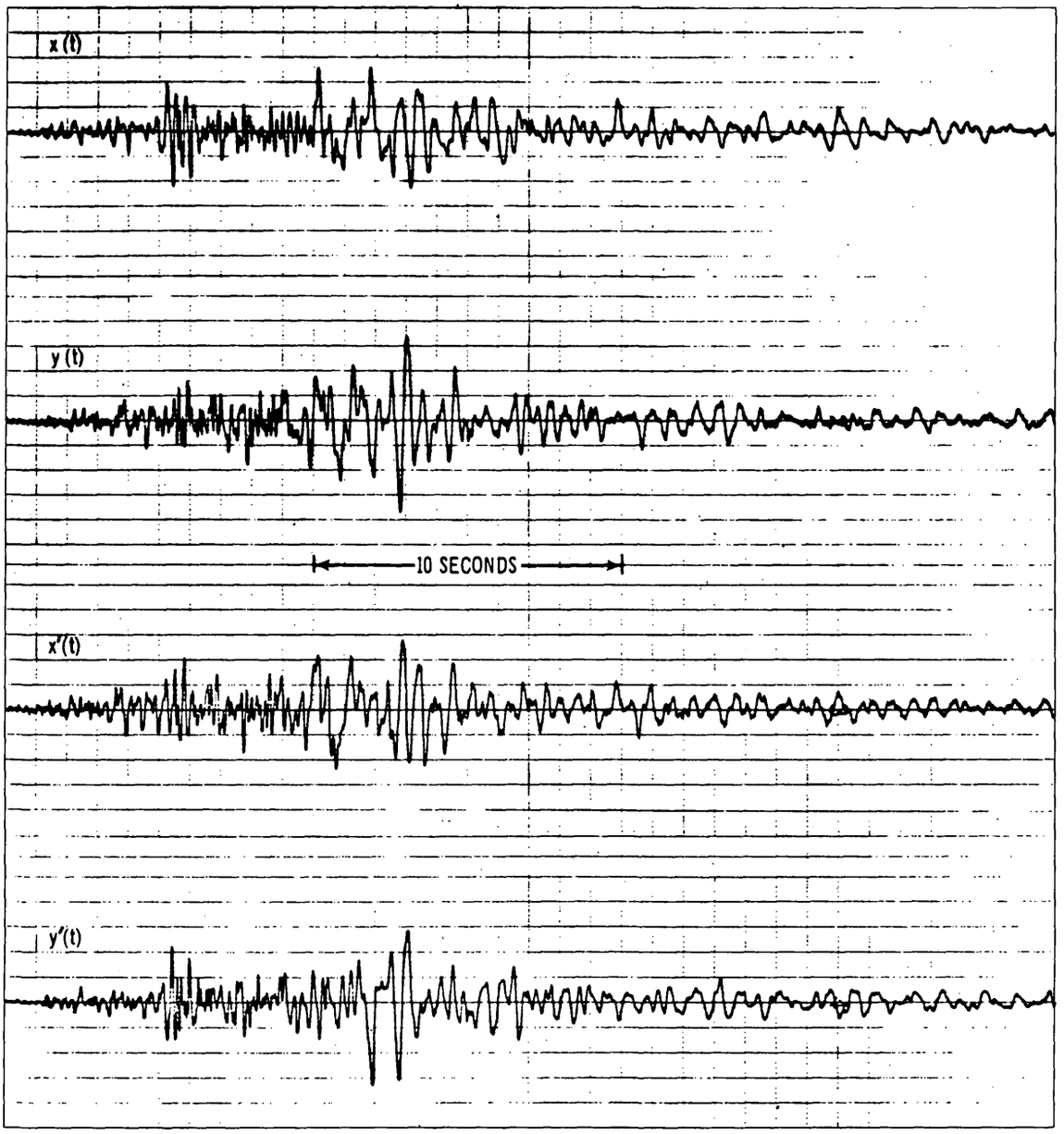

FIGURE 9.—Example of a 45° rotation of instrumental axes of ground motion where $x(t)$ and $y(t)$ are the time histories along the original axis and $x'(t)$ and $y'(t)$ are the rotated components.

$$\frac{\omega_n S}{S^2 + 2h\omega_n S + {\omega_n}^2}, \qquad (6)$$

where S is the Laplace transform variable.

The computational procedure for deriving the PSRV spectrum can be separated into analog and digital functions (fig. 10). The filtering is most efficiently done in the analog section, using 10 parallel band-pass filters (fig. 11). The procedures of checking out the analog program, normalizing and scaling of the data, and storing the peak values of the filter response are performed in the digital section. The digital section acts as the "executive," controlling the program flow and positioning the analog recorders. For a 5-percent-damped PSRV, a typical damping value used in research studies, the response of 49 band-pass filters are needed to cover the period range, 0.05 to 6.0 seconds.

The 5-percent-damped spectrum is generated by repeating the filtering process 5 times. To avoid resetting the filter coefficients for each of the 5 passes, the time-history data are time scaled, a procedure which has the effect of shifting the band-pass-filter center frequencies. The time scaling is implemented by digitizing the input data and dumping them back into the analog section. The outputs of the filters are redigitized and the peak absolute values of each filter output are extracted to form the spectrum.

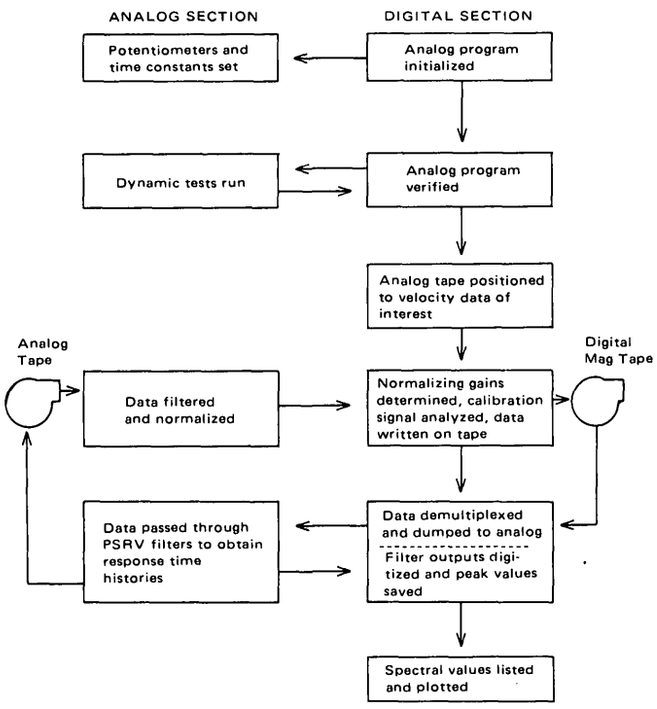

FIGURE 10.—Generalized block diagram of hybrid system pseudorelative velocity program.

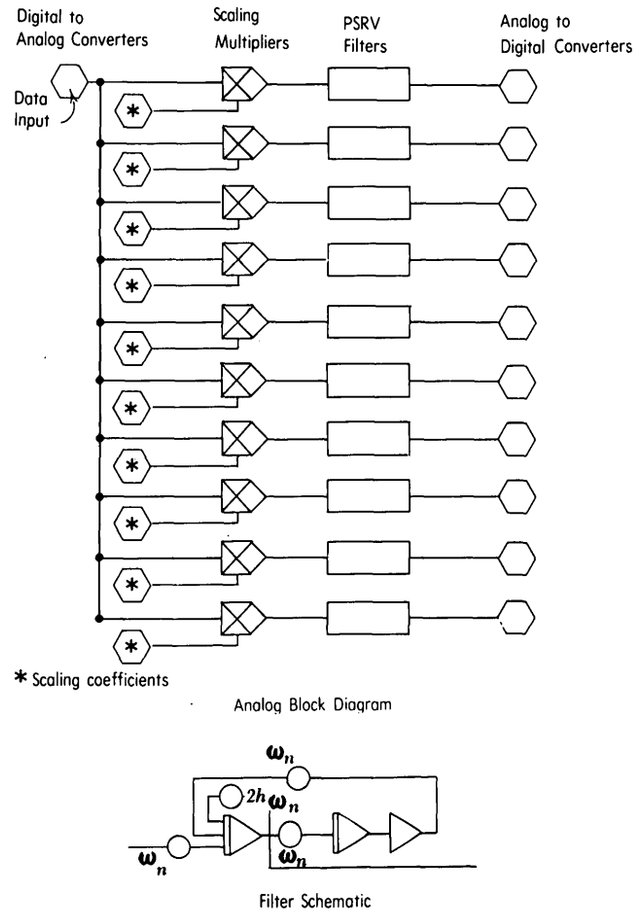

FIGURE 11.—Analog program for deriving pseudorelative velocity (PSRV) in hybrid computer system. ω_n is rotational frequency and h is a constant equal to 0.707.

Two examples of 5-percent-damped PSRV spectra are shown in figure 12. These spectra are plotted on logarithmic tripartite paper, a display which permits the researcher to analyze simultaneously the pseudo-absolute acceleration, PSRV, and relative displacement spectra. These three spectra contain important imformation about the response of an ensemble of viscously damped, simple harmonic oscillators to an input ground motion.

Figure 13 illustrates the well-known fact that the low-damped PSRV spectrum is proportional to the smoothed Fourier amplitude spectrum.

In recent years, a number of individuals (Pilant and Knopoff, 1964; Trifunas, 1971, Hays and others, 1973, and Perez 1973) have utilized the response time histories generated during the derivation of a response spectrum. These time histories (and their envelopes) contain time-dependent spectral information and are more useful than the standard response spectrum for analyzing seismic signals and structural response.

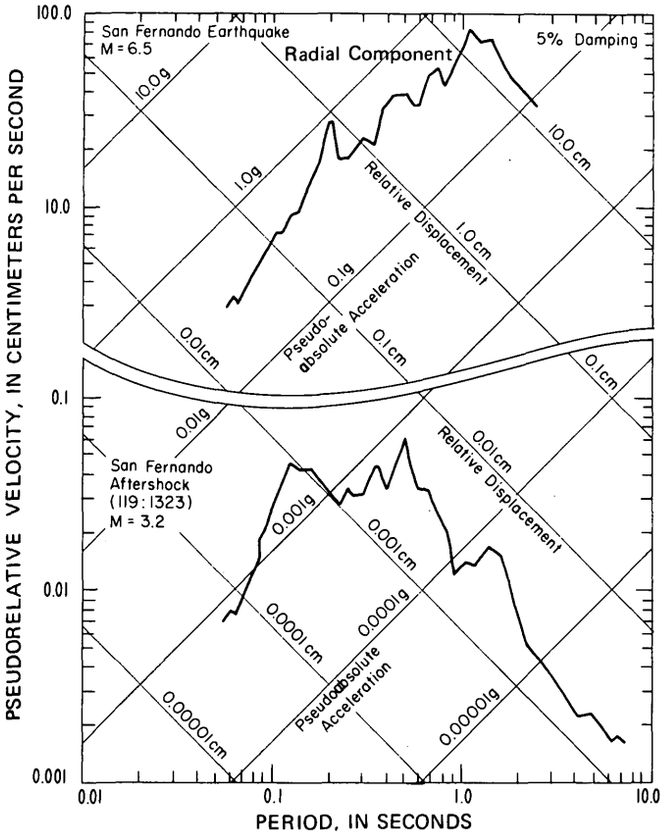

FIGURE 12.—5-percent-damped, pseudorelative velocity (PSRV) spectra derived from the San Fernando earthquake and an aftershock. Both events were recorded at the Glendale, Calif., station.

Figure 14 illustrates the multiple-filtration process used on the hybrid computer to derive time-dependent response envelopes. A seismogram is input to a filter system consisting of three elements: (1) a narrow band-pass filter; (2) an absolute-value operator; and (3) a low-pass filter. The output of the total filter system for each narrow band-pass filter is a time-dependent response envelope. An example of a time-dependent response spectrum is shown in figure 15 for the N65°E component of ground motion from the 1966 Parkfield, Calif., earthquake.

Derivation of relative transfer functions between sites

The transfer functions between sites contain useful information about relative site response. These transfer functions are calculated on the hybrid system, using either smoothed Fourier amplitude spectra or 5-percent-damped PSRV spectra to calculate spectral ratios between sites where ground-motion records have been obtained. Some researchers perfer one spectral representation over the other; however, the essential relative-site-response information is contained in either transfer function (fig. 16).

SUMMARY

The hybrid computer, which combines both analog and digital computational techniques, is an efficient general purpose system for processing seismic data needed in engineering-seismology research. The system can be used to process ground-motion time histories of any type (acceleration, velocity, or displacement) recorded in any format (paper, film, magnetic tape, or digital mode). From the basic data, catalog of other ground-motion types and response spectra are derived. Other spectral representations such as Fourier and power spectral density can also be derived on the hybrid system, if desired. These data catalogs are used in a wide variety of research. For example, they are used to evaluate source, path, and site effects—important elements of the ground-motion prediction problem (Hays and others, 1975; Joyner and Chen, 1975; and Borcherdt, ed., 1975). Peak-amplitude and spectral-response data are used to derive empirical attenuation laws needed in seismic-risk assessment (Algermissen, 1973, Navarro, 1975). Ground-motion data are used to evaluate structural response and damage (Page and others, 1975; URS/John Blume and Associates, 1975; and Hays, 1976) and are used in system-design applications (Construction Engineering Research Laboratory, 1976).

Figures 13–16 follow "References Cited."

REFERENCES CITED

Algermissen, S. T., 1973, The problem of seismic zoning, *in* Building practices for disaster mitigation—Proceedings of a workshop: U.S. Depart. of Commerce, Building Science Series 46, p. 112–125.

Bekey, G. A., and Karplus, W. J., 1968, Hybrid Computation: New York, John Wiley and Sons, Inc., 464 p.

Borcherdt, R. D., ed., 1975, Studies for seismic zonation of the San Francisco Bay region: U.S. Geol. Survey Prof. Paper 941-A, 88 p.

Frock, J. A., 1968, Engineering report—ERC data processing system: U.S. Dept. Commerce Natl. Tech. Inf. Service, NVO–1163–168, 225 p.

Hays, W. W., 1976, Evaluation of the seismic response in the Sylmar-San Fernando area, Calif., from the 1971 San Fernando earthquake, *in* Speicalty conference on dynamic response of structures—Instrumentation, testing methods, and system identification, Hart, G. C., chm.: American Soc. Civil Eng., Eng. Mech Div., Specialty conference on dynamic response of structures—instrumentation testing methods and system identification, Univ. Calif., Los Angeles, 1976, Proc., p. 502–511.

Hays, W. W., Algermissen, S. T., Espinosa, A. F., Perkins, D. M., and Rinehart, W. A., 1975, Guidelines for developing design earthquake response spectra: U.S. Army Construction Eng. Research Lab. Tech. Rep. M–114 349 p.

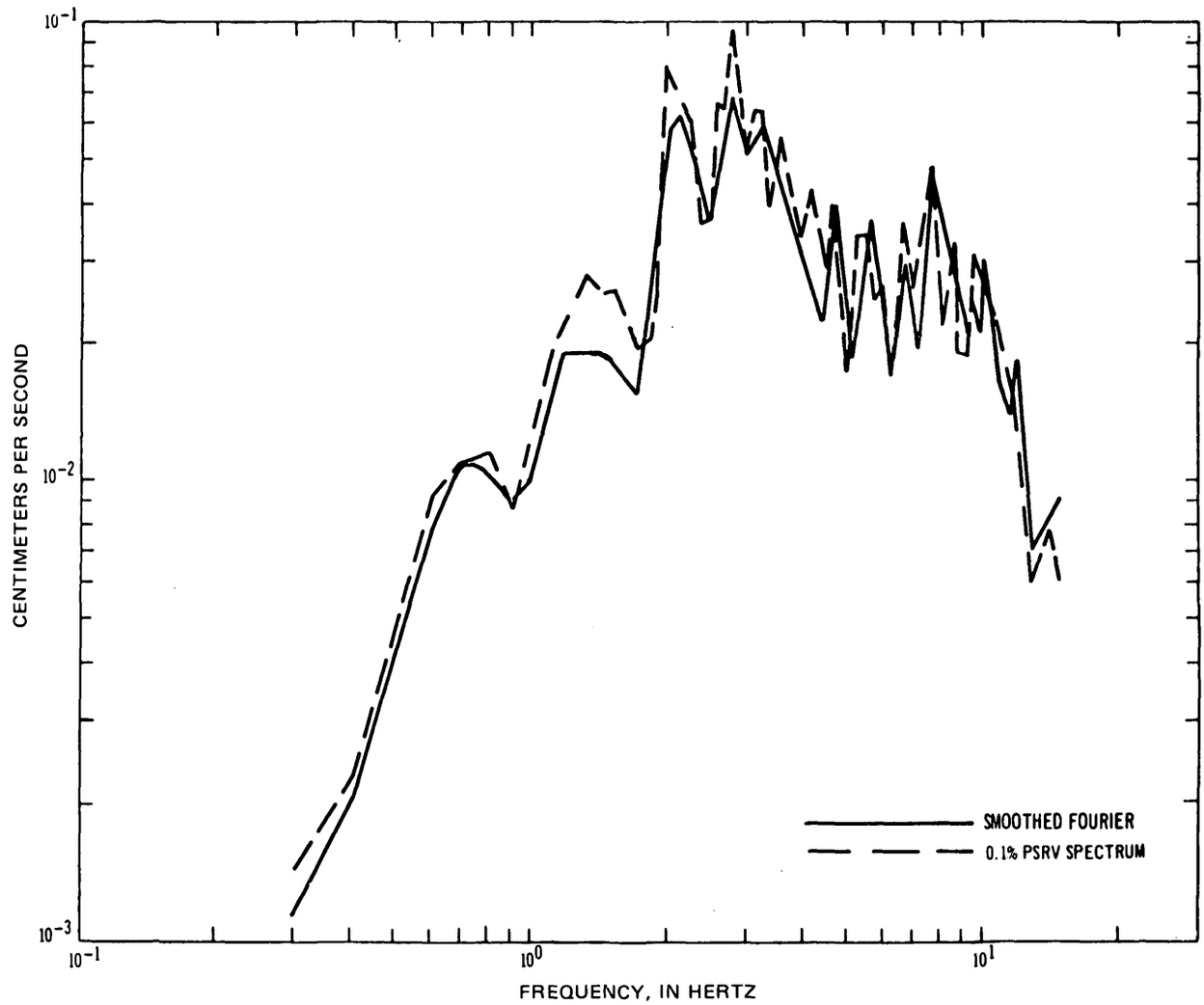

FIGURE 13.—Comparison of the smoothed Fourier amplitude spectrum and 0.1-percent-damped pseudorelative-velocity spectrum of the same aftershock record.

Hays, W. W., Bennett, T. J., and Brumley, M. D., 1973, Time dependent spectral analysis of ground motion: U.S. Dept. Commerce, Natl. Tech. Inf. Service, NVO-1163-TM-37/LL, 42 p.

Joyner, W. B., and Chen, A. T. F., 1975, Calculation of nonlinear ground response in earthquakes: Seismol. Soc. America Bull., v. 65, p. 1315–1336.

King, K. W., 1969, Ground motion and structural response instrumentation, chap. 8 *of* Technical discussions of off-site safety programs for underground nuclear detonations: U.S. Dept. Commerce, Natl. Tech. Inf. Service, NVO-40, p. 83–97.

Navarro, R., 1975, Seismic attenuation studies at the Idaho National Engineering Laboratory: U.S. Geol. Survey Open-File Report 75-512, p. 66.

Page, R. A., Blume, J. A., and Joyner, W. B., 1975, Earthquake shaking and damage to buildings: Science, v. 189, p. 601–608.

Perez, V., 1973, Velocity response envelope spectrum as a function of time, for the Pacoima Dam, San Fernando Earthquake, February 9, 1971: Seismol. Soc. America Bull. v. 63, no. 1, p. 299–313.

Pilant, W. L., and Knopoff, 1964, Observations of multiple seismic events: Seismol. Soc. America Bull., v. 54, p. 19–39.

Trifunac, M. D., 1971, Response envelope spectrum and interpretation of strong earthquake ground motion: Seismol. Soc. America Bull., v. 61, p. 343–356.

URS/John A. Blume and Associates, Engineers, 1975, Effects prediction guidelines for structures subjected to ground motion: Report JAB-99-115, UC-11 to U.S. Energy Research and Devel. Adm., 389 p.

U.S. Army Construction Engineering Research Laboratory, 1976, Seismic design—Proceedings of a seminar at Champaign, Ill.: Construction Eng. Research Lab. Tech. Rept. available from U.S. Dept. Army, Const. Eng. Research Lab., P.O. Box 4005, Champaign, Ill. 61820.

Wallace, R. E., 1974, Goals, strategy, and tasks of the earthquake hazard reduction program: U.S. Geol. Survey Circ. 701, p. 26.

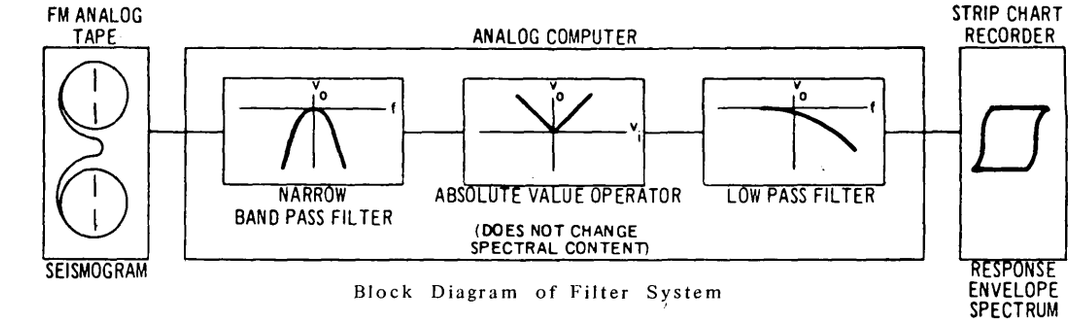

Block Diagram of Filter System

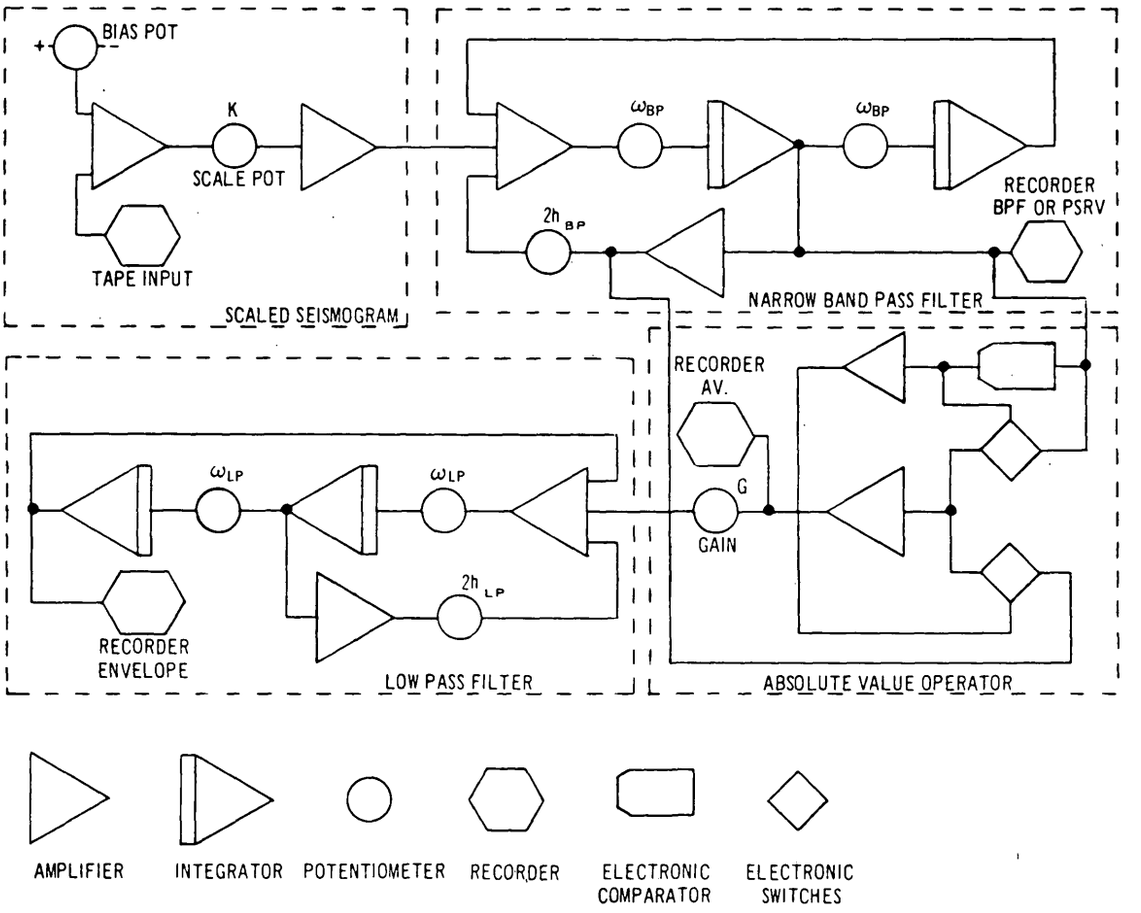

Analog Schematic of Filter System

FIGURE 14.—Hybrid-computer filter system used to generate time-dependent response envelopes. Symbols used are: V_o, output of the transfer function; V_i, input of the transfer function; f, frequency; K, normalizing scale factor; ω_{BP}, center frequency (radiance) of the band-pass filter; h_{BP}, damping of band-pass filter; ω_{LP}, corner frequency (radians) of the low-pass filter; h_{LP}, damping of low-pass filter; and G, scaling gain.

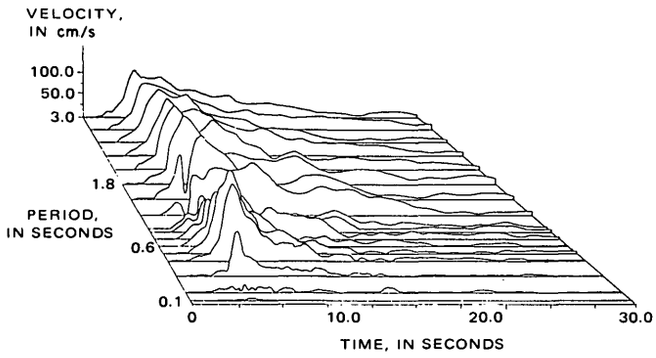

FIGURE 15.—Response-envelope spectrum, 1966 Parkfield, Calif., earthquake, N 65° E component.

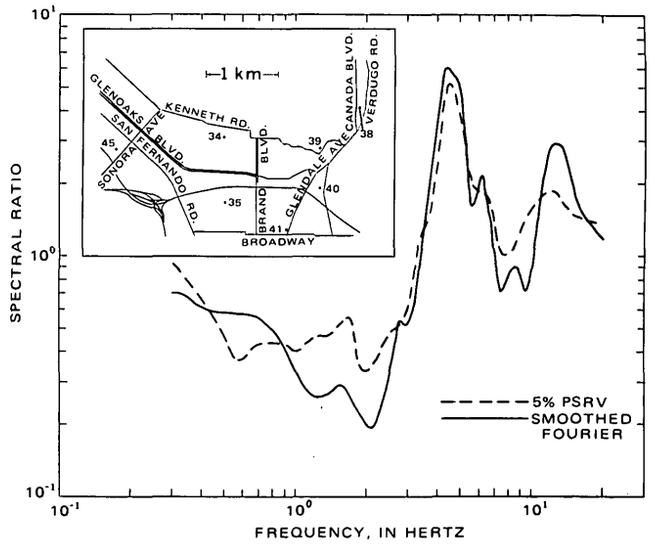

FIGURE 16.—Comparison of relative transfer functions obtained from smoothed Fourier amplitude and 5-percent-damped pseudorelative velocity spectra; Station 38 to Station 41, Glendale, Calif.

RECENT PUBLICATIONS OF THE U.S. GEOLOGICAL SURVEY

The following books may be ordered from the Branch of Distribution, U.S. Geological Survey, 1200 South Eads Street, Arlington, VA 22202 (an authorized agent of the Superintendent of Documents, Government Printing Office). Prepayment is required. Remittances should be sent by check or money order payable to U.S. Geological Survey. Give series designation and number, such as Bulletin 1368–A, and the full title. Prices of Government publications are subject to change. Increases in costs make it necessary for the Superintendent of Documents to increase the selling prices of many publications offered. As it is not feasible for the Superintendent of Documents to correct the prices manually in all the previous announcements and publications stocked, the prices charged on your order may differ from the prices printed in the announcements and publications.

Professional Papers

P 456–E. Middle Paleozoic sedimentary phosphate in the Pensacola Mountains, Antarctica, by J. B. Cathcart and D. L. Schmidt. 1977. p. E1–E18. 65¢.

P 581–F. Stratigraphy and Tertiary development of the continental margin east of Florida, by John Schlee. 1977. p. F1–F25; plate in pocket. $2.35.

P 608–B. General geology and petrology of the Precambrian crystalline rocks, Park and Jefferson Counties, Colorado, by C. C. Hawley and R. A. Wobus. 1977. p. B1–B77; plate in pocket. $3.75.

P 867–C. Tectonic events since early Paleozoic in the Carlin-Pinon Range area, Nevada, by J. F. Smith, Jr., and K. B. Ketner. 1977. p. C1–C18. 65¢.

P 880. Geology of the Apollo 14 landing site in the Fra Mauro highlands, by G. A. Swann, N. G. Bailey, R. M. Batson, R. E. Eggleton, M. H. Hait, H. E. Holt, K. B. Larson, V. S. Reed, G. G Schaber, R. L. Sutton, N. J. Trask, G. E. Ulrich, and H. G. Wilshire, 1977. 103 p.; plates in pocket. $7.05.

P 984. Geology of an Upper Cretaceous copper deposit in the Andean Province, Lassiter Coast, Antarctic Peninsula, by P. D. Rowley, P. L. Williams, and D. L. Schmidt. 1977. 36 p. $1.15.

P 991. Thermal loading of natural streams, by A. P. Jackman and Nobuhiro Yotsukura. 1977. 39 p. 70¢.

P 995. Conodont color alteration—an index to organic metamorphism, by A. G. Epstein, J. B. Epstein, and L. D. Harris. 1977. 27 p. $1.10.

P 1018. Characteristics of thin-skinned style of deformation in the southern Appalachians, and potential hydrocarbon traps, by L. D. Harris and R. C. Milici. 1977. 40 p.; plates in pocket. $4.

Bulletins

B 1397–B. Mineral resources of the Laramie Peak study area, Albany and Converse Counties, Wyoming, by Kenneth Segerstrom, and R. C. Weisner, *with a section on* Aeromagnetic interpretation, by M. D. Kleinkopf. 1977. p. B1–B35; plate in pocket. $1.80.

B 1403. Mineral resources of the Granite Fiords Wilderness Study Area, Alaska, by H. C. Berg, R. L. Elliott, J. G. Smith, T. L. Pittman, and A. L. Kimball, *with a section on* Aeromagnetic data, by Andrew Griscom. 151 p.; plates in pocket. $3.75.

B 1422–B. The Maudlow and Sedan Formations of the Upper Cretaceous Livingston Group on the west edge of the Crazy Mountains basin, Montana, by Betty Skipp and L. W. McGrew. 1977. p. B1–B68. $1.15.

B 1422–E. Stewart Gulch Tongue—A new tongue of the Eocene Green River Formation, Piceance Creek basin, Colorado, by W. J. Hail, Jr. 1977. p. E1–E8. 35¢.

B 1423. Geology of the Red Mountain mining district, Esmeralda County, Nevada, by W. J. Keith. 1977. 45 p.; plates in pocket. $2.40.

B 1425. Geology of the Ketchikan D–1 and Bradfield Canal A–1 quadrangles, southeastern Alaska, by J. G. Smith. 1977. 49 p.; plate in pocket. $2.

Water-Supply Papers

W 2041. Elements needed in design of a ground-water-quality monitoring network in the Hawaiian Islands, by K. J. Takasaki. 1977. 23 p.; plates in pocket. $6.35.

W 2044. Modeling chloride movement in the alluvial aquifer at the Rocky Mountain Arsenal, Colorado, by L. F. Konikow, 1977. 43 p. 75¢.

Back issues of the "Journal of Research of the U.S. Geological Survey" available at reduced prices—for limited time only. Copies of individual issues of volumes 1, 2, 3, and 4, published in 1973–76, are available at $1.25 per issue until December 31, 1977, or sooner if stocks become depleted. Order from U.S. Geological Survey, Branch of Distribution (Book Sales), 1200 South Eads Street, Arlington, VA 22202. Prepayment is required. Make check or money order payable to U.S. Geological Survey.

TECHNICAL INFORMATION OFFI
U S GEOLOGICAL SURVEY TOPO D
NATIONAL CENTER STOP 520
RESTON VA 22092